# MODELING AND CONTROL
# OF AN IMPROVED
# HYBRID PNEUMATIC-ELECTRIC ACTUATOR

MODELING AND CONTROL OF

AN IMPROVED HYBRID PNEUMATIC-ELECTRIC ACTUATOR

By Mantian Xue, B.A.

A Thesis

Submitted to School of Graduate Studies

In Partial Fulfillment of Requirements

For the Degree

Master of Applied Science

McMaster University

MASTER OF APPLIED SCIENCE (2013)

McMaster University

(Mechanical Engineering)

Hamilton, Ontario

TITLE:       Modeling and Control of an Improved Hybrid Pneumatic-Electric Actuator

AUTHOR:      Mantian Xue, B.A. (Northeastern University, China)

SUPERVISOR:      Dr. Gary M. Bone, Professor

NUMBER OF PAGES:      xxxv, 261

# ABSTRACT

Combining the advantages from electric motor and the pneumatic actuator, the hybrid pneumatic-electric actuator is expected to be safe, low-cost, clean, high power to weight ratio, and to provide precise position control. In this thesis, the modeling and control of an improved hybrid pneumatic-electric actuator prototype is presented.

The actuator's main components consist of a low-friction pneumatic cylinder, two on/off solenoid valves, and a small DC motor. The cylinder and motor are connected to a common output shaft using gears. The shaft rotates a single-link robot arm. Its position is measured by an incremental encoder. The prototype was improved by incorporating faster switching valves, flow controls, a faster valve drive circuit, a high resolution encoder rather than the existing linear potentiometer, more accurate pressure sensors and stronger gears.

A system dynamic model without the valve dynamic was developed identified and validated using open-loop experiments. The valve models for a discrete input and PWM input were then developed and validated separately. The use of bipolynomial function and artificial neural network fitting methods for modeling the valve mass flow rates were compared. The combined system model with valve dynamics was validated experimentally.

Two model-based nonlinear position controllers, using the backstepping and discrete-valued model predictive control (DVMPC) methods, were designed, simulated

and extensively tested. Testing was done with the actuator operating using the cylinder alone, the motor alone and in hybrid mode using the cylinder and motor together. Operating in the hybrid mode reduced the root-mean-square error (RMSE) up to 80%.

A stability analysis for the backstepping control including the valve modeling error, friction model error, and electric motor torque modeling error was performed. Compensation terms were designed to improve the performance for the two controllers. Additional stability analyses were performed for backstepping controller with a feedback term and the DVMPC with motor control. A payload estimation algorithm was proposed and shown to enhance the robustness of the DVMPC operating in vertical configuration.

Simulations and experiments demonstrated that the model-based controllers performed well for both vertical and horizontal configurations. Regarding robustness to payload mismatch, if the payload was within the load capacity of the hybrid actuator, the model-based controllers were both insensitive to the payload variations in horizontal configuration. The backstepping controller was also robust to the payload variations in the vertical configuration.

In experiments, the backstepping control in hybrid actuation mode produced a RMSE of 0.0066 radian for a 2 Hz sine wave desired position trajectory with a 0.3 radian amplitude. With DVMPC, this value decreased to 0.0045 radian. These tracking errors were shown to be 30 to 50% less than those produced by a modified linear position plus velocity plus acceleration controller.

# ACKNOWLEGEMENT

My sincere gratitude first goes to my supervisor Dr. Gary M. Bone for his guidance, and support through the two years of my graduate study. He has walked me through all of the stages of this research. Without him, this thesis could never have been finished.

Secondly, I would like to express my thanks to my colleagues: Justin Flett, Graham Ashby, and Darren Van Rooyen for their advices and help. I also thank the technicians: Jim McLaren, Joe Verhaeghe, and Mark Mackenzie for their valuable support and suggestions on the test setup. And I would like to thank all my friends for their encouragement.

Finally, I would like to give my special thanks to my beloved parents for their unconditional encouragement and support.

# CONTENTS

# LIST OF FIGURES

# LIST OF TABLES

xvii

# LIST OF APPENDIX TABLES

# ABBREVIATIONS

| | |
|---|---|
| ADC | analog to digital convertor |
| ANN | artificial neural network |
| ARX | autoregressive with external input |
| DOF | degree of freedom |
| DVMPC | discrete-valued model predictive control |
| DZC | dead zone compensation |
| FF | feedforward |
| IDC | inverse dynamic control |
| MAE | maximum absolute error |
| PD | proportional plus derivative |
| PID | proportional plus integral plus derivative |
| PVA | position plus velocity plus acceleration |
| PWM | pulse-width modulation |
| RMSE | root mean square error |
| SSA | steady-state amplitude |
| SSE | steady-state error |
| ZOH | zero-holder hold |
| DC | direct current |
| SISO | single input single output |

# NOMENCLATURE

$A_a, A_b$    Piston areas in chambers $A$ and $B$, respectively

$C_{vf}, \tau_{vf}$    Coefficients of viscous friction

$C_{sf}$    Coefficient of static friction

$C_{fill}$    Filling coefficient for the solenoid valve alone

$C_{flow\_c\_fill}$    Filling coefficient for the solenoid valve with flow control

$C_{dis}$    Discharging coefficient for the solenoid valve alone

$C_{flow\_c\_dis}$    Discharging coefficient for the solenoid valve with flow control

$c_{forget}$    Forgetting factor

$e, \hat{e}$    Error, predicted error

$\tilde{e}, \dot{\tilde{e}}$    Measured position and velocity tracking errors

$I_{eq}$    Equivalent inertia

$I_{arm}$    Inertia of the arm

$I_{payload}$    Inertia of the payload

$I_{block}$    Inertia of the slide block

$\hat{I}^*_{payload}$    Estimated inertia of the payload

| | |
|---|---|
| $\hat{I}_{payload}$ | Smoothed estimated inertia of the payload |
| $K_{amp}$ | Amplifier gain of the motor |
| $K_p, K_v, K_a, K_{ff\_v}, K_{ff\_a}$ | PVA controller parameters |
| $K_{bs\_motor,p}, K_{bs\_motor,d}$ | Electric motor compensation parameters for backstepping controller |
| $K_{IDC,p}, K_{IDC,d}$ | Inverse dynamic controller gains |
| $K_t$ | Motor torque constant |
| $k_1, k_2, k_3, k_4$ | Backstepping controller gains |
| $k$ | Ratio of specific heats of air |
| $L_{arm}$ | Effective length of the arm |
| $L_{payload}$ | Effective distance to the payload |
| $M_{arm}$ | Mass of the arm |
| $M_{payload}$ | Mass of the payload |
| $\hat{\dot{m}}_a, \hat{\dot{m}}_b$ | Predicted mass flow rate into the chamber A and B |
| $\dot{m}_{choked}$ | Choked mass flow rate |
| $\dot{m}_{a,ff}, \dot{m}_{b,ff}$ | FF desired mass flow rates |
| $N_p$ | Prediction horizon |
| $P_0$ | Atmospheric pressure |

| | |
|---|---|
| $P_s$ | Supply pressure |
| $P_{down}$ | Downstream pressure |
| $P_{up}$ | Upstream pressure |
| $P_a, P_b$ | Absolute pressure inside chamber A and B |
| $\hat{P}_a, \hat{P}_b$ | Predicted absolute pressure inside chamber A and B |
| $P_{a,ff}, P_{b,ff}$ | FF desired chamber pressures |
| $T_{pwm\_period}$ | PWM period |
| $T_s$ | The sampling period |
| $U_{PVA\_MAX}$ | PVA control parameter |
| $u_{\text{virtual}}$ | Virtual control input for PVA control |
| $u_{bs,va}, u_{bs,vb}$ | Backstepping control signals |
| $z_1, z_2, z_3, z_4$ | Backstepping controller states |
| $\theta_{threshold}$ | Threshold of position error for payload estimation |
| $\theta, \dot{\theta}, \ddot{\theta}$ | Angular position, velocity and acceleration |
| $\theta_d, \dot{\theta}_d, \ddot{\theta}_d$ | Desired angular position, velocity and acceleration |
| $\hat{\theta}, \hat{\dot{\theta}}, \hat{\ddot{\theta}}$ | Predicted angular position, velocity and acceleration |
| $\tau_{motor\_PD}$ | Backstepping control motor feedback term |
| $\tau_{e,threshold}$ | Threshold of torque error for payload estimation |

| | |
|---|---|
| $\hat{\tau}_c$ | Predicted pneumatic cylinder torque |
| $\tau_{motor}$ | Electric motor torque |
| $\hat{\tau}_{motor}$ | Predicted electric motor torque |
| $\hat{\tau}_{friction}$ | Predicted friction torque |
| $\hat{\tau}_g$ | Predicted gravity torque |
| $\tau_{bs,motor}$ | Backstepping control signal |

# CHAPTER 1.          INTRODUCTION

## 1.1    Traditional Industrial Robots

In this thesis, the term "robot" refers to a programmable robotic arm. Due to the continuing growth of global manufacturing demands, traditional industrial robots have grown in popularity and are used the all over the world to improve industrial productivity (http://www.ifr.org/). The area of industrial robots usage was mainly limited to material handling, robotic welding, robotic assembly, robotic dispensing, and robotic processing because of the process operation is relatively simple and the design of robot is limited by the development of hardware and software(Jobin 2012). Compared with humans, traditional industrial robots have superior strength and endurance, but they are more dangerous and have vastly inferior intelligence. Their use frees people from dirty, dull, and/or dangerous tasks, and has been shown to increase employment (Shafi 2012).

The strength and speed of traditional industrial robots, along with their design, can make them unsafe. Although the number is small, the accidents caused by robots can be catastrophic for workers, employers, and robot manufacturers. Nicolaisen (1987) studied both non-fatal and fatal accidents caused by industrial robots, and concluded that for safety problems "A solution to the problems will neither arrive on its own, nor emerge from the transformation of any single phenomenal idea. As a rule it consists rather of a more or less successful combination of different partial solutions which have frequently emerged in laborious small-scale work by the groups taking part in the project. ".

The effort made to keep human workers safe is remarkable. The safety regulations today in the manufacturing environment are extensive, and sometimes seen as overcautious. A safe working environment is typically created by isolating the robot(s) using physical barriers and/or sensors for detecting human presence and stopping the robot. However, the design of industrial robots makes them inherently unsafe. One important hazard of a traditional industrial robot comes from the way its joints are actuated. With few exceptions, electric motors are used because of their high accuracy, quickness, and ease of control. The motor is connected to gearbox in order to provide sufficiently large torque. The output shaft of the gearbox drives the joint and moves one link of the robot arm. If an impact of a human and the operating robot happens, it may cause serious or even fatal injuries. Although sensors and software can be used to avoid collisions, they do provide adequate reliability. For a robot to be inherently safe it must not cause serious injuries even when sensor and software faults occur. This means the inherent safety must come from the mechanical design of the robot.

From the designer's and consumer's perspectives, the lack of inherently safety is the Achilles' heel of industrial robots. It prevents robots from expanding into other industrial and service areas where isolating robots is not a feasible safety solution.

## 1.2   Collaborative Robots

Only a few inherently safe robots have been sold, and one is currently available on the market. Guizzo and Ackerman (2012) introduced the robot "Baxter", made by Rethink Robotics, in 2012. They emphasized that the traditional actuation approach (i.e.

motors plus gearboxes) is good for certain jobs such as welding cars in factories, however it is a hazardous to human workers near the robot. Baxter, on the other hand, is friendly to workers because its "series elastic actuators" are designed to be mechanically compliant. Rather than a rigid connection, the motor and gearbox drive a spring, which in turn drives the joint. If an impact happens, due to its compliance, the spring is able to absorb the collision energy to prevent serious human injuries. This elastic actuation solution is indeed inherently safe. However, its maximum load capacity, speed and the accuracy are poor compared to traditional industrial robots. Guizzo and Ackerman (2012) claimed that the robot has an accuracy of about 0.5~1cm, a maximum speed of 0.6 m/s and can lift up to 2.25kg.  Robots like Baxter, although sufficiently safe, will not be capable of working on operations where high accuracy, high speed or high loads are required. For example, it would not be capable of assembling electronic circuit boards, or assembling cars, or opening lids when used as a personal robot assistant.

## 1.3   The Need for a Hybrid Pneumatic-Electric Actuator

The collaborative robot Baxter is a revolutionary product. However, its limited load and speed capabilities, and inadequate accuracy, make it human friendly but not useful enough for widespread application. The future generation of collaborative robots needs to be more accurate while retaining the same (or higher) level of safety. Furthermore, it should be affordable to all manufacturers and even ordinary consumers. To achieve such goals, a new actuation solution is required.

Baxter's elastic actuator is inherently safe because of its spring. However, it has problems with limited accuracy and the relatively small maximum torque.

Electric motor is easy to control, and can provide high accuracy, and rapid response. However, it needs a gearbox to amplify its torque which inevitably also amplifies it friction and reflected inertia. This amplified friction and reflected inertia can produce large impact forces. Consequently, a robot arm driven by a motor with a large ratio gearbox is dangerous when a collision takes place.

A pneumatic actuator provides a high power to weight ratio, and is relatively low cost. Most importantly, it is even inherently safe. It is driven by the pressurized air which has natural compliance. The challenge of using a pneumatic actuator for a robot joint is attaining the required fast and accurate position control due to the nonlinearity of the compressed air.

If the pneumatic and electric actuator can be properly combined together, the new actuator will have inherent safety, high accuracy, sufficient torque and relatively low cost. A prototype of such an actuator, a "hybrid pneumatic-electric actuator" was presented by Bone and Chen (2012). Their experiments proved that the prototype hybrid actuator has a high accuracy relative to a pneumatic actuator, and produces a sufficiently large torque (i.e. similar to a small traditional industrial robot). Improving the performance and robustness of such a hybrid actuator is necessary for its practical application, and is the subject of this thesis.

## 1.4    Objective and Organization of the Thesis

The main objectives of the thesis are to improve the modeling and control performance of a hybrid pneumatic-electric actuator for robotics applications. The actuator prototype will also be improved. The new prototype will be modeled together with two new valve dynamics models. Two nonlinear controllers will be designed, simulated and tested in different conditions. Robustness of the proposed controllers will be investigated in simulation and experiments.

The organization of the thesis is as follows: Chapter 2 reviews the most important literature on pneumatic and hybrid actuator modeling and servo controller design. The system architecture and derivation of the system model are introduced in Chapter 3. The system model includes the valve dynamics and mechanical dynamics. The model is validated by open-loop experiments. In Chapter 4, two model-based nonlinear controllers, backstepping control and discrete-valued model predictive control, are designed. They are compared to a PVA controller in simulation and experiment. In Chapter 5, simulations are used to investigate the performance of the two designed nonlinear controllers under different operating conditions. The robustness of the controllers is studied for two actuator combinations (i.e. pneumatic alone and hybrid) by simulating payload mismatch, and horizontal vs. vertical motion. Similar experiments were done to verify the simulation results. These are reported and discussed in Chapter 6. Conclusions are drawn in Chapter 7. The achievements of the result are also summarized, and recommendations for future work are suggested.

# CHAPTER 2.    LITERATURE REVIEW

## 2.1   Introduction

In this thesis, system modeling, control algorithm development, and hardware architecture will be investigated for a novel hybrid actuator. Two nonlinear controllers will be designed and tested. The most important relevant publications will be reviewed in this chapter. Section 2.2 reviews the literature on hardware design of hybrid actuators. Section 2.3 reviews the system modeling literature. Section 2.4 reviews the papers on position servo control of pneumatic and hybrid pneumatic-electric actuators. Section 2.5 summarizes the findings.

## 2.2   Hybrid Actuator Design

There is very little existing literature on the design the pneumatic-electric hybrid actuator, especially for the purpose of robotic actuation.    It is important to note that a pneumatic actuator may be connected either in series or in parallel to an electric actuator. The series connection may be used to increase the accuracy and range of motion, but it will not increase the power output of the hybrid actuator.  When the actuators are connected in parallel the accuracy and power output can both be increased.  Since an actuator with high accuracy and high power (particularly high torque) is necessary for robots, this thesis will concentrate on only parallel connected hybrid pneumatic-electric actuators.

The concept of hybrid pneumatic-electric actuation for a robotic manipulator was first proposed in 1987 by Petrosky (1988). His design concept consisted of a rotary pneumatic actuator connected directly to an electric motor. He wished to create a lightweight high torque actuator and to reduce the possibility of the motor overheating by providing most of the torque pneumatically. No evidence of a product (or even a prototype) was found in the literature.

Later, Mills simulated an electric motor connected in parallel with a pneumatic muscle together to drive a robot link (Mills 1993). His goal was to achieve independent torsional stiffness control and joint position control by applying an appropriate control algorithm. Simulation results were given to show the effectiveness of proposed hybrid actuator and control strategies. No hardware experiments were performed.

Takemura et al. (2000) proposed another hybrid actuator design. A pneumatic motor was connected to a smaller electric motor in parallel through gears. The gear ratio between DC motor and pneumatic motor was 1:2. The DC motor provided 1/3 of the total output torque, and was used to make the hybrid actuator easier to control. A pneumatic motor is not a good choice for an inherently safe actuator since its seals produce a large friction torque.

Zinn et al. (2004) proposed a new actuation concept for robotic manipulator called $DM^2$ actuation. With this concept, two actuators are located at different positions on the robot. The larger actuator is a series elastic actuator that is located at the base of the arm, and the smaller one is an electric motor located at the joint. They are connected in parallel

at the joint by a cable. The series elastic actuator is intended to provide the majority of the low frequency component of the torque with high compliance. The small electric motor is intended to provide the majority of the high frequency torque. In addition to providing high performance and inherent safety, this actuator distribution design was expected to greatly reduce the effective inertia of the robot. The proposed actuation method was demonstrated on a 2-DOF prototype robot arm.

Following Zinn et al.'s $DM^2$ actuation concept, Shin et al. (2010) proposed an improved version of $DM^2$, and built a prototype named the Stanford S2$\rho$ 1.5 robot. In the new design, the series elastic actuator was replaced by four pneumatic muscle actuators to provide a faster response. The pressure inside each muscle was controlled by a pair of proportional valves, one for filling and one for discharging. The specifications of the electric motor were not provided. The proposed hybrid actuator was capable of tracking a 26 Hz small amplitude sine wave position trajectory. Using the pneumatic muscles alone, the prototype was capable of tracking a 6 Hz sine wave trajectory with the same amplitude. No payload was used. Their controller design will be reviewed later in section 2.4.

Bone and Chen (2012) proposed a different pneumatic-electric hybrid actuator design. A low friction double-acting pneumatic cylinder was connected in parallel with an electric motor using three gears. Two on/off solenoid valves were used with the pneumatic actuator. Solenoid valves are known to be less expensive than proportional valves (e.g. $120 CAD for a FESTO solenoid on/off valve vs. $970 CAD for a FESTO

proportional valve). This fact, plus the use of two valves rather than eight, means that the valves cost roughly 95% less than those used with the Stanford S2$\rho$ 1.5 robot. The electric motor is connected to output shaft through a 5:1 ratio transmission which greatly reduces friction torque compared with the high ratio gearboxes (e.g. 100:1) typically used with robots. The motor alone is able to provide about 12% of the total torque. Their controller design will also be reviewed in section 2.4.

## 2.3    System Modeling

The electric-pneumatic hybrid actuator combines pneumatic power with electric power. The pneumatic actuator will provide the majority of the torque, with the remainder provided by the electric motor. Therefore the pneumatic actuator will dominate the dynamic behavior of the hybrid actuator. The dynamics of the actuator are primarily influenced by the flow characteristics of the valves. Thus, the flow characteristics of the valves are extremely important.  There are three types of pneumatics valves.  On/off solenoid valves cannot maintain a state other than on or off, however they can be used with pulse-width modulation (PWM) to provide a continuously variable flow rate. Proportional valves are designed to provide a continuously variable flow rate.  Servo valves are designed for faster and more accurate performance than proportional valves. The related literature will be reviewed in this section.  The focus will be on on/off solenoid valves since they will be used in the hybrid prototype presented in sections of System Modeling and Controller Design and Experiment in Chapter 3.

van Varseveld and Bone (1997) proposed a novel PWM algorithm for using on/off valves for position control. The proposed PWM algorithm set the two three-way valve inputs in a nonlinear manner to compensate for the valve dead zones. Unlike regular linear PWM algorithms, the proposed PWM scheme has a linear output/input (actuator velocity/PWM duty cycle) relationship. The PWM algorithm was validated by measuring actuator velocity with different PWM inputs. Later, an autoregressive with external input (ARX) model with six parameters was obtained by using open-loop test data. The pneumatic servo system was much less expensive than those developed by previous researchers using proportional valves.

Wang et al. (1998) proposed a switching model to describe the three-way on/off valve switching characteristics and a novel way of estimating on/off valve model parameters. Open-loop experiments of different supply pressures were used to measure the switching on/off delay. The mass flow rates were obtained by solving mass flow rate equation and perfect gas equation. The nine valve model parameters were estimated by minimizing the error between measurements and the simulated model. Finally, the obtained model was validated by open-loop experiments.

Messina et al. (2005) investigated in details of an analytical model of the dynamics of pneumatic actuator controlled by PWM. Experiments were performed at different initial position with different duty cycles. The analytical model was developed based on three main assumptions, namely: "the thermodynamic quantities in all their occurring events are considered spatially averaged, other forms of energy are considered

negligible, chambers are considered perfectly and pneumatically insulated, the influences

of the connecting tubes is neglected and, finally, the supply conditions are assumed to be

instantaneously constant." The measurement of the valve's plunger suggested that the

three-way valve dynamics introduced a delay of about 2 ms with respect to the PWM

control signal. The system model had 46 parameters and was validated through

experiments. The simulated position of the pneumatic actuator varied up to 3 mm relative

to its measured position.

Ahn and Yokota (2005) proposed a modified PWM control algorithm for a

pneumatic servo system. Eight two-way on/off solenoid valves were used. Compared to

traditional PWM scheme, a minimal pulse width time was added to avoid the dead zone

of the valves with 14 parameters. The control inputs to the valves were set to zero when

the position error was within a certain threshold. The parameter identification and

validation of the valve model was not provided.

Smaoui et al. (2006) designed a servo pneumatic system using backstepping

control method. Their pneumatic actuation system used two three-way servo valves. The

valves were assumed to be identical. The relationship of input voltage, chamber pressure,

and mass flow rate into the chamber were described by a static function. They made the

same suppositions as Shearer (1956).  They did not provide information on the valve

parameters, the parameter estimation method, or model validation.

Shen et al. (2006) proposed a novel nonlinear model based PWM pneumatic servo

system. PWM controlled three-way on/off solenoid valves were used. The nonlinear

averaging technique was used as the basis of controller development. However, the valve modeling was similar to Smaoui et al. (2006). The same assumptions were made. The mass flow rate through the valve orifice was divided into choked and unchoked regimes. The valve model had one unknown parameter and the system was modeled by 11 parameters. The four different discrete modes of valve switching are described respectively. The parameter identification and validation of the valve model was not provided.

Rao and Bone (2008) designed a backstepping controller for a miniature servo pneumatic system. The experiments were conducted by using 9.5 mm bore and 6.4 mm pneumatic cylinders, and four two-way proportional valves. A novel mass flow rate model with nine parameters was developed for the proportional valve since it had a different structure compared to traditional spool servo valve. The mass flow rates at different chamber pressure and valve input were estimated from the pressure response. Tests were performed for step inputs in valve voltage and a fixed piston position. Then the surface of estimated mass flow rate was fitted by a $2^{nd}$ order bipolynomial function. The rest of the system model was obtained by mechanistic modeling. The derived model was validated through open-loop experiments.

Carneiro and de Almeida (2012) constructed a novel pneumatic servo system model for control purposes. The system consisted of two three-way servo valves, two pressure sensors, a position sensor, an accelerometer and a pneumatic cylinder. An artificial neural network (ANN) with two inputs (valve input voltage and chamber

pressure) and two hidden layers was used to fit the mass flow rate model. The first and second hidden layers have ten and six neurons, respectively. A friction model was also obtained using the same ANN structure. A reduced order pressure model was shown, which according to the author outperformed classical pressure models. The number of valve model parameters was not provided. System model validation was provided by experiments. The detailed information on the open-loop tests used for collecting the training data set for the ANNs was not provided.

Hodgson et al. (2012) designed a sliding mode controller for an electro-pneumatic positioning system. The system included one pneumatic cylinder and four two-way on/off valves. Two valves were connected to each chamber of the cylinder. The mass flow rate through the valve orifice was described by the standard choked flow and unchoked flow equations with two parameters. The on/off states of the four valves have 16 combinations or modes. The paper only utilized seven of these modes. The dynamic model of the pneumatic actuator described by nine parameters with a seven mode discrete input was presented. The parameter identification and validation of the model was not provided.

Bone and Chen (2012) designed a novel predictive controller for a hybrid electric-pneumatic actuator. The pneumatic actuation part was similar to pneumatic servo systems, and consisted of one double acting pneumatic cylinder with two three-way on/off valves. The mass flow rate was modeled for each state of the on/off valve. The mass flow rate through orifice is divided into choked flow and unchoked flow depending on upstream and downstream pressures. The two parameters of the mass flow rate model were

obtained through open-loop experiment data fitting. A friction model combining viscous friction with Coulomb friction model was identified.

## 2.4    Position Servo Control

This section will focus on the important literature on linear and nonlinear controller design for pneumatic and hybrid actuators.

van Varseveld and Bone (1997) proposed a PWM controlled pneumatic servo system using an extended discretized proportional plus integral plus derivative (PID) controller. The novel PWM algorithm set each of the two on/off valves differently at their dead zones. Several ARX models were obtained from open-loop experiments with different initial positions. A conventional discretized PID controller was extended with friction compensation, position feedforward (FF), and bounded integral action. The PID controller gains were found using the mid-stroke position ARX model parameters and a single tuning parameter. Experiments under various conditions were performed using the proposed PWM scheme (running at 62.5 Hz) and controller. The worst case steady-state error (SSE) was 0.21 mm. A following error less than 2 mm was achieved for S-curve profiles.  A 0.11 mm step movement was also achieved. These experiments were performed horizontally without payload. An additional experiment with a 4.6 kg payload was done, the response was stabilized further confirmed the robustness of designed controller.

Ning and Bone (2002) designed a linear PVA/PV controller for a pneumatic servo system with one proportional valve. The term PVA/PV was used since their controller

switched the noisy acceleration feedback off when the position error was within certain threshold. This was found to shorten the settling time. A friction compensation term was added to avoid dead zone of the cylinder. A SSE of 0.01mm was verified experimentally for vertical and horizontal motions with a 5 kg payload. Ning and Bone (2005) presented a pole placement method for designing the PVA controller more systematically. A model-based FF term was also added into control signal. Experiments under a wide range of conditions were performed. They achieved a SSE of 0.01 mm and tracking errors less than 3 mm. The sampling rate was 500 Hz in both papers.

Ahn and Yokota (2005) proposed an intelligent switching controller for a pneumatic actuator using eight on/off valves. To provide a sufficiently large force in a short time period, the mass flow rate was increased by operating two valves in parallel. A PVA controller with modified PWM control signal was designed. To improve robustness of the controller, four payloads (0, 10, 20, 30 kg) were first selected. A PVA controller was manually tuned for each payload and the controller gains were recorded. Learning vector quantization neural network (LVQNN) was trained to identify the payload. The training data was obtained for 12 different cases of external load (0 to 32 kg). The controllers were switched online based on the output of the LVQNN. With no payload and a 600 mm step reference, the maximum overshoot was within 0.3%. Using the proposed modified PWM approach produced a 0.2 mm SSE while conventional PWM produced a 1.75 mm SSE. The results of a controller without switching (i.e. with fixed PVA gains) for four different external loads were shown to be significantly worse.

15

Shen et al. (2006) applied PWM sliding mode control to a pneumatic servo system with two on/off valves. The controller was designed based on a full nonlinear system model. They obtained this continuous input model by converting a discrete-input model using the nonlinear averaging approach. The designed sliding mode controller had four parameters and they were tuned manually in experiments. The valve control PWM period was at 25 Hz. Sine wave trajectories with frequencies of 0.25 Hz, 0.5 Hz, and 1 Hz were used with a payload of 10 kg. The pneumatic system operated horizontally. The maximum errors for all of the trajectories were larger than 5 mm.

Smaoui et al. (2006) proposed a pneumatic servo actuation system with two proportional valves using backstepping control. Feedback linearization was used to transform the pneumatic subsystem into pure integrators. Assuming no modeling error, they proved the global asymptotical stability. The designed backstepping controller had five gains. The efficient tuning method was not introduced. An experimental result for tracking a trajectory defined by a fifth-order polynomial function with no payload was shown. The maximum absolute error (MAE) was 1.62 mm. The steady state error is about 0.1 mm.

Rao and Bone (2008) designed a backstepping controller for a miniature pneumatic servo system with four servo valves. Including modeling errors, if the gains can be made sufficiently large then the designed backstepping controller is "globally asymptotically uniformly bounded and the tracking error can be made arbitrarily small." The desired mass flow rate was implemented by solving the quadratic equation obtained

from their valve model. The four controller gains were manually tuned. Experiments were conducted for S-curve and sine wave trajectories with three payloads (nominal, larger, smaller). With a 1.5 kg payload, the MAE was 0.5 mm for a 1 Hz sine wave trajectory, and the SSE was within 0.05 mm for an S-curve trajectory.

Hodgson et al. (2012) proposed a novel sliding mode controller for an electro-pneumatic positioning system with four on/off valves and seven discrete input modes. The designed controller had five parameters and the tuning method was introduced for smooth motion with the least valve switching activity. For 0.1 Hz to 1.5 Hz sine wave trajectories and 1 kg payload hanging from a pulley, the worst case root mean square error (RMSE) was 3 mm.

The remainder of this section covers hybrid pneumatic-electric actuators. Takemura et al. (2000) designed a point to point (PTP) controller and a trajectory tracking controller for their hybrid electric-pneumatic motor. For the purpose of PTP, the pneumatic motor was under sliding mode control. In the controller, the acceleration obtained by differentiating the position signal was replaced by an estimate based on the differential pressure in order to remove the acceleration feedback noise. Proportional plus derivative (PD) control was applied to the electric motor. For the purpose of high speed stopping accuracy, the PTP control concept was proposed. When the error is relatively large, the output shaft is mainly controlled by the pneumatic motor. When the error is small, the output shaft is only controlled by the electric motor. Experiments were performed with a vane-type pneumatic motor (279 W) and a DC motor (90 W), and a 1.5

kg payload attached the output shaft. A worst case SSE of 0.6 degrees was achieved for the hybrid actuator, compared to 1.0 degrees for the pneumatic motor operating alone.

Shin et al. (2010) designed and built a hybrid actuator based safety robot the Stanford S2ρ 1.5. The designed controller decompose desired torque input to low and high frequency components. The high frequency input was commanded directly to the electric motor as error. A linear closed-loop PID controller with a load cell was designed for indivdial pneumatic muscle (four in total) to provide the major torque. The nonlinearity of the pneumatic muscle was compensated by adaptive gains with respect to the pneumatic muscle length. The muscle length was obtained by solving an analytical model using the load cell feedback. Experiments were performed without external payload. The closed-loop PID control achieved 6 Hz bandwidth of the macro force control loop. The macro + micro hybrid actuation achieved a 26 Hz bandwidth of force control loop. The information on tracking errors was not provided. The maximum effective mass of the S2ρ 1.5 is 0.98 kg.

Bone and Chen (2012) designed a discrete-valued model predictive controller plus inverse dynamics controller (DVMPC + IDC) for their hybrid pneumatic- electric actuator. The pneumatic actuator was controlled using DVMPC and two on/off valves. The two on/off valves have four possible combinations in one sampling period. In their design, the valve input was assumed to be constant over the prediction horizon. It was chosen from the set of four valve input combinations by an exhaustive search which minimized the predicted sum of squared tracking errors. The IDC was applied to the

electric motor. An integral term was added in to reduce the SSE. For a 0.35 m arm and 17.1 kg equivalent mass of moving elements, they achieved a 2.5% MAE for vertical cycloidal trajectory using the pneumatic actuator alone. With the hybrid actuator the MAE was reduced to 0.37% for the same trajectory.

## 2.5   Conclusions

Up to today, the design of hybrid actuator follows the same idea of  Petrosky (1988). The existing design of hybrid pneumatic-electric actuator mainly has several forms: pneumatic motor + electric motor, pneumatic muscle actuator + electric motor, and pneumatic cylinder actuator + electric motor. For the purpose of safety robot joint actuation, the pneumatic motor + electric motor is not applicable for such application since the friction torque of pneumatic motor is relatively large such that it is not safe when impacts happens. The pneumatic muscle actuator + electric motor were adopted by the Stanford S2$\rho$ 1.5. The demonstrated experimental results were impressive. However, the payload capacity is therefore limited by the small torque that can be proveded from pneumatic muscle. The Stanford S2$\rho$ 1.5 used four pneumatic muscle plus at least eight proportional valves to solve the problem. Compared to pneumatic muscle, the cylinder has its own advantages. Most importantly it is capable of providing sufficient large torque with less nonlinearity.

The most on/off valve models built for control purposes were mainly based on the work of Shearer (1956). The exception is the analytical valve dynamic model with 46 related parameters developed by Messina et al. (2005). Using on/off discrete states at a

single sampling period, the finite combination of valve input could be used to calculate corresponding mass flow rate. However, modeling of mass flow rate dynamics for on/off valve with a PWM input was rare.

The linear and nonlinear controller combination dominated the choice of hybrid actuation control strategy. The separate controller design methodology was adopted by Takemura et al. (2000), Shin et al. (2010), Bone and Chen (2012). This is because of the bandwidth of the actuators is very different. The model-based nonlinear controller such as sliding mode control(Hodgson et al. 2012), backstepping control(Rao and Bone 2008) is able to stabilize pneumatic actuator. The linear PID or its variants has been used for electric motor control for years. The problem of such design is that it is difficult to prove the hybrid actuator with designed controllers has global asymptotical stability.

Based on above analysis, this thesis will focus on improving current hybrid actuator prototype built by Bone and Chen (2012). Develop accurate mass flow rate model for on/off solenoid valves with single discrete input and also PWM inputs.

Extend the backstepping controller designed for a pneumatic actuator by Rao (2005) and the DVMPC + IDC presented by Bone and Chen (2012), apply these two model-based nonlinear controller to the new prototype hybrid pneumatic-electric actuator.

# CHAPTER 3.    SYSTEM MODELING

## 3.1   Introduction

Classical controllers, such as PID, do not require a system model. When the system dynamics are very nonlinear, this type of controller is usually unable to stabilize the system. Model-based controllers are capable of stabilizing such systems. However, obtaining a sufficiently accurate model of the system may be difficult. The hybrid actuator has nonlinear dynamics mainly due to the compressibility of the air in the pneumatic actuator and the valve flow rate characteristics.   To allow model-based controllers to be developed in this thesis a dynamic model must first be derived.

In this chapter, system hardware is introduced first. Then, the modeling equations for different system orientations are derived. The valve flow rate model for a discrete input is presented. For a PWM input, the valve flow rate is modeled using surface fitting based on experiments. Two surface fitting methods are used to obtain models for each valve. Their accuracy and ease of implementation is compared.   Finally, the derived system model and valve models are validated by comparing simulation with open-loop experiments.

## 3.2   System Hardware

### 3.2.1   Choice of Valves and Drive Electronics

The pneumatic actuator will provide the majority of hybrid actuator torque therefore the pneumatic performance is critical. Thus, if each valve with its drive electronics has a fast response and produces a large mass flow rate, the desired chamber pressure will be established within the minimal period of time. Two makes of valves will be evaluated to determine which is more suitable for the actuator. Experiments will be performed and comparison results will be shown in this section.

The on/off valves candidates are: MAC, model number 34B-AAA-GDFB-1BA, and FESTO, model number MHE2-MS1H-3/2G-M7. According to their specifications, the FESTO valve should switch faster than the MAC valve.

The valve driver candidates are: Opto 22 ODC5 solid state relay, and Texas Instruments LM1949-based circuit. The LM1949 is expected to perform better since it is designed specifically for driving solenoid valves. According to its manual, it can directly sense the actual solenoid current, then drives the current until it is several times larger than the holding current at the start of the input pulse. Then the current is automatically reduced for the remainder of the input pulse to allow the valve to be de-energized more rapidly. Thus, the opening and closing delays of the valve will both be reduced.

The comparison results were obtained using a simple procedure. First, the piston position was fixed at its far limit to create a constant chamber volume. Next, the input to

the valve driver was turned on at 1 s, and then off from 4 s to 6 s. At the same time, the chamber pressure was recorded at a rate of 1 kHz.

Experimental results are shown Figure 3.1. Note that a SMC AS2200 flow control valve is connected between the solenoid valve and the chamber. Based on the data shown in the valve filling plots, the difference between the switching on delay times was mainly caused by the inherent difference of the valves, and the LM1949 driver had very little effect. However, based on the valve discharging plots, the LM1949 did noticeably reduce the switching off delay time.
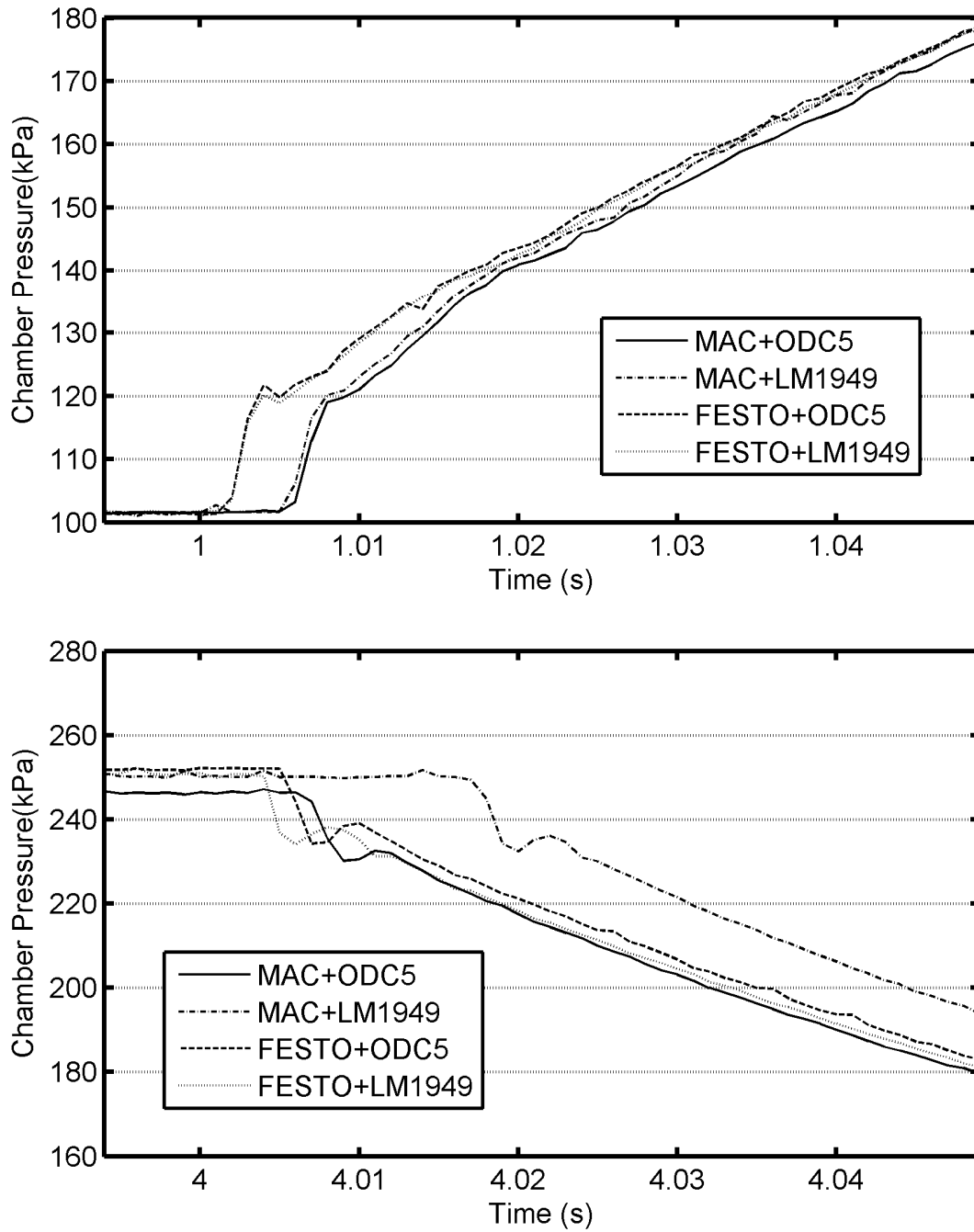
Figure 3.1  Comparison of valve filling (top) and discharging (bottom) for the candidate valves and valve drivers.

### 3.2.2   System Architecture

The system schematic is shown in Figure 3.2. A three way on/off solenoid valve, in series with a flow control valve, is connected to the chamber of the cylinder which controls air flow into and exhaust out of the cylinder. A linear potentiometer is attached to slide block in order to measure the position of the piston. An incremental encoder is installed on the output shaft, measures the angular position of the arm. Two pressure sensors are used to measure the chamber pressure. A PC based data acquisition and control system reads sensors signals and send control command to solenoid valves and electrical motor. The solenoid valves are driven by circuit to reduce switch delay. The electrical motor is driven by an amplifier.

The on/off valves are made by FESTO with model number MHE2-MS1H-3/2G-M7, the electric motor is a Maxon RE40. The flow control valve is made by SMC, model number SMC AS2200. The cylinder is made by Airpot, model number E24D5.0N. The encoder is made by Quantum Devices, model QR12. The pressure sensors are SSI Technologies, model P51-50-A-B-I36-5V-R. The valve controller is a circuit based on the Texas Instruments LM1949 chip. The linear potentiometer is made by Novotechnik model number T100 with a range of 0-100 mm. The sensor data is collected and control signal is sent by a National Instruments PCIe-6365 card installed in a 64 bit Windows 7 PC with a 3.10 GHz Intel i5-2400 processor and 8.00 GB RAM. The control system is programmed in C and a 1 kHz sampling frequency is used.
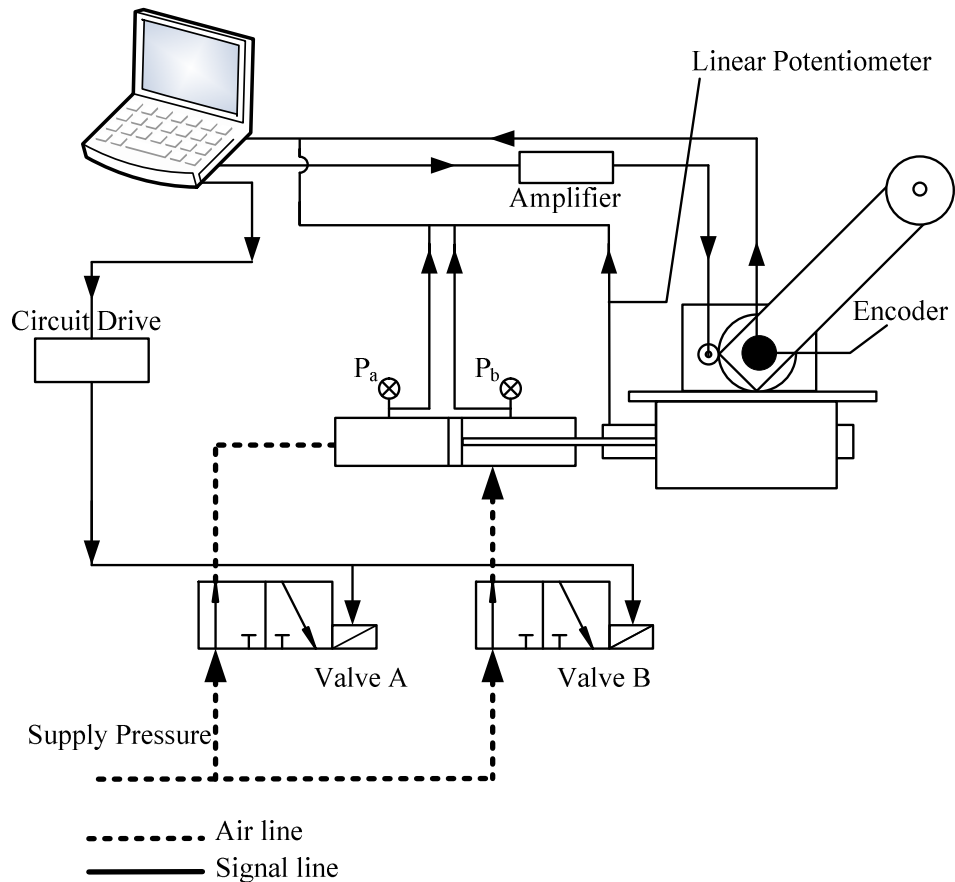
Figure 3.2  System schematic diagram

Compared to the previous prototype developed by Bone and Chen (2012), the new prototype incorporates several improvements.

1.  Faster solenoid valves. The previous prototype used MAC valve with ODC5 valve driver. According to the open-loop experiment results shown in Figure 3.1 the MAC + ODC 5 is significantly slower than the improved prototype using a FESTO valve with LM1949 based circuit drive.

2. The previous prototype used a linear potentiometer. Its voltage output was discretized by a 12-bit analog to digital convertor (ADC) giving a 0.00065 radians resolution for the position feedback. The angular position of the arm was estimated by gear radius. The improved prototype improves the position feedback by adding an encoder with a linear potentiometer. The encoder produces 80000 counts per revolution, gives a 0.00007854 radians resolution.

3. The improved prototype incorporates a National Instruments PCIe-6365 card with a 16 bit ADC for discretizing output voltage from the linear potentiometer and the pressure sensors. Compared to the previous 12 bit ADC, it enhanced the ADC precision by 16 times.

4. The previous prototype used pressure sensors made by Omega Engineering, model number PX138-030D5V. The improved prototype replaced them with more accurate ones made by SSI Technologies with the model P51-50-A-B-I36-5V-R.

5. The valves are driven by a LM1949-based valve control circuit in the improved prototype. Compared to the old one driven by ODC 5, it will decrease the current for holding the valve state. The resulting de-energizing process of the solenoid on/off valve therefore will be shortened.

6. The improved prototype is equipped with stronger stainless steel gears, compared to the old brass ones.

### 3.3    Modeling Equations without Valve Dynamics

### 3.3.1    Actuator Orientation

Bone and Chen designed a hybrid actuator and model-based control methods that allow the actuator to operate in the vertical plane (Bone and Chen 2012). Since motion in the horizontal plane is also useful for many robot applications such as material handling, the associated dynamic models for both orientations will be derived in this chapter.

### 3.3.2    Horizontal System Dynamics Modeling

Firstly, the horizontal configuration dynamics will be modeled.  Figure 3.3 shows the top view of the system and a free body diagram of the equivalent inertia. The gravity has no impact on the system dynamics in this orientation. The only load torque source is the friction torque.
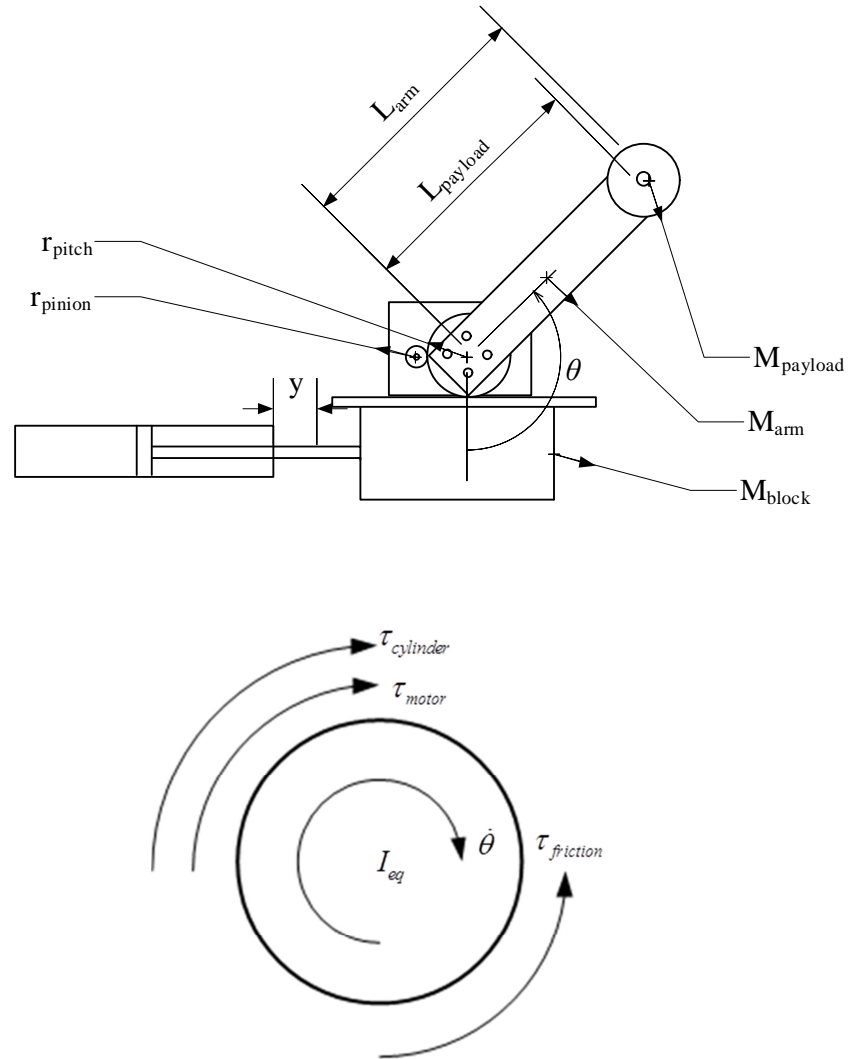
Figure 3.3 Top view of the horizontal configuration (top) and free body diagram of the equivalent inertia (bottom).

The total applied torque for horizontal configuration is

$$\tau_{total} = \tau_{cylinder} + \tau_{motor} - \tau_{friction} \qquad (3.3.1)$$

where $\tau_{cylinder}$ is the torque provided by the pneumatic cylinder, $\tau_{motor}$ is the torque provided by the electric motor, and $\tau_{friction}$ is the total friction torque. The horizontal system dynamics equation is:

$$\ddot{\theta} = \frac{\tau_{total}}{I_{eq}} \tag{3.3.2}$$

where $I_{eq}$ is the system's equivalent inertia.

### 3.3.2.1  Cylinder Torque

Cylinder torque can be calculated by using measured chamber pressures:

$$\tau_{cylinder} = \left[ P_a A_a - P_b A_b - P_0 (A_a - A_b) \right] r_{pitch} \tag{3.3.3}$$

where $P_a, P_b$ are the pressures in chamber A and B respectively; $A_a, A_b$ are piston areas in chamber A and B respectively; $r_{pitch}$ is the diameter of the output gear; and $P_0$ is the atmosphere pressure.

### 3.3.2.2  Electrical Motor and Gear Torque

Assuming perfect gear efficiency, the motor torque with the gear transmission can be calculated by:

$$\tau_{motor} = K_t i_m = K_t K_{amp} u_{motor} r_{gear} \tag{3.3.4}$$

where $K_t$ is the torque constant of the motor, $K_{amp}$ is the amplifier gain, $u_{motor}$ is the control signal (output voltage from the controller), and $r_{gear}$ is the gear ratio which is 5:1.

### 3.3.2.3 Equivalent Inertia

For horizontal and vertical configuration, the system has the same equivalent inertia:

$$I_{eq} = I_{arm} + I_{payload} + I_{block} = \frac{1}{3} M_{arm} L_{arm}^2 + M_{payload} L_{payload}^2 + M_{block} r_{pitch}^2 \quad (3.3.5)$$

where $M_{arm}, M_{payload}$ and $M_{block}$ are mass of the arm, payload, and the block respectively.

### 3.3.2.4 Overall Model

Combining the above results together, the overall horizontal system model without valve dynamics is obtained:

$$
\begin{aligned}
kRT\dot{m}_a &= (y_{a0} + \theta r_{pitch}) A_a \dot{P}_a + k P_a \dot{\theta} r_{pitch} A_a, \\
kRT\dot{m}_b &= (y_{b0} - \theta r_{pitch}) A_b \dot{P}_b - k P_b \dot{\theta} r_{pitch} A_b, \text{ and} \\
I_{eq}\ddot{\theta} &= \tau_{motor} + \tau_{cylinder} - \tau_{friction}
\end{aligned}
\quad (3.3.6)
$$

where

$$
\begin{aligned}
\tau_{motor} &= K_t K_{amp} u_{motor} r_{gear} \\
\tau_{cylinder} &= \left[ P_a A_a - P_b A_b - P_0 (A_a - A_b) \right] r_{pitch} \\
I_{eq} &= \frac{1}{3} M_{arm} L_{arm}^2 + M_{payload} L_{payload}^2 + M_{block} r_{pitch}^2
\end{aligned}
$$

and $\dot{m}_a$ and $\dot{m}_b$ are the mass flow rates through the valves into cylinder chambers A and B, respectively. They will be modeled in Section 3.6 and Section 3.7.

31

### 3.3.3  Vertical System Dynamics Modeling

Unlike the horizontal configuration, the load torque in the vertical configuration is the summation of gravity torque and friction torque. The free body diagram of the equivalent inertia is shown in Figure 3.4.
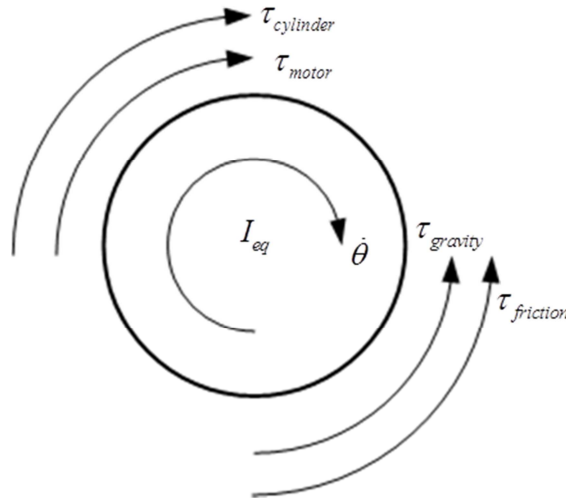


Figure 3.4  Free body diagram of vertical configuration equivalent inertia

The vertical system torque equation then becomes

$$\tau_{total} = \tau_{cylinder} + \tau_{motor} - \tau_{friction} - \tau_{gravity} \qquad (3.3.7)$$

### 3.3.3.1  Gravity Torque

In vertical configuration we have gravity torque contributions from the arm and payload as follows:

$$\tau_{arm} = \frac{1}{2} M_{arm} L_{arm} g \sin\theta \qquad (3.3.8)$$

$$\tau_{payload} = M_{payload} L_{payload} g \sin\theta \tag{3.3.9}$$

Note that the block moves horizontally so it is not affected by gravity, and the total gravity torque is:

$$\tau_{gravity} = \tau_{arm} + \tau_{payload} \tag{3.3.10}$$

### 3.3.3.2   Overall Model

Combining (3.3.7) to (3.3.10), the overall model of system in vertical configuration becomes

$$\begin{aligned}
kRT\dot{m}_a &= (y_{a0} + \theta r_{pitch})A_a\dot{P}_a + kP_a\dot{\theta}r_{pitch}A_a \\
kRT\dot{m}_b &= (y_{b0} - \theta r_{pitch})A_b\dot{P}_b - kP_b\dot{\theta}r_{pitch}A_b \\
I_{eq}\ddot{\theta} &= \tau_{motor} + \tau_{cylinder} - \tau_{gravity} - \tau_{friction}
\end{aligned} \tag{3.3.11}$$

## 3.4   Friction Model

### 3.4.1   Friction Model

The friction torque depends on the specific hardware components, especially the pneumatic seals. Following Chen (2012), the Coulomb plus viscous friction torque model was found to be suitable:

$$\tau_{friction} = \begin{cases} \tau_{cylinder} + \tau_{motor} - \tau_{gravity} & \dot{\theta} = 0, \tau_{cylinder} + \tau_{motor} - \tau_{gravity} \leq \tau_{sf} \\ \tau_{sf} & \dot{\theta} = 0, \tau_{cylinder} + \tau_{motor} - \tau_{gravity} > \tau_{sf} \\ \tau_{cf} sign(\dot{\theta}) + C_{vf}\dot{\theta} & \dot{\theta} \neq 0 \end{cases} \tag{3.4.1}$$

### 3.4.2   Static Friction Torque Identification

From (3.3.1) and (3.3.2) the friction torque becomes

$$\tau_{friction} = \tau_{cylinder} + \tau_{motor} - \ddot{\theta} I_{eq} \qquad (3.4.2)$$

When angular acceleration and angular velocity are close to zero and the cylinder

torque is not used, the static friction can be estimated by

$$\tau_{sf} \approx \tau_{motor} \qquad (3.4.3)$$

To identify this static friction torque, open-loop experiments were performed

using a test program based on the following pseudo-code:

> *If (movement of output shaft > encoder resolution)*
> > *Stop test and record the motor torque value*
> *Else*
> > *Increase motor torque by a small amount*

It was found that the static friction differed in different locations of the piston, and

varied with time. Thus tests in different locations were done repeatedly and their average

was taken as the value of the static friction torque.  The test results and average value are

listed in Table 3.4.1.

Table 3.4.1 Static friction torque test results

|  | Test Results (Nm) | | | | | |
|---|---|---|---|---|---|---|
|  | Test 1 | Test 2 | Test 3 | Test 4 | Test 5 | Test 6 |
| Left End | 0.343 | 0.408 | 0.367 | 0.382 | 0.370 | 0.339 |
| Middle | 0.402 | 0.347 | 0.348 | 0.339 | 0.328 | 0.351 |
| Right End | 0.257 | 0.282 | 0.283 | 0.265 | 0.283 | 0.297 |
| Average | 0.329 | | | | | |

### 3.4.3    Coulomb and Viscous Friction Identification

After an initial acceleration period, the arm will reach a roughly constant velocity when a constant motor torque is applied. The corresponding equation is:

$$\tau_{motor} \approx \tau_{cf} sign(\dot{\theta}) + C_{vf}\dot{\theta} \qquad (3.4.4)$$

The angular velocity in this equation was estimated by taking the numerical derivative of the measured position. By using (3.4.4), two parameters can be identified by performing two tests. Then $\tau_{cf}, C_{vf}$ can be solved

$$C_{vf} = \frac{\tau_{motor\_1} - \tau_{motor\_2}}{\dot{\theta}_1 - \dot{\theta}_2} \quad \text{and} \qquad (3.4.5)$$

$$\tau_{cf} = \tau_{motor\_1} - C_{vf}\dot{\theta}_1 \qquad (3.4.6)$$

where the subscripts 1 and 2 refer to data from the first and second test sets, respectively.

The test results are shown in Table 3.4.2. The mean valves of the motor torque are $\tau_{motor\_1} = 0.25\,\text{Nm}$ and $\tau_{motor\_2} = 0.27\,\text{Nm}$. The mean velocities are $\dot{\theta}_1 = 0.859\,\text{rad/s}$ and $\dot{\theta}_2 = 1.269\,\text{rad/s}$. Substituting these results into (3.4.5) and (3.4.6) gives:

$$\begin{aligned}
C_{vf} &= \frac{\tau_{motor\_1} - \tau_{motor\_2}}{\dot{\theta}_1 - \dot{\theta}_2} = \frac{0.25 - 0.27}{0.859 - 1.269} = 0.0488 \\
\tau_{cf} &= \tau_{motor\_1} - C_{vf}\dot{\theta}_1 = 0.25 - 0.0488 * 0.859 = 0.2081
\end{aligned} \qquad (3.4.7)$$

Table 3.4.2 Coulomb and viscous friction test results

| Test No. | Test Set | Velocity (rad/s) | Motor Torque(Nm) |
|----------|----------|------------------|------------------|
| 1 | 1 | 0.832 | 0.25 |
| 2 |   | 0.893 | 0.25 |
| 3 |   | 0.840 | 0.25 |
| 4 |   | 0.891 | 0.25 |
| 5 |   | 0.801 | 0.25 |
| 6 |   | 0.899 | 0.25 |
| Average |   | 0.859 | 0.25 |
| 1 | 2 | 1.189 | 0.27 |
| 2 |   | 1.193 | 0.27 |
| 3 |   | 1.184 | 0.27 |
| 4 |   | 1.332 | 0.27 |
| 5 |   | 1.360 | 0.27 |
| 6 |   | 1.357 | 0.27 |
| Average |   | 1.269 | 0.27 |

## 3.5   Valve Dynamics for a Discrete Input

### 3.5.1   Introduction

As further explained in Chapter 4, a model which predicts the mass flow rate after the valve turns on or off is required for model-based control. Due to manufacturing tolerances, valve A and valve B in Figure 3.2 are not identical so it was necessary to model the two valves separately.

### 3.5.2   Procedure for Data Collection

Simple open-loop tests were performed to observe the dynamics characteristics of the valves. The piston was fixed at the far end of the stroke in order to maximize the chamber volume. The initial pressure in the chamber was atmospheric pressure. Next, the input to the valve driver was turned on at 1 s, and then off from 4 s to 6 s. At the same time, the chamber pressure was recorded at a rate of 1 kHz.

### 3.5.3   Mass Flow Rate Modeling

During the filling and discharging, the dynamic behavior of the flow can be divided into two distinct regimes: choked flow and unchoked flow. At the beginning of the pressure rise or fall, a rapid pressure change can be observed. It is a short approximately linear segment. The existence of choked flow is determined by the ratio of upstream pressure $P_{up}$ and downstream pressure $P_{down}$ for ideal gas (Jones and Hawkins 1986). When the following condition holds, the choked flow occurs. If it doesn't hold, then the flow is unchoked.

$$\frac{P_{down}}{P_{up}} \leq 0.53 \tag{3.5.1}$$

Applying first law of thermodynamics and the ideal gas law to the chamber gives

$$v\dot{P} + kP\dot{v} = kRT\dot{m} \tag{3.5.2}$$

With the hybrid actuator, the chamber A and B volumes and their derivatives can be calculated by:

$$v_a = (y_{a0} + y)A_a$$
$$v_b = (y_{b0} - y)A_b$$
$$\dot{v}_a = \dot{y}A_a$$
$$\dot{v}_b = \dot{y}A_b$$

If the piston is fixed, the chamber volume will be maximized, and the derivative of the chamber volume $\dot{v} = 0$. The mass flow rate can be estimated by the following equation:

$$\dot{m} = \frac{v\dot{P}}{kRT} \tag{3.5.3}$$

where $\dot{m}$ is the mass flow rate of the valve, $v$ is the volume of the chamber, $\dot{P}$ is the rate of pressure change inside the chamber.

For choked flow, the mass flow rate is constant and may be obtained by substituting the rate of pressure change of the linear segment into(3.5.3).

For unchoked flow, the simplified versions of Shearer's equations (Shearer 1956) proposed by Bone and Chen (2012) will be used, as follows:

$$\dot{m} = c_{fill}\sqrt{P_s - P}$$
$$\dot{m} = c_{dis}(P_0 - P) \tag{3.5.4}$$

where $c_{fill}$ is filling coefficient and $c_{dis}$ is discharging coefficient, $P_s$ is supply pressure and $P_0$ is atmosphere pressure.

## 3.6    Valve Plus Flow Control Modeling

### 3.6.1    Introduction

For the purpose of actuating of collaborative robot, it is necessary to minimize potential hazard of the hybrid actuator. The low friction cylinder and small gear ratio design benefit the inherent safety. However in the horizontal configuration, a very small external load can make pneumatic servo control quite difficult. One reason for this is the on/off solenoid valve makes the chamber pressures fluctuate at a high frequency. At the same time, the low friction does not provide any significant damping to the actuator. Thus, the actuator has little resistance to the high frequency chatter caused by the pressurized air. When the external load is small, the pneumatic actuator may chatter due to the rapid change of chamber pressures, making precise servo control difficult. To alleviate this problem, flow controls were included as shown in Figure 3.2 in order to limit the pressure fluctuations and smooth the pneumatic torque.

### 3.6.2    Modeling

In this section, the model is derived for solenoid valve A.  Please note that the same model applies to valve B. For the filling case, Figure 3.5 shows the schematic of adding the flow control after the valve. The flow control connected to valve A can be regarded as another valve. Consequently, this structure is equivalent to two valves in series.
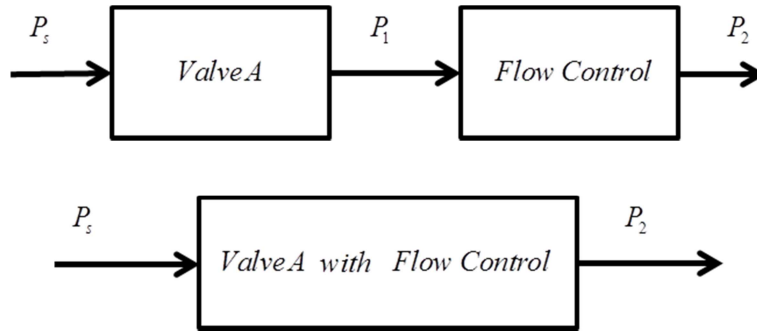
Figure 3.5 Solenoid valve and flow control in series for the filling case.

To derive the model for filing, valve A is assumed to initially be off, with $P_1 = P_2 = P_0$. Assuming the orifice area of the flow control is larger than for valve A, when valve A is turned on the intermediate pressure $P_1$ will not build up rapidly relative to $P_2$. Therefore, if $\dfrac{P_s}{P_1} \geq \dfrac{1}{0.53}$, the flow is choked at the valve A and the flow control valve will be unchoked since its upstream intermediate pressure $P_1$ stays close to its downstream chamber pressure $P_2$, the mass flow rate is then calculated by:

$$\dot{m} = m_{choked\_fill}, \quad \text{if} \quad \frac{P_s}{P_1} \geq \frac{1}{0.53} \tag{3.6.1}$$

where $m_{choked\_fill}$ is the filling mass flow rate of the valve A with choked flow. If $\dfrac{P_s}{P_1} < \dfrac{1}{0.53}$, the flow through the valve A will also be unchoked. At the same time the mass flow rates through the valve and flow control must be equal. In equation form:

$$\dot{m} = C_{fill\_V_1} \sqrt{P_s - P_1}$$
$$\dot{m} = C_{fill\_V_2} \sqrt{P_1 - P_2} \tag{3.6.2}$$

From(3.6.2),

$$C^2_{fill\_V_1}(P_s - P_1) = C^2_{fill\_V_2}(P_1 - P_2) \tag{3.6.3}$$

So that intermediate pressure $P_1$ can be solved as

$$P_1 = C_{r1}P_s + C_{r2}P_2 \tag{3.6.4}$$

where $C_{r1} = \dfrac{C^2_{fill\_V_1}}{C^2_{fill\_V_1} + C^2_{fill\_V_2}}$ , $C_{r2} = \dfrac{C^2_{fill\_V_2}}{C^2_{fill\_V_1} + C^2_{fill\_V_2}}$ and note that

$$C_{r1} + C_{r2} = 1 \tag{3.6.5}$$

Substituting (3.6.4) (3.6.5) into (3.6.2) we obtain the model of valve filling with flow control

$$\dot{m} = \begin{cases} m_{choked\_fill}, & \text{if } \dfrac{P_s}{P_1} \geq \dfrac{1}{0.53} \\[2ex] C_{flow\_c\_fill}\sqrt{P_s - P_2} & \text{if } \dfrac{P_s}{P_1} < \dfrac{1}{0.53} \end{cases} \tag{3.6.6}$$

where the coefficient of filling with flow control $C_{flow\_c\_fill}$ is analytically calculated by:

$$C_{flow\_c\_fill} = \left. C_{fill\_V_1} C_{fill\_V_2} \middle/ \sqrt{C^2_{fill\_V_1} + C^2_{fill\_V_2}} \right.$$

The discharging schematic is similar to the filling one, and is depicted by Figure 3.6.
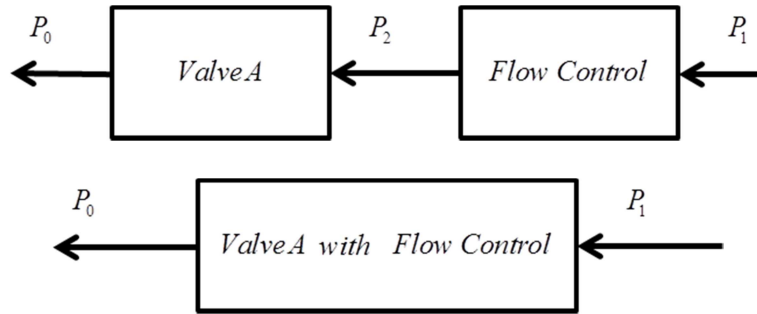
Figure 3.6 Solenoid valve and flow control in series for the discharging case.

The orifice area assumption is repeated from the previous section. Following a similar argument, when valve A is choked the mass flow rate is:

$$\dot{m} = m_{choked\_dis}, \quad \text{if } \frac{P_2}{P_0} \geq \frac{1}{0.53} \tag{3.6.7}$$

where $m_{choked\_dis}$ is the discharging mass flow rate of the valve A with choked flow. If $\frac{P_2}{P_0} < \frac{1}{0.53}$ then both will be unchoked, with equal mass flow rates given by:

$$\dot{m} = C_{dis\_V_1}(P_0 - P_2)$$
$$\dot{m} = C_{dis\_V_2}(P_2 - P_1) \tag{3.6.8}$$

Solving (3.6.8) for intermediate pressure $P_2$ gives:

$$P_2 = C_{dis\_r1}P_0 + C_{dis\_r2}P_1 \tag{3.6.9}$$

where $C_{dis\_r1} = \dfrac{C_{dis\_V_1}}{C_{dis\_V_1} + C_{dis\_V_2}}, C_{dis\_r2} = \dfrac{C_{dis\_V_2}}{C_{dis\_V_1} + C_{dis\_V_2}}$

Substituting (3.6.9) into (3.6.8):

$$\dot{m} = \begin{cases} m_{choked\_dis}, & \text{if } \dfrac{P_2}{P_0} \geq \dfrac{1}{0.53} \\[3ex] C_{flow\_c\_dis}(P_0 - P_1) & \text{if } \dfrac{P_2}{P_0} < \dfrac{1}{0.53} \end{cases} \tag{3.6.10}$$

where the coefficient of discharging with flow control $C_{flow\_c\_dis}$ is analytically calculated

by: $\quad C_{flow\_c\_dis} = \dfrac{C_{dis\_V_1} C_{dis\_V_2}}{C_{dis\_V_1} + C_{dis\_V_2}}$

The derived valve plus flow control models (3.6.6) and (3.6.10) are similar in form to Bone and Chen (2012) equations with smaller fill and discharge coefficients. When the valve input has high frequency variation, the addition of the flow control will smooth the fluctuation of chamber pressure.

The valve plus flow control model parameters were identified for valves A and B by curve fitting the open-loop experiment data with (3.6.6) and (3.6.10). Preliminary calculations revealed that $P_1 \approx P_2$ so the model was simplified by replacing the intermediate pressure with the chamber pressure in (3.6.6) and (3.6.10). The estimated parameters of the two valves are given by Table 3.6.1. Filling and discharging simulation and experiment results for each valve are shown in Figure 3.7 and Figure 3.8. The results demonstrate that the models fit both the transient and steady-state pressures well.

Table 3.6.1 Calculated valve filling and discharging parameters

|  | $C_{fill}$ | $C_{dis}$ | $m_{choked\_fill}$ (kg/s) | $m_{choked\_dis}$ (kg/s) |
|---|---|---|---|---|
| **Valve A** | $1.5 \times 10^{-6}$ | $3.7 \times 10^{-9}$ | $7.8 \times 10^{-4}$ | $3.5 \times 10^{-4}$ |
| **Valve B** | $1.5 \times 10^{-6}$ | $3.7 \times 10^{-9}$ | $1.3 \times 10^{-3}$ | $3.9 \times 10^{-4}$ |
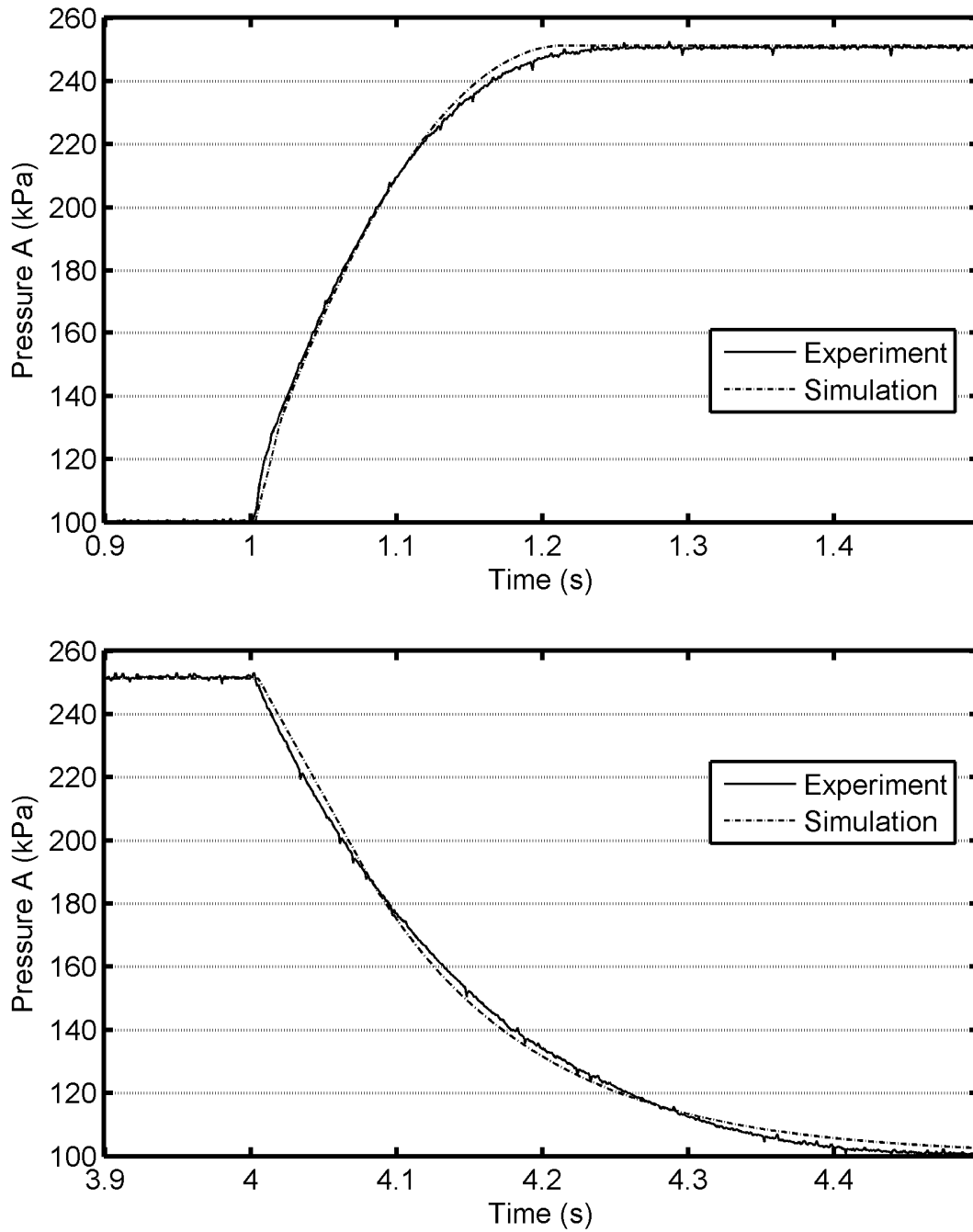
Figure 3.7 Comparison of valve A filling and discharging simulation and experiment results for $P_s$= 251 kPa.
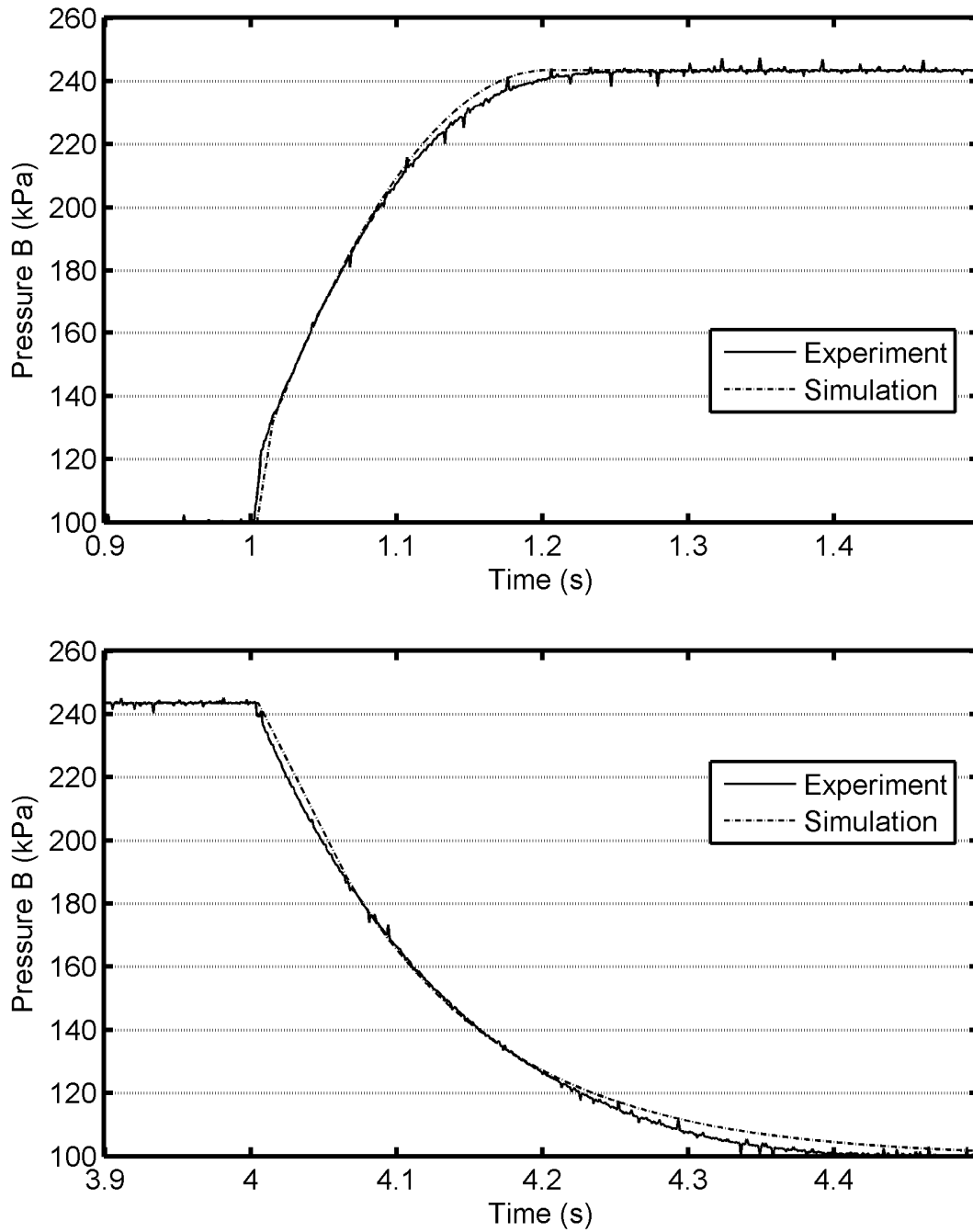
Figure 3.8 Comparison of valve B filling and discharging simulation and experiment results for $P_s$= 243 kPa.

## 3.7    Valve Dynamics with PWM Input

### 3.7.1    Introduction

On/off valve modeling with discrete input is useful for predicting pressure changes after a valve is turned on and off. However, such a model is not able to directly obtain the average mass flow rate for a given PWM input and chamber pressure. As will be discussed in Chapter 4, such a model is necessary for a model-based controller with a continuous control signal. In this section, a valve model for PWM input will be developed. In this thesis, "PWM input" refers to the PWM duty cycle.  The PWM duty cycle is defined as the width of the on pulse divided by the PWM period, and cannot be less than zero or greater than one.

### 3.7.2    Procedure for Data Collection

Similar to on/off valve modeling, the tests were performed when piston was fully extended and fixed. In such case, the mass flow rate is proportional to chamber pressure change rate as described by (3.5.3).

There are three variables in this valve model for PWM input: chamber pressure, mass flow rate, and PWM input. Note that the supply pressure is fixed and the model is specific to that pressure. Chamber pressure can be measured by pressure sensors. PWM input is assigned by controller. Mass flow rate is estimated using chamber rate of pressure change. The purpose of the tests is to measure the chamber pressure for a series of different PWM inputs and then calculate the mass flow rates.

It was first necessary to choose the PWM period. Because of the discontinuity of the on/off valve, the mass flow rate is estimated by its average during one PWM period under a certain chamber pressure. A small PWM period is desirable since it will allow the controller to change the mass flow rate rapidly. On the other hand, the valve itself has switching delay because energizing and de-energizing the solenoid coil takes time. It is meaningless to choose a PWM period smaller than the dead zone of the valve because it cannot turn on/off within such a short time. Even when the chosen PWM period is slightly larger than the dead zone, it is still not acceptable since the adjustable zone is too small.

Figure 3.9 and Figure 3.10 demonstrates two PWM periods selection has different impact to the solenoid on/off valve response to valve input.  The valve dead zone is formed by switch on and off delays. The Figure 3.9 shows impact of selecting a relatively large PWM period. If the valve is commanded to turn off outside of the valve dead zone, the valve will be actually turned off within the PWM period. The Figure 3.10 describes when selecting a relatively small PWM period. If the valve is commanded to turn off outside of the valve dead zone, the valve will not able to be switched off until the next PWM period.
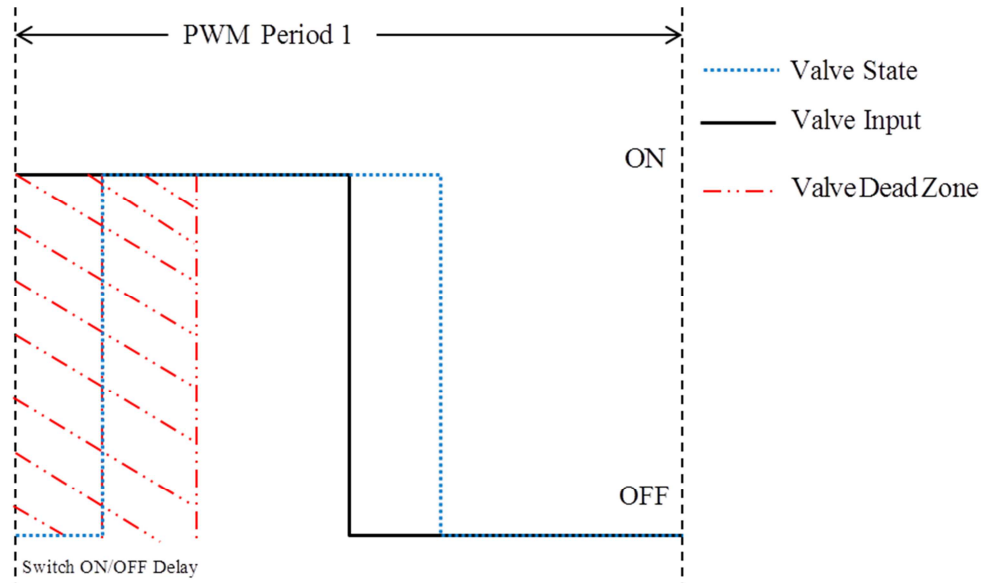
Figure 3.9 Illustration of a large PWM period
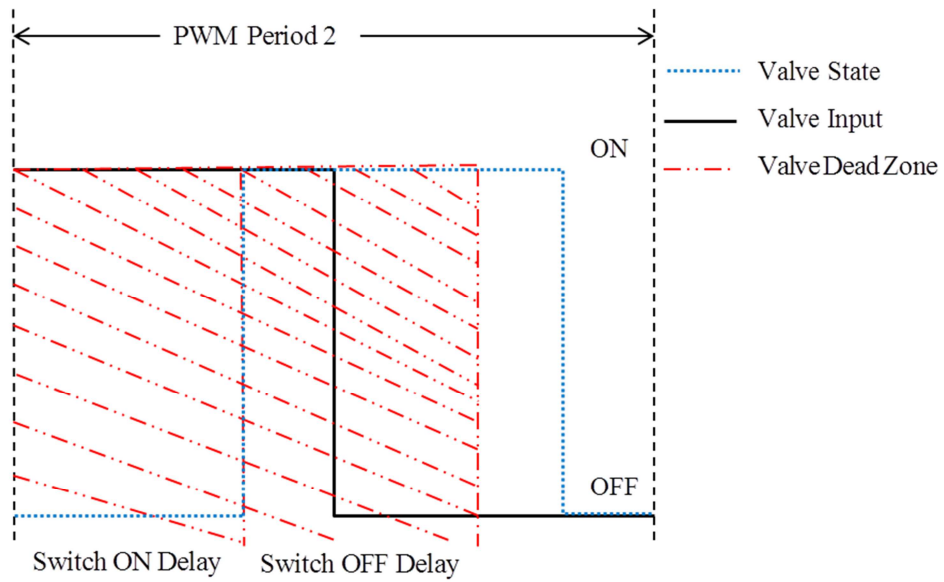


Figure 3.10 Illustration of a small PWM period

According to its manual, the FESTO valve has a 1.7ms of switching on delay and 2ms of switching off delay. That is 3.7ms of dead zone in total. This means the PWM frequency should be around 270 Hz. Considering that valve switching time will be reduced slightly by the valve drive circuit, that the chosen frequency candidates were 200 Hz, 250Hz, and 300Hz.

The experimental setup was the same as used for on/off valve modeling. The piston was fixed at the right limit position of the cylinder. In the experiments, the PWM input started from 0.0001 and was increased by a 0.05 step size until it reached 0.9501. The sampling frequency was set to 1 kHz. The pressure sensor signal was filtered by a zero-phase shift digital low pass filter with a 50 Hz cutoff frequency to get remove most of the high frequency noise. The results for different PWM frequencies are shown in Figure 3.11, Figure 3.12, and Figure 3.13.
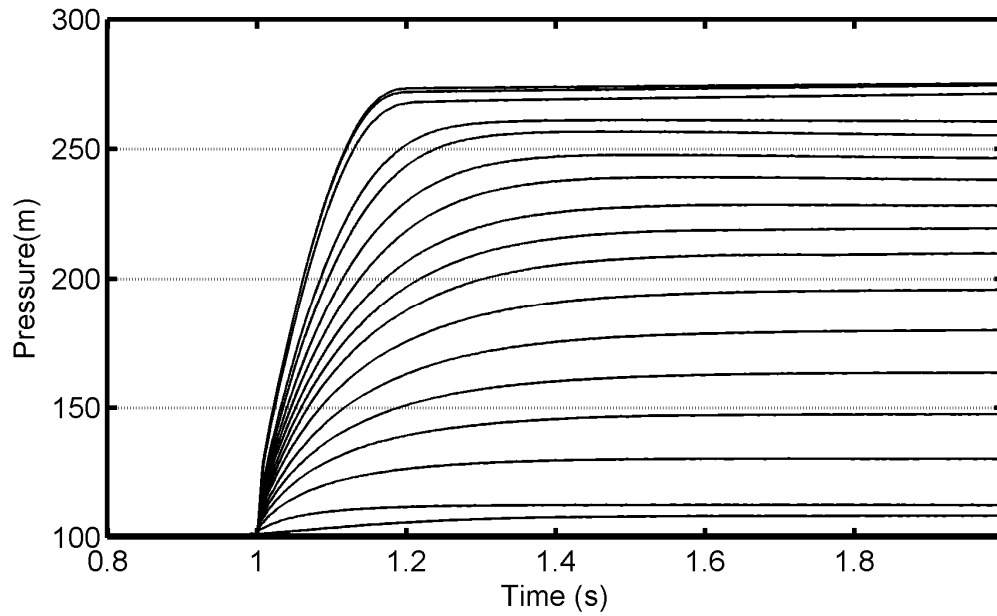
Figure 3.11  Pressure responses for a range of duty cycles and a PWM Frequency of 200 Hz
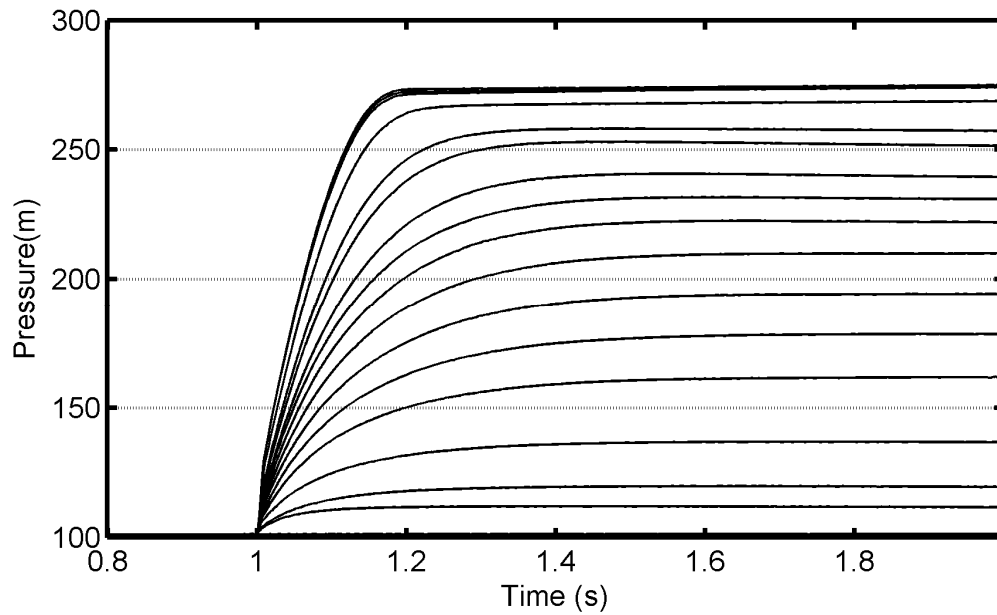


Figure 3.12 Pressure responses for a range of PWM inputs and a PWM Frequency of 250 Hz
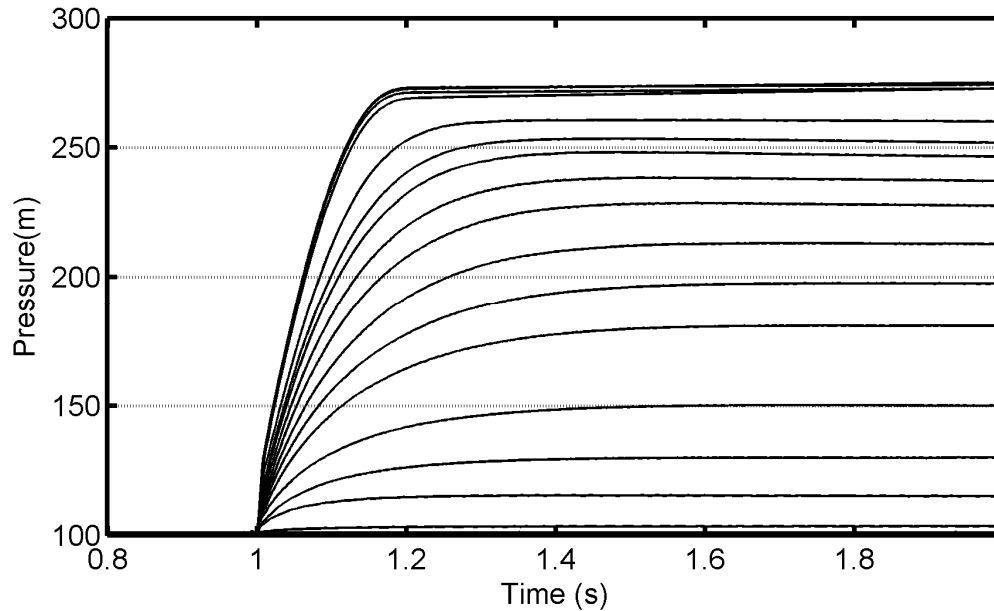
Figure 3.13  Pressure responses for a range of PWM inputs and a PWM Frequency of 300 Hz

The 200 Hz and 250 Hz pressure responses are shown in Figure 3.11 and Figure 3.12 respectively. Ideally, the incremental changes of 0.05 in the PWM input should produce a uniform distribution of changes in the chamber pressures. From the plots, the 200Hz results show a more even distribution compared to the 250Hz results. With the 250Hz result, several input values produce nearly overlapping pressure responses, which is not the case with the 200Hz results. Figure 3.13 shows chamber pressure response when PWM frequency is at 300Hz. Again, it shows a worse distribution of pressure changes compared with the lower frequencies.

With the PWM frequency chosen to be 200 Hz (i.e. PWM period $T_{pwm\_period} = 5$ ms), the next problem was to select the PWM input resolution to use for data collection. For the purpose of better modeling accuracy, a smaller resolution is normally desirable. At the same time, to avoid handling an extremely large number of data points, the resolution shouldn't be excessively small. The maximum mass flow rate is an important parameter since it will affect the chamber filling and discharging speed. Hence, the selected PWM input resolution should be the largest value that does not change this number. Experiments were performed at 200Hz PWM frequency, with the PWM input starting at 0.0001 and increased with different step sizes. The chamber pressure change rate was used to calculate maximum mass flow rate.   Based the results given in Table 3.7.1 the PWM input resolution was chosen as 0.01.

Table 3.7.1 Maximum mass flow rate obtained using different PWM resolutions

| PWM Resolution | 0.01 | 0.02 | 0.03 | 0.04 | 0.05 | 0.0625 |
|---|---|---|---|---|---|---|
| Max Mass Flow Rate ( $10^{-4}$ Kg/s ) | 7.3689 | 7.4239 | 7.4251 | 7.3434 | 7.2085 | 6.9359 |

### 3.7.3   Polynomial Surface Fitting Method

Open-loop tests were performed in order to collect data representing the relationship between the PWM input, chamber pressure and averaged mass flow rate for each valve. For a certain chamber pressure and given PWM input, the resulting mass flow rate could be calculated since it is proportional to chamber pressure change rate. The

mass flow rate data can be represented by an interpolated surface.   An example of a

measured mass flow rate surface is shown in Figure 3.14.
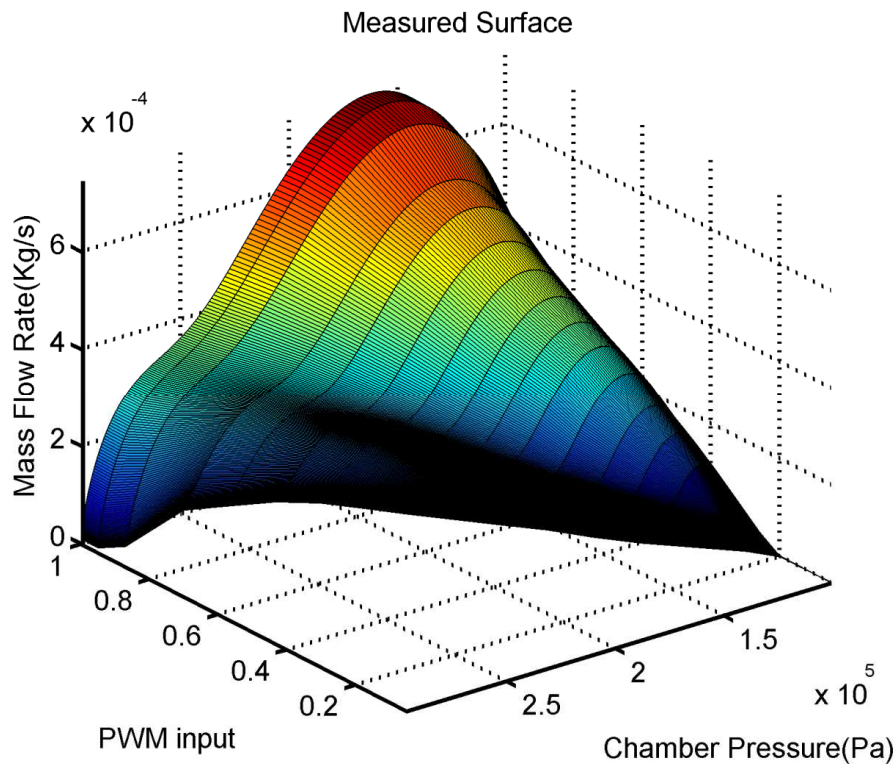


Figure 3.14 Measured mass flow rate surface for valve A filling

The website http://www.zunzun.com provides various functions and fitting targets

for curve and surface fitting. The settings were the same as in the previous work (Rao

2005; Rao and Bone 2008). The fitting target was lowest sum of squared absolute errors.

The surface function was a bipolynomial function. For example, (3.7.1) is used to

describe valve A filling surface as shown below:

$$\dot{m} = a_1 + b_1 u^0 P_a^{\,1} + c_1 u^0 P_a^{\,2} + d_1 u^1 P_a^{\,0} + e_1 u^1 P_a^{\,1} + f_1 u^1 P_a^{\,2}$$
$$+ g_1 u^2 P_a^{\,0} + h_1 u^2 P_a^{\,1} + i_1 u^2 P_a^{\,2} \tag{3.7.1}$$

where $u$ is the PWM input, $P_a$ is the chamber pressure in Pa and $a_1, b_1, c_1, d_1, e_1, f_1, g_1, h_1, i_1$ are the fitting coefficients.
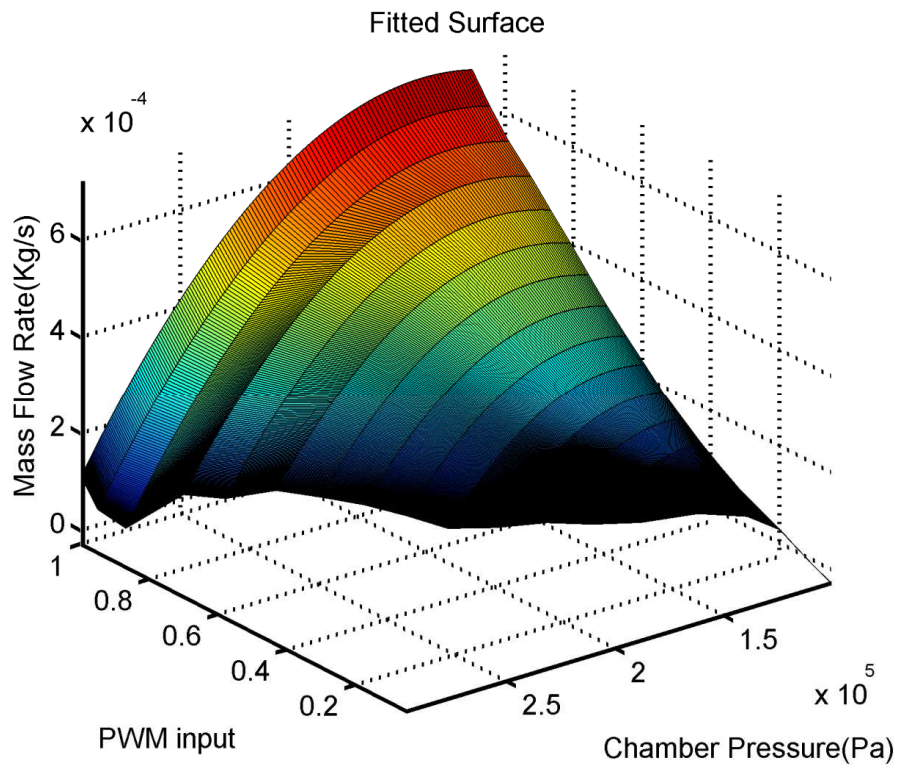


Figure 3.15  Fitted mass flow rate surface for valve A filling

The fitted surface is shown in Figure 3.15. Compared with the measured surface, the fitted surface is smoother with reasonable accuracy. Its fitting errors will be analyzed in Section 3.7.5. The next problem is how to calculate the required PWM input from the desired mass flow rate and given chamber pressure. When desired mass flow rate $\dot{m}_d$ and current chamber A pressure $P_a$ are given, (3.7.1) becomes a quadratic equation:

$$C_{21}u^2 + C_{11}u + C_{01} = 0 \tag{3.7.2}$$

where

$$C_{21} = g_1 + h_1 P_a + i_1 P_a{}^2$$
$$C_{11} = d_1 + e_1 P_a + f_1 P_a{}^2$$
$$C_{01} = a_1 + b_1 P_a + c_1 P_a{}^2 - \dot{m}_d$$

Normally there are two solutions for quadratic equation as follows:

$$u_1 = \frac{-C_{11} + \sqrt{C_{11}^2 - 4C_{21}C_{01}}}{2C_{21}}, u_2 = \frac{-C_{11} - \sqrt{C_{11}^2 - 4C_{21}C_{01}}}{2C_{21}} \tag{3.7.3}$$

Only one $u$ corresponds to a certain chamber pressure and a certain mass flow rate. This means only one of these two solutions is correct. According to Rao and Bone (2008), $u_1$ is the correct solution of the quadratic equation.

### 3.7.4   Artificial Neural Network Fitting Method

For control purposes, it is preferable to obtain required PWM input directly from the desired mass flow rate and given chamber pressure. The previous section presented a bipolynomial surface fitting method. It fitted a surface to the mass flow rate first and then back-solved for the desired PWM input from a quadratic equation constructed by the

fitted parameters and measured chamber pressure. Although the desired PWM input is obtained from chamber pressure and mass flow rate eventually, it is inconvenient and its performance is limited due to the low order of the bipolynomial function.

In this section an ANN will be fit such that the desired PWM input can be obtained directly from the fitted surface. This approach has been used in recent literature for a pneumatic actuation system with two servo valves (Carneiro and de Almeida 2012). Generally speaking, if a proper ANN structure is chosen, the fitting performance is guaranteed no matter how severe the nonlinearity of the measured surface is.

### 3.7.4.1   Introduction of ANN

Inspired by animal brain, ANN is a model that is mainly used in machine learning and pattern recognition. In our case, the relationship between mass flow rate, chamber pressure and valve PWM input is the pattern that we would like to recognize.

The basic structure of the ANN is shown in Figure 3.16. This network has one hidden layer of $n$ neurons and one output layer composed by one neuron. The measured mass flow rate and chamber pressure are the inputs to the network. The PWM input is the target output to be fitted. With this ANN, $w_{11}, w_{12}, ... w_{1n}$ are the weights for the mass flow rate input; $w_{21}, w_{22}, ... w_{2n}$ are the weights for the chamber pressure input; $w_{out,11}, w_{out,21}, ... w_{out,n1}$ are the output weights; and $b_1, b_2, ... b_n$ and $b_{out,1}$ are the bias values.
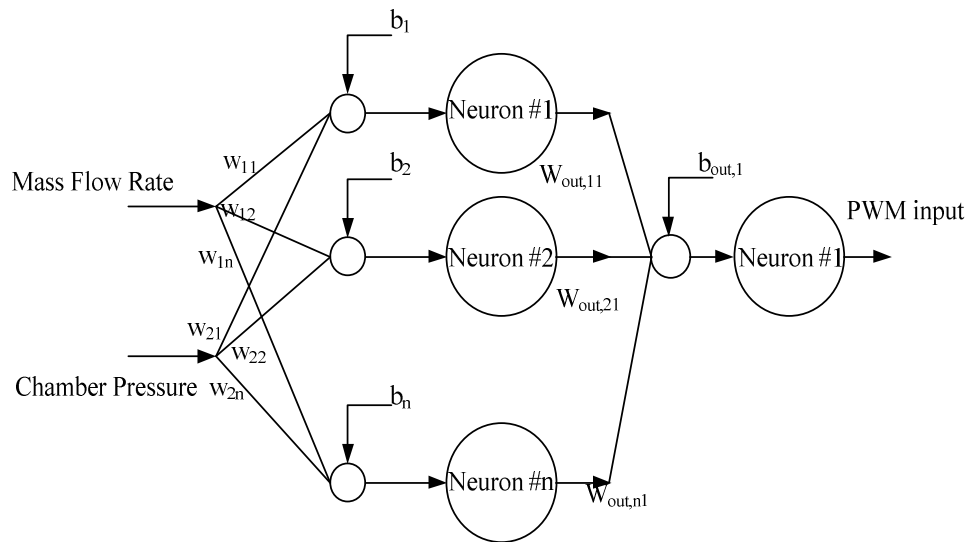
Figure 3.16 Structure of ANN

### 3.7.4.2   ANN Fitting

The ANN fitting begins with random initial guesses for the weights and bias values. Starting with a given set of training data, a search algorithm is performed iteratively based on initial guess and fitting error. The fitting error is the difference between the PWM input calculated by the ANN and the actual PWM input. The weights and bias are updated during the search. When desired the performance is reached, the training process will stop, and the fitting results will be recorded.

The same open-loop experiment data as the previous section were used for the training and testing data sets. The Matlab Neural Network Toolbox with its default settings was used to train the ANN. Theoretically, if a sufficiently large number of layers and neurons are chosen, a ANN is capable of approximating any nonlinear surface very

accurately. However the size of training data set and time consumption of training might be a problem. Additionally, implementing a large ANN in a control program is inconvenient simply because the number of parameters increases proportionally with the size of the network.

For simplicity of implementation and acceptable fitting performance, the default structure of the ANN toolbox was chosen. There are 11 neurons in total, one hidden layer with 10 neurons and one output layer with only one neuron, giving a total of 41 parameters.

The PWM inputs of the valve A filling process were interpolated to form a surface with the result shown in Figure 3.17.  Due to the random start for the parameters the results of the training varied.  Several training runs were performed and the results with the lowest fitting error were saved. The trained ANN parameters are given below:

1. Bias of input and weights of inputs

$$
\begin{bmatrix} b_1 \\ b_2 \\ b_3 \\ b_4 \\ b_5 \\ b_6 \\ b_7 \\ b_8 \\ b_9 \\ b_{10} \end{bmatrix} = \begin{bmatrix} -12.4054 \\ -1.4358 \\ 5.3147 \\ 1.8780 \\ -4.0271 \\ 2.3824 \\ -4.2864 \\ 2.1661 \\ 22.0482 \\ 25.6241 \end{bmatrix}, \quad \begin{bmatrix} w_{11} & w_{21} \\ w_{12} & w_{22} \\ w_{13} & w_{23} \\ w_{14} & w_{24} \\ w_{15} & w_{25} \\ w_{16} & w_{26} \\ w_{17} & w_{27} \\ w_{18} & w_{28} \\ w_{19} & w_{29} \\ w_{110} & w_{210} \end{bmatrix} = \begin{bmatrix} 11.8147 & 1.3297 \\ 0.8000 & 0.5800 \\ -6.9546 & 11.7696 \\ 3.8428 & -0.3688 \\ -5.3597 & 1.2927 \\ -9.2571 & -8.3012 \\ -5.8060 & 1.3390 \\ 2.1675 & 3.1484 \\ 17.1827 & 4.2028 \\ 19.8040 & 5.9010 \end{bmatrix}
$$

2. Bias and weights of output

$$
b_{out} = -2.7861, \quad \begin{bmatrix} w_{out,1} \\ w_{out,2} \\ w_{out,3} \\ w_{out,4} \\ w_{out,5} \\ w_{out,6} \\ w_{out,7} \\ w_{out,8} \\ w_{out,9} \\ w_{out,10} \end{bmatrix} = \begin{bmatrix} 4.5190 \\ 4.2678 \\ 0.0619 \\ 0.2384 \\ 6.1520 \\ 0.1097 \\ -5.3997 \\ 0.1386 \\ 18.8966 \\ -6.9451 \end{bmatrix}
$$
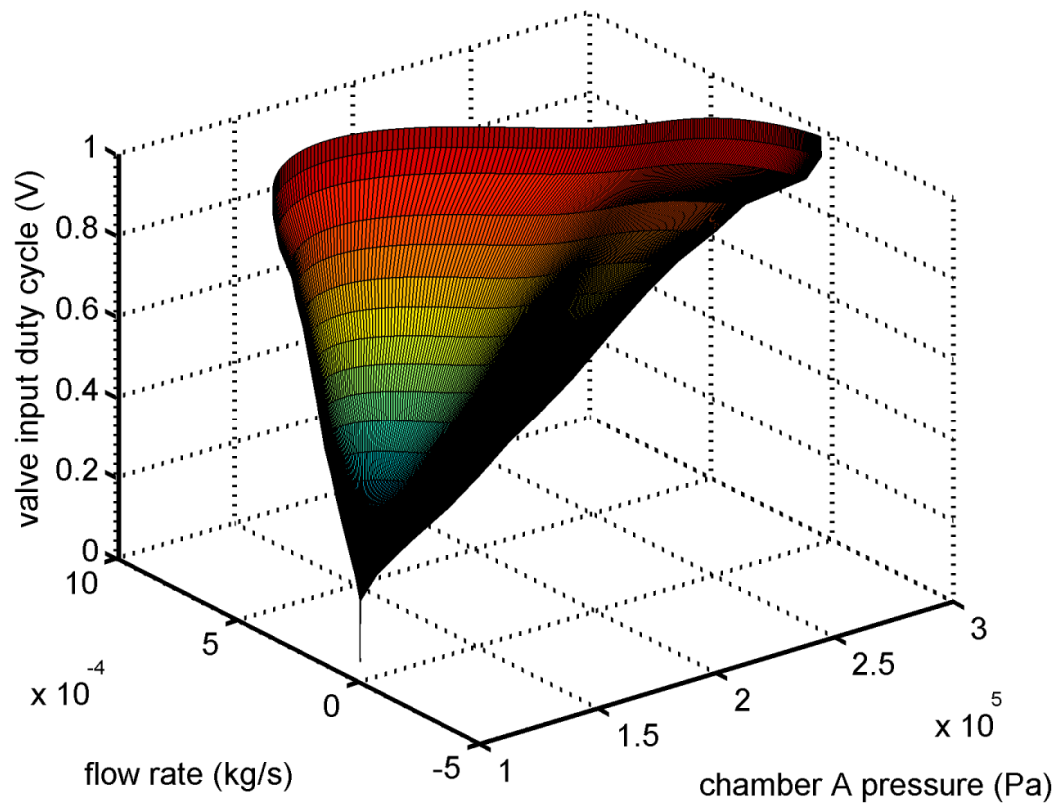
Figure 3.17 Interpolated PWM input surface for valve A filling

The trained ANN was then validated by using a separate set of input testing data to obtain the ANN output. The results are given in Figure 3.18.
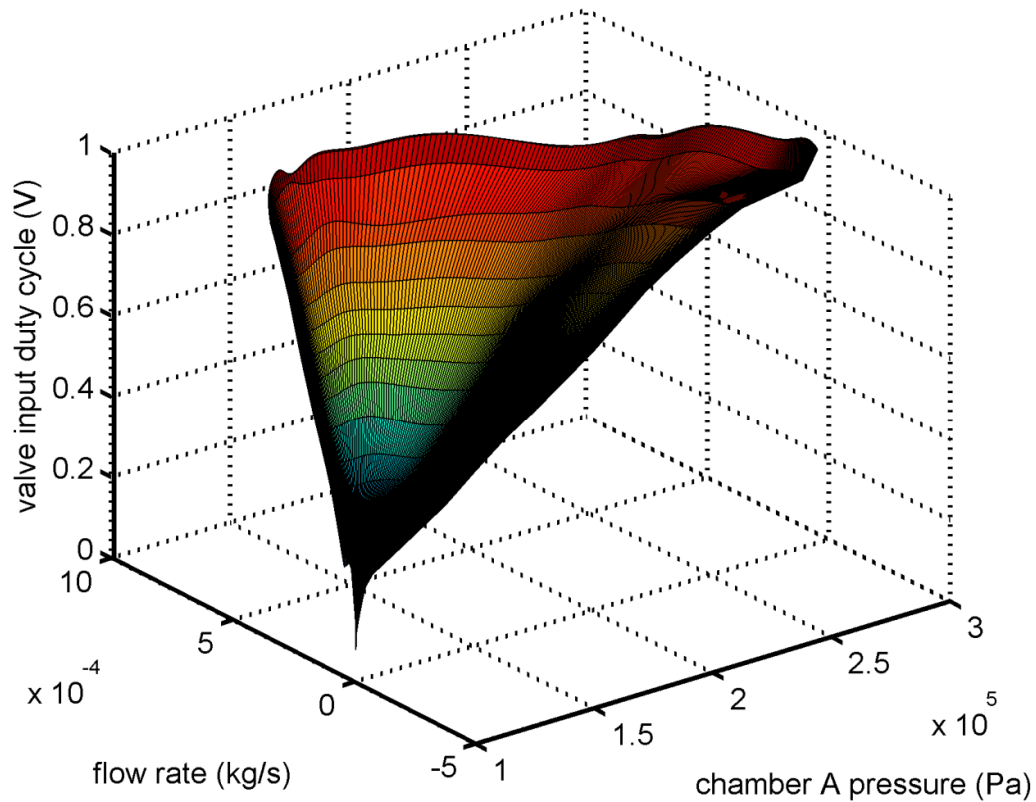
Figure 3.18 Fitted PWM input ANN surface for valve A filling

### 3.7.5    Comparison of the Two Fitting Methods

Two indices will be used for comparing the fitting accuracy of the two methods. The ANN fits mass flow rate and chamber pressure as the input, and the PWM input as the fitting target. The bipolynomial method only fits the mass flow rate for given PWM input and chamber pressure. The fitting targets of the two methods are different. To compare the two methods for PWM input fitting, the PWM input from the bipolynomial fitting was obtained as described in Section 3.7.3. The resulting PWM inputs are then

compared using RMSE and relative error indices.  The RMSE and the relative error, $\varepsilon$, are calculated by:

$$\text{RMSE} = \sqrt{\frac{1}{n}\sum_{i=1}^{n}e_i^2} \quad \text{and} \tag{3.7.4}$$

$$\varepsilon = \left|\frac{u_{fit} - u_{\text{target}}}{u_{\text{target}}}\right| \times 100\% \tag{3.7.5}$$

where $e$ is the fitting error; and $u_{fit}, u_{\text{target}}$ are the fitted and actual PWM input values, respectively.

The comparison of maximum relative errors is given in Table 3.7.2. This reflects the worst case of fitting for a single point. The RMSE results are compared in Table 3.7.3. RMSE indicates the average error over the surface. The results are similar to the relative error comparison.

Table 3.7.2 Maximum relative error (Unit: %)

|  | Valve A | | Valve B | |
|---|---|---|---|---|
|  | **Fill** | **Discharge** | **Fill** | **Discharge** |
| **ANN** | 149 | 211 | 148 | 240 |
| **Bipolynomial** | 169 | 574 | 151 | 597 |

Table 3.7.3 RMSE

|  | Valve A | | Valve B | |
|---|---|---|---|---|
|  | **Fill** | **Discharge** | **Fill** | **Discharge** |
| **ANN** | 0.0238 | 0.0242 | 0.0488 | 0.0250 |
| **Bipolynomial** | 0.0446 | 0.0466 | 0.0651 | 0.0702 |

The ANN fitting is superior according to the comparison results. The ANN reduced fitting RMSE by up to 70%, the maximum relative error for valve discharge surface reduced more than 50%.

However, the bipolynomial method will be used for the remainder of this thesis for the following reasons:

1) Bipolynomial fitting has significantly smaller number of coefficients. The ANN needs 41 per case (41×4 in total), while the bipolynomial only requires 9 per case (9×4 in total). Shown in Table 3.7.4 when a different type of valve was used, the number of valves might change and the number of valve model parameters will increase accordingly. For example, Rao (2005) incorporated four two-way servo valves for the pneumatic actuation system. If the same ANN fitting method was applied to his system, the number of parameters will increased to 328 compare to 76 using the bipolynomial method. In addition, for the improved prototype, the ANN with five times more parameters only achieved an average reduction of RMSE by 50%.

Table 3.7.4 Number of the parameters for the two methods versus valve numbers

| Number of valves | 2 (Current system) | 4 (Rao 2005) |
|---|---|---|
| ANN parameters | 164 | 328 |
| Bipolynomial parameters | 36 | 76 |

2) The ANN training was done using the Matlab Toolbox. It randomly sets a group of initial gains at the beginning of training. The searching algorithm is also

unlikely to find a global minimal solution. The results of training were different

due to the different local minimal solutions.

3) The implementation of ANN in C with more than 160 parameters will make the

hybrid actuator with such control system difficult to maintain and upgrade.

## 3.8    Validation of the System Model

The previous sections have derived the system model equations and the model

parameters have also been identified. In this section, simulation results using the system

model will be compared with open-loop experiment results. Because the model is

analogous in different system orientations, only the horizontal configuration will be

validated in this section.

The validation was done in two parts. In the first part, the system model was used

with the valves turned off. When the valves were off the chambers of the cylinder were

open to the atmosphere. This allowed the dynamics of the mechanical and electrical

elements to be validated separately from the pneumatic actuator. In the second part, the

valves were switched using a PWM input in order to validate the response under

combined electric and pneumatic actuation.

### 3.8.1    System Model with Valves Off

The validation of the system model with the valves off follows the procedure

given below:

(1) Set initial chamber pressure to atmospheric pressure and set the piston position.

Choose a motor torque trajectory as input.

(2) Set cylinder torque to zero, calculate friction torque.

(3) Calculate total torque with (3.3.1) and arm acceleration from (3.3.2)

(4) Calculate arm velocity and acceleration using numerical integration.

A clipped sine wave control signal was used in both simulation and experiment. This input is good for a wide range examination of the model. The comparison of displacement in simulation and experiment is given in Figure 3.19. This result shows the derived model predicts the real system dynamics well when the valves are off.
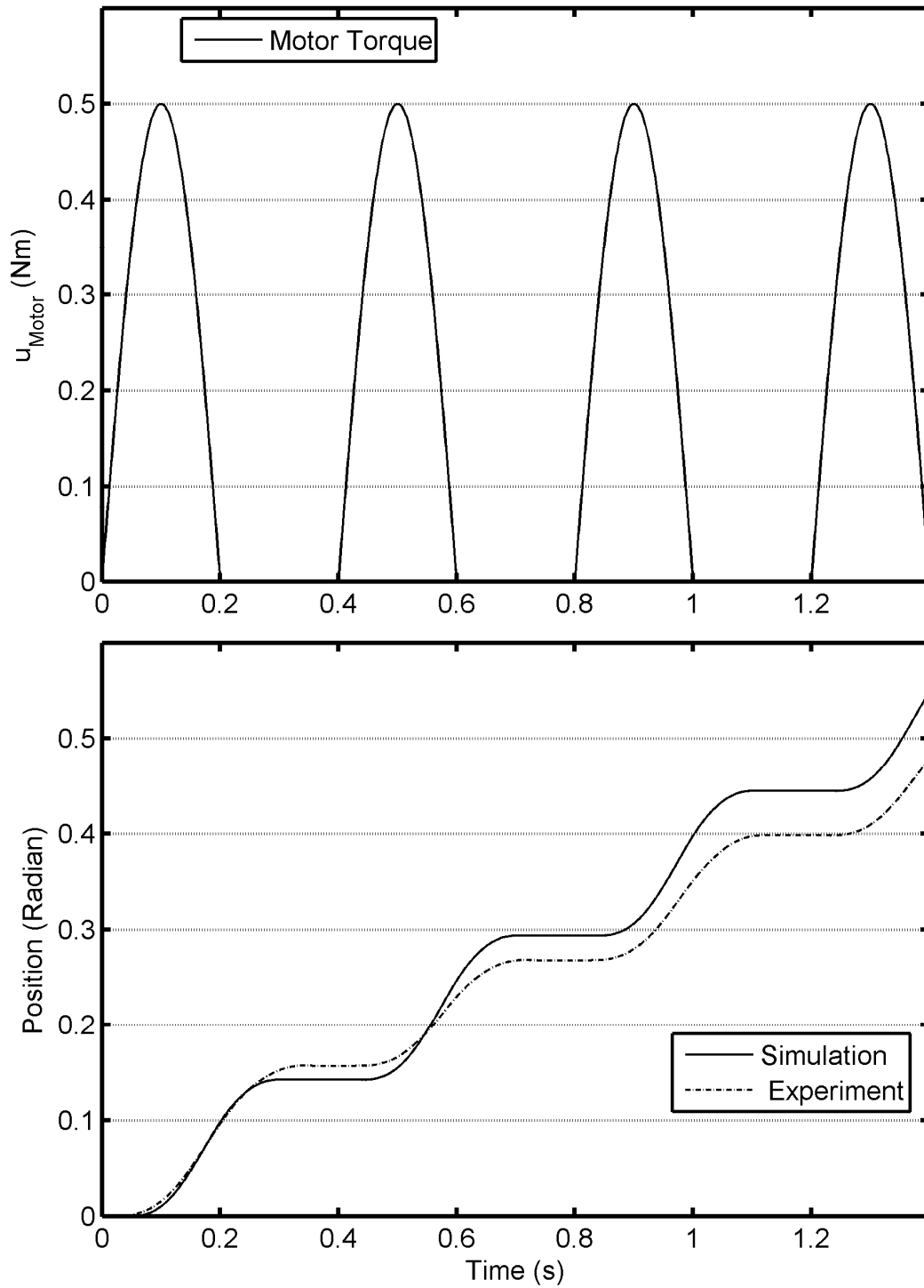
Figure 3.19  Comparison of open-loop simulation and experiment with valves off.

### 3.8.2 System Model with PWM Valve Inputs

Using similar method, the system model with PWM valve inputs will be examined in this section. In the simulation, the following steps were used:

(1) Set initial chamber pressure to atmospheric pressure. Choose clipped sine wave trajectories for the PWM valve inputs.

(2) Calculate mass flow rates from (3.6.6) and (3.6.10).

(3) Calculate pressure derivatives from (3.3.6)

(4) Calculate chamber pressures $P_a$ and $P_b$ using numerical integration.

(5) Calculate cylinder torque and friction torque using (3.7.6) and(3.7.7), respectively.

(6) Calculate total torque with (3.3.1) and arm acceleration with (3.3.2)

(7) Calculate arm velocity and acceleration using numerical integration.

The comparison of chamber pressures and position results are given in Figure 3.20. Experimental results showed the veracity of the derived valve model.  The overall model predicts the real system dynamics well.
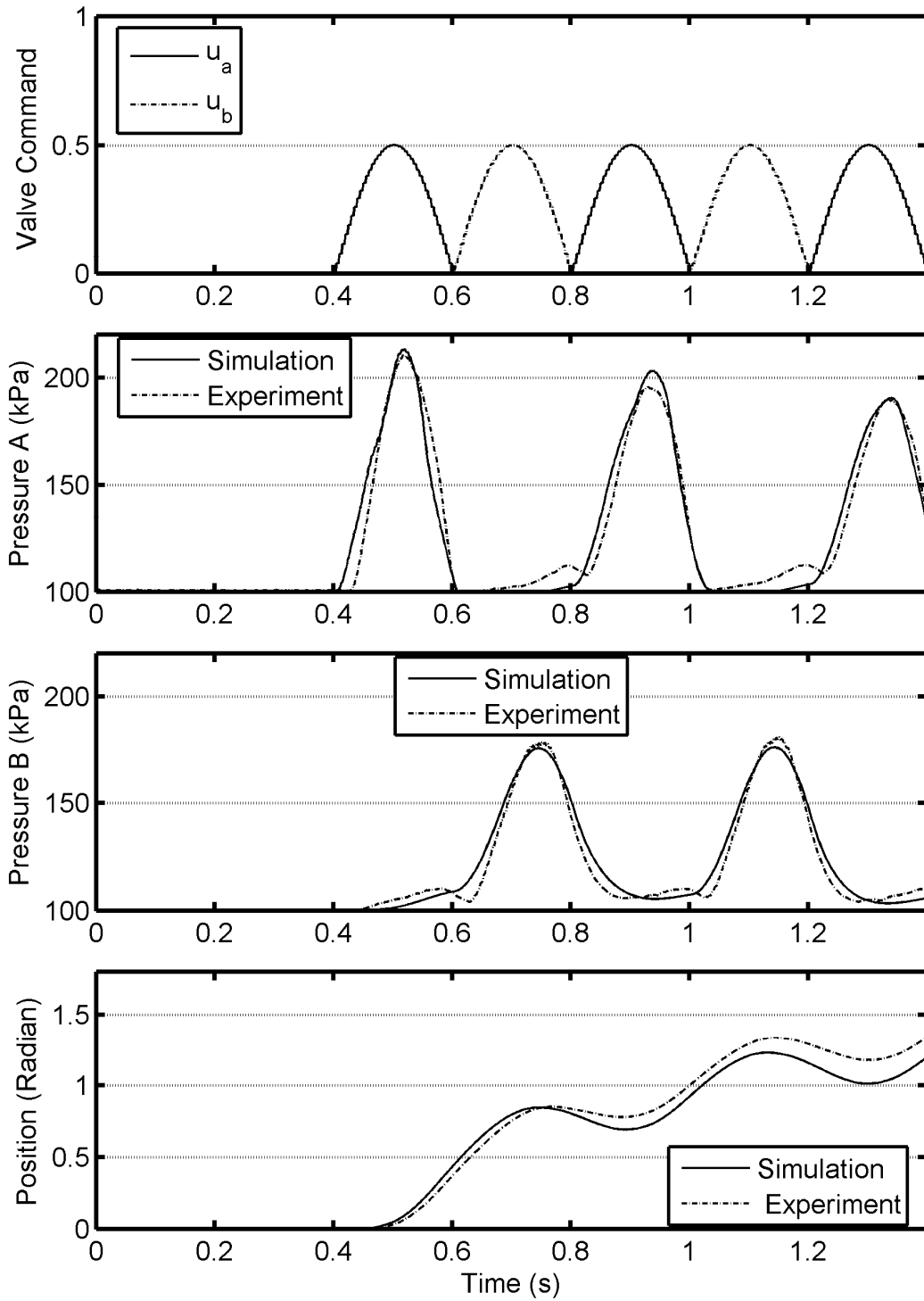
Figure 3.20   Comparison of simulation and experiments

## 3.9   Conclusions

The system model has been derived in this chapter. The system dynamics, without the valve dynamics, were derived based on physical laws. The unknown parameters were identified by experiments using different setups. The mass flow rate model of the valve for on/off action was obtained next. A model for the flow control was introduced and included in the valve model. Valve model parameters were obtained by curve fitting simulations to the experiments data. For PWM inputs, mass flow rate models for both valves were developed based on experiment results and surface fitting using a bipolynomial function and a ANN. The two methods were compared for RMSE and relative error. The ANN was superior in the fitting accuracy however the bipolynomial method was selected due to its relative ease of implementation for real-time control. The system model was validated by comparing simulation and experiment results. The results demonstrated that the derived model represents the actual system well.

# CHAPTER 4.      CONTROLLER DESIGN AND EXPERIMENT

## 4.1   Introduction

The system dynamic model combined with valve model was derived and validated in previous chapter. In this chapter, the design and implementation of three controllers will be presented. The effectiveness of the designed controllers will be examined by preliminary simulation and experiment for the hybrid actuator. First, a linear PVA controller will be designed and manually tuned for comparison purpose. Simulation and experiment will be used to validate the designed controller. Next, backstepping control with compensation and DVMPC + IDC will be designed based on nonlinear system model. The stability of these controllers will be analyzed. The performance of these controllers will be tested in the same experiment setup. Finally, the comparison of the performance of the three controllers will be given.

## 4.2   Linear PVA control

### 4.2.1   Introduction

For the purpose of comparison with the proposed nonlinear controllers, a linear controller will be introduced to set a benchmark. In this section, the PVA controller will be designed, implemented, and tested.

### 4.2.2   PVA Control Design

The linear single input single output (SISO) PVA controller for pneumatic servo system presented by Ning and Bone (2002) will be modified in this section. This

controller incorporates PVA feedback, FF compensation, and dead zone compensation. The PVA control schematic for a pneumatic actuator is shown Figure 4.1.

The controller output signal is supposed to drive a single valve in order for the pneumatic actuator to track the reference trajectory. However, in the current system there are two valves that each requires an input.
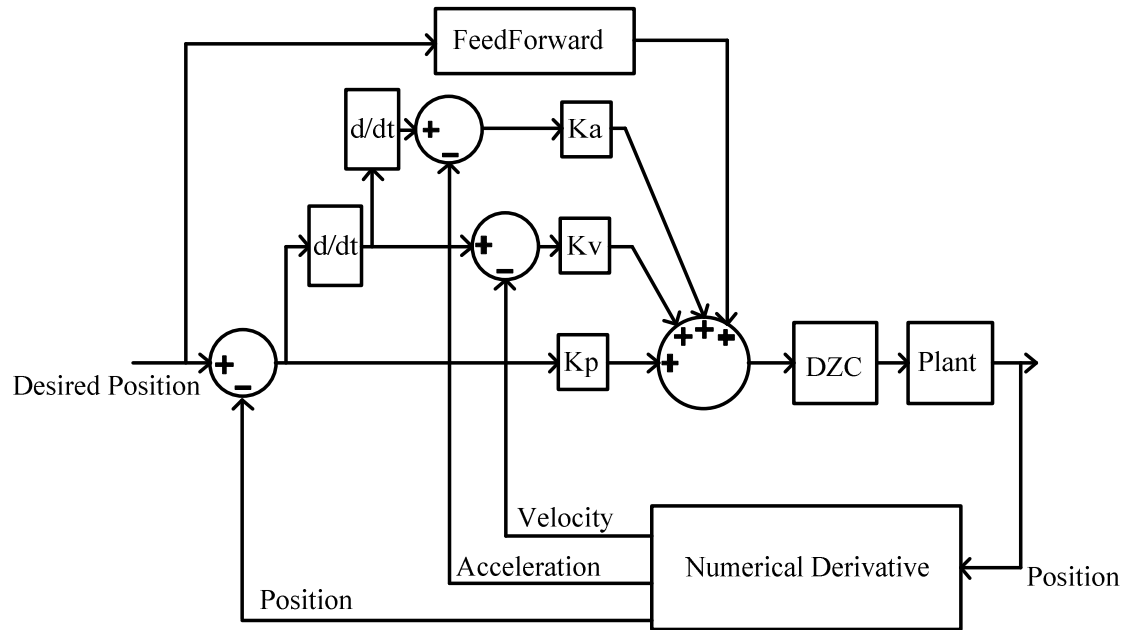


Figure 4.1 The PVA+FF+DZC control schematic

To solve this problem, the virtual control input $u_{\text{virtual}}$ is designed:

$$u_{\text{virtual}} = \frac{K_p e + K_v \dot{e} + K_a \ddot{e}}{U_{PVA\_MAX}} \tag{4.2.1}$$

where $K_p, K_v, K_a, U_{PVA\_MAX}$ should be tuned to keep $u_{\text{virtual}} \in \begin{bmatrix} -1 & 1 \end{bmatrix}$. And the position error $e = \theta_d - \theta$, velocity error $\dot{e} = \dot{\theta}_d - \dot{\theta}$, acceleration error $\ddot{e} = \ddot{\theta}_d - \ddot{\theta}$.

Recall that the hybrid actuator has only an encoder and a linear potentiometer for position measurement. The velocity and acceleration will be derived by taking the numerical derivatives of the measured position. To remove most of the sensor noise, these estimated signals were filtered by a $2^{nd}$-order digital Butterworth 50 Hz low pass filter implemented in software.

The inspiration for this virtual input came from the physics of the double acting cylinder controlled by two valves. For example, a positive $u_{\text{virtual}}$ means there are positive errors that need to be corrected, which in turn means that the actual position is smaller than the reference position. When valve A operates, the pressurized air will push the piston towards positive direction. Consequently the actual position error will be corrected.

The remaining problem is how to convert the virtual input signal $u_{\text{virtual}}$ into PWM inputs for the two valves. Since the two valves both have dead zones using virtual control signal cannot be used directly. Small PWM input might cause no actual position response because of the valve dead zone and actuator friction. To solve this problem, a mapping function $\xi(\cdot)$ is used for the dead zone compensation. It converts the desired virtual input into the range $[u_{Va\_PWM\_Min}, u_{Va\_PWM\_Max}]$. Within this range the PWM input to velocity mapping of the valve is dead zone free. This was implemented with the PVA controller as follows:

$$if\ u_{\text{virtual}} > 0,\ \begin{cases} u_{Va\_PWM} = \xi(u_{\text{virtual}}, u_{a\_PWM\_Min}, u_{a\_PWM\_Max}), \\ u_{Vb\_PWM} = 0 \end{cases}$$

$$if\ u_{\text{virtual}} < 0,\ \begin{cases} u_{Va\_PWM} = 0, \\ u_{Vb\_PWM} = \xi(u_{\text{virtual}}, u_{b\_PWM\_Min}, u_{b\_PWM\_Max}) \end{cases} \quad (4.2.2)$$

$$if\ u_{\text{virtual}} = 0,\ \begin{cases} u_{Va\_PWM} = 0, \\ u_{Vb\_PWM} = 0 \end{cases}$$

It should be noted that this strategy is totally different than the dead zone compensation presented in Ning and Bone (2002).

When desired position trajectory changes suddenly, the PVA feedback control needs at least one sampling period to respond because the PVA control signal is calculated from the position, velocity and acceleration errors. In order to make system response faster, the following FF control signal is introduced:

$$u_{\text{ff}} = K_{ff\_v} \dot{\theta}_d + K_{ff\_a} \ddot{\theta}_d \quad (4.2.3)$$

where $\dot{\theta}_d$ and $\ddot{\theta}_d$ are desired velocity and desired acceleration, respectively; and $K_{ff\_v}$ and $K_{ff\_a}$ are the corresponding FF gains. These gains were manually tuned.

### 4.2.3   PVA Control Simulations and Experiments

The designed controller will be tested using the trajectories listed in Table 4.2.1. The simulations and experiments were done in the horizontal configuration and with only the pneumatic actuator. The control parameters listed in Table 4.2.2 were manually tuned. The simulation and experiment results are shown in Figure 4.2 to Figure 4.9.

Table 4.2.1 List of trajectories used for PVA control

|   | **Test trajectory** |
|---|---|
| **1** | Cycloidal (Rao and Bone 2008) |
| **2** | Ramp |
| **3** | Sine wave at 1 Hz with 0.5 radian amplitude |
| **4** | Sine wave at 2 Hz with 0.3 radian amplitude |

Table 4.2.2 Parameters used for PVA+FF+DZC

| **Parameters** | **Value** | **Unit** |
|---|---|---|
| $K_p$ | 140 | $\text{rad}^{-1}$ |
| $K_v$ | 45 | $\text{s} \cdot \text{rad}^{-1}$ |
| $K_a$ | 1 | $\text{s}^2 \cdot \text{rad}^{-1}$ |
| $K_{ff\_v}$ | 1 | $\text{s} \cdot \text{rad}^{-1}$ |
| $K_{ff\_a}$ | 0.1 | $\text{s}^2 \cdot \text{rad}^{-1}$ |
| $U_{PVA\_MAX}$ | 10 | 1 |
| $T_{pwm\_period}$ | 5 | ms |
| $P_s$ | 3E5 | Pa |
| $P_0$ | 1E5 | Pa |
| $u_{a\_PWM\_Min}$ | 0.08 | 1 |
| $u_{a\_PWM\_Max}$ | 0.80 | 1 |
| $u_{b\_PWM\_Min}$ | 0.08 | 1 |
| $u_{b\_PWM\_Max}$ | 0.72 | 1 |
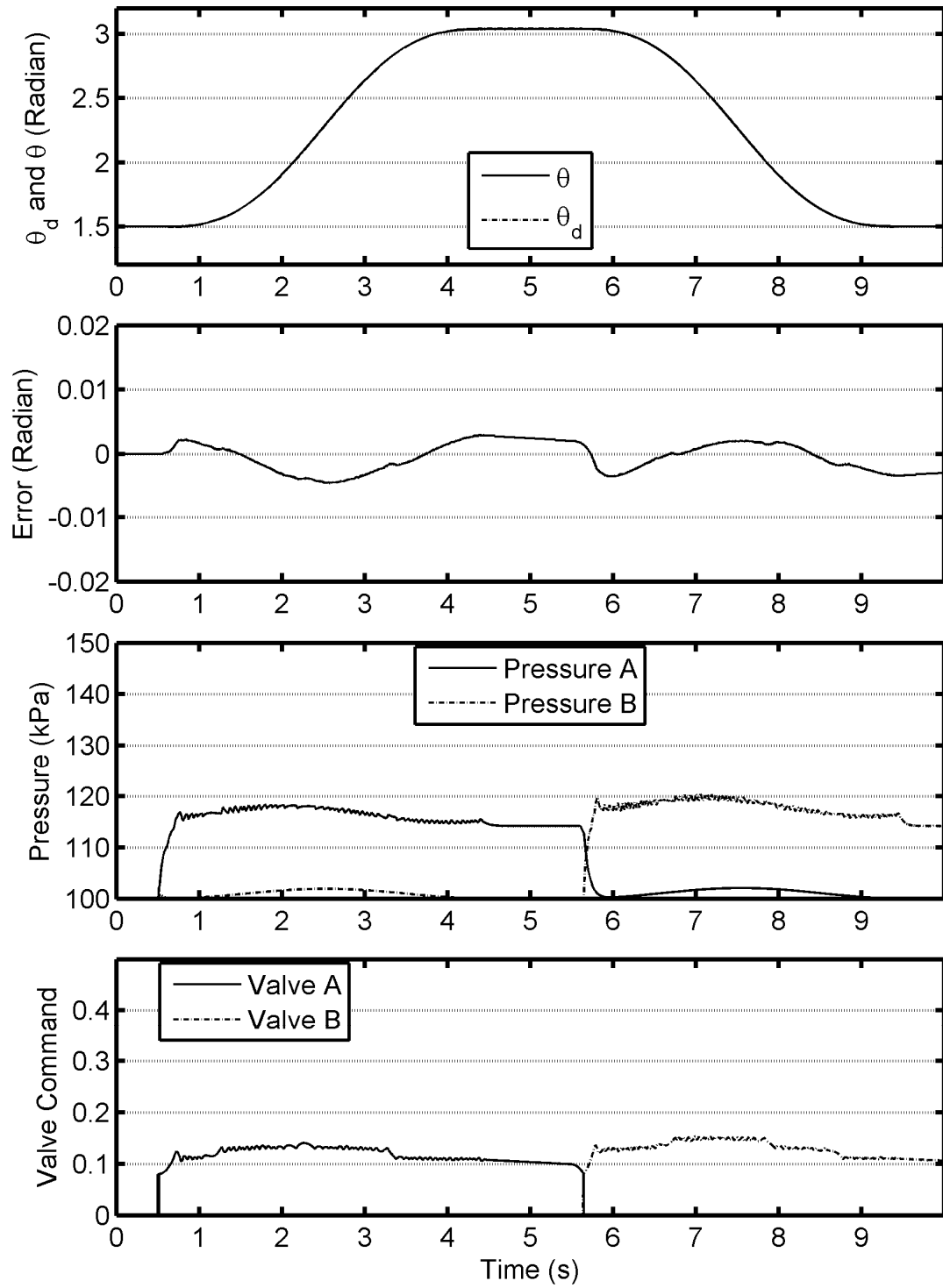
Figure 4.2 Trajectory 1 simulation with PVA+FF+DZC
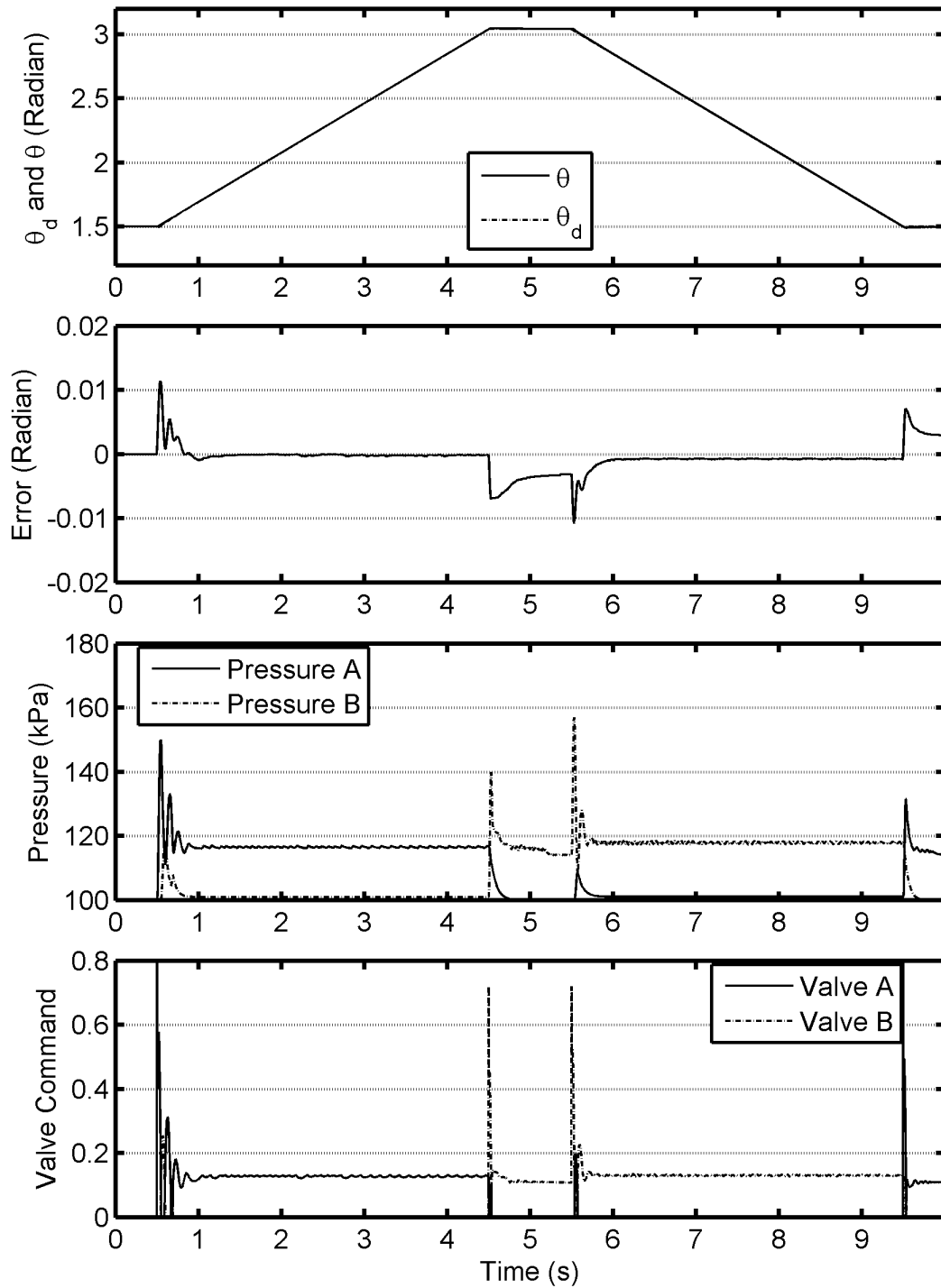
Figure 4.3 Trajectory 2 simulation with PVA+FF+DZC
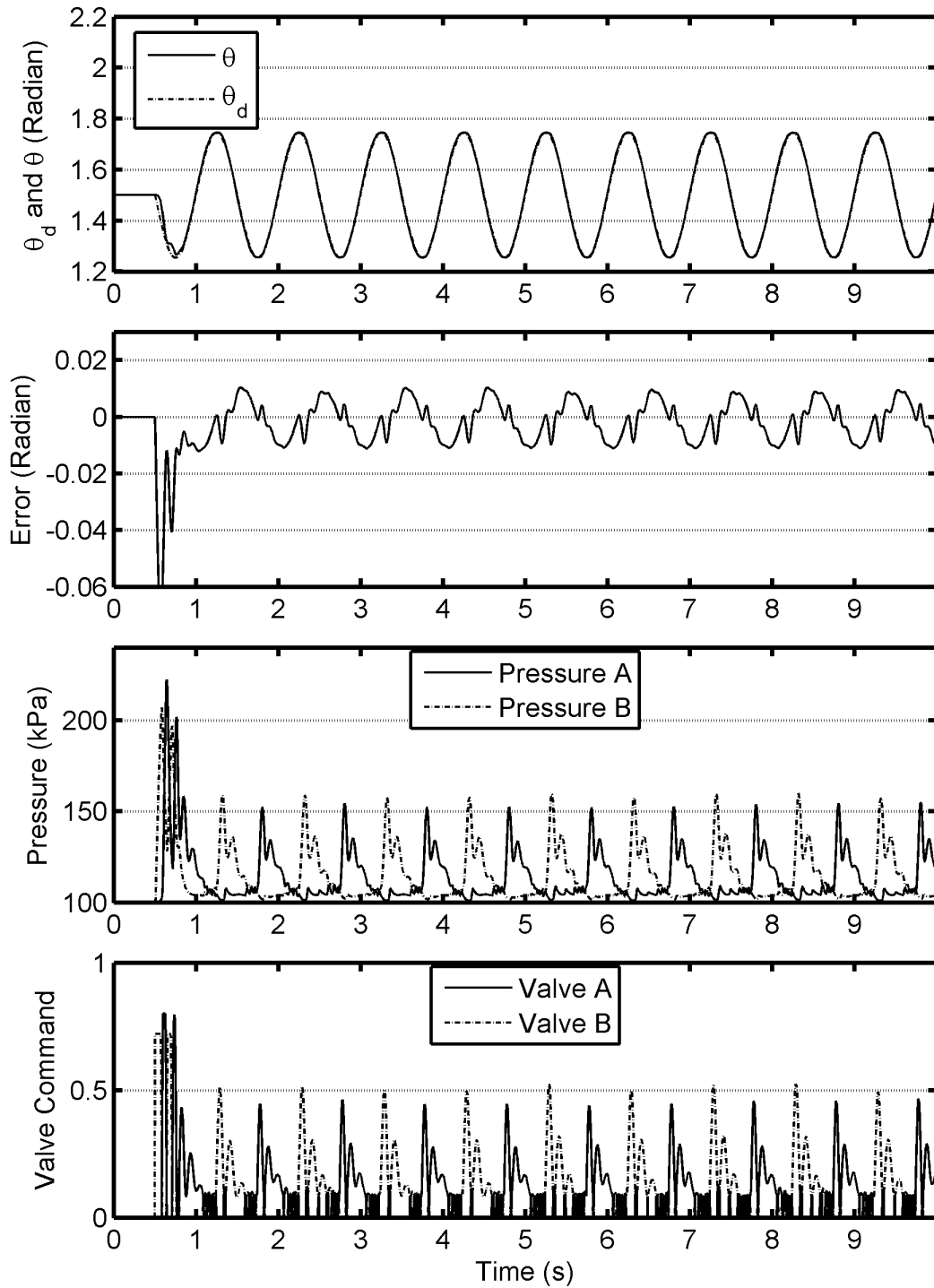
Figure 4.4 Trajectory 3 simulation with PVA+FF+DZC
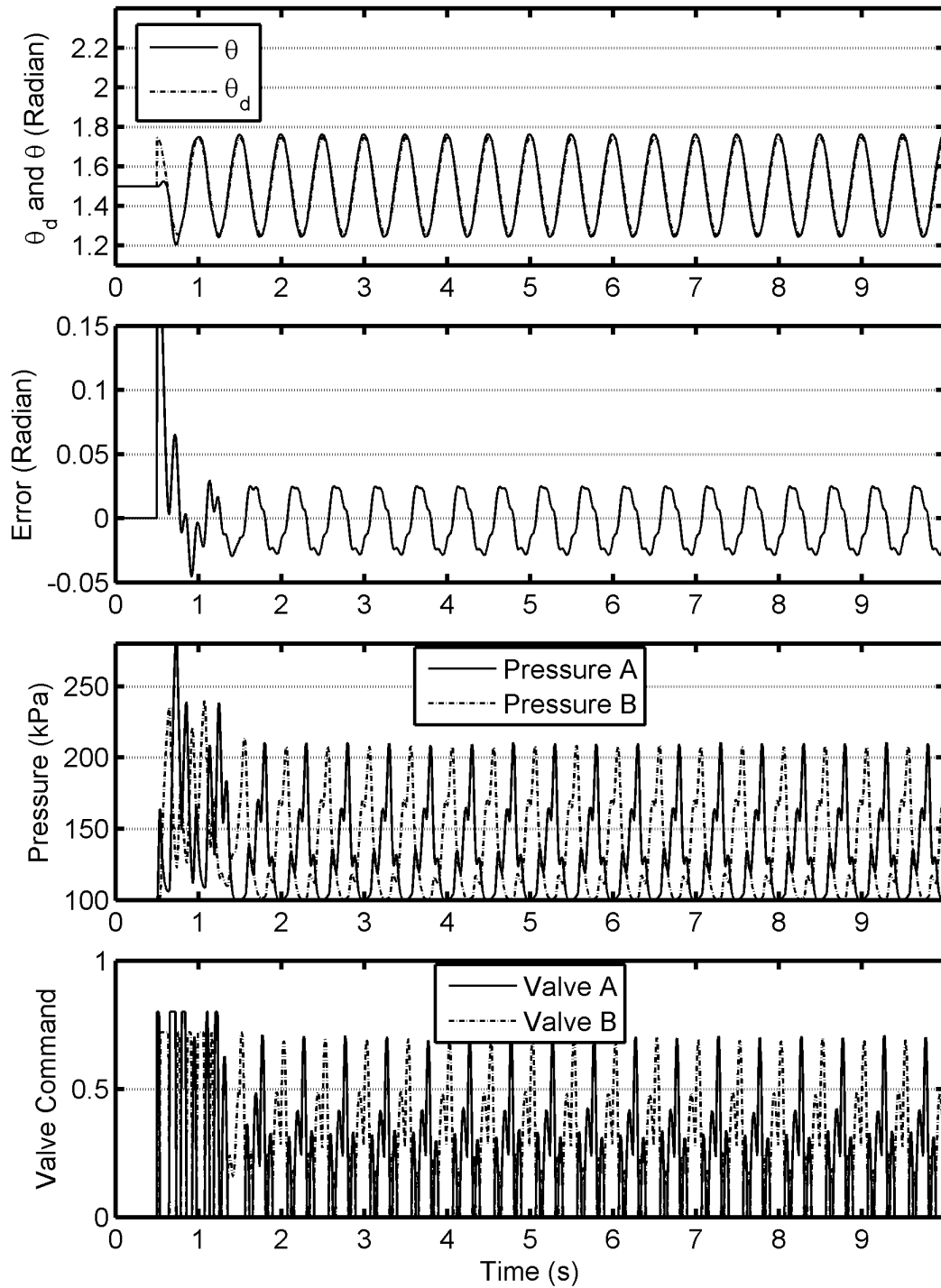
Figure 4.5 Trajectory 4 simulation with PVA+FF+DZC
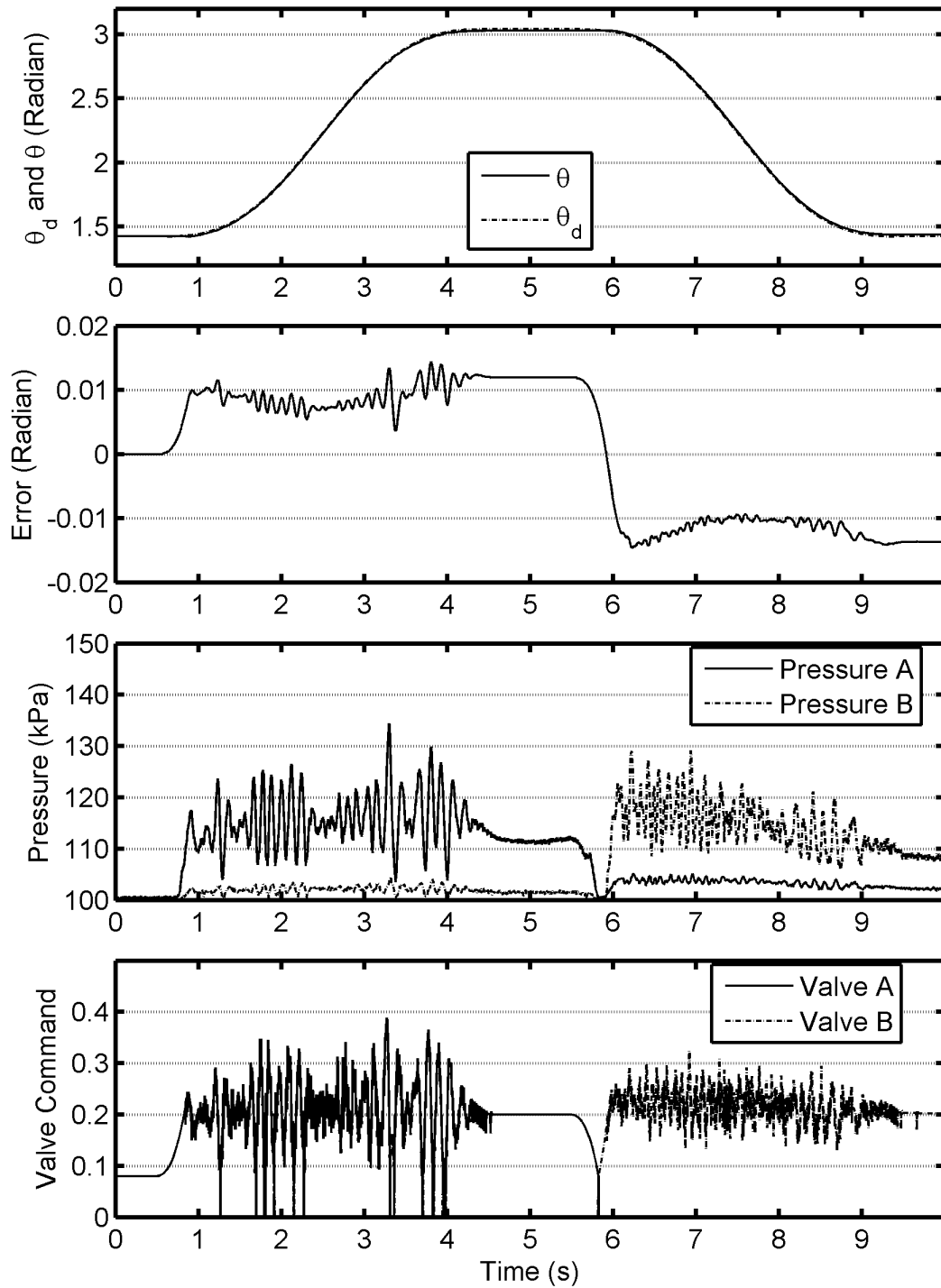
Figure 4.6  Trajectory 1 experiment with PVA+FF+DZC
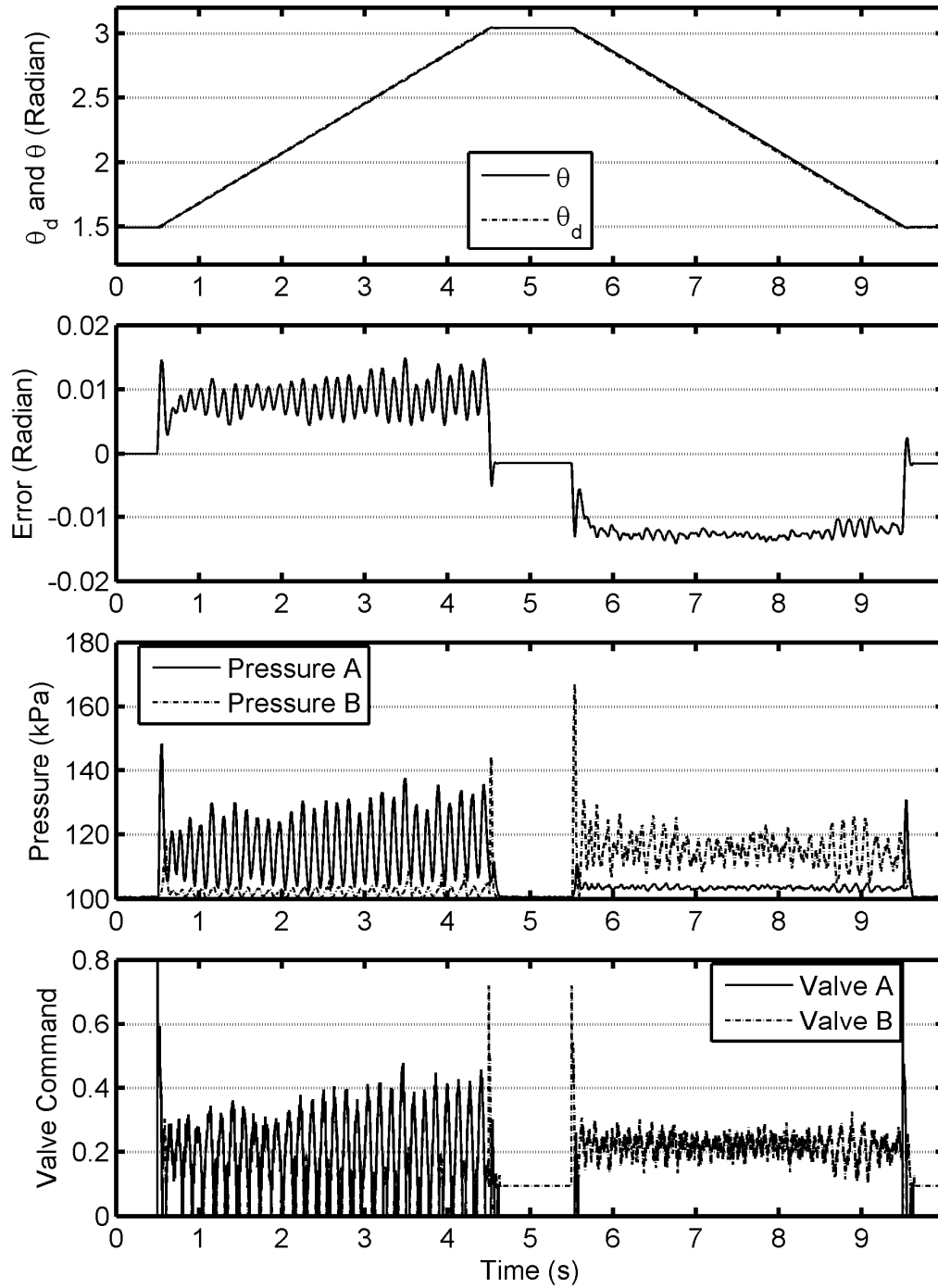
Figure 4.7 Trajectory 2 experiment with PVA+FF+DZC
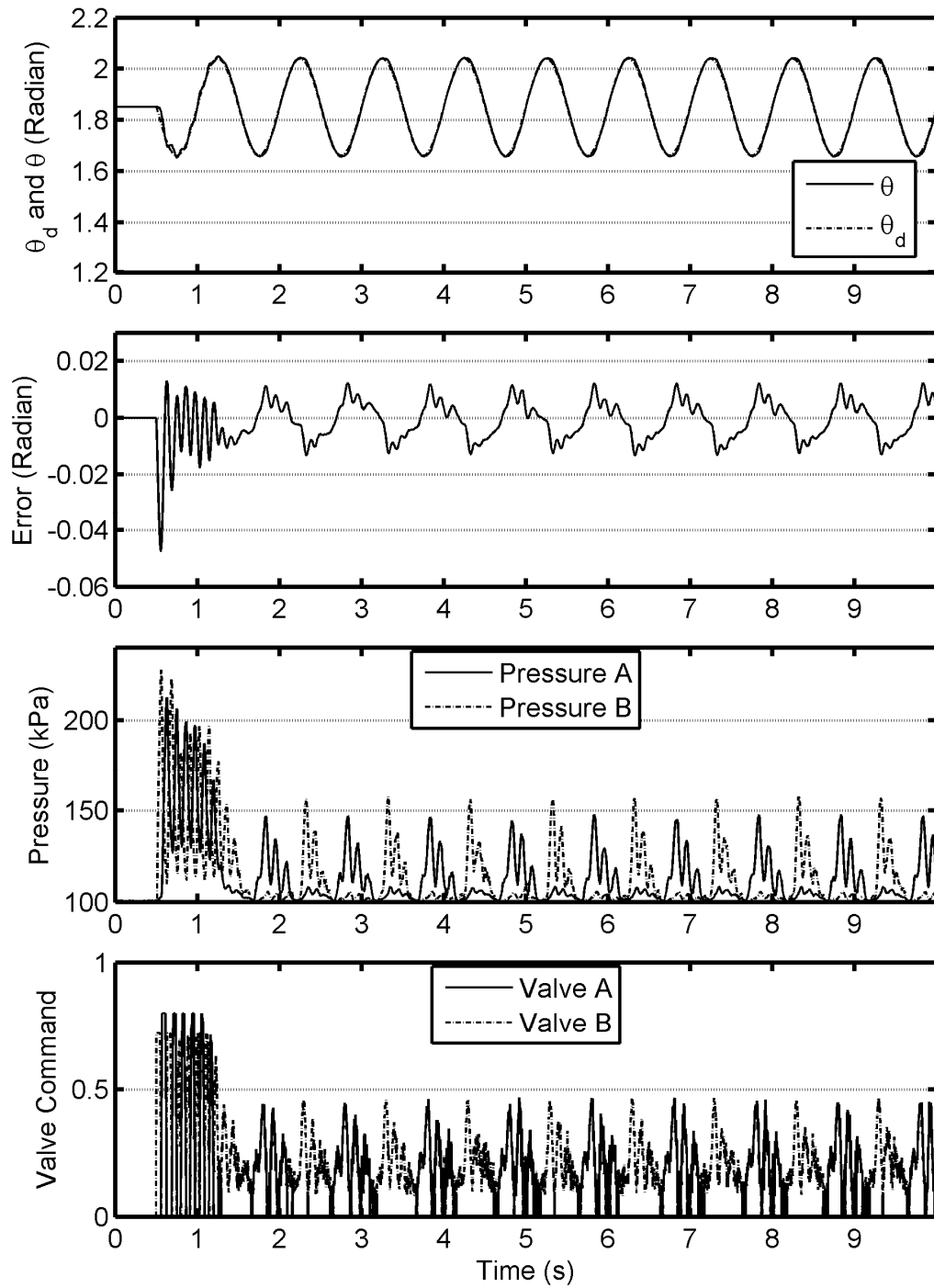
Figure 4.8 Trajectory 3 experiment with PVA+FF+DZC
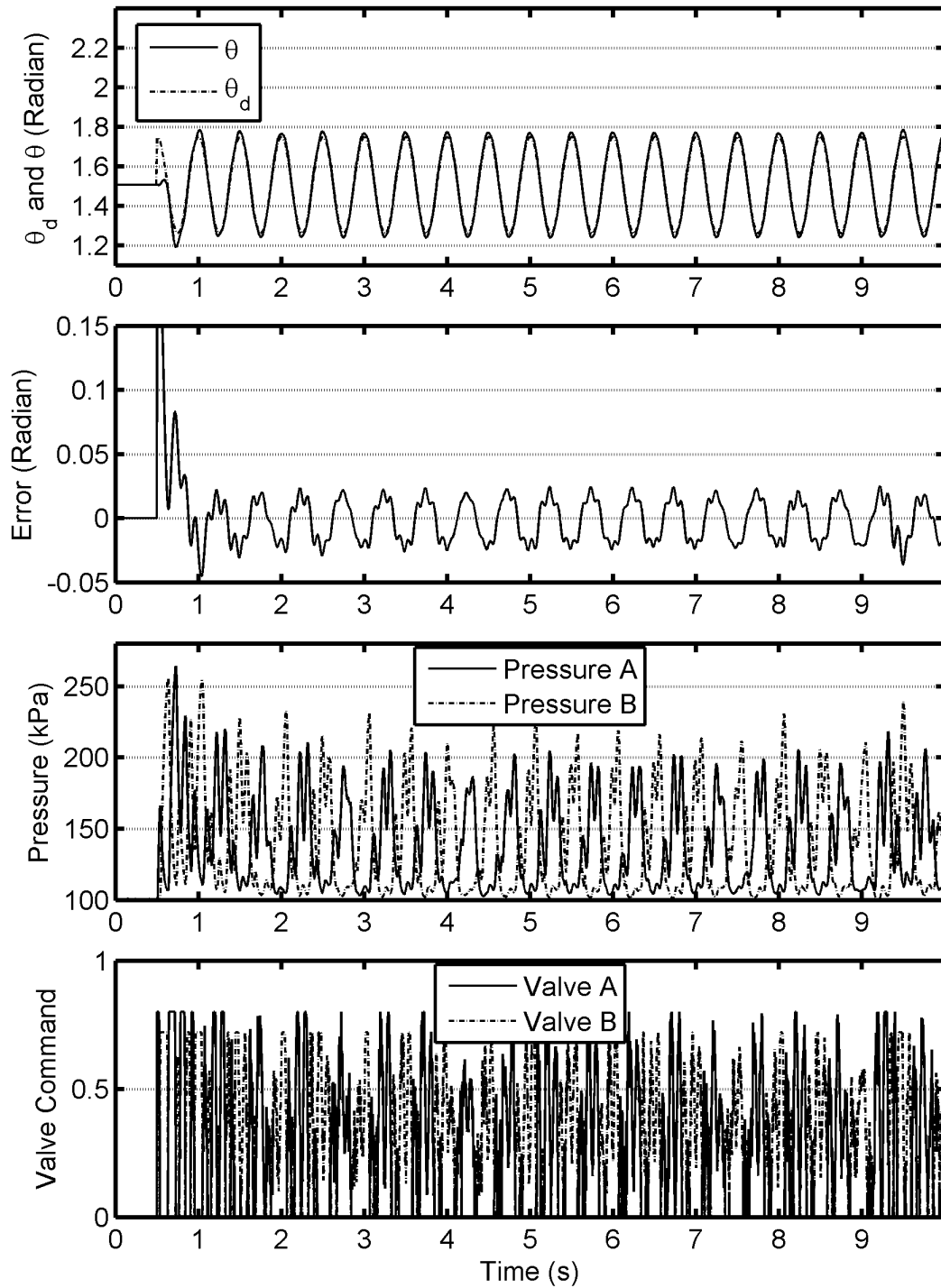
Figure 4.9 Trajectory 4 experiment with PVA+FF+DZC

## 4.3   Backstepping Control

### 4.3.1   Introduction

Backstepping control is a technique for developing a controller which stabilizes a class of nonlinear systems. The design of backstepping control follows a recursive procedure, starting from the innermost subsystem which is related to the control input. Then the process repeatedly backs out to the next outer subsystem until it reaches the external control targets.

In this section, a backstepping controller for the hybrid actuator will be designed and tested.  This controller is an extension of the pneumatic actuator controller presented by Rao and Bone (2008).

### 4.3.2   Backstepping Control Design Procedure

For convenience of designing the controller, the system variables will be denoted by the following symbols:

$$x_1 = \theta, x_2 = \dot{\theta}, x_3 = P_a, x_4 = P_b, x_5 = \dot{m}_a, x_6 = \dot{m}_b, \text{ and } x_m = \tau_{motor} \qquad (4.3.1)$$

After substituting (4.3.1) into the system model derived in Chapter 3 it can be rewritten in the following format:

$$\dot{x}_1 = x_2 \qquad (4.3.2)$$

$$\dot{x}_2 = \frac{1}{I_{eq}}\left\{\left[x_3 A_a - x_4 A_b - P_0(A_a - A_b)\right]r_{pitch} + x_m - \tau_{gravity} - \tau_{friction}\right\}$$

(4.3.3)

$$\dot{x}_3 = -\frac{kr_{pitch}}{y_{a0} + x_1 r_{pitch}}x_2 x_3 + \frac{kRT}{(y_{a0} + x_1 r_{pitch})A_a}x_5 \text{ and}$$

(4.3.4)

$$\dot{x}_4 = \frac{kr_{pitch}}{y_{b0} - x_1 r_{pitch}}x_2 x_4 + \frac{kRT}{(y_{b0} - x_1 r_{pitch})A_b}x_6$$

(4.3.5)

We begin the backstepping design by first defining the tracking error as

$$z_1 = x_{1d} - x_1$$

(4.3.6)

Its derivative when considering (4.3.2) should be

$$\dot{z}_1 = \dot{x}_{1d} - x_2$$

(4.3.7)

Choosing $V_1 = (1/2)\gamma_1 z_1^2$ as a Lyapunov function for (4.3.6), where $\gamma_1 = 1\ kgs^{-2}$, a stabilizing function is selected as

$$\alpha_1 = k_1 z_1 + \dot{x}_{1d}$$

(4.3.8)

The control error is therefore:

$$z_2 = \alpha_1 - x_2 \qquad (4.3.9)$$

So the derivative of $V_1$ is

$$\dot{V}_1 = -k_1\gamma_1 z_1^2 + \gamma_1 z_1 z_2 \qquad (4.3.10)$$

The derivative of Lyapunov function (4.3.10) is non-positive if $z_2$ were zero. To meet this condition, another Lyapunov function $V_2 = V_1 + (1/2)\gamma_2 z_2^2$ is chosen, where $\gamma_2 = 1\,kg$. To calculate the derivative of $V_2$, the derivative of $z_2$ is required. Considering (4.3.3), (4.3.8) and (4.3.9), we obtain

$$\dot{z}_2 = (k_1\dot{z}_1 + \ddot{x}_{1d}) - \frac{1}{I_{eq}}\left\{[x_3 A_a - x_4 A_b - P_0(A_a - A_b)]r_{pitch} + x_m - \tau_{gravity} - \tau_{friction}\right\}$$

$$(4.3.11)$$

Substituting (4.3.11), the derivative of $V_2$ is then:

$$\dot{V}_2 = \gamma_1(-k_1 z_1^2 + z_1 z_2) + \gamma_2 z_2(k_1\dot{z}_1 + \ddot{x}_{1d})$$
$$- \frac{\gamma_2 z_2}{I_{eq}}\left\{[x_3 A_a - x_4 A_b - P_0(A_a - A_b)]r_{pitch} + x_m - \tau_{gravity} - \tau_{friction}\right\} \quad (4.3.12)$$

To keep $\dot{V}_2$ non-positive, a virtual driven torque from pneumatic cylinder and electric motor is designed as follows:

$$(\alpha_2 A_a - \alpha_3 A_b)r_{pitch} + \alpha_m = I_{eq}\beta + \tau_{gravity} + \hat{\tau}_{friction} + P_0(A_a - A_b)r_{pitch} \quad (4.3.13)$$

where $\beta = \ddot{x}_{1d} + k_1 \dot{z}_1 + (\gamma_1 / \gamma_2) z_1 + k_2 z_2$ . The variables $\alpha_2, \alpha_3$ and $\alpha_m$ are the desired chamber pressure A, desired chamber pressure B, and desired motor torque, respectively. We define pressure tracking errors and motor torque tracking error as

$$z_3 = \alpha_2 - x_3 \qquad (4.3.14)$$

$$z_4 = \alpha_3 - x_4 \text{ and} \qquad (4.3.15)$$

$$z_m = \alpha_m - x_m \qquad (4.3.16)$$

Substituting (4.3.13)-(4.3.16) into(4.3.12) yields

$$\dot{V}_2 = -\gamma_1 k_1 z_1^2 - \gamma_2 k_2 z_2^2 + \frac{\gamma_2 z_2}{I_{eq}} [(\tau_{friction} - \hat{\tau}_{friction})$$
$$+ (z_3 A_a - z_4 A_b) r_{pitch} + z_m] \qquad (4.3.17)$$

The friction modeling error is bounded by $\Delta \tau_{friction}$

$$\left| \tau_{friction} - \hat{\tau}_{friction} \right| \leq \Delta \tau_{friction} \qquad (4.3.18)$$

Consequently, when using the virtual driven torque as input, the subsystem will be stabilized. However, it is impossible to determine the desired $\alpha_2, \alpha_3$ and $\alpha_m$ with only one constraint (4.3.13). In order to solve the desired chamber pressures and the motor torque, the following two additional conditions must be satisfied

$$P_s - \alpha_2 = \alpha_3 - P_0 \text{ and} \tag{4.3.19}$$

$$\alpha_m = K_{portion}(\alpha_2 A_a - \alpha_3 A_b)r_{pitch} \tag{4.3.20}$$

The purpose of constraint (4.3.19) is to set the desired pressures of chambers A and B symmetrically around the nominal pressure. In such case, the pressure changes in two chambers will be distributed evenly as shown in Figure 4.10. In the constraint (4.3.20), $K_{portion}$ is a constant which represents the ratio of the motor torque to the total torque. This parameter should be determined by the relationship of the motor's peak torque specification, the supply pressure $P_s$ and atmosphere pressure $P_0$.
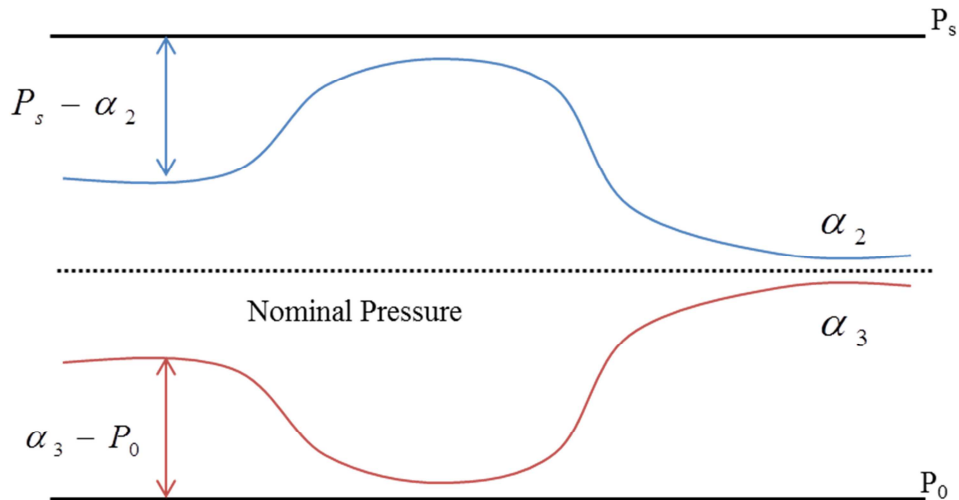


Figure 4.10   Illustration of the constraint on the desired chamber pressures.

From (4.3.13), (4.3.19) and (4.3.20) the following solutions are derived,

$$\alpha_2 = \frac{(P_s + P_0)A_b}{(A_a + A_b)} + \frac{I_{eq}\beta + \tau_{gravity} + \hat{\tau}_{friction} + P_0(A_a - A_b)r_{pitch}}{(1 + K_{protion})(A_a + A_b)r_{pitch}} \qquad (4.3.21)$$

$$\alpha_3 = \frac{(P_s + P_0)A_a}{(A_a + A_b)} - \frac{I_{eq}\beta + \tau_{gravity} + \hat{\tau}_{friction} + P_0(A_a - A_b)r_{pitch}}{(1 + K_{protion})(A_a + A_b)r_{pitch}} \text{ and} \qquad (4.3.22)$$

$$\alpha_m = \frac{K_{portion}}{1 + K_{portion}} \left[ I_{eq}\beta + \tau_{gravity} + \hat{\tau}_{friction} + P_0(A_a - A_b)r_{pitch} \right] \qquad (4.3.23)$$

The goal is to stabilize $(z_1, z_2, z_3, z_4, z_m)$ system. As is commonly done, we assume that after the analog voltage signal is sent to the amplifier, the motor torque is precisely and instantly established. Thus the motor torque control error $z_m$ can be regarded as equaling zero. Now the goal is simplified to stabilizing the $(z_1, z_2, z_3, z_4)$ system. We select the following Lyapunov function

$$V_3 = V_2 + \frac{1}{2}\gamma_3 z_3^2 + \frac{1}{2}\gamma_3 z_4^2 \qquad (4.3.24)$$

where $\gamma_3 = 1\, m^2 kg^{-1}s^{-2}$. The derivative of (4.3.24) is calculated by:

$$\dot{V}_3 = \dot{V}_2 + \gamma_3 z_3 \dot{z}_3 + \gamma_3 z_4 \dot{z}_4 \qquad (4.3.25)$$

In order to obtain the derivative, $\dot{z}_3$ and $\dot{z}_4$ are required. Combining (4.3.21), (4.3.14) and (4.3.4)

$$\dot{z}_3 = \dot{\alpha}_2 - \dot{x}_3$$

$$= \frac{I_{eq}\dot{\beta} + \dot{\hat{\tau}}_{friction}}{(1+K_{protion})(A_a+A_b)r_{pitch}} + \frac{kr_{pitch}}{y_{a0}+x_1 r_{pitch}}x_2 x_3$$

$$- \frac{kRT}{(y_{a0}+x_1 r_{pitch})A_a}x_5 \qquad\qquad (4.3.26)$$

$$= \frac{I_{eq}\dot{\beta} + \dot{\hat{\tau}}_{friction}}{(1+K_{protion})(A_a+A_b)r_{pitch}} + \frac{kx_2 x_3 r_{pitch}A_a - kRTx_5}{(y_{a0}+x_1 r_{pitch})A_a}$$

Similarly, from (4.3.22), (4.3.15) and (4.3.5)

$$\dot{z}_4 = \dot{\alpha}_3 - \dot{x}_4$$

$$= -\frac{I_{eq}\dot{\beta} + \dot{\hat{\tau}}_{friction}}{(1+K_{protion})(A_a+A_b)r_{pitch}} - \frac{kr_{pitch}}{y_{b0}-x_1 r_{pitch}}x_2 x_4$$

$$- \frac{kRT}{(y_{b0}-x_1 r_{pitch})A_b}x_6 \qquad\qquad (4.3.27)$$

$$= -\frac{I_{eq}\dot{\beta} + \dot{\hat{\tau}}_{friction}}{(1+K_{protion})(A_a+A_b)r_{pitch}} + \frac{-kx_2 x_4 r_{pitch}A_b - kRTx_6}{(y_{b0}-x_1 r_{pitch})A_b}$$

Substituting (4.3.26) and (4.3.27) into (4.3.25), the derivative of $V_3$ is:

$$\dot{V}_3 = \dot{V}_2 + \gamma_3 z_3 \dot{z}_3 + \gamma_3 z_4 \dot{z}_4$$

$$= -\gamma_1 k_1 z_1^2 - \gamma_2 k_2 z_2^2 + z_m \frac{\gamma_2 z_2}{I_{eq}} + \frac{\gamma_2 z_2}{I_{eq}}(\tau_{friction} - \hat{\tau}_{friction})$$

$$+ \gamma_3 z_3 [\frac{\gamma_2 z_2 A_a r_{pitch}}{\gamma_3 I_{eq}} + \frac{I_{eq}\dot{\beta} + \dot{\hat{\tau}}_{friction}}{(1 + K_{protion})(A_a + A_b)r_{pitch}}$$

$$+ \frac{kx_2 x_3 r_{pitch}}{y_{a0} + x_1 r_{pitch}} - \frac{kRT}{(y_{a0} + x_1 r_{pitch})A_a} x_5]$$

$$- \gamma_3 z_4 [\frac{\gamma_2 z_2 A_b r_{pitch}}{\gamma_3 I_{eq}} + \frac{I_{eq}\dot{\beta} + \dot{\hat{\tau}}_{friction}}{(1 + K_{protion})(A_a + A_b)r_{pitch}}$$

$$+ \frac{kx_2 x_4 r_{pitch}}{y_{b0} - x_1 r_{pitch}} + \frac{kRT}{(y_{b0} - x_1 r_{pitch})A_b} x_6] \qquad (4.3.28)$$

We choose virtual mass flow rates for chamber A and chamber B as follows

$$\alpha_4 = \frac{(y_{a0} + x_1 r_{pitch})A_a}{kRT}(k_3 z_3 + \frac{\gamma_2 z_2}{\gamma_3 I_{eq}}A_a r_{pitch}$$

$$+ \frac{I_{eq}\dot{\beta} + \dot{\hat{\tau}}_{friction}}{(1 + K_{protion})(A_a + A_b)r_{pitch}} + \frac{kx_2 x_3 r_{pitch}}{y_{a0} + x_1 r_{pitch}}) \qquad (4.3.29)$$

$$\alpha_5 = \frac{(y_{b0} - x_1 r_{pitch})A_b}{kRT}(k_4 z_4 - \frac{\gamma_2 z_2}{\gamma_3 I_{eq}}A_b r_{pitch}$$

$$- \frac{I_{eq}\dot{\beta} + \dot{\hat{\tau}}_{friction}}{(1 + K_{protion})(A_a + A_b)r_{pitch}} - \frac{kx_2 x_4 r_{pitch}}{y_{b0} - x_1 r_{pitch}}) \qquad (4.3.30)$$

We define two mass flow rate tracking errors as

$$z_5 = \alpha_4 - x_5 \tag{4.3.31}$$

$$z_6 = \alpha_5 - x_6 \tag{4.3.32}$$

Substituting (4.3.29), (4.3.30), (4.3.31) and (4.3.32) into (4.3.28)

$$
\begin{aligned}
\dot{V}_3 = &-\gamma_1 k_1 z_1^2 - \gamma_2 k_2 z_2^2 - \gamma_3 k_3 z_3^2 - \gamma_4 k_4 z_4^2 \\
&+ z_m \frac{\gamma_2 z_2}{I_{eq}} + \frac{\gamma_2 z_2}{I_{eq}}(\tau_{friction} - \hat{\tau}_{friction}) \\
&+ \frac{kRT}{(y_{a0} + x_1 r_{pitch})A_a}\gamma_3 z_3 z_5 + \frac{kRT}{(y_{b0} - x_1 r_{pitch})A_b}\gamma_3 z_4 z_6
\end{aligned}
\tag{4.3.33}
$$

Assuming valve modeling errors are bounded by $|z_5| < \Delta\dot{m}_a$ and $|z_6| < \Delta\dot{m}_b$, the motor torque modeling error $z_m$ is zero and the displacement is bounded by the stroke such that

$$\left|\frac{kRT}{(y_{a0} + x_1 r_{pitch})A_a}\right| \leq \psi_a \tag{4.3.34}$$

$$\left|\frac{kRT}{(y_{b0} - x_1 r_{pitch})A_b}\right| \leq \psi_b \tag{4.3.35}$$

Hence (4.3.33) is bounded since all the terms are bounded, as follows:

$$
\begin{aligned}
\dot{V}_3 \leq &-\gamma_1 k_1 z_1^2 - \gamma_2 k_2 z_2^2 - \gamma_3 k_3 z_3^2 - \gamma_4 k_4 z_4^2 \\
&+ \frac{\gamma_2 z_2}{I_{eq}}\Delta\tau_{motor} + \frac{\gamma_2 z_2}{I_{eq}}\Delta\tau_{friction} + \psi_a \gamma_3 z_3 \Delta\dot{m}_a + \psi_b \gamma_3 z_4 \Delta\dot{m}_b
\end{aligned}
\tag{4.3.36}
$$

From(4.3.37), the $(z_1, z_2, z_3, z_4)$ system will be globally asymptotically uniformly bounded and the tracking error $z_1$ can be made arbitrarily small by selecting sufficiently large values for $k_1$, $k_2$, $k_3$ and $k_4$. Finally, the backstepping control signals are calculated by:

$$
\begin{aligned}
u_{bs,va} &= \lambda_a(\alpha_4, P_a), \\
u_{bs,vb} &= \lambda_b(\alpha_5, P_b), \text{ and} \\
\tau_{bs,motor} &= \frac{K_{portion}}{1 + K_{portion}} \left[ I_{eq}\beta + \tau_{gravity} + \hat{\tau}_{friction} + P_0(A_a - A_b)r_{pitch} \right]
\end{aligned}
\tag{4.3.38}
$$

where $\lambda_a(\cdot)$ and $\lambda_b(\cdot)$ are the mass flow rate models of valves A and B, respectively. The desired mass flow rates $\alpha_4$ and $\alpha_5$ were given by (4.3.29) and (4.3.30).

### 4.3.3   Compensation Torques

In this section, a feedback term for the electric motor and a FF term for pneumatic cylinder will be introduced. The stability of the backstepping control with the feedback term will be analyzed.   The FF term will not affect the closed-loop stability.   Both compensation torques are expected to improve the tracking performance, as further explained below.

### 4.3.3.1   Electric Motor Compensation

With the hybrid actuator, the majority of the torque is to be provided by the pneumatic cylinder. The cylinder torque is established through the compressed air applied to the piston in the two chambers. The dynamics of the air and other pneumatic components make it difficult to provide cylinder torque quickly and precisely. Meanwhile, electrical motor torque can be provided almost instantly with adequate precision. In order

to utilize motor more efficiently, an additional feedback compensation of the motor is introduced in this section.

The electric motor is much faster than pneumatic cylinder in the sense of torque establishment. However, the backstepping controller is based on the process of cylinder torque establishment. The desired motor torque is set by (4.3.39) to be a fraction of the desired motor torque. The rapid torque response of the electric motor was ignored by the backstepping controller design. Hence, it is desirable to add a feedback term to the motor torque.

The feedback compensation can be calculated based on position and velocity errors:

$$\tau_{motor\_PD} = K_{bs\_motor,p}\tilde{e} + K_{bs\_motor,d}\dot{\tilde{e}} \qquad (4.3.40)$$

where $\tilde{e} = \theta_d - \theta, \dot{\tilde{e}} = \dot{\theta}_d - \dot{\hat{\theta}}$ are position and velocity tracking errors. $K_{bs\_motor,p}, K_{bs\_motor,d}$ are controller gains. The motor torque command is then:

$$\tau_{motor} = \tau_{bs,motor} + \tau_{motor\_PD} \qquad (4.3.41)$$

## 4.3.3.2 Stability Analysis of the Backstepping Controller with Electric Motor Feedback Compensation

The introduced feedback term for electric motor may have an unexpected impact on the backstepping controller. It is necessary to analysis the stability of the backstepping controlled system with such an additional feedback term.

Recall that in backstepping controller, the original desired motor torque is calculated by:

$$u_m = \frac{K_{portion}}{1 + K_{portion}} \left[ I_{eq}\beta + \tau_{gravity} + \hat{\tau}_{friction} + P_0(A_a - A_b)r_{pitch} \right] \qquad (4.3.42)$$

with the additional feedback term it becomes:

$$\begin{aligned} u_{m,FB} = \frac{K_{portion}}{1 + K_{portion}} [I_{eq}\beta + \tau_{gravity} + \hat{\tau}_{friction} \\ + P_0(A_a - A_b)r_{pitch}] + \tau_{motor\_PD} \end{aligned} \qquad (4.3.43)$$

where $\tau_{motor\_PD} = K_{bs\_motor,p}\tilde{e} + K_{bs\_motor,d}\dot{\tilde{e}}$. Considering (4.3.6), (4.3.8) and (4.3.9), the feedback term can be written in the form:

$$\tau_{motor\_PD} = (K_{bs\_motor,p} - K_{bs\_motor,d}k_1)z_1 + K_d z_2 \qquad (4.3.44)$$

The motor torque tracking error in (4.3.16) was assumed to be zero to simplify the backstepping controller design. Since the new feedback term is added, the amended motor torque tracking error becomes:

$$z_{m,FB} = z_m + (u_{m,FB} - u_m) = \tau_{motor\_PD} \qquad (4.3.45)$$

If the designed backstepping is otherwise unchanged, the derivative of the chosen Lyapunov function $V_2$ with (4.3.45) becomes:

$$\begin{aligned} \dot{V}_2 = -\gamma_1 k_1 z_1^2 - \gamma_2 k_2 z_2^2 \\ + \frac{\gamma_2 z_2}{I_{eq}}[(\tau_{friction} - \hat{\tau}_{friction}) + (z_3 A_a - z_4 A_b)r_{pitch} + \tau_{motor\_PD}] \end{aligned} \qquad (4.3.46)$$

Substituting (4.3.44) into (4.3.46):

$$\dot{V}_2 = -\gamma_1 k_1 z_1^2 - \gamma_2 k_2 z_2^2$$
$$+ \frac{\gamma_2 z_2}{I_{eq}} [(\tau_{friction} - \hat{\tau}_{friction}) + (z_3 A_a - z_4 A_b) r_{pitch}] \qquad (4.3.47)$$
$$+ a z_1 z_2 + b z_2^2$$

where the coefficients $a$ and $b$ are:

$$a = \frac{\gamma_2 (K_{bs\_motor,p} - K_{bs\_motor,d} k_1)}{I_{eq}}, \text{ and } b = \frac{K_{bs\_motor,d} \gamma_2}{I_{eq}} \qquad (4.3.48)$$

The derivative of the chosen Lyapunov function $V_3$ considering (4.3.47) gives

$$\dot{V}_3 = -\gamma_1 k_1 z_1^2 - \gamma_2 k_2 z_2^2 - \gamma_3 k_3 z_3^2 - \gamma_4 k_4 z_4^2$$
$$+ a z_1 z_2 + b z_2^2 + \frac{\gamma_2 z_2}{I_{eq}} (\tau_{friction} - \hat{\tau}_{friction})$$
$$+ \frac{kRT}{(y_{a0} + x_1 r_{pitch}) A_a} \gamma_3 z_3 z_5 + \frac{kRT}{(y_{b0} - x_1 r_{pitch}) A_b} \gamma_3 z_4 z_6$$
$$= -\gamma_1 k_1 z_1^2 + a z_1 z_2 - (\gamma_2 k_2 - b) z_2^2 - \gamma_3 k_3 z_3^2 - \gamma_4 k_4 z_4^2$$
$$+ \frac{kRT}{(y_{a0} + x_1 r_{pitch}) A_a} \gamma_3 z_3 z_5 + \frac{kRT}{(y_{b0} - x_1 r_{pitch}) A_b} \gamma_3 z_4 z_6 \qquad (4.3.49)$$
$$= -(\gamma_1 k_1 - \frac{a^2}{2}) z_1^2 - (\frac{\sqrt{2}}{2} a z_1 - z_2)^2$$
$$- (\gamma_2 k_2 - b - 1) z_2^2 - \gamma_3 k_3 z_3^2 - \gamma_4 k_4 z_4^2$$
$$+ \frac{kRT}{(y_{a0} + x_1 r_{pitch}) A_a} \gamma_3 z_3 z_5 + \frac{kRT}{(y_{b0} - x_1 r_{pitch}) A_b} \gamma_3 z_4 z_6$$

From (4.3.49), we can see if $\gamma_1 k_1 > \dfrac{a^2}{2}$, $\gamma_2 k_2 > b + 1$, and $k_3$ and $k_4$ are sufficiently large,

the $\dot{V}_3$ will be non-positive with the similar discussion in backstepping control design

section, in which all of the individual terms are separately bounded. Considering (4.3.48),

solving the inequalities for the backstepping gains $k_1$ and $k_2$ gives

$$k_1 > \frac{\gamma_2 K_{bs\_motor,p}}{I_{eq}\sqrt{2\gamma_1} + \gamma_2 K_{bs\_motor,d}} \text{ and } k_2 > \frac{1}{\gamma_2} + \frac{K_{bs\_motor,d}}{I_{eq}} \tag{4.3.50}$$

Consequently, the backstepping controller with electric motor feedback term will be globally asymptotically uniformly bounded and the tracking error $z_1$ can be made arbitrarily small by selecting sufficiently large values for $k_1, k_2, k_3$ and $k_4$ ; selecting appropriate values of $K_{bs\_motor,p}$ and $K_{bs\_motor,d}$ that satisfy the conditions defined in (4.3.50).

Note that the analysis above was based on the worst case in which the motor torque is not bounded. In our prototype, the motor torque is limited to the maximum output of the analog output voltage, namely the maximum torque is under 0.159 Nm. In expression form:

$$\left| \tau_{motor\_PD} \right| \leq \tau_{motor\_max} \tag{4.3.51}$$

The derivative of the chosen Lyapunov function $V_3$ considering (4.3.51) becomes

$$\begin{aligned}
\dot{V}_3 = &-\gamma_1 k_1 z_1^2 - \gamma_2 k_2 z_2^2 - \gamma_3 k_3 z_3^2 - \gamma_4 k_4 z_4^2 \\
&+ \tau_{motor\_max} + \frac{\gamma_2 z_2}{I_{eq}}(\tau_{friction} - \hat{\tau}_{friction}) \\
&+ \frac{kRT}{(y_{a0} + x_1 r_{pitch})A_a}\gamma_3 z_3 z_5 + \frac{kRT}{(y_{b0} - x_1 r_{pitch})A_b}\gamma_3 z_4 z_6
\end{aligned} \tag{4.3.52}$$

Similar to the backstepping control design analysis, the individual terms of $\dot{V}_3$ are bounded. The backstepping controller with the feedback term will be globally

asymptotically uniformly bounded and the tracking error $z_1$ can be made arbitrarily small by only selecting sufficiently large values for $k_1, k_2, k_3$ and $k_4$.

### 4.3.3.3   Pneumatic Cylinder Feedforward Compensation

Feedback control action is useful for providing robustness to system uncertainty but is somewhat slow since an error must occur before the controller reacts.  Since FF control can produce a more rapid response to changes in the desired trajectory, a FF compensator was developed for the pneumatic actuator. The FF compensation torque should also provide the benefit of avoiding motor saturation and the associated performance deterioration.

Recalling Chapter 3, the dynamics equation for the hybrid actuator is:

$$I_{eq}\ddot{\theta} = \tau_{motor} + \tau_{cylinder} - \tau_{gravity} - \tau_{friction} \qquad (4.3.53)$$

When the desired position is $\theta_d$, the desired trajectory is $\dot{\theta}_d$, the desired angular acceleration is $\ddot{\theta}_d$. The corresponding sum of desired torques is given by:

$$\tau_{cylinder\_d} + \tau_{motor\_d} = I_{eq}\ddot{\theta}_d + \tau_{gravity\_d} + \tau_{friction} \qquad (4.3.54)$$

Assuming the desired motor torque is zero, the desired pneumatic cylinder torque term can be estimated by:

$$\tau_{cylinder\_d} = I_{eq}\ddot{\theta}_d + \tau_{gravity\_d} + \hat{\tau}_{friction} \qquad (4.3.55)$$

To solve individual desired pressures for each chamber, a constraint is needed. An actuator with higher stiffness is better able to resist disturbance torques. To satisfy the objectives of evenly distributing the differential chamber pressure, and providing the

higher pressures needed for higher stiffness, the desired pressures should change around a nominal pressure with the same amplitude of $\Delta P$ (see Figure 4.10). Thus, the desired chamber pressures are:

$$P_{a,ff} = P_{nominal} + \Delta P, \text{ and } P_{b,ff} = P_{nominal} - \Delta P \tag{4.3.56}$$

where the pressure difference can be calculated by:

$$\Delta P = \frac{\dfrac{\tau_{cylinder\_d}}{r_{pitch}} - P_{nominal}(A_a - A_b) + P_0(A_a - A_b)}{A_a + A_b} \tag{4.3.57}$$

To obtain the desired chamber pressures, the desired FF mass flow rates for both valves are consequently:

$$\begin{aligned}
\dot{m}_{a,ff} &= \frac{(y_{a0} + \theta r_{pitch})A_a \dot{P}_{a,ff} + kP_{a,ff}\dot{\theta} r_{pitch} A_a}{kRT} \\
\dot{m}_{b,ff} &= \frac{(y_{b0} - \theta r_{pitch})A_b \dot{P}_{b,ff} - kP_{b,ff}\dot{\theta} r_{pitch} A_b}{kRT}
\end{aligned} \tag{4.3.58}$$

where $\dot{P}_{a,ff}$ and $\dot{P}_{b,ff}$ are calculated by numerical derivative:

$$\begin{aligned}
\dot{P}_{a,ff}(t_k) &= \left( P_{a,ff}(t_i) - P_{a,ff}(t_i - T_{pwm\_period}) \right) / T_{pwm\_period} \\
\dot{P}_{b,ff}(t_k) &= \left( P_{b,ff}(t_i) - P_{b,ff}(t_i - T_{pwm\_period}) \right) / T_{pwm\_period}
\end{aligned}$$

where $t_i$ is the current sampling time instant, and $T_{pwm\_period}$ is the PWM period.

When the FF compensator is combined with the backstepping controller the desired mass flow rates are given by:

$$\begin{aligned}
\dot{m}_a &= \dot{m}_{a,ff} + \dot{m}_{a,fb} \\
\dot{m}_b &= \dot{m}_{b,ff} + \dot{m}_{b,fb}
\end{aligned} \tag{4.3.59}$$

where $\dot{m}_{a,fb}$ and $\dot{m}_{b,fb}$ equal $\alpha_4$ and $\alpha_5$, respectively. Finally the PWM input for each valve can be calculated using the method presented in Section 3.7.

### 4.3.4   Preliminary Simulation and Experiment Results

To verify the effectiveness of the proposed backstepping controller, preliminary simulations and experiments with roughly tuned gains were performed for the horizontal configuration. The hybrid pneumatic-electric actuator can be operated in three actuation modes, namely pneumatic mode, electric motor mode, and the hybrid mode. These are listed in Table 4.3.1.

Table 4.3.1 Hybrid pneumatic-electric actuator modes

| **Pneumatic** | Electric motor is turned off, only pneumatic actuation is used. |
|---|---|
| **Electric motor** | Solenoid valves are turned off, only electric motor actuation is used. |
| **Hybrid** | Both of the actuators are used. |

To limit the amount of figures, the RMSE results for the hybrid mode under backstepping control will be listed in the comparison section, section 4.5. The trajectory used are listed in Table 4.2.1 and the controller parameters are listed in Table 4.3.2

Table 4.3.2  Backstepping controller parameters.

| Pneumatic Parameters | Value | Unit | Electric Motor Parameters | Value | Unit |
|:---:|:---:|:---:|:---:|:---:|:---:|
| $k_1$ | 60 | $s^{-1}$ | $K_{bs\_motor,p}$ | 85 | $Nm \cdot rad^{-1}$ |
| $k_2$ | 20 | $s^{-1}$ | $K_{bs\_motor,d}$ | 14 | $Nm \cdot rad^{-1} \cdot s$ |
| $k_3$ | 65 | $s^{-1}$ | $K_{proportion}$ | 0.1 | 1 |
| $k_4$ | 65 | $s^{-1}$ | | | |
| $T_{pwm\_period}$ | 5 | ms | | | |
| $T_s$ | 1 | ms | | | |

The same parameters were used for both simulation and experiment. Figure 4.11, Figure 4.12, and Figure 4.13 shows the simulation results for FF control only, backstepping control only, and FF + backstepping respectively. The FF control alone achieved position tracking with errors less than 0.06 radian. The backstepping controller tracked the reference trajectory with a maximum error of 0.01 radian accuracy. The proposed backstepping + FF controller has a maximum error less than 0.003 radian.  The backstepping + FF controller was simulated for the remainder of given trajectories. Simulation results given in Figure 4.14 to Figure 4.20

Figure 4.14 to Figure 4.16 demonstrate the simulations using backstepping + FF controller for tracking trajectories 2, 3 and 4. For the ramp trajectory, the tracking error has a relative large overshoot at the abrupt change of velocity point.  For 1 Hz and 2 Hz sine waves, the backstepping + FF controller has a similar overshoot at the beginning.

After the initial transient the error magnitudes are less than 0.01 radian for both trajectories.

Figure 4.17 to Figure 4.20 shows the experiment results of using backstepping + FF controller for trajectory 1, 2, 3 and 4, respectively. It can be observed that the maximum overshoot occurs at the beginning, which is similar to the simulations. Unlike the simulations, these results for trajectories 1 and 2 show a low amplitude oscillation of the error. The error has also increased. For the 1 Hz sine wave, after the initial transient, the maximum magnitude of the error is 0.016 radian (i.e. 60% increase). For the 2 Hz sine wave the maximum error magnitude increased by 200% to 0.03 radian.
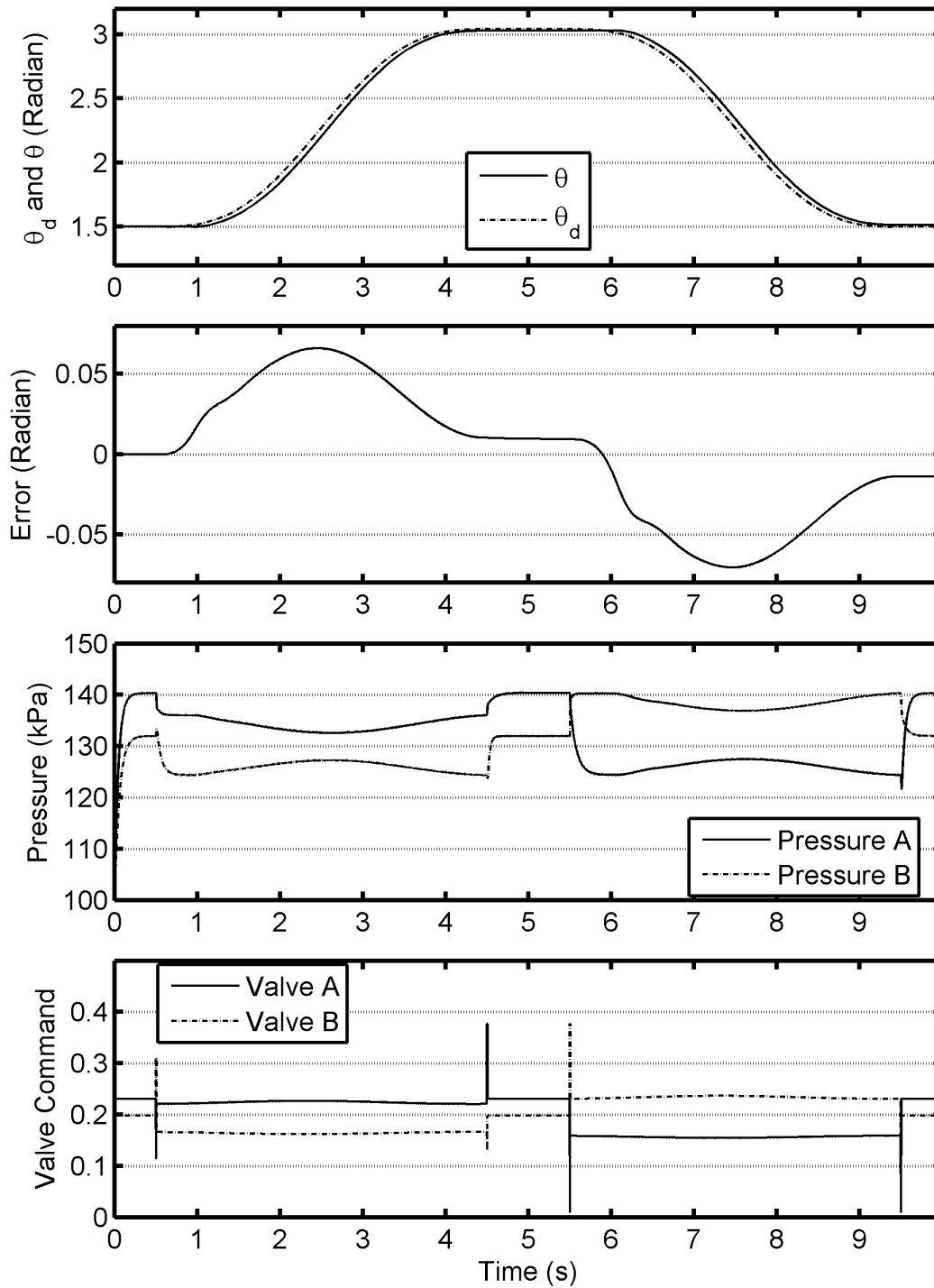
Figure 4.11 FF control only, trajectory 1, simulation, pneumatic mode
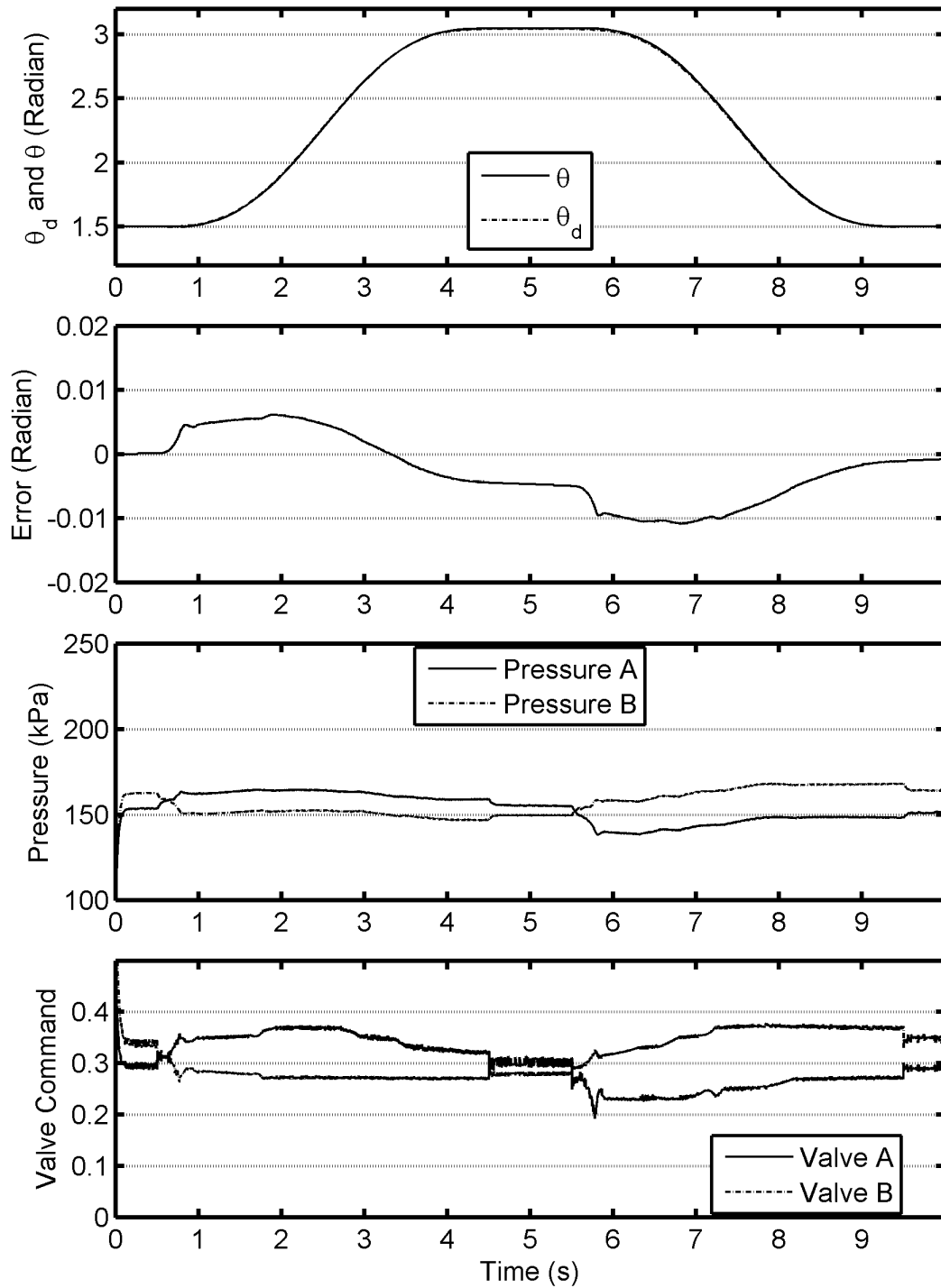
Figure 4.12 Backstepping control only, trajectory 1, simulation, pneumatic mode
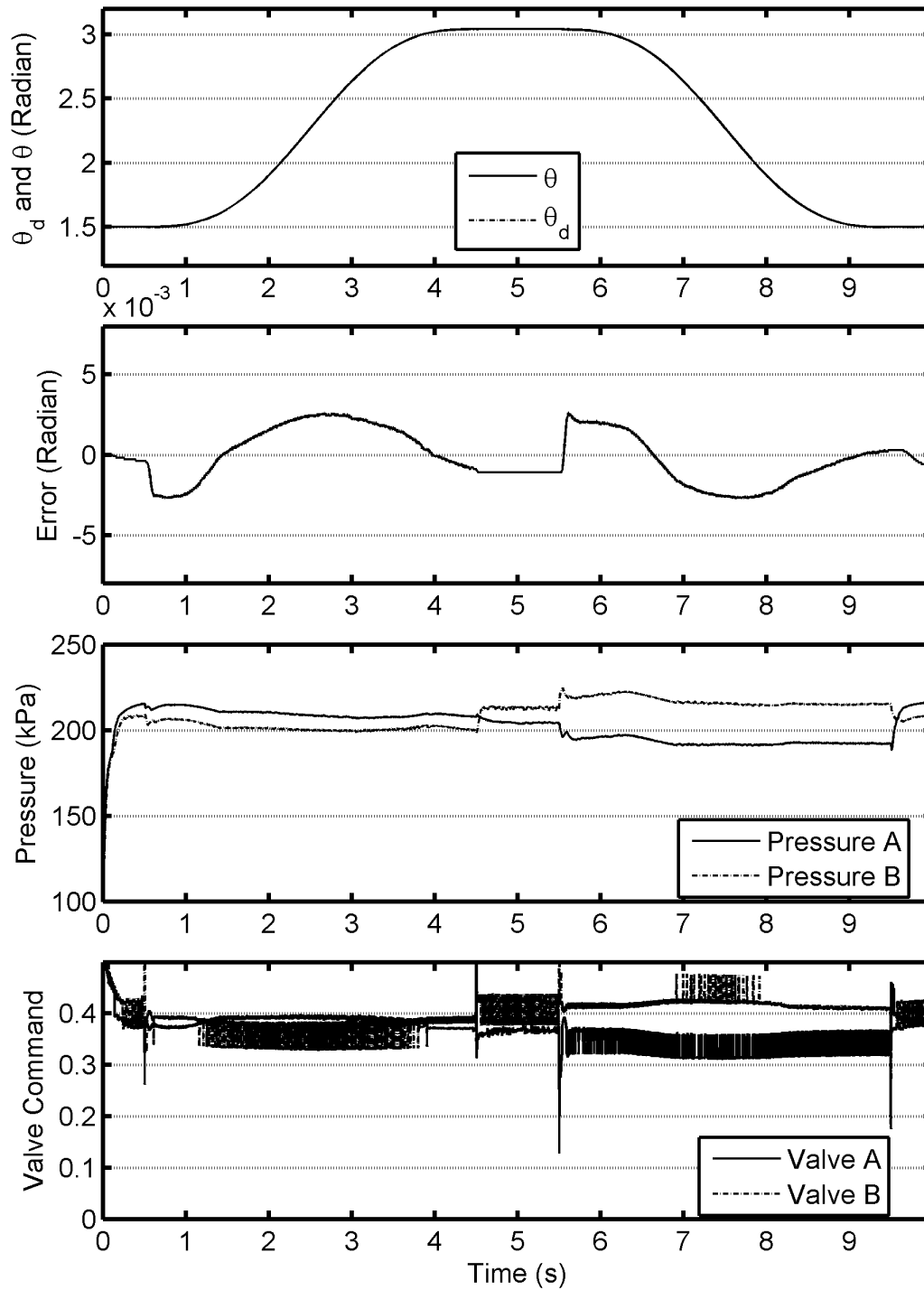
Figure 4.13 Backstepping + FF control, trajectory 1, simulation, pneumatic mode
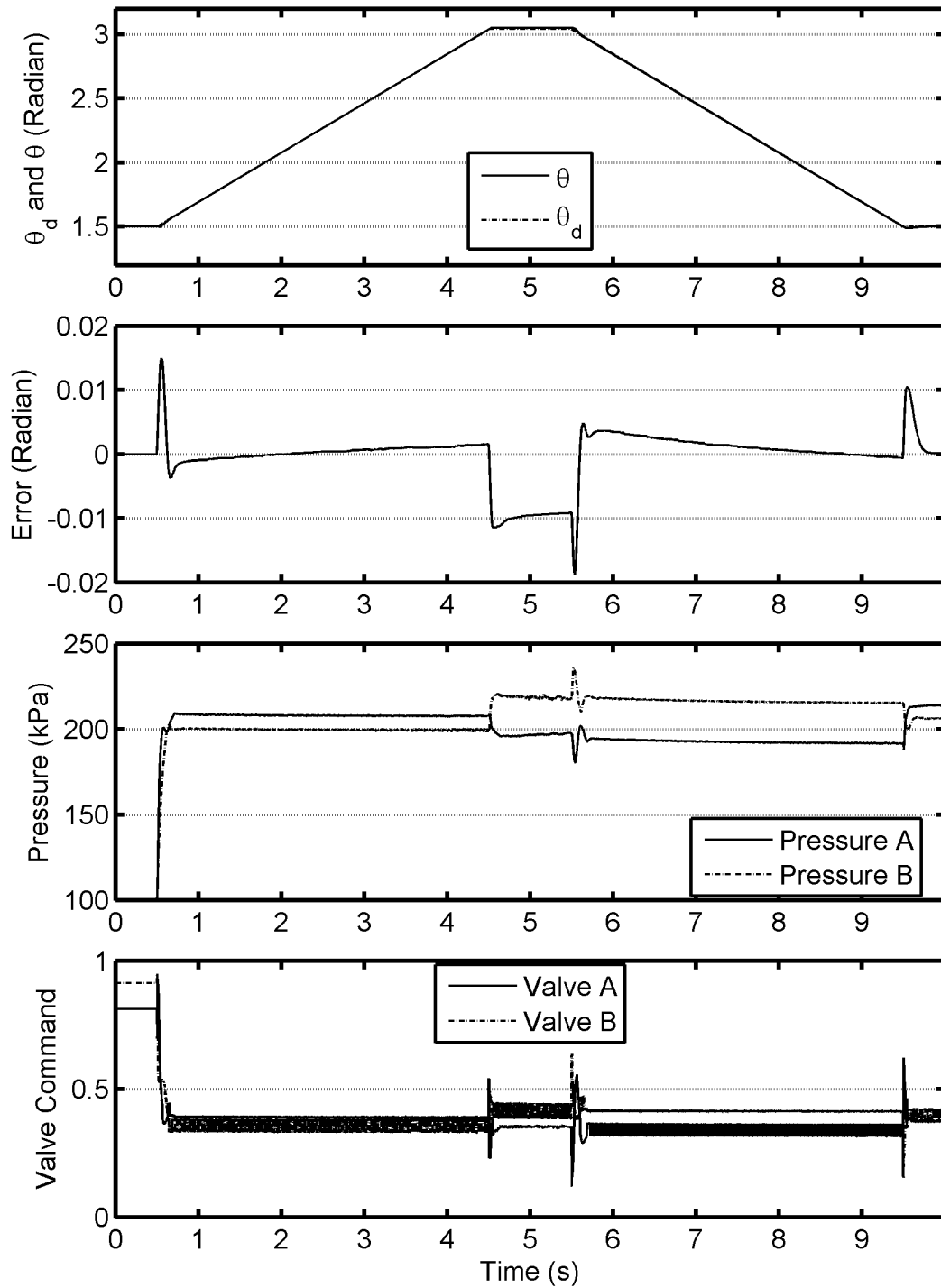
Figure 4.14 Trajectory 2, simulation, pneumatic mode, backstepping + FF control.
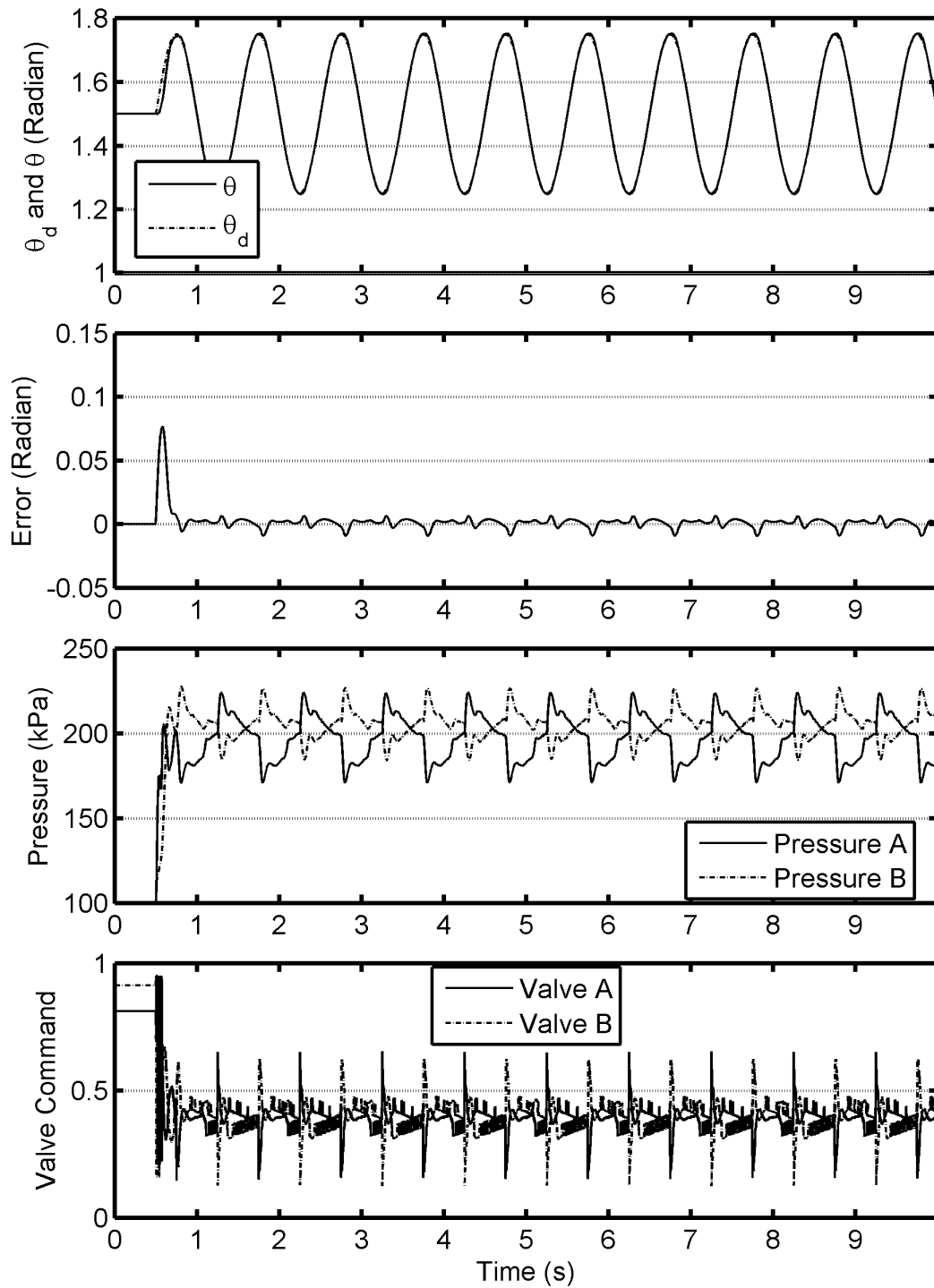
Figure 4.15 Trajectory 3, simulation, pneumatic mode, backstepping + FF control.
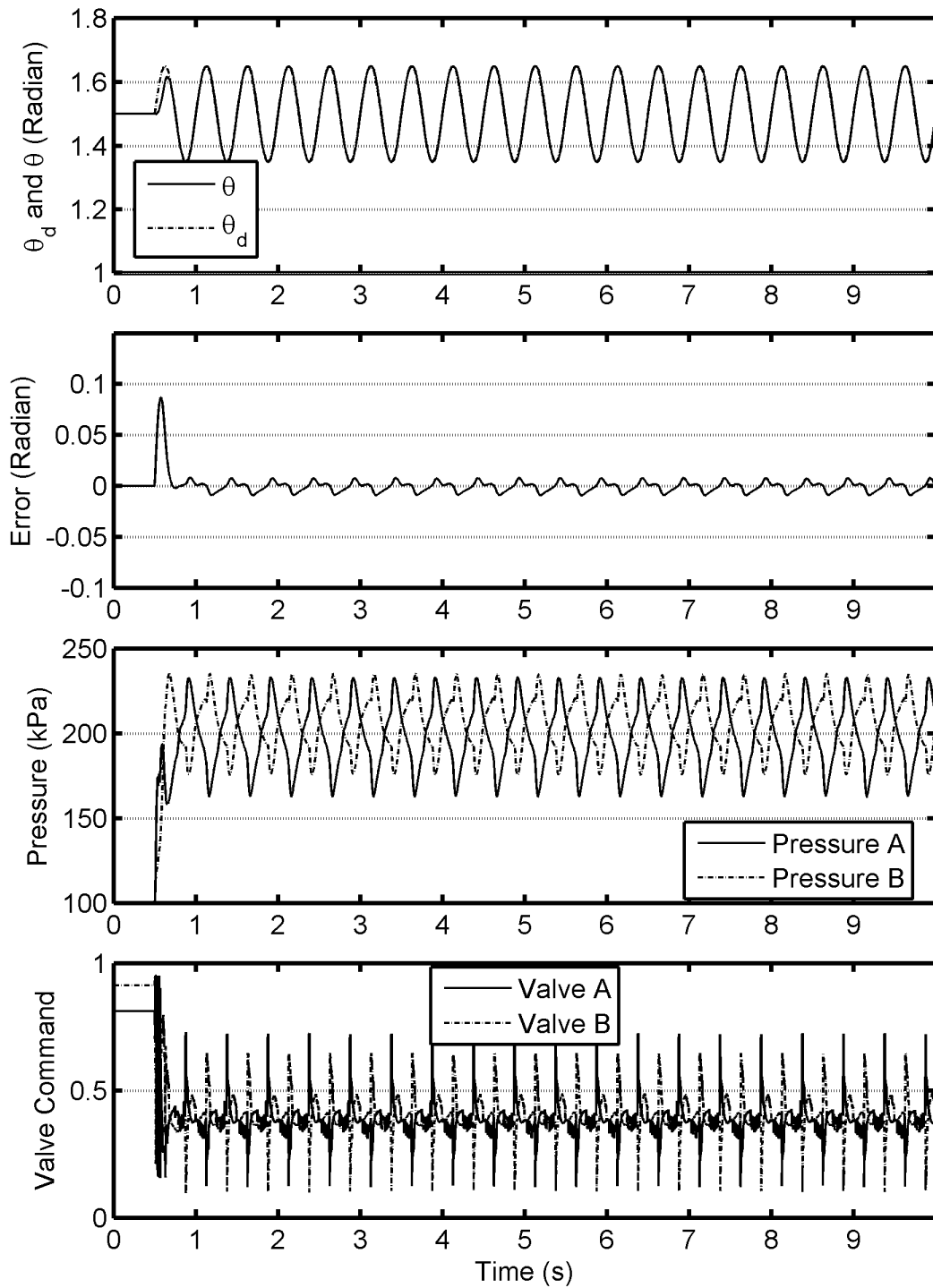
Figure 4.16 Trajectory 4, simulation, pneumatic mode, backstepping + FF control.
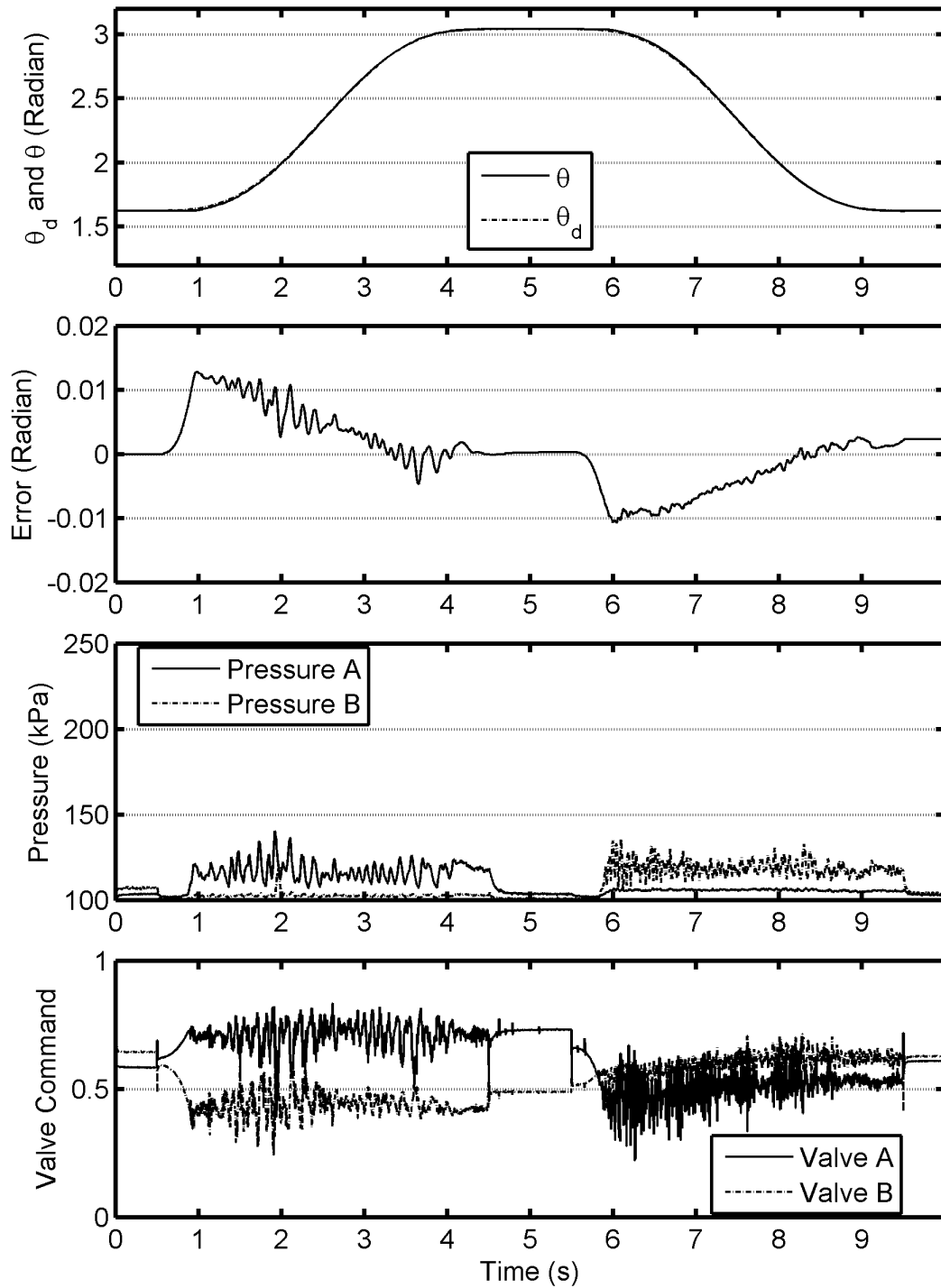
Figure 4.17 Trajectory 1 experiment, pneumatic mode, backstepping + FF control.
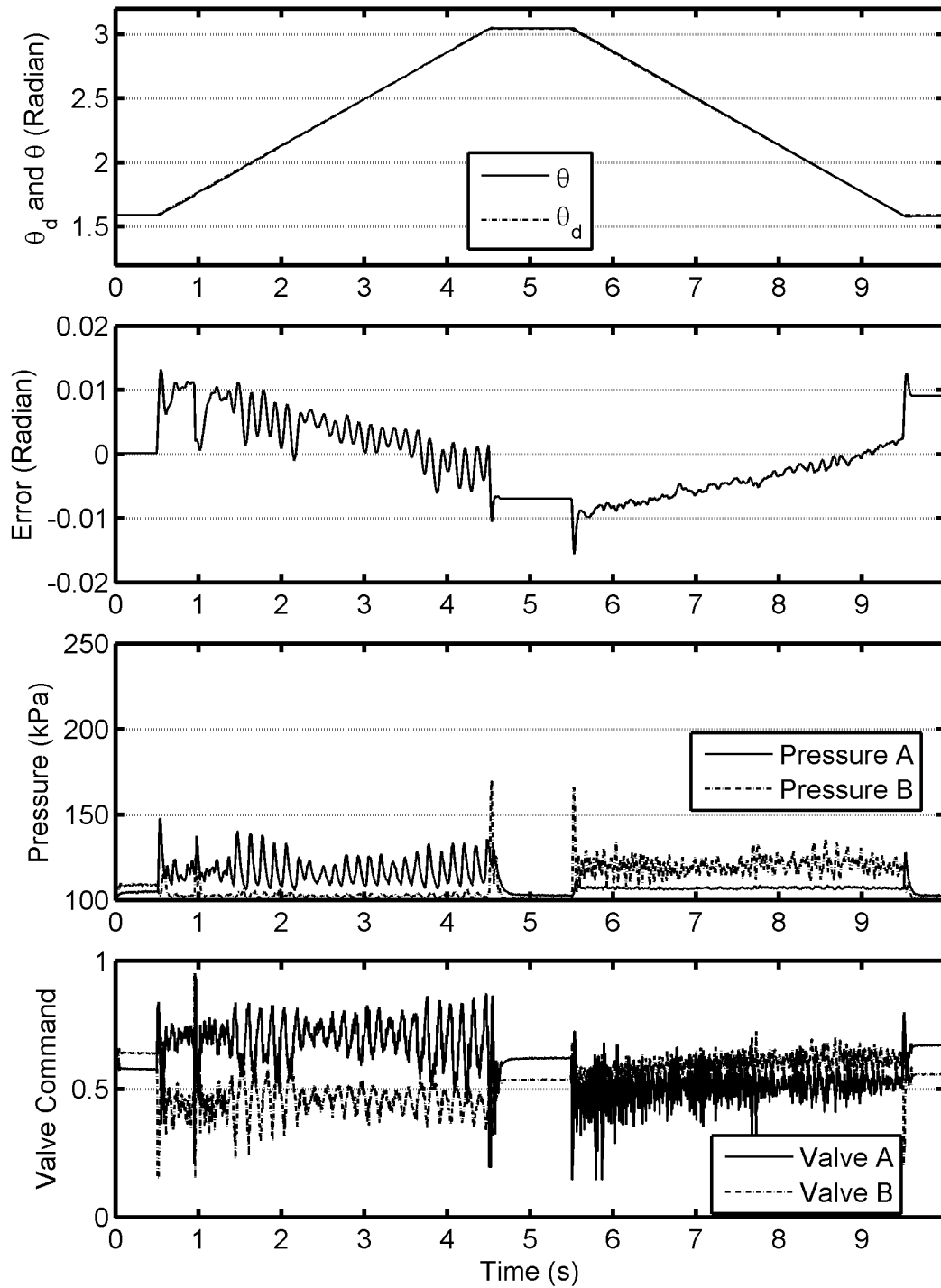
Figure 4.18  Trajectory 2 experiment, pneumatic mode, backstepping + FF control.
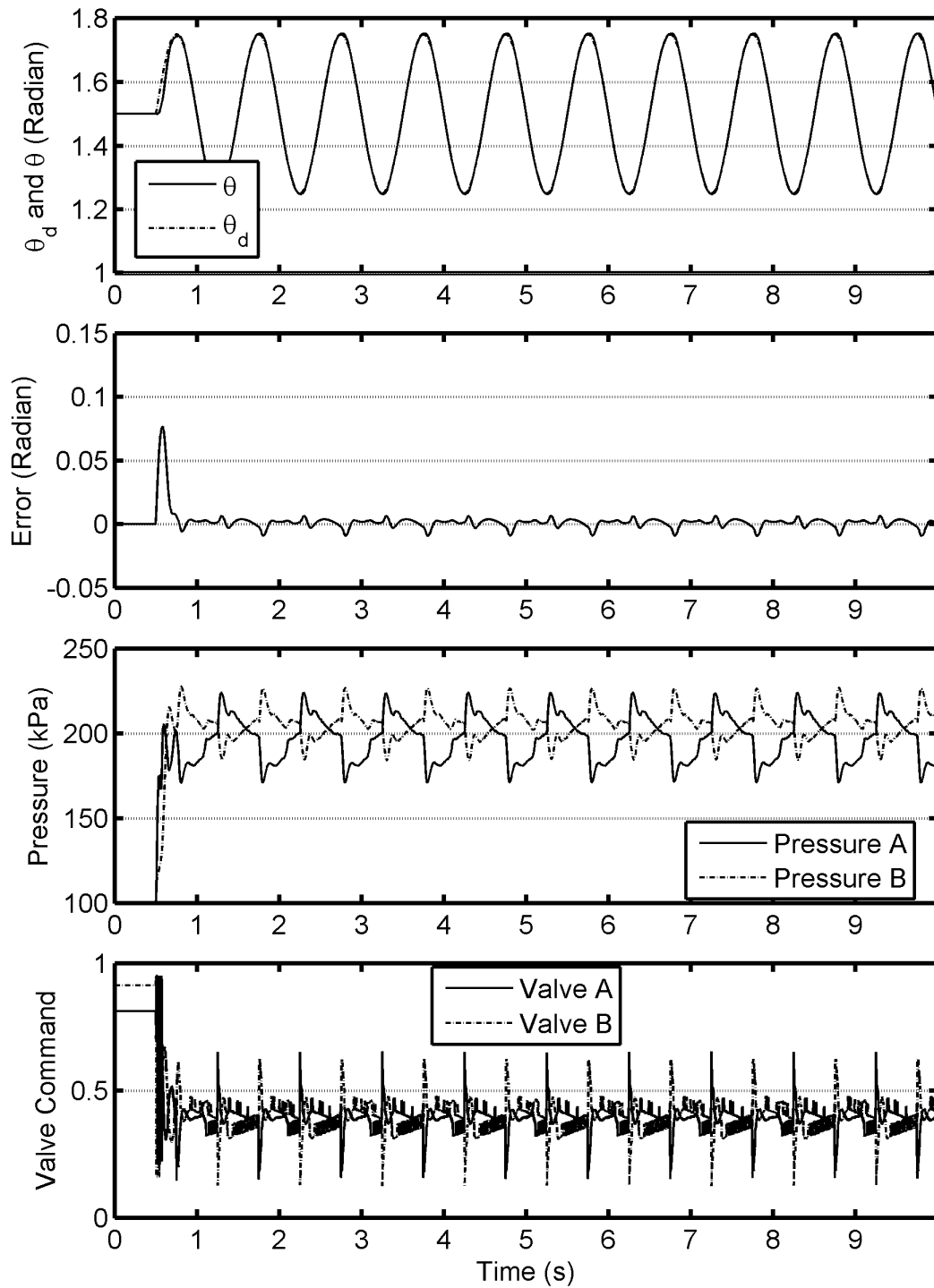
Figure 4.19 Trajectory 3 experiment, pneumatic mode, backstepping + FF control.
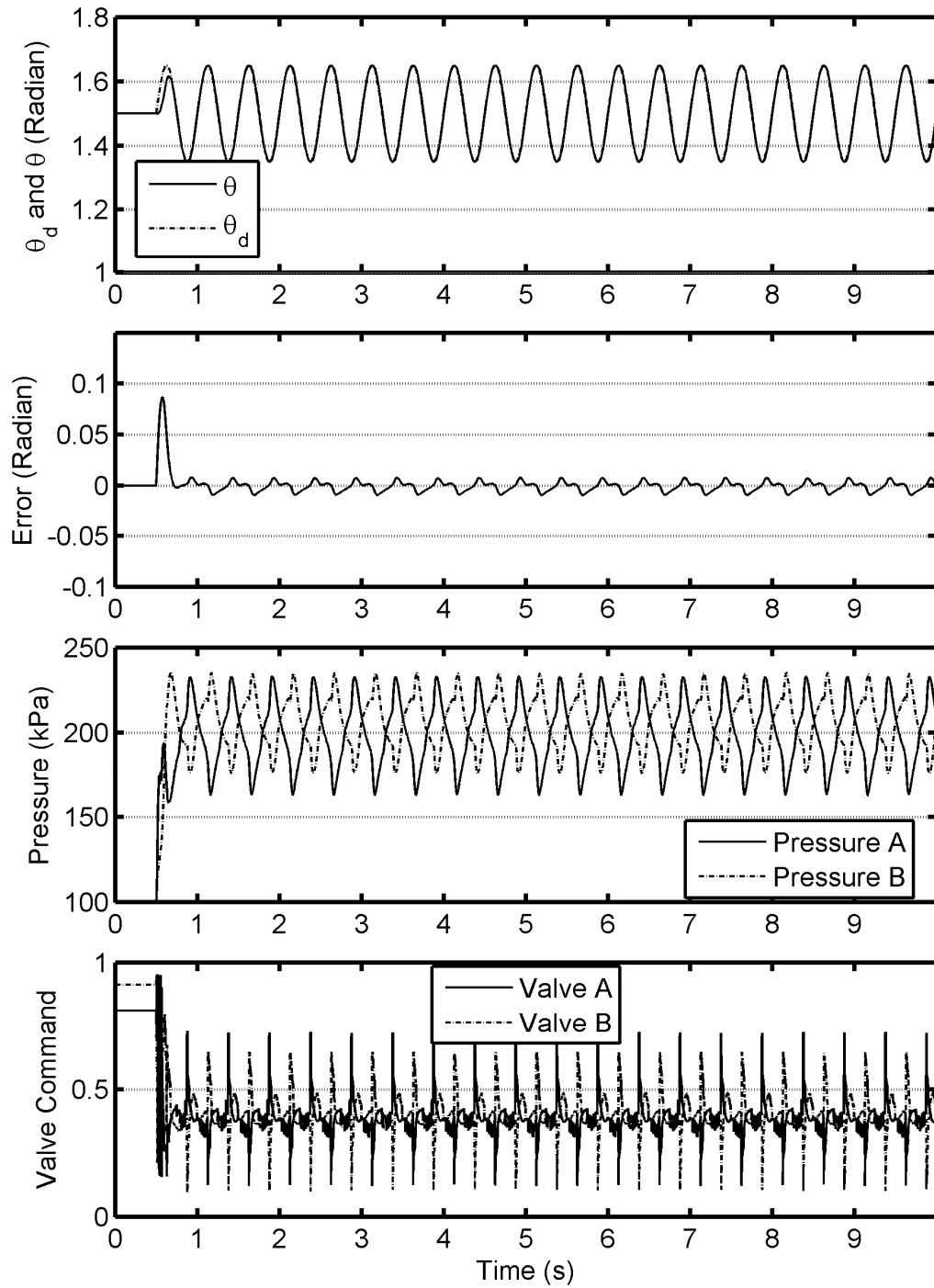
Figure 4.20 Trajectory 4 experiment, pneumatic mode, backstepping + FF control.

## 4.4 Discrete-valued Model Predictive Control plus Inverse Dynamics Control

### 4.4.1 Introduction

Model predictive control is a model-based nonlinear control design method. Specifically, it "is a form of control in which the current control action is obtained by solving, at each sampling instant, a finite horizon open-loop optimal control problem, using the current state of the plant as the initial state; the optimization yields an optimal control sequence and the first control in this sequence is applied to the plant. An important advantage of this type of control is its ability to cope with hard constraints on controls and states." (Mayne et al. 2000). With our hybrid actuator, the two solenoid on/off valves have a limited number of combinations within a finite prediction horizon. Since a system model has been developed, it is possible to maximize the predicted performance by exhaustively searching all possible input combinations of the valves. The DVMPC for hybrid actuator was designed and tested with the previous version of the hybrid actuator prototype by Chen (2012), Bone and Chen (2012). In this section DVMPC will be extended and implemented on the improved version of hybrid actuator prototype. Then, a novel payload estimation algorithm is proposed to improve robustness of DVMPC + IDC. The performance of these controllers will be compared to the backstepping + FF controller is section 4.5.

**4.4.2    Model Predictive Control Algorithm for the Pneumatic Actuator**

The piston of the pneumatic cylinder is driven by compressed air, which is controlled by a solenoid on/off valve for each chamber independently. Each valve has only two discrete states, namely either on or off. It is not difficult to predict the system performance indices (i.e. a cost function defined by the designer) for all possible valve input combination within a limited time horizon. By comparing the performance indices, controller chooses which set of the input is more suitable.

Two on/off solenoid valves have 4 possible combinations at each sampling time. One of these will be used as the DVMPC output $u_p$ as described in Table 4.4.1.

Table 4.4.1 Discrete-valued MPC control signals

| Valve A | Valve B | Control Output $u_p$ |
|---------|---------|----------------------|
| OFF | OFF | 0 |
| ON | OFF | 1 |
| OFF | ON | 2 |
| ON | ON | 3 |

In the DVMPC, the cost function to be minimized is defined as:

$$
\begin{aligned}
J &= \sum_{j=1}^{N_p} \Big[ \theta_d(t_i + jT_s) - \hat{\theta}(t_i + jT_s, \hat{u}_p(t_i + jT_s)) \Big]^2 \\
&= \sum_{j=1}^{N_p} \hat{e}(t_i + jT_s, \hat{u}_p(t_i + jT_s))^2
\end{aligned}
\tag{4.4.1}
$$

where $t_i$ is the current sampling time instant, $T_s$ is the sampling time period, $\theta_d$ is desired position trajectory, $\hat{\theta}$ is the predicted actuator position with the predicted input $\hat{u}_p$, $\hat{e}$ is

the predicted tracking error, $N_P$ is the prediction horizon. The cost function is calculated

for each of valve input combination and then an exhaustive search will be used to find the

optimal input $u_p$ .

$$u_p(t_i) = \arg\min \sum_{j=1}^{N_p} \hat{e}(t_i + jT_s, \hat{u}_p(t_i + jT_s))^2 \qquad (4.4.2)$$

Subject to:
$$u_p \in \{0,1,2,3\}$$
$$\hat{\theta}(t_i + jT_s) = f\left(\theta, P_a, P_b, u_p, \hat{u}_p\right) \quad \text{for } j = \{1, 2, ..., N_p\}$$

For one sampling period, there are only 4 possible inputs to system. However, for

a period of two the possible input combination increases to 16, for a period of three it

increases to 64. In order to reduce computation load, a constant valve input during a

prediction horizon will be adopted. This means for a prediction horizon, the predicted

input $\hat{u}_p$ will remain unchanged. In such case, the number of optimal solution candidates

will be limited to 4. Consequently, this optimization problem can be easily solved online

in real-time.

The arm position of the hybrid actuator over prediction horizon for a valve input is

calculated as follows:

    1) Set $j = 0$;

    2) Calculate $t_k = t_i + jT_s$;

    3) If $t_k = t_i$ then use the measured pressures and position data from the sensors:

$$\hat{P}_a(t_k) = P_a(t_i)$$

$$\hat{P}_b(t_k) = P_b(t_i)$$

$$\hat{\theta}(t_k) = \theta(t_i)$$

$$\hat{\dot{\theta}}(t_k) = \left(\theta(t_i) - \theta(t_i - T_s)\right)/T_s$$

where $\hat{P}_a$ and $\hat{P}_b$ are predicted pressures, $\hat{\theta}$ is predicted position, $\hat{\dot{\theta}}$ is the predicted velocity.

4) If $t_k > t_i$ then:

$$\hat{P}_a(t_k) = \hat{P}_a(t_k - T_s) + T_s \hat{\dot{P}}_a(t_k - T)$$

$$\hat{P}_b(t_k) = \hat{P}_b(t_k - T_s) + T_s \hat{\dot{P}}_b(t_k - T)$$

$$\hat{\theta}(t_k) = \hat{\theta}(t_k - T_s) + T_s \hat{\dot{\theta}}(t_k - T_s)$$

$$\hat{\dot{\theta}}(t_k) = \hat{\dot{\theta}}(t_k - T_s) + T_s \hat{\ddot{\theta}}(t_k - T_s)$$

5) Calculate predicted mass flow rates using:

$$\hat{\dot{m}}_a(t_k) = \lambda_a \left( \hat{P}_a(t_k), \hat{u}_a(t_k) \right)$$

$$\hat{\dot{m}}_b(t_k) = \lambda_b \left( \hat{P}_b(t_k), \hat{u}_b(t_k) \right)$$

$$\lambda_{valve}(P,0) = \begin{cases} -\dot{m}_{choked} & \text{if } P > \dfrac{P_0}{0.53} \\ C_{valve\_dis}(P_0 - P) & \text{otherwise} \end{cases} \qquad (4.4.3)$$

$$\lambda_{valve}(P,1) = \begin{cases} \dot{m}_{choked} & \text{if } P_s > \dfrac{P_0}{0.53} \\ C_{valve\_fill}\sqrt{P_s - P} & \text{otherwise} \end{cases}$$

6) Calculate the derivatives of the predicted pressures

$$\hat{\dot{P}}_a(t_k) = f_a \left( \hat{\theta}(t_k), \hat{\dot{\theta}}(t_k), \hat{\dot{m}}_a(t_k) \right) \qquad (4.4.4)$$

115

$$\hat{\dot{P}}_b(t_k) = f_b\left(\hat{\theta}(t_k), \hat{\dot{\theta}}(t_k), \hat{\dot{m}}_b(t_k)\right) \tag{4.4.5}$$

where $f_a(\cdot)$ and $f_b(\cdot)$ are the system model (3.3.6) derived in Chapter 3.

7) Obtain the predicted pneumatic cylinder torque, $\hat{\tau}_c(t_k)$ using

$$\hat{\tau}_c(t_k) = \left[\hat{P}_a(t_k)A_a - \hat{P}_a(t_k)A_b - P_0(A_a - A_b)\right]r_{pitch} \tag{4.4.6}$$

8) If in vertical configuration, compute the predicted gravity torque, $\hat{\tau}_g(t_k)$, using $\hat{\theta}(t_k)$.

$$\hat{\tau}_g(t_k) = \hat{\tau}_{arm}(t_k) + \hat{\tau}_{payload}(t_k) \tag{4.4.7}$$

where

$$\hat{\tau}_{arm}(t_k) = \frac{1}{2}M_{arm}L_{arm}g\sin\left(\hat{\theta}(t_k)\right)$$

$$\hat{\tau}_{payload}(t_k) = M_{payload}L_{payload}g\sin\left(\hat{\theta}(t_k)\right)$$

else

$$\hat{\tau}_g(t_k) = 0 \tag{4.4.8}$$

9) Compute the predicted friction torque, $\hat{\tau}_f(t_k)$, using $\dot{\theta}_d$ in place of $\dot{\theta}$.

10) Compute the predicted acceleration, $\hat{\ddot{\theta}}(t_k)$, using the system dynamics model with $\hat{\tau}_m(t_k) = 0$, and the other predicted torques.

11) Set $j = j+1$.

12) If $j \le N_p$ then go to step 2.

13) Stop.

### 4.4.3   Zero-Order Hold for the Pneumatic Actuator

The actual solenoid valves need time to energize or de-energize the coil when they are commanded to switch on/off. If the valve is commanded to switch on at $nT_s$ and $(n+2)T_s$ and it is commanded to switch off at $(n+1)T_s$ where the sampling time period $T_s$ in data acquisition is 1 ms, the solenoid valve will stay on for the three sampling time periods rather than switching off at the commanded time. Such responses are typically approximated by a unity gain with a valve switching on delay and switching off delay.

To avoid the problem caused by valve responses, a zero-order hold ($ZOH$) is used to maintain the valve switch command for a certain period of time. The holding time period should be longer than the delay on plus delay off time periods. The same method was applied to the previous version of hybrid actuator prototype designed and used by Chen (2012), and Bone and Chen (2012).

According to the FESTO manual, the switch on delay is 1.7 ms, and off delay is 2 ms for the new on/off valves. The delay reduction due to the drive circuit will be ignored to be conservative. To ensure each valve switches on/off in agreement with its command, the zero-order hold time was chosen to be 5 ms.

### 4.4.4   Inverse Dynamics Control of the Electric Motor

The majority of the torque of the pneumatic-electric actuator should be provided by the pneumatic cylinder. For this reason, in DVMPC the position of actuator is predicted by assuming the motor torque is zero (see step 10 of the DVMPC algorithm).

The electric motor has an advantage of establishing a torque very rapidly compared to the pneumatic cylinder. In the hybrid actuator, the motor is intended to respond to the high frequency errors in torque/position. It is also capable of reducing the steady state error.

The IDC technique has been successfully used with high performance robot arms (Spong and Vidyasagar 1989). It was also applied to the previous version of hybrid actuator prototype (Bone and Chen 2012), and was compared to the PD control for the previous hybrid actuator (Chen 2012). To apply the IDC to our hybrid actuator, we first write the system dynamics in the form:

$$\ddot{\theta} = \frac{\tau_{motor} + \tau_{cylinder} + \tau_{gravity} - \tau_{friction}}{I_{eq}} \tag{4.4.9}$$

Then applying the IDC law from section 8.3 of Spong and Vidyasagar (1989) gives:

$$\tau_{motor}(t_i) = \tau_{rem}(t_i) + K_{IDC,p}\tilde{e}(t_i) + K_{IDC,d}\dot{\tilde{e}}(t_i) \tag{4.4.10}$$

with

$$\tau_{rem}(t_i) = \hat{I}_{eq}(t_i)\ddot{\theta}_d(t_i) - \hat{\tau}_c(t_i) - \hat{\tau}_g(t_i) + \hat{\tau}_f(t_i)$$
$$\tilde{e}(t_i) = \theta_d(t_i) - \theta(t_i)$$
$$\dot{\tilde{e}}(t_i) = \dot{\theta}_d(t_i) - \dot{\hat{\theta}}(t_i)$$

where $\tilde{e}$ and $\dot{\tilde{e}}$ are the measured position and velocity tracking errors, respectively; $\hat{I}_{eq}$ is the estimated equivalent inertia as defined by the user, or by the payload estimator (later introduced in section 4.4.6) when it is used; $\tau_c$ is given by (4.4.6); $\tau_g$ is given by (4.4.7) if the configuration is vertical or (4.4.8) if it is horizontal; $\tau_f$ is obtained as described in step 9) of the DVMPC algorithm; and $\tau_{rem}$ is the remainder of the desired torque.

### 4.4.5   Stability Analysis of the DVMPC + IDC

The previous two sections have finished the design of controllers for the pneumatic actuator and electric motor respectively. In this section, the stability analysis of the combined DVMPC + IDC will be performed.

Assuming the motor will not be saturated during the control, substituting (4.4.10) into (4.4.9) gives

$$\tilde{\ddot{e}}(t_i) + \frac{K_{IDC,d}}{I_{eq}} \tilde{\dot{e}}(t_i) + \frac{K_{IDC,p}}{I_{eq}} \tilde{e}(t_i) = -\Delta I_{eq} \ddot{y}_d(t_i)$$
$$-\Delta \tau_{cylinder} - \Delta \tau_{gravity} - \Delta \tau_{friction}$$

(4.4.11)

where $\tilde{\dot{e}}(t_i)$ is the measured angular acceleration error; and $\Delta \tau_{cylinder}, \Delta \tau_{gravity}, \Delta \tau_{friction}, \Delta I_{eq}$ are the estimation errors. They are calculated by:

$$\Delta \tau_{cylinder} = \tau_{cylinder}(t_i) - \hat{\tau}_{cylinder}(t_i)$$
$$\Delta \tau_{gravity} = \tau_{gravity}(t_i) - \hat{\tau}_{gravity}(t_i)$$
$$\Delta \tau_{friction} = \hat{\tau}_{friction}(t_i) - \tau_{friction}(t_i)$$
$$\Delta I_{eq} = \hat{I}_{eq}(t_i) - I_{eq}(t_i)$$
$$\tilde{\ddot{e}}(t_i) = \ddot{\theta}_d(t_i) - \ddot{\theta}(t_i)$$

Additionally, the measured position velocity and acceleration tracking errors can be written as:

$$\tilde{e}(t_i) = e(t_i) + \Delta_{e(t_i)}$$
$$\tilde{\dot{e}}(t_i) = \dot{e}(t_i) + \Delta_{\dot{e}(t_i)}$$
$$\tilde{\ddot{e}}(t_i) = \ddot{e}(t_i) + \Delta_{\ddot{e}(t_i)}$$

(4.4.12)

where $\Delta_{\dot{e}}$ and $\Delta_e$ are due to sensor noise; and $e(t_i)$ and $\dot{e}(t_i)$ are the actual tracking errors.

Substituting (4.4.13) into (4.4.11) gives

$$\ddot{e}(t_i) + \frac{K_{IDC,d}}{I_{eq}}\dot{e}(t_i) + \frac{K_{IDC,p}}{I_{eq}}e(t_i) = \Delta \tag{4.4.13}$$

where $\Delta$ is the sum of the system uncertainty, sensor noise, and the estimation error. In equation form:

$$\Delta = -\Delta I_{eq}\ddot{y}_d(t_i) - \Delta\tau_{cylinder} - \Delta\tau_{gravity}$$
$$-\Delta\tau_{friction} - \Delta_{\ddot{e}(t_i)} - \frac{K_{IDC,p}}{I_{eq}}\Delta_{e(t_i)} - \frac{K_{IDC,d}}{I_{eq}}\Delta_{\dot{e}(t_i)} \tag{4.4.14}$$

Note that the sum $\Delta$ is bounded because all of the individual terms in (4.4.14) are bounded. The second order linear system in $e$ is guaranteed to converge to a bounded value since all of its coefficients are positive. Thus, the hybrid actuator with the DVMPC + IDC is guaranteed to be bounded-input, bounded-output stable under the condition that the electric motor is never saturated.

Note that, such a second order linear system in $e$ in (4.4.15) can be written in standard form:

$$\ddot{e}(t_i) + 2\zeta\omega\dot{e}(t_i) + \omega^2 e(t_i) = \Delta \tag{4.4.16}$$

where $\omega$ is the undamped natural frequency, and $\zeta$ is the damping ratio. If the desired values of $\omega$ and $\zeta$ are given then the controller gains can be using:

$$K_{IDC,p} = I_{eq}\omega^2 \text{ and}$$
$$K_{IDC,d} = I_{eq}2\zeta\omega \tag{4.4.17}$$

### 4.4.6   Model-Based Payload Estimation Algorithm

The DVMPC controller uses the payload mass to predict gravity torque and equivalent inertia, which are part of the system dynamics. In practice, there may be a mismatch between the modeled payload and the actual payload. Such a payload mismatch will degrade the DVMPC tracking performance. It is particularly undesirable if the payload is underestimated since that the make the desired pneumatic cylinder torque too small. If so, the compensation term in IDC will potentially saturate the electric motor. Recalling the assumption made in the stability analysis, the saturation of the motor might cause instability of the position tracking.

To improve the robustness of the DVMPC to payload mismatch, the following payload inertia estimation algorithm is proposed for the vertical configuration:

1)  Set an initial estimation, $\hat{I}_{payload}(0)$

2)  Estimate the total inertia using:

$$\hat{I}_{eq}(t_i) = I_m + I_{slide} + I_{arm} + \hat{I}_{payload}(t_i) \qquad (4.4.18)$$

where $\hat{I}_{payload}(t_i)$ is the current estimate.

3)  Compute torque error using:

$$\tau_e(t_i) = \hat{I}_{eq}(t_i)\ddot{\theta}_d(t_i) + \tilde{\tau}_g(t_i) - \tau_m(t_i) - \tilde{\tau}_c(t_i) \qquad (4.4.19)$$

4)  If $\tau_e(t_i) > \tau_{e,threshold}$ then continue, else go to step 11.

121

5)  If $\left|\theta(t_i)\right| > \theta_{threshold}$ then continue, else go to step 11.

6)  Estimate gravity torque using:

$$\hat{\tau}_g(t_i) = \tilde{\tau}_c(t_i) + \tau_m(t_i) - \hat{I}_{eq}(t_i)\ddot{\theta}_d(t_i) \tag{4.4.20}$$

7)  Estimate payload torque using:

$$\hat{\tau}_{payload}(t_i) = \hat{\tau}_g(t_i) - \tilde{\tau}_{arm}(t_i) + \tau_{slide}(t_i) \tag{4.4.21}$$

8)  Estimate actual payload inertia using:

$$\hat{I}^*_{payload}(t_i) = \frac{\hat{\tau}_{payload}(t_i)r_{pitch}}{g\sin\theta(t_i)} \tag{4.4.22}$$

9)  Smooth the estimation using:

$$\hat{I}_{payload}(t_i + T_s) = c_{forget}\hat{I}_{payload}(t_i) + (1 - c_{forget})\hat{I}^*_{payload}(t_i) \tag{4.4.23}$$

10) Stop.

11) Keep estimation same as the prior value, i.e.:

$$\hat{I}_{payload}(t_i + T_s) = \hat{I}_{payload}(t_i) \tag{4.4.24}$$

In this algorithm, step 4 is used to turn off the estimator to prevent the drift that could happen when the torque error is small. Step 5 is necessary to prevent payload estimation in step 8 from becoming numerically unreliable since $\hat{\tau}_{payload}(t_i) \to 0$ and $\sin\theta(t_i) \to 0$ when $\theta(t_i) \to 0$. Finally, step 9 is used to smooth out variations in the estimates. The parameter $c_{forget}$ is analogous to the forgetting factor used in classical recursive least-squares estimation, and it should be set within the interval of (0.9, 1).

The smoothness of the payload estimation is necessary because as mentioned in last section: the electric motor controller gains are calculated and updated accordingly to the equivalent inertia $I_{eq}$ estimate. If the estimate is not smooth, the motor may saturate, and the tracking error might not convergent to a bounded value.

### 4.4.7   Payload Estimation Experiment

To verify the effectiveness of payload estimation, experiments were performed. The estimation algorithm was first implemented on the previous version of hybrid actuator prototype used by Bone and Chen (2012).

The experiment setup is slightly different compared to the backstepping experiments. The MAC valve was in place of FESTO valve, smaller resolution of encoder, and the ODC5 was used to drive the valve. The hybrid arm was operating vertically with different payload masses. Trajectories are similar to current version, however, it moves back at vertical position first, then started the move. The payload estimation algorithm was turned on and off manually before experiments. The parameters used were listed in Table 4.4.2.

Table 4.4.2  Payload estimation parameters

| Parameters | Value | Unit |
|:---:|:---:|:---:|
| $N_p$ | 100 | $s^{-1}$ |
| $c_{forget}$ | 0.999 | $s^{-1}$ |
| $\tau_{e,threshold}$ | 0.15 | Nm |
| $\theta_{threshold}$ | 0.318 | rad |

For the purpose of validating payload mass estimation algorithm, the mass of actual payload was unknown to the controller. The position tracking results without and with payload estimation are shown in Figure 4.21 and Figure 4.22 respectively.  The tracking error in the "without estimator" case is noticeably bigger than the "with estimator" case. The inertia estimate reached steady state within about 2 seconds.  The performance of the payload estimation algorithm will be studied further in Chapter 5 and Chapter 6.
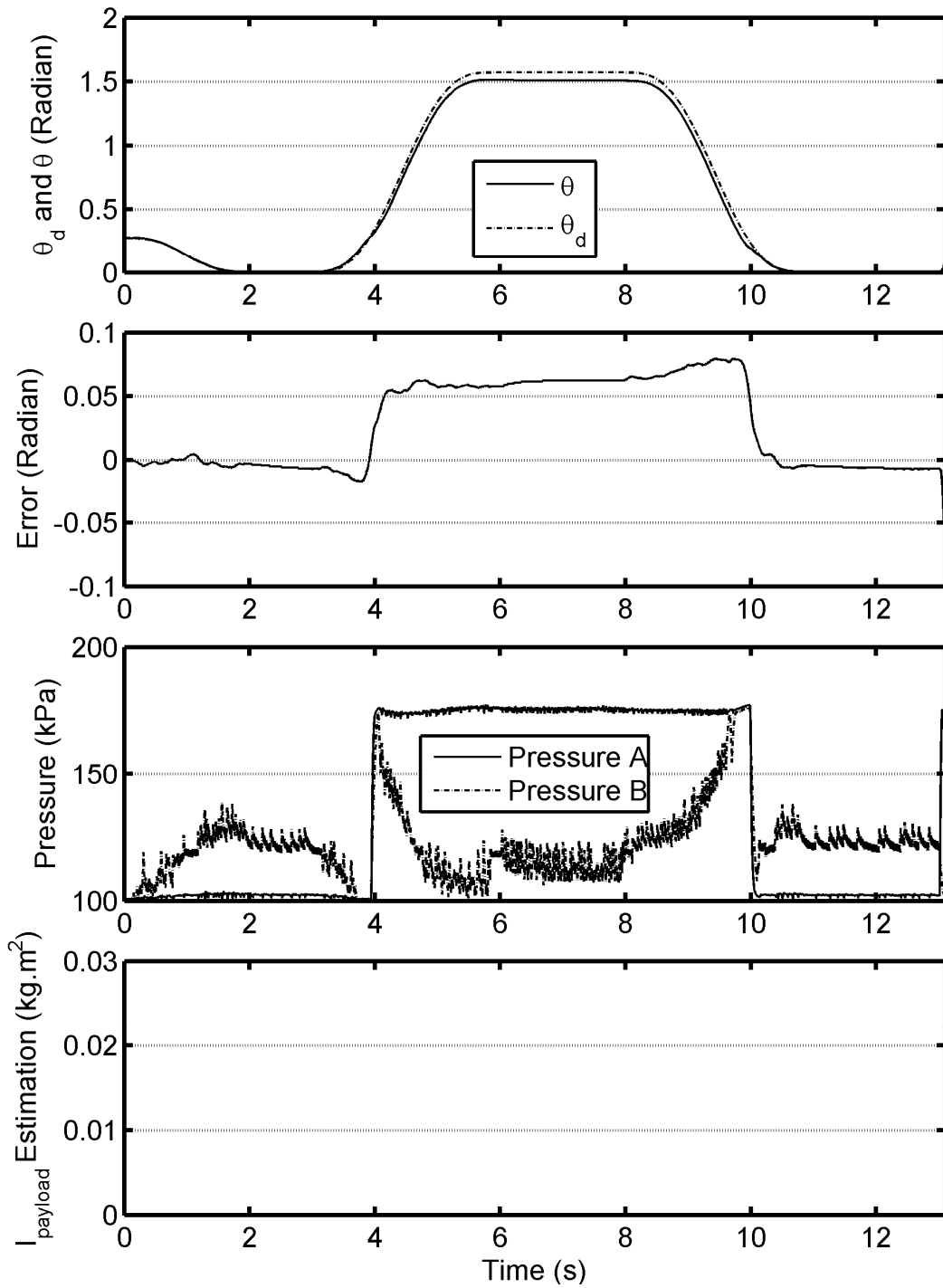
Figure 4.21 Position tracking experiment with previous prototype, payload mismatch

without payload estimation
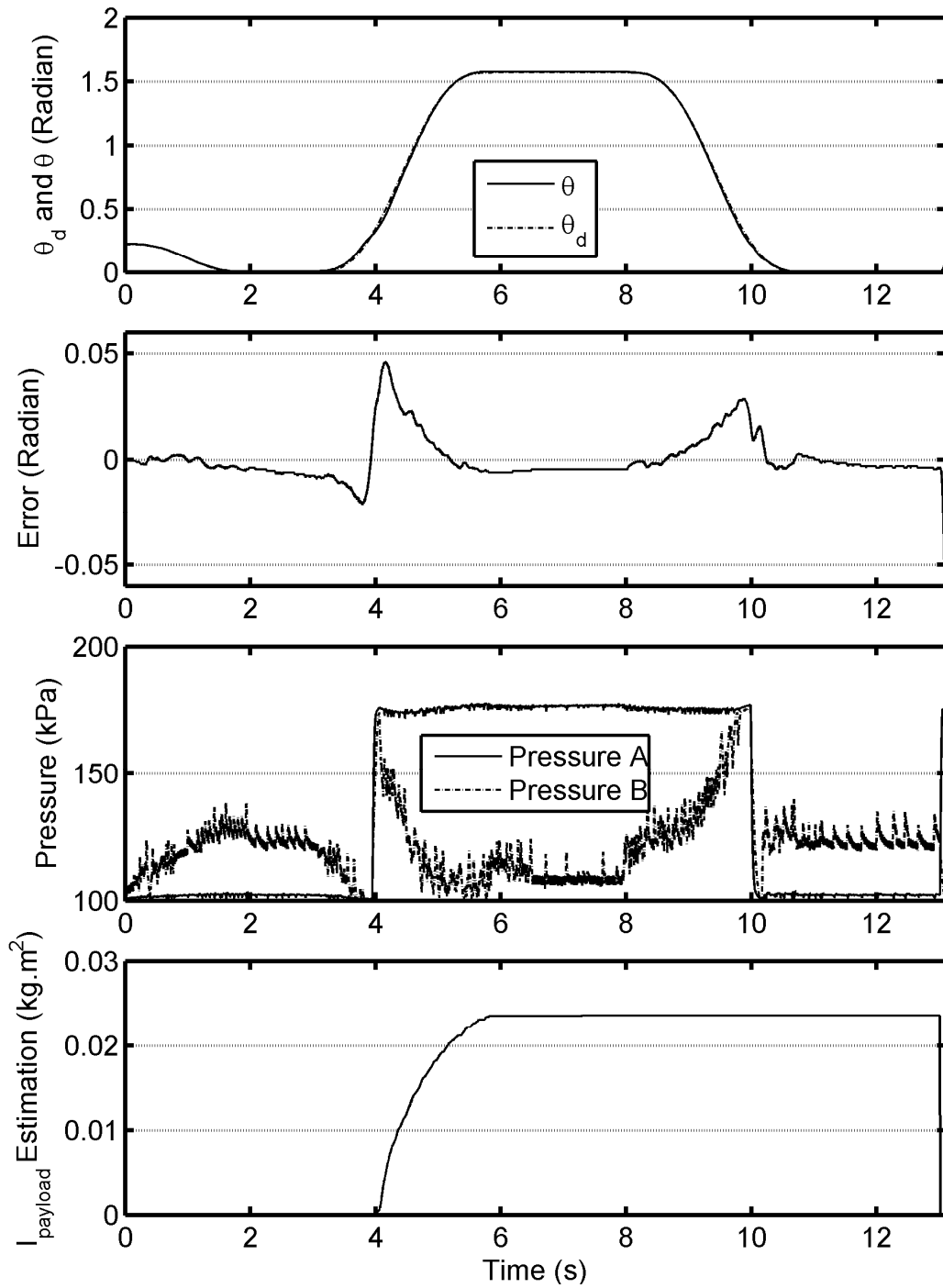
Figure 4.22 Position tracking experiment with previous prototype, payload mismatch with payload estimation

### 4.4.8   Preliminary Simulation and Experiment Results

The performance of the designed controllers will be studied in this section. The experiment and simulation results of current hardware and old hardware setup will both be given.

### 4.4.8.1   Previous Hardware Experimental Results

DVMPC + IDC + Payload Estimation was tested using the old hardware which was also being used to test DVMPC+IDC by Bone and Chen (2012).  The pneumatic mode and hybrid modes were chosen to examine the RMSE improvement after electric motor was included. The hybrid arm was operated vertically. The actual values of the payload mass were unknown to controller.  The mismatch of the equivalent inertia between controller and actual payload was 90%.  A cycloidal trajectory was used to be the position reference.

RMSE results of the experiments are listed in Table 4.4.3. In pneumatic mode, when the estimator was used the controller the RMSE was reduced RMSE by 80%, and the SSE was reduced by 90%. In hybrid mode, adding the estimator reduced the RMSE by more than 90%, and the SSE reduced by more than 95%. With the estimator on, the hybrid mode improved the performance by reducing RMSE by 50% and SSE by 80% compared to the pneumatic mode.

Table 4.4.3  Experiment RMSE value results for vertical cycloidal trajectory tracking

| Actuator | Estimator | Mismatch (%) | RMSE (radian) | SSE (radian) | Equivalent Inertia in Controller ($kg \cdot m^2$) |
|---|---|---|---|---|---|
| Pneumatic | OFF | 90 | 0.0524 | 0.0630 | 0.0275 |
| | ON | 90 | 0.0120 | 0.0049 | 0.0275 |
| Hybrid | OFF | 90 | 0.0319 | 0.0220 | 0.0275 |
| | ON | 90 | 0.0058 | 0.0007 | 0.0275 |

## 4.4.8.2   Current Hardware Simulation and Experimental Results

Proposed DVMPC + IDC controller was tested using current hardware. The hybrid actuator operated horizontally. When chamber pressure fluctuates aggressively, the actuator will oscillate.  Payload mass for experiment is zero. All trajectories listed in Table 4.2.1 will be used in simulation and experiments. The manually tuned parameters are listed in Table 4.4.4 and Table 4.4.5.

Table 4.4.4  DVMPC Simulation parameters

| Parameters | Value | Unit |
|---|---|---|
| $N_p$ | 30 | 1 |
| $ZOH$ | 5 | ms |
| $K_{IDC,p}$ | 59.2 | $Nm \cdot rad^{-1}$ |
| $K_{IDC,d}$ | 2.4 | $Nm \cdot rad^{-1} \cdot s$ |
| $T_s$ | 1 | ms |

Table 4.4.5 DVMPC Experiment parameters

| Parameters | Value | Unit |
|:---:|:---:|:---:|
| $N_p$ | 60 | 1 |
| *ZOH* | 5 | ms |
| $K_{IDC,p}$ | 9.5 | $\mathrm{Nm \cdot rad^{-1}}$ |
| $K_{IDC,d}$ | 0.67 | $\mathrm{Nm \cdot rad^{-1} \cdot s}$ |
| $T_s$ | 1 | ms |

Simulation results of four trajectories in pneumatic mode are first given in Figure 4.23, Figure 4.24, Figure 4.25, and Figure 4.26 respectively. The errors of trajectory 1 and 2 were reduced by over 50% compared to the backstepping + FF simulations. However, the chamber pressures were not distributed evenly as backstepping control, especially for trajectory 1. Such a distribution of chamber pressures will not provide the high stiffness that is desirable for disturbance rejection.

Experiment results for the same mode are given in Figure 4.27 to Figure 4.30. The magnitudes of the tracking errors were much larger than with the simulations. For example, with the sine wave trajectories the maximum error magnitudes increased by about 900%. The tracking errors were similar in magnitude to those produced by the backstepping + FF controller. It can also be observed that the errors for the sine wave trajectories were more random than the backstepping ones.
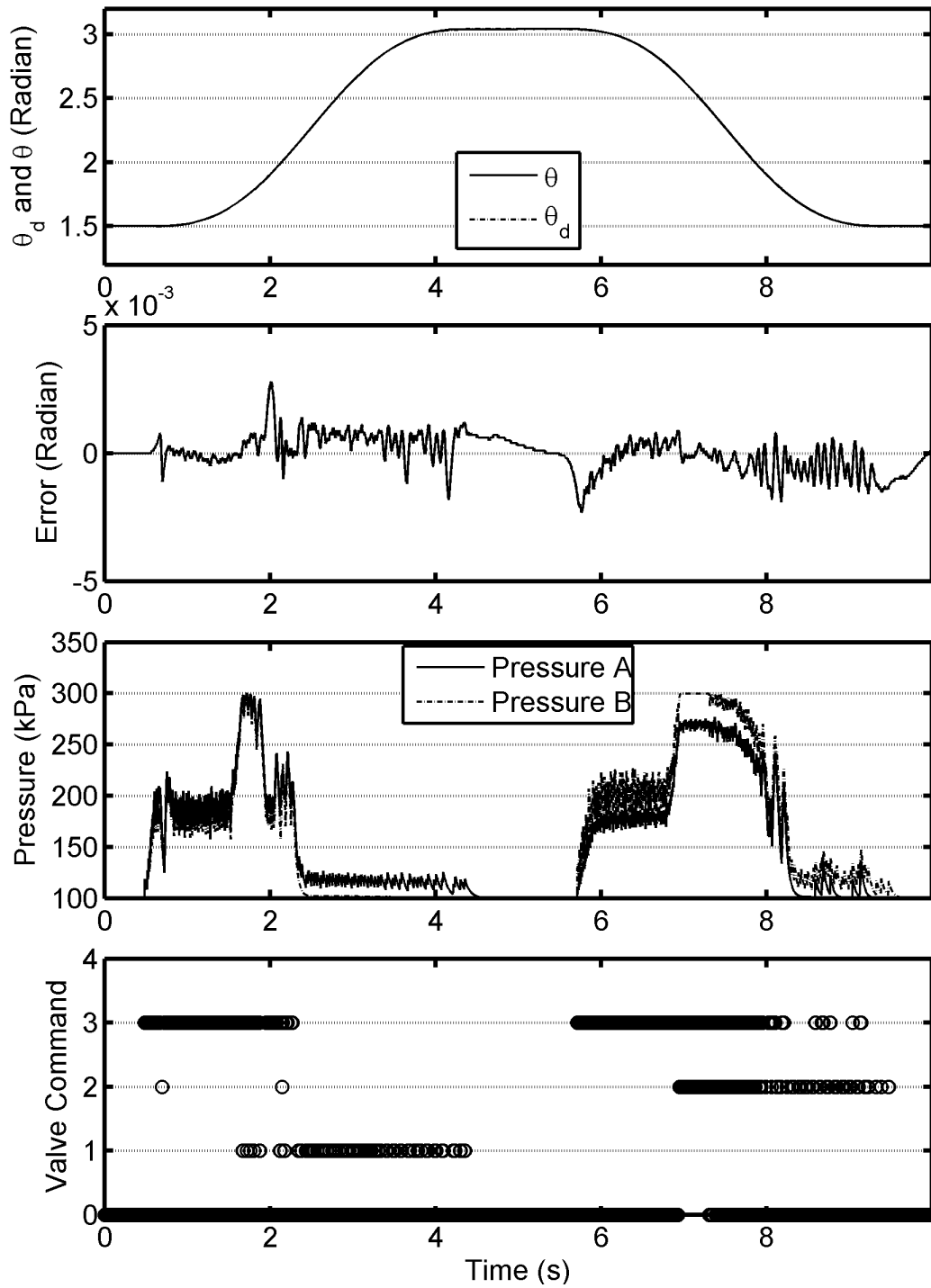
Figure 4.23 Trajectory 1, simulation, pneumatic mode, DVMPC
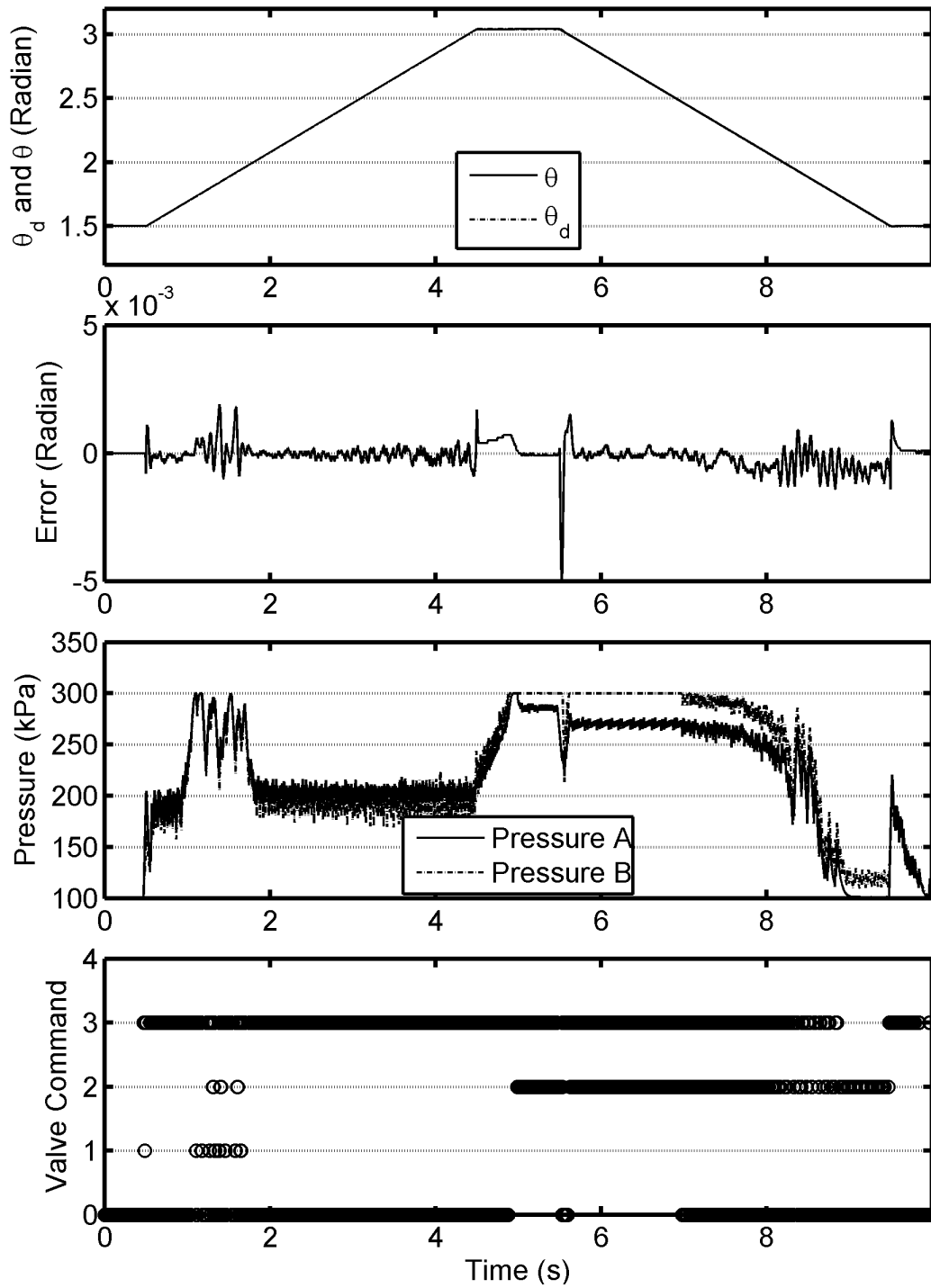
Figure 4.24 Trajectory 2, simulation, pneumatic mode, DVMPC
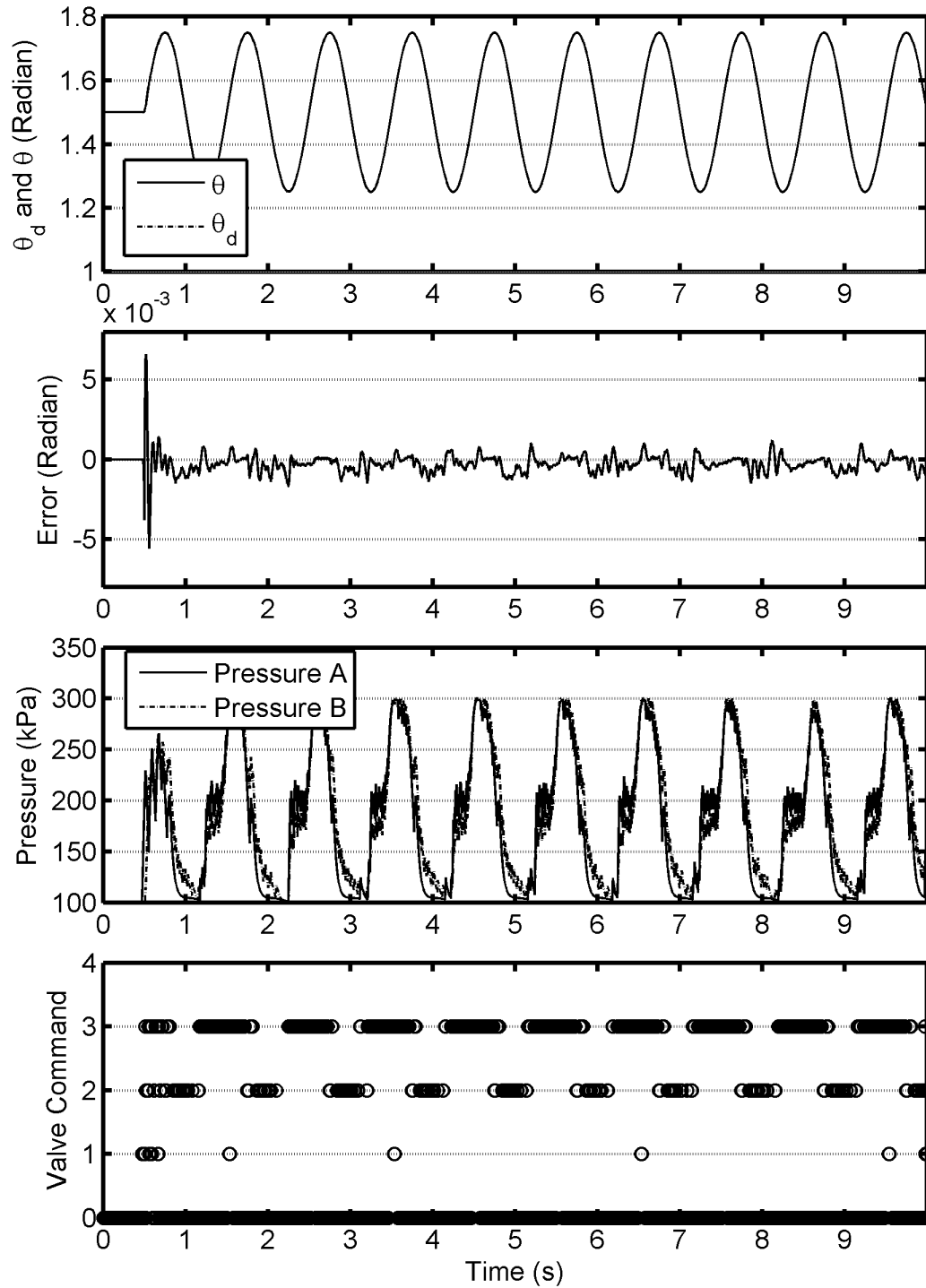
Figure 4.25 Trajectory 3, simulation, pneumatic mode, DVMPC
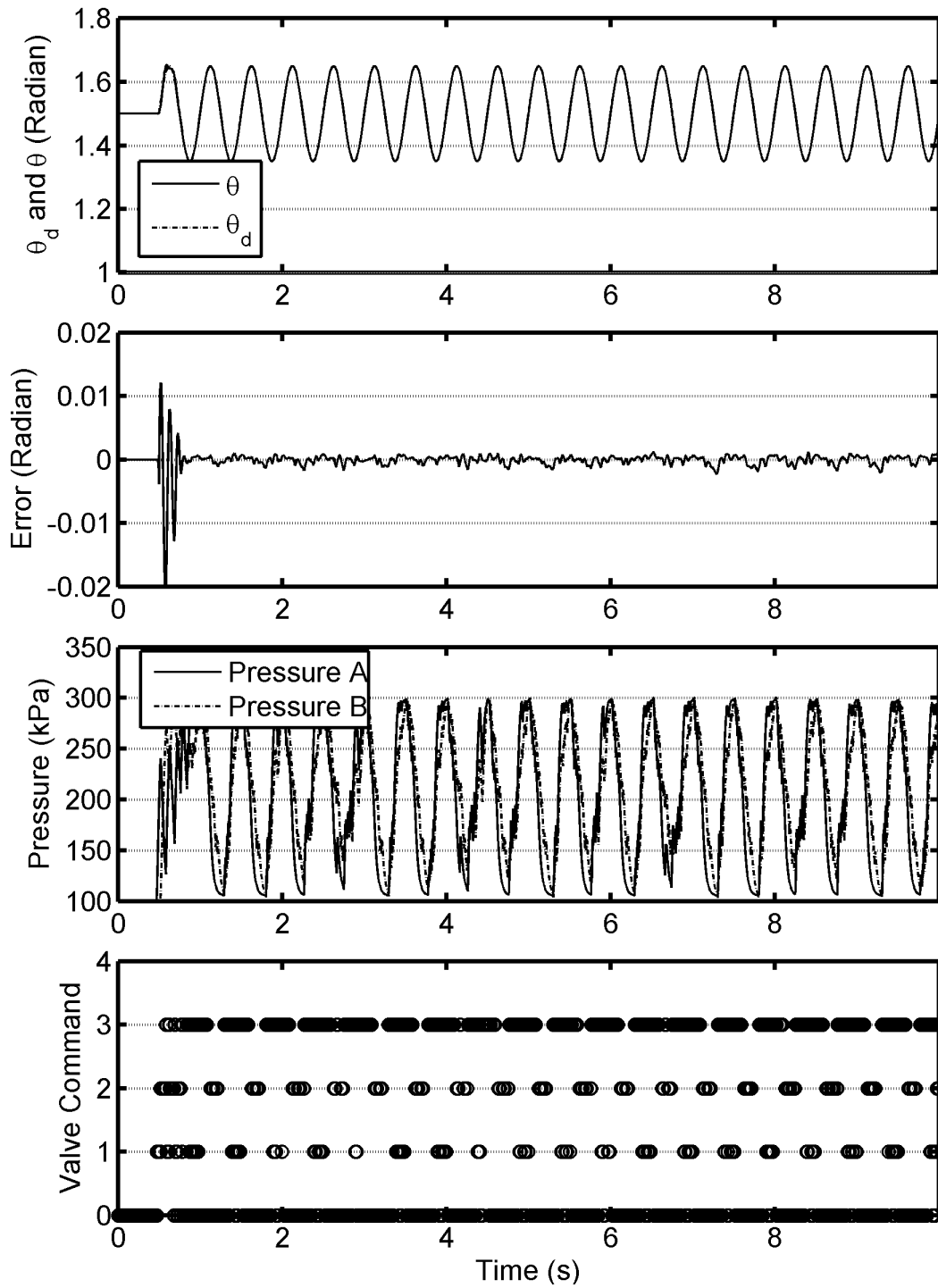
Figure 4.26 Trajectory 4, simulation, pneumatic mode, DVMPC
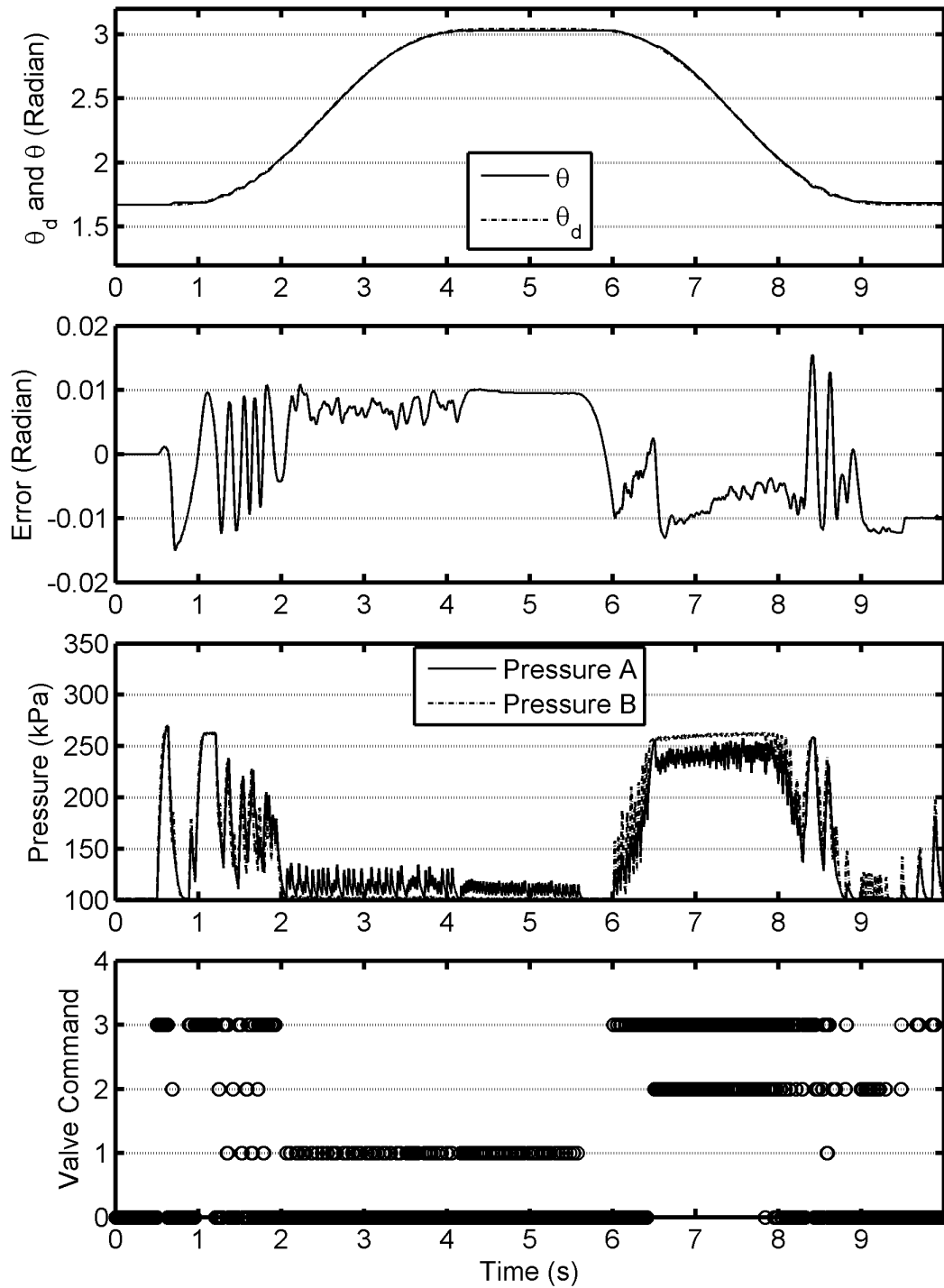
Figure 4.27 Trajectory 1, experiment, pneumatic mode, DVMPC
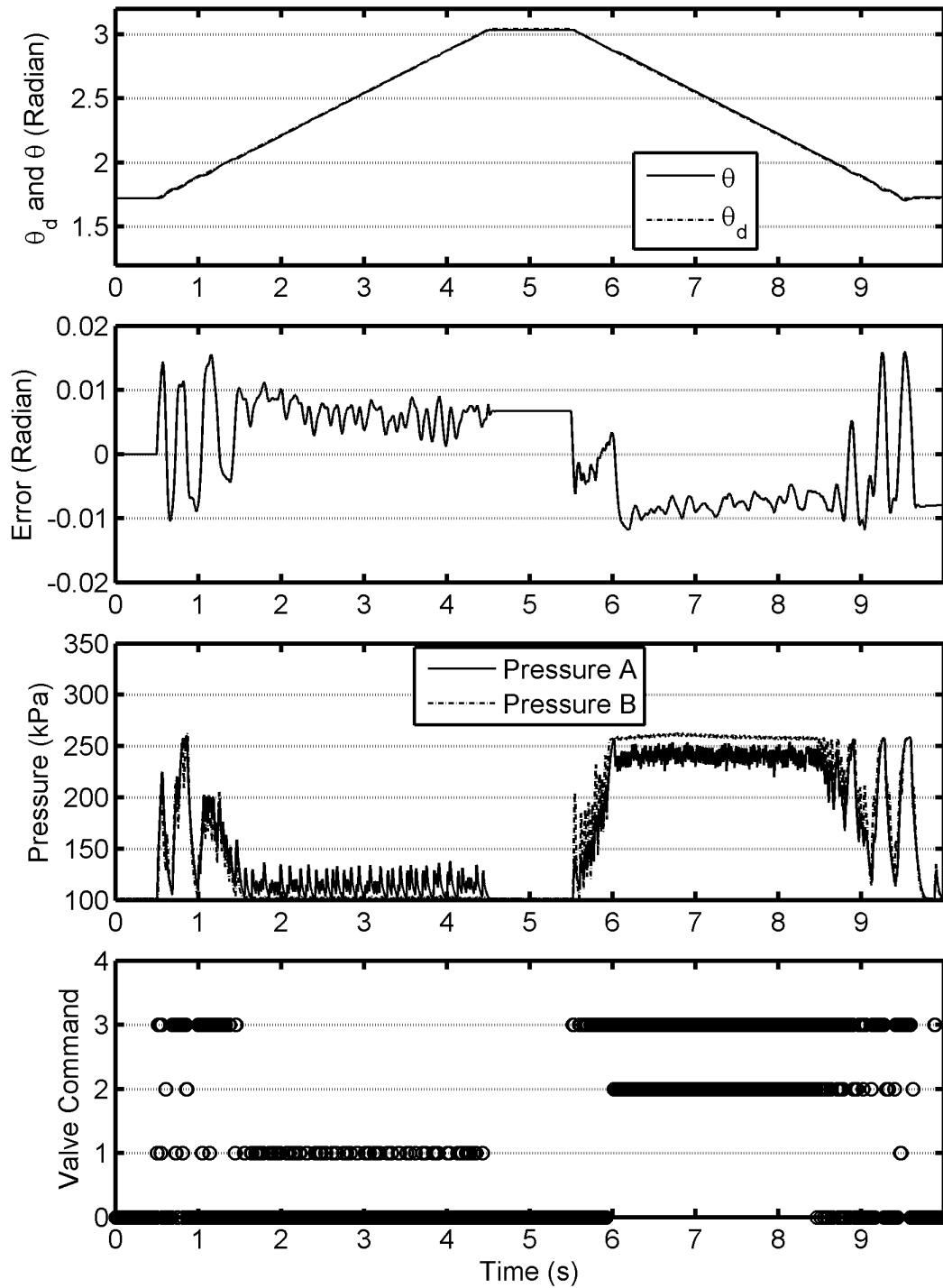
Figure 4.28 Trajectory 2, experiment, pneumatic mode, DVMPC
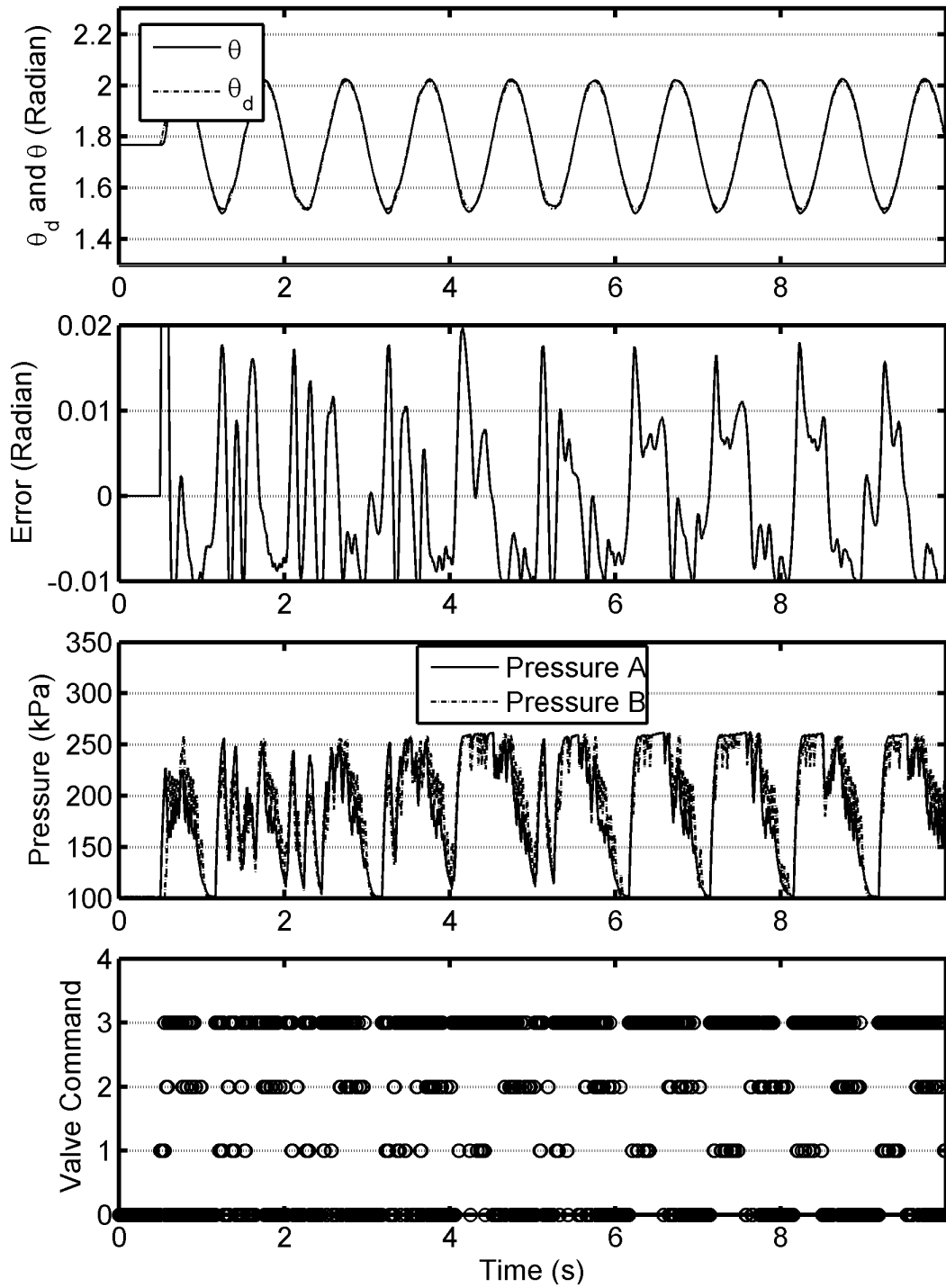
Figure 4.29 Trajectory 3, experiment, pneumatic mode, DVMPC
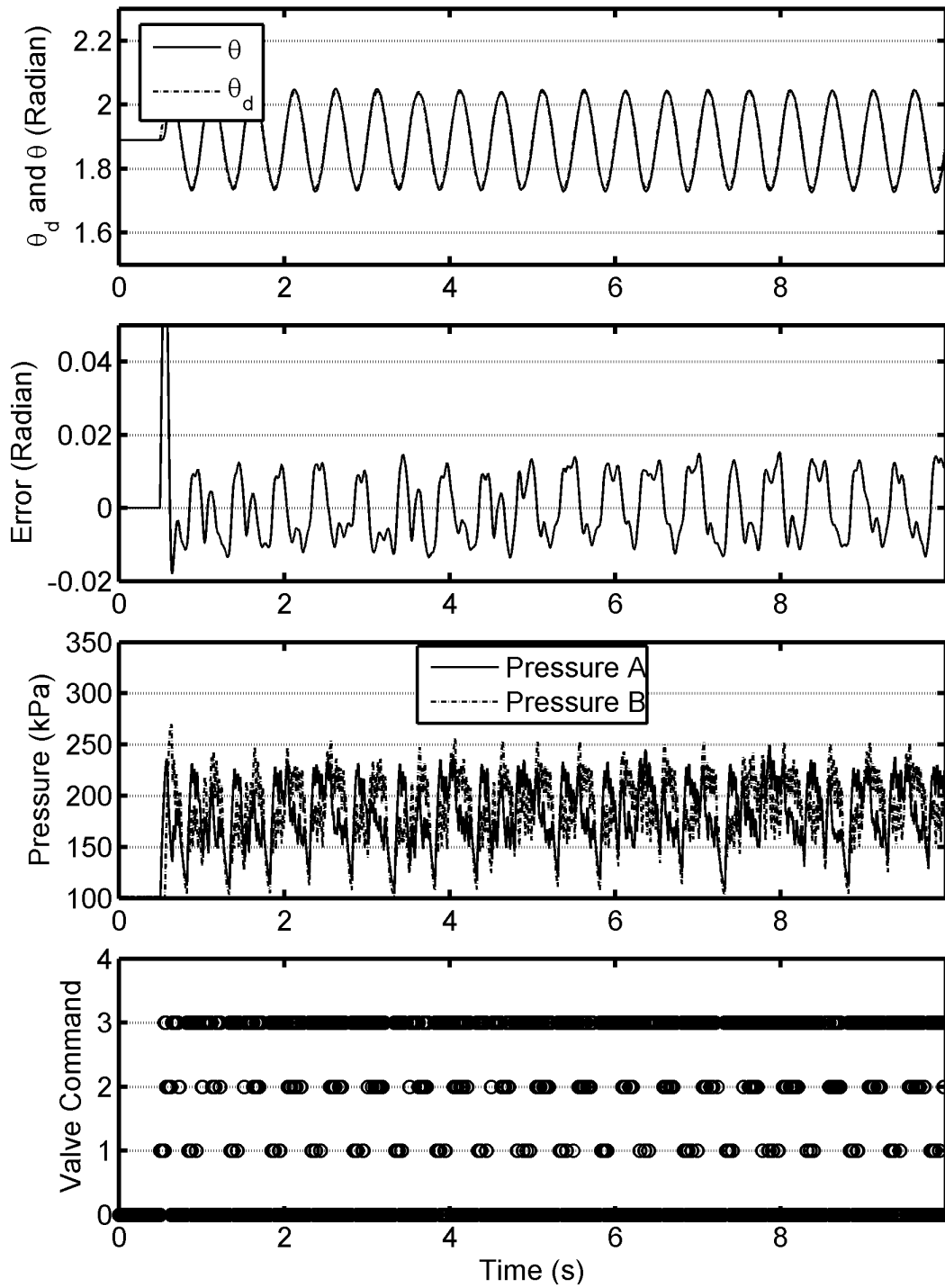
Figure 4.30 Trajectory 4, experiment, pneumatic mode, DVMPC

## 4.5    Comparison of Controllers

Simulations of the three controllers were done for the list of trajectories given Table 4.2.1. The RMSE values of different actuation modes are shown in Table 4.5.1, Table 4.5.2, and Table 4.5.3. In pneumatic mode, linear PVA had the worst performance. DVMPC performed slightly better than backstepping + FF control. In electric motor mode, the DVMPC performance was slightly better. In hybrid mode, the performance of both nonlinear controllers was very similar. The hybrid mode produced the best tracking performance amongst the three modes.

Table 4.5.1 Pneumatic mode simulation RMSE (radian) results

|  | Trajectory 1 | Trajectory 2 | Trajectory 3 | Trajectory 4 |
|---|---|---|---|---|
| **PVA+FF+DZC** | $1.29 \times 10^{-2}$ | $8.15 \times 10^{-3}$ | $3.06 \times 10^{-2}$ | $5.70 \times 10^{-2}$ |
| **Backstepping + FF** | $2.34 \times 10^{-3}$ | $3.92 \times 10^{-3}$ | $7.73 \times 10^{-3}$ | $9.02 \times 10^{-3}$ |
| **DVMPC** | $6.84 \times 10^{-4}$ | $4.84 \times 10^{-4}$ | $6.84 \times 10^{-4}$ | $1.68 \times 10^{-3}$ |

Table 4.5.2 Electric motor mode simulation RMSE (radian) results

|  | Trajectory 1 | Trajectory 2 | Trajectory 3 | Trajectory 4 |
|---|---|---|---|---|
| **Backstepping + FF** | $4.76 \times 10^{-3}$ | $4.53 \times 10^{-3}$ | $9.93 \times 10^{-3}$ | $1.25 \times 10^{-2}$ |
| **DVMPC** | $4.24 \times 10^{-4}$ | $4.73 \times 10^{-4}$ | $4.00 \times 10^{-3}$ | $4.81 \times 10^{-3}$ |

Table 4.5.3 Hybrid mode simulation RMSE (radian) results

|  | Trajectory 1 | Trajectory 2 | Trajectory 3 | Trajectory 4 |
|---|---|---|---|---|
| **Backstepping + FF** | $1.45 \times 10^{-3}$ | $1.39 \times 10^{-3}$ | $4.84 \times 10^{-3}$ | $6.02 \times 10^{-3}$ |
| **DVMPC** | $4.03 \times 10^{-4}$ | $3.32 \times 10^{-4}$ | $8.78 \times 10^{-4}$ | $1.37 \times 10^{-3}$ |

Experiments with the three actuation modes for all trajectories were done for both nonlinear controllers. Each of the experiments was repeated for five times in order to show its repeatability. The RMSE values for all of the cases are shown in Table 4.5.4, Table 4.5.5, and Table 4.5.6.

Figure 4.31 compares the tracking error performance of three controllers for trajectory 1 in pneumatic mode and hybrid mode. The PVA controller unsurprisingly has the worst tracking performance. In hybrid mode, the two nonlinear controllers have close performance.

In pneumatic mode, compared to PVA, the backstepping and DVMPC controllers reduced the average RMSE by 60%, excluding the 1 Hz sine wave trajectory. When tracking a 0.3 radian amplitude 2 Hz sine wave reference, the backstepping and DVMPC controller achieved an average RMSE value of 0.01 radian.

In hybrid mode, the two nonlinear controllers have really close performance for all trajectories according to RMSE values listed in Table 4.5.6. Compared to pneumatic mode, the hybrid actuator has reduced the average RMSE by 70% for both nonlinear controllers. When tracking a 0.3 radian amplitude 2 Hz sine wave trajectory, the average RMSE was 0.005 radian or 50% less than with the pneumatic mode.

When the sine wave frequency was higher, the pneumatic mode tracking performance for both controllers became worse due to the saturation of valves. However, the hybrid mode was less impacted thanks to the torque rapidly provided by the electric motor. Even for normal trajectories such as cycloidal, Figure 4.31 shows the benefit of

including the electric motor. The maximum tracking error reduces about 60% when the electric motor is turned on.

Table 4.5.4 Pneumatic mode experimental RMSE (radian) results

| **PVA + FF + DZC RMSE value** (radian) | | | | | |
|---|---|---|---|---|---|
| **Trajectory** | **Test 1** | **Test 2** | **Test 3** | **Test 4** | **Test 5** | **Mean** |
| **1** | $1.03\times10^{-2}$ | $1.03\times\times10^{-2}$ | $1.05\times\times10^{-2}$ | $1.08\times\times10^{-2}$ | $1.07\times\times10^{-2}$ | $1.05\times10^{-2}$ |
| **2** | $9.67\times10^{-3}$ | $9.75\times10^{-3}$ | $9.77\times10^{-3}$ | $9.91\times10^{-3}$ | $9.83\times10^{-3}$ | $9.79\times10^{-3}$ |
| **3** | $7.46\times10^{-3}$ | $6.82\times10^{-3}$ | $6.73\times10^{-3}$ | $6.86\times10^{-3}$ | $7.38\times10^{-3}$ | $7.05\times10^{-3}$ |
| **4** | $2.50\times10^{-2}$ | $2.16\times10^{-2}$ | $1.85\times10^{-2}$ | $1.60\times10^{-2}$ | $1.33\times10^{-2}$ | $1.89\times10^{-2}$ |
| **Backstepping + FF RMSE value** (radian) | | | | | |
| **Trajectory** | **Test 1** | **Test 2** | **Test 3** | **Test 4** | **Test 5** | **Mean** |
| **1** | $5.00\times10^{-3}$ | $5.21\times10^{-3}$ | $5.42\times10^{-3}$ | $5.32\times10^{-3}$ | $5.25\times10^{-3}$ | $5.24\times10^{-3}$ |
| **2** | $5.92\times10^{-3}$ | $5.85\times10^{-3}$ | $6.18\times10^{-3}$ | $6.40\times10^{-3}$ | $6.08\times10^{-3}$ | $6.09\times10^{-3}$ |
| **3** | $1.45\times10^{-2}$ | $1.03\times10^{-2}$ | $1.06\times10^{-2}$ | $1.13\times10^{-2}$ | $1.03\times10^{-2}$ | $1.14\times10^{-2}$ |
| **4** | $1.14\times10^{-2}$ | $1.29\times10^{-2}$ | $1.12\times10^{-2}$ | $1.09\times10^{-2}$ | $1.21\times10^{-2}$ | $1.17\times10^{-2}$ |
| **DVMPC RMSE value** (radian) | | | | | |
| **Trajectory** | **Test 1** | **Test 2** | **Test 3** | **Test 4** | **Test 5** | **Mean** |
| **1** | $7.93\times10^{-3}$ | $8.23\times10^{-3}$ | $7.68\times10^{-3}$ | $7.49\times10^{-3}$ | $7.50\times10^{-3}$ | $7.77\times10^{-3}$ |
| **2** | $7.18\times10^{-3}$ | $6.49\times10^{-3}$ | $7.45\times10^{-3}$ | $6.56\times10^{-3}$ | $6.90\times10^{-3}$ | $6.92\times10^{-3}$ |
| **3** | $9.20\times10^{-3}$ | $9.01\times10^{-3}$ | $10.17\times10^{-3}$ | $8.89\times10^{-3}$ | $8.89\times10^{-3}$ | $9.23\times10^{-3}$ |
| **4** | $9.92\times10^{-3}$ | $11.04\times10^{-3}$ | $9.64\times10^{-3}$ | $9.29\times10^{-3}$ | $8.78\times10^{-3}$ | $9.73\times10^{-3}$ |

Table 4.5.5 Electric motor mode experimental RMSE (radian) results

| Backstepping + FF RMSE value (radian) | | | | | | |
|---|---|---|---|---|---|---|
| **Trajectory** | **Test 1** | **Test 2** | **Test 3** | **Test 4** | **Test 5** | **Mean** |
| **1** | $3.47\times10^{-3}$ | $3.50\times10^{-3}$ | $3.5\times10^{-3}$ | $3.62\times10^{-3}$ | $3.64\times10^{-3}$ | $3.55\times10^{-3}$ |
| **2** | $2.89\times10^{-3}$ | $2.92\times10^{-3}$ | $2.9\times10^{-3}$ | $2.92\times10^{-3}$ | $2.92\times10^{-3}$ | $2.91\times10^{-3}$ |
| **3** | $7.73\times10^{-3}$ | $8.11\times10^{-3}$ | $7.82\times10^{-3}$ | $8.24\times10^{-3}$ | $8.60\times10^{-3}$ | $8.10\times10^{-3}$ |
| **4** | $1.29\times10^{-2}$ | $1.94\times10^{-2}$ | $1.68\times10^{-2}$ | $1.90\times10^{-2}$ | $2.28\times10^{-2}$ | $1.82\times10^{-2}$ |
| DVMPC RMSE value (radian) | | | | | | |
| **Trajectory** | **Test 1** | **Test 2** | **Test 3** | **Test 4** | **Test 5** | **Mean** |
| **1** | $1.33\times10^{-3}$ | $1.28\times10^{-3}$ | $1.67\times10^{-3}$ | $1.65\times10^{-3}$ | $1.56\times10^{-3}$ | $1.50\times10^{-3}$ |
| **2** | $1.35\times10^{-3}$ | $1.58\times10^{-3}$ | $1.38\times10^{-3}$ | $1.46\times10^{-3}$ | $1.46\times10^{-3}$ | $1.45\times10^{-3}$ |
| **3** | $1.43\times10^{-2}$ | $7.04\times10^{-3}$ | $7.00\times10^{-3}$ | $6.60\times10^{-3}$ | $6.47\times10^{-3}$ | $8.28\times10^{-3}$ |
| **4** | $0.93\times10^{-2}$ | $1.12\times10^{-2}$ | $2.04\times10^{-2}$ | $1.47\times10^{-2}$ | $0.78\times10^{-2}$ | $1.27\times10^{-2}$ |

Table 4.5.6  Hybrid mode experimental RMSE (radian) results

| Backstepping + FF RMSE value (radian) | | | | | | |
|---|---|---|---|---|---|---|
| **Trajectory** | **Test 1** | **Test 2** | **Test 3** | **Test 4** | **Test 5** | **Mean** |
| **1** | $1.67\times10^{-3}$ | $1.85\times10^{-3}$ | $1.91\times10^{-3}$ | $1.90\times10^{-3}$ | $1.96\times10^{-3}$ | $1.86\times10^{-3}$ |
| **2** | $2.14\times10^{-3}$ | $2.18\times10^{-3}$ | $2.19\times10^{-3}$ | $2.19\times10^{-3}$ | $2.17\times10^{-3}$ | $2.17\times10^{-3}$ |
| **3** | $4.74\times10^{-3}$ | $4.45\times10^{-3}$ | $4.79\times10^{-3}$ | $4.42\times10^{-3}$ | $4.93\times10^{-3}$ | $4.67\times10^{-3}$ |
| **4** | $5.57\times10^{-3}$ | $7.01\times10^{-3}$ | $7.37\times10^{-3}$ | $6.21\times10^{-3}$ | $6.71\times10^{-3}$ | $6.57\times10^{-3}$ |
| DVMPC RMSE value (radian) | | | | | | |
| **Trajectory** | **Test 1** | **Test 2** | **Test 3** | **Test 4** | **Test 5** | **Mean** |
| **1** | $1.55\times10^{-3}$ | $1.63\times10^{-3}$ | $1.79\times10^{-3}$ | $1.95\times10^{-3}$ | $2.43\times10^{-3}$ | $1.87\times10^{-3}$ |
| **2** | $1.91\times10^{-3}$ | $1.93\times10^{-3}$ | $1.97\times10^{-3}$ | $1.49\times10^{-3}$ | $1.55\times10^{-3}$ | $1.77\times10^{-3}$ |
| **3** | $4.19\times10^{-3}$ | $4.28\times10^{-3}$ | $4.35\times10^{-3}$ | $4.28\times10^{-3}$ | $4.46\times10^{-3}$ | $4.31\times10^{-3}$ |
| **4** | $4.74\times10^{-3}$ | $4.47\times10^{-3}$ | $4.48\times10^{-3}$ | $4.64\times10^{-3}$ | $4.68\times10^{-3}$ | $4.60\times10^{-3}$ |
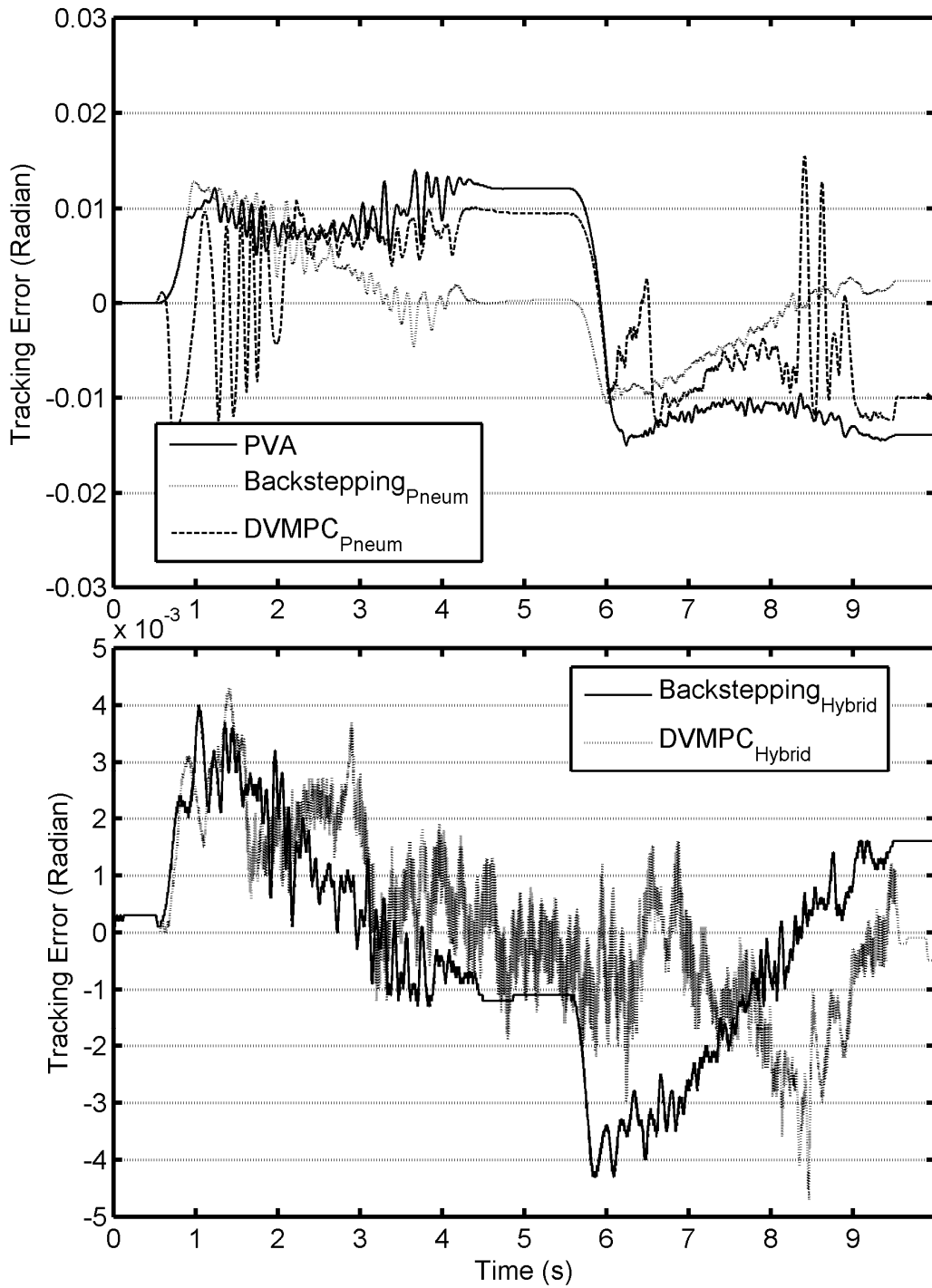
Figure 4.31 Trajectory 1 experiment, tracking error comparison

## 4.6 Conclusions

A modified linear PVA controller and two model-based nonlinear position controllers (i.e. backstepping + FF and DVMPC+IDC) were designed in this chapter. The two model-based nonlinear position controllers outperformed the modified linear PVA controller in pneumatic only mode in both the simulations and experiments for the horizontal configuration.

In the pneumatic mode simulations, the DVMPC + IDC produced much smaller tracking errors than the other two controllers in all of the four trajectories. In pneumatic mode experiments, the backstepping + FF controller performed better in trajectory 1 and 2. The DVMPC + IDC was slightly better at sine wave trajectories.

In the electric motor mode simulations, the DVMPC + IDC noticeably outperformed the backstepping + FF controller. In the electric motor mode experiments, the performance of the backstepping + FF controller was slightly inferior for trajectories 1, 2 and 4.

In the hybrid mode simulations, the DVMPC + IDC was superior for all of the 4 trajectories. In the hybrid mode experiments, the backstepping + FF controller had a similar performance with DVMPC + IDC for trajectories 1, 2 and 3. The DVMPC + IDC was slightly better for trajectory 4.

The difference between the simulations and experiments for DVMPC + IDC might have been caused by the difference of the controller gains. Unlike the backstepping

+ FF controller gains which were the same for both simulations and experiments, the

DVMPC + IDC used two sets of different gains.

# CHAPTER 5.     SIMULATION

## 5.1   Introduction

In the preliminary simulations and experiments included in Chapter 4, except for the results with the previous hardware in section 4.4.8.1, the controllers assumed the payload mass was zero while the actual payload was zero as well, and the hybrid actuator was only operated horizontally. Additional simulations and experiments are needed to study the performance of the controllers over a wider range of conditions.  In this chapter, the following situations will be simulated and discussed:

1. Comparison of backstepping alone and backstepping + compensation.

2. The impact on DVMPC of different values of the prediction horizon.

3. Payload mass mismatch in backstepping, backstepping + compensation, DVMPC, DVMPC + IDC, and DVMPC + IDC + payload estimator for horizontal and vertical orientation will be examined.

4. Discuss the limitations of the bipolynomial valve model compared with an ideal valve model when using a simulated plant for backstepping control.

## 5.2   Backstepping Controller Compensation

In the previous chapter, the electric and pneumatic compensations were designed separately for the backstepping controller. Their purpose is to help the backstepping controlled hybrid actuator respond more quickly to rapid trajectory changes. The electric motor compensation depends on feedback of the position and velocity tracking. The

cylinder torque FF compensation heavily relies on the accuracy of the system model. The combination of these two compensations should improve the tracking performance of backstepping control. In this section, the simulations will be performed to study their effectiveness.

### 5.2.1   Electric Motor Compensation

The electric motor compensation torque does not rely on the accuracy of system modeling. The performance degradation of the model-based backstepping controller due to model mismatch will be compensated by this torque component.

The simulation assumes payload mass is zero for both controller and actual plant. The only mismatch is due to the difference between the bipolynomial valve model used by the controller (presented in section 3.7) and the valve model (3.6.6) used by the plant. The hybrid actuator operates in hybrid mode to enable both electric motor and pneumatic cylinder. It is operated horizontally same as Chapter 4. Only trajectory 1 (cycloidal) and trajectory 4 (2Hz sine wave) were chosen to be the references because of the similarity of the rest of trajectories. The gains of backstepping controller were kept the same as in Chapter 4, and the pneumatic compensation was switched off.

The Figure 5.1 and Figure 5.2 shows the comparison of backstepping controller alone versus backstepping controller with electric motor compensation in hybrid mode. RMSE values of the simulation are listed in Table 5.2.1. When the compensation is turned on, the RMSE value reduces significantly, 40% and 70% for trajectory 1 and 4, respectively. This is because the electric motor compensation contains feedback of

position and velocity error. The additional motor torque is generated to correct such errors. Whereas in backstepping controller, the original desired motor torque is actually only a certain portion of total desired torque. In which way, the advantage of electric motor is not fully utilized. Notice that this motor compensation only works when the original motor torque is not saturated.
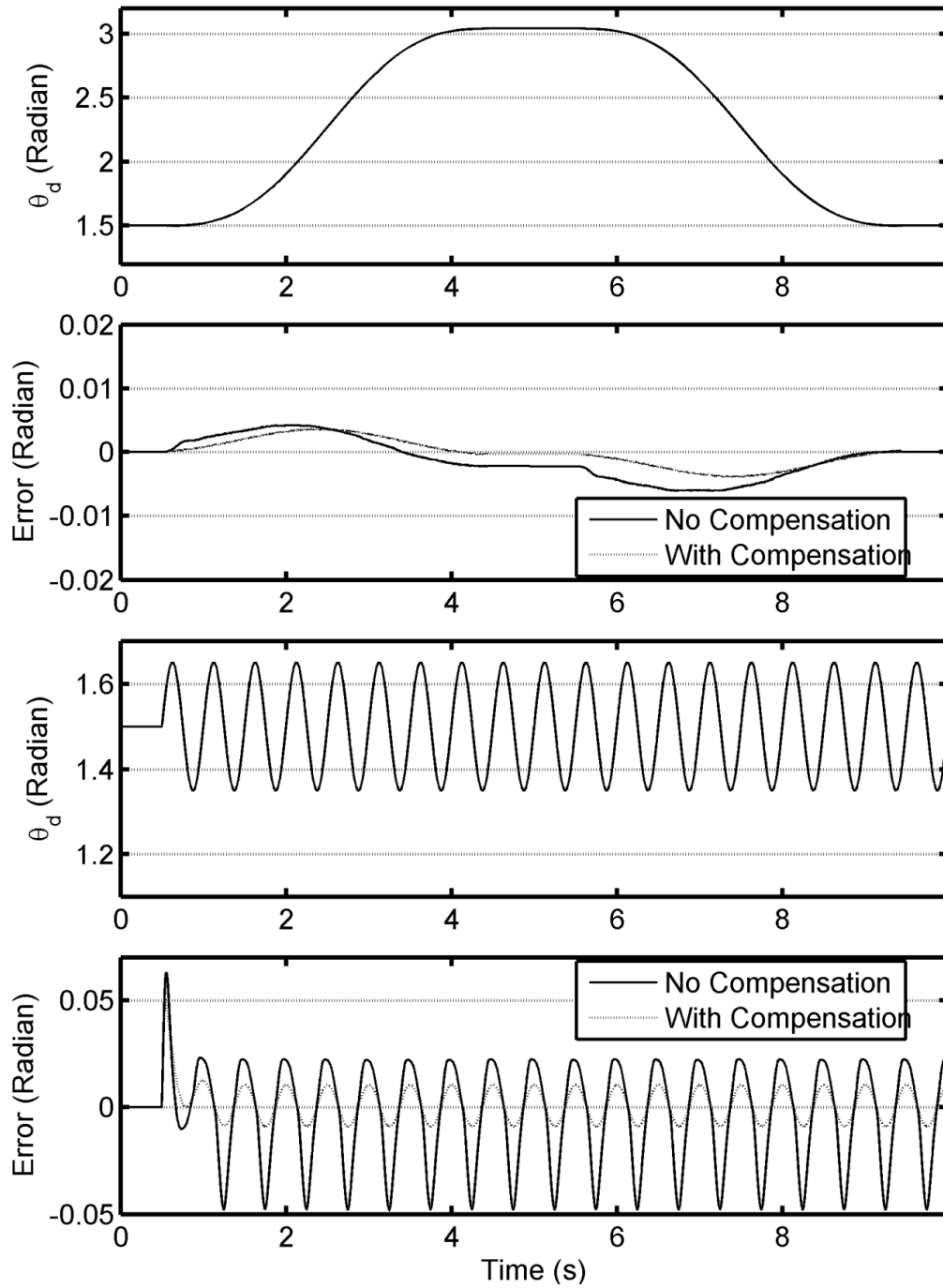
Figure 5.1 Backstepping control, hybrid mode with only electric motor compensation, simulation
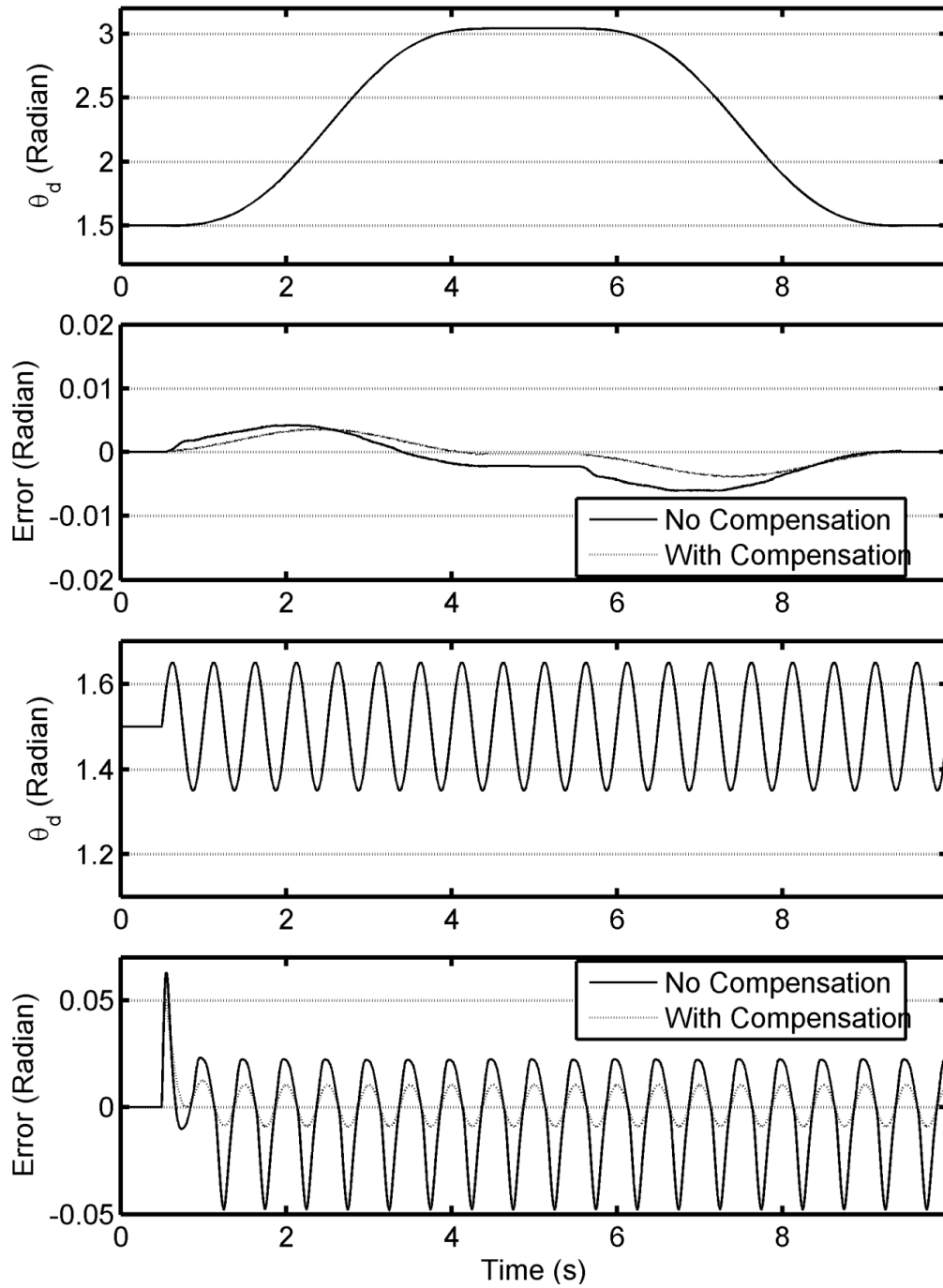
Figure 5.2 Backstepping control, hybrid mode with only electric motor
compensation, simulation

Table 5.2.1  RMSE values (radian) of electric motor compensation

|  | **No compensation** | **With compensation** |
|---|---|---|
| **Trajectory 1** | $3.20 \times 10^{-3}$ | $2.04 \times 10^{-3}$ |
| **Trajectory 4** | $2.33 \times 10^{-2}$ | $8.06 \times 10^{-3}$ |

### 5.2.2   Pneumatic Cylinder FF Compensation

The effectiveness of the FF term was shown in Chapter 4. A FF only controller was used to track trajectory 1 in simulation. The RMSE value of the tracking was moderate. However, such results alone are not sufficient to prove that adding FF compensation to backstepping controller will produce improved performance. In this section, the FF compensation will be turned on and combined with backstepping controller in simulation. As before, only trajectory 1 (cycloidal) and trajectory 4 (2 Hz sine wave) will be used.

The simulation environment remains the same as the previous section except that the electric motor is switched off. The RMSE results are listed in Table 5.2.2. The comparison of no FF compensation and with FF compensation is shown in Figure 5.3. The compensation uses the one step ahead desired position trajectory to calculate the desired mass flow rate and pressure. This led to overcompensation in some cases. For example, with the cycloidal trajectory in Figure 5.3 the error is negative when the

commanded motion starts, and has a larger magnitude than the no compensation case. However the overall performance was significantly improved. With FF compensation, the average RMSE values were reduced by over 70%.

Table 5.2.2  RMSE value (radian) of pneumatic cylinder FF compensation

|  | No compensation | With compensation |
|---|---|---|
| **Trajectory 1** | $1.47 \times 10^{-2}$ | $2.34 \times 10^{-3}$ |
| **Trajectory 4** | $3.97 \times 10^{-2}$ | $9.85 \times 10^{-3}$ |
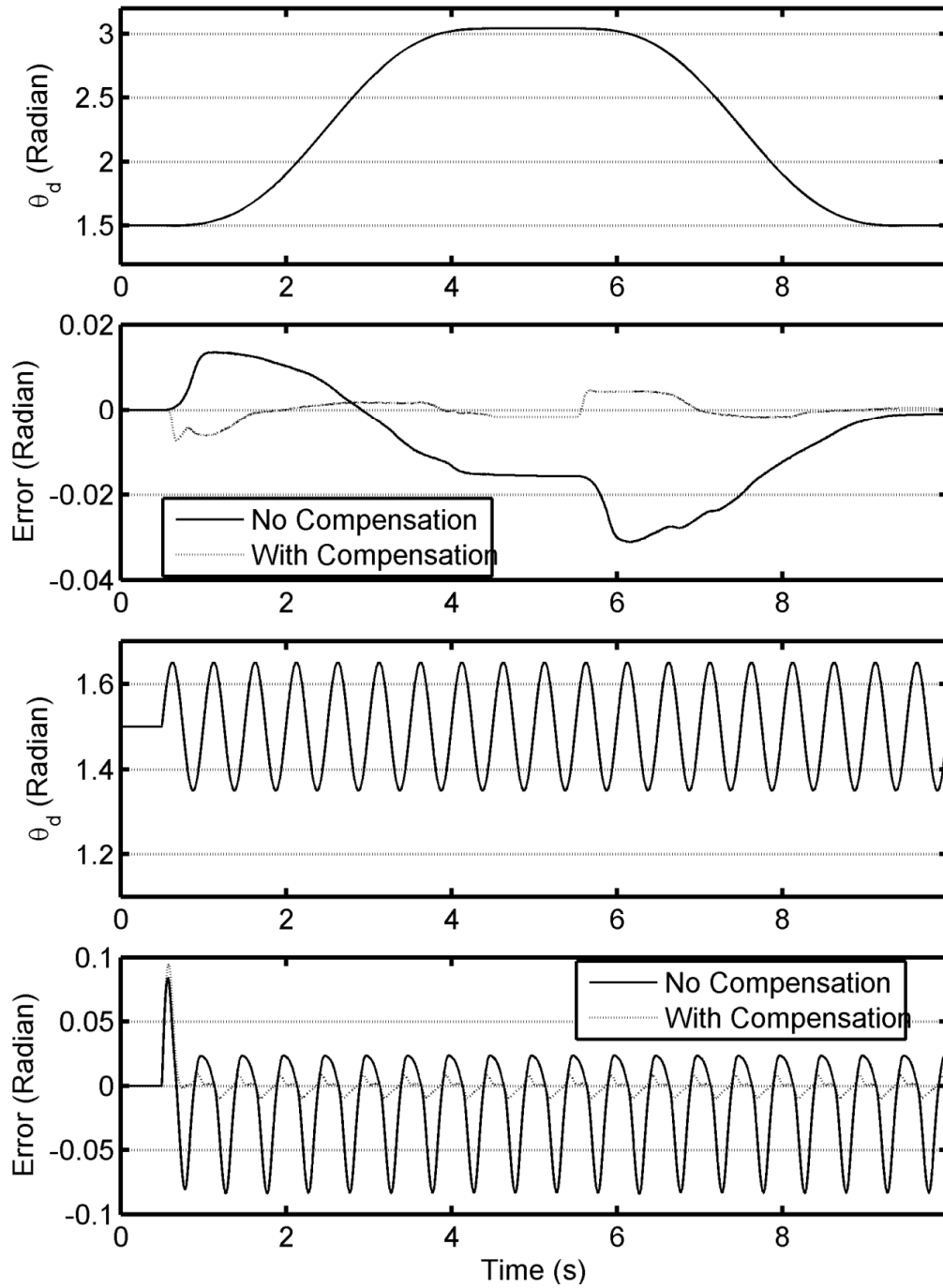
Figure 5.3 Backstepping control, hybrid mode with only pneumatic cylinder FF compensation, simulation

## 5.3   DVMPC Prediction Horizon Selection

The prediction horizon for DVMPC was roughly selected in Chapter 4. It relates to the controller performance in a non-intuitive way. It is necessary to explore how the performance is affected by the selection of prediction horizon. This section will focus on selecting a proper prediction horizon in horizontal configuration and assuming the payload mass is zero. As before, only trajectory 1 (cycloidal) and trajectory 4 (2 Hz sine wave) will be used.

The results of different prediction horizon for trajectory 1 and trajectory 4 are listed in Table 5.3.1. When horizon is small, the DVMPC controller is not capable of tracking both trajectories and the RMSE values are very large. After dropping when $N_p = 30$, the RMSE tended to increase with the prediction horizon. This happens because a larger horizon makes the controller more conservative. Based on these results, $N_p = 40$ will be used for the remaining simulations.
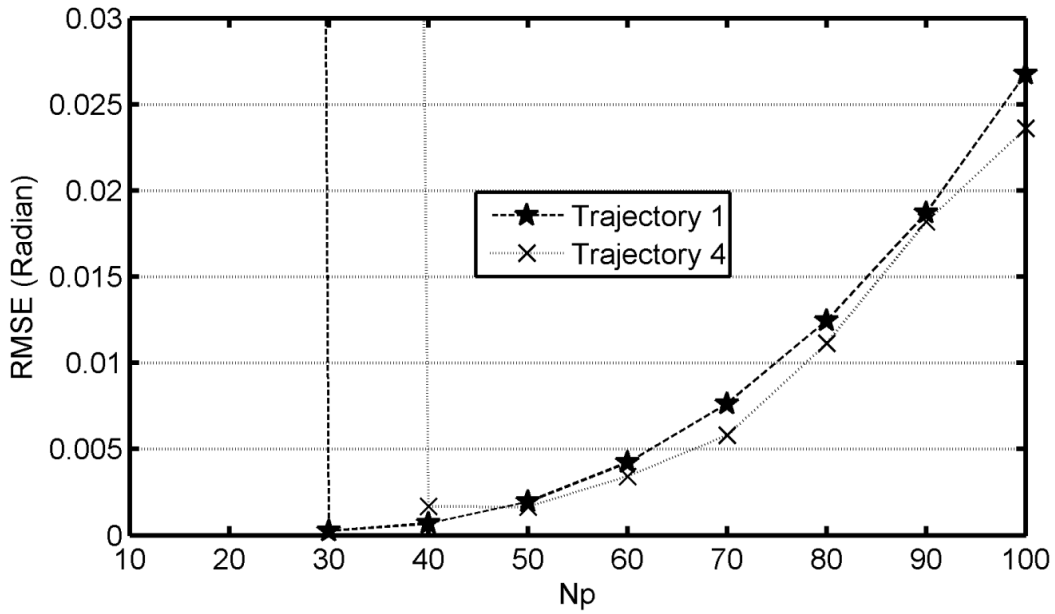
Figure 5.4 RMSE values (radian) for DVMPC with different prediction horizons

Table 5.3.1   RMSE value (radian) of different prediction horizon

| | Trajectory 1 | Trajectory 4 |
|---|---|---|
| $N_p = 10$ | 0.0362 | 0.0311 |
| $N_p = 20$ | 0.9949 | 0.1033 |
| $N_p = 30$ | $2.60 \times 10^{-4}$ | 0.6334 |
| $N_p = 40$ | $6.84 \times 10^{-4}$ | $1.68 \times 10^{-3}$ |
| $N_p = 50$ | $1.94 \times 10^{-3}$ | $1.64 \times 10^{-3}$ |
| $N_p = 60$ | $4.22 \times 10^{-3}$ | $3.41 \times 10^{-3}$ |
| $N_p = 70$ | $7.63 \times 10^{-3}$ | $5.80 \times 10^{-3}$ |
| $N_p = 80$ | $1.24 \times 10^{-2}$ | $1.11 \times 10^{-2}$ |
| $N_p = 90$ | $1.87 \times 10^{-2}$ | $1.81 \times 10^{-2}$ |
| $N_p = 100$ | $2.68 \times 10^{-2}$ | $2.36 \times 10^{-2}$ |

## 5.4    Payload Mismatch Simulations

When hybrid actuator operates in horizontal and vertical configurations, as introduced in Chapter 3, the system dynamics change due to the absence/presence of the gravity torque. The gravity is torque, due to the arm and payload, will increase the required torque when moving upwards. It is essential to study the compensations and payload estimation algorithm in both configurations. Trajectory 1 (cycloid) and trajectory 4 (2 Hz sine wave) will be chosen as position reference for most cases.

### 5.4.1    Horizontal Configuration with Payload Mismatch

In the previous simulations and experiments the payload mass assumed by the controller and the actual payload were both zero. In practice, the payload mass may vary during the task. For instance, the collaborative robot with hybrid actuator can be used to serve drinks with different volumes.  It is necessary to maintain the controller performance in such cases. In this section, the payload mass mismatch will be tested for the two nonlinear controllers.

Three different payloads are used by the controllers to calculate the equivalent inertia. The actual payloads (in the plant) with varying degrees of mismatch are listed in Table 5.4.1.

Table 5.4.1  Payload mass mismatch in simulation

| | Small | | | Nominal | | | Large | | |
|---|---|---|---|---|---|---|---|---|---|
| **Control Payload Mass (kg)** | 0.2 | | | 0.5 | | | 0.8 | | |
| **Actual Payload Mass (kg)** | 0.1 | 0.2 | 0.3 | 0.1 | 0.5 | 0.9 | 0.4 | 0.8 | 1.2 |
| **Mismatch (%)** | -50 | 0 | 50 | -80 | 0 | 80 | -50 | 0 | 50 |

Table 5.4.2  Converted equivalent inertia mismatch in simulation

| | Small | | | Nominal | | | Large | | |
|---|---|---|---|---|---|---|---|---|---|
| **Control inertia(kg·m$^2$)** | 0.051 | | | 0.092 | | | 0.133 | | |
| **Actual inertia (kg·m$^2$)** | 0.037 | 0.051 | 0.065 | 0.037 | 0.092 | 0.147 | 0.078 | 0.133 | 0.188 |
| **Mismatch (%)** | -27 | 0 | 27 | -60 | 0 | 60 | -41 | 0 | 41 |

### 5.4.1.1  Backstepping Control

The backstepping controller was simulated in the pneumatic mode and hybrid mode. In pneumatic mode, the pneumatic cylinder FF compensation is turned on and off for the mismatch cases. The hybrid mode has compensations from the pneumatic cylinder and the motor respectively. These two compensations are turned on and off separately for all payload mismatch cases.

The backstepping controller types are listed in Table 5.4.3.  The RMSE values for different payload mismatches and different controller types are listed in Table 5.4.4 to Table 5.4.6. Note that in pneumatic mode only the cylinder torque is used, thus it will be pointless to have the motor compensation in pneumatic mode.

156

In all payload scenarios, when using trajectory 1, the degree of mismatch doesn't have much impact on controller performance even without compensation. This is because trajectory 1 is smooth in position and velocity reference, the overall system dynamics has a limited variation regarding to different payloads. However for trajectory 4, the controller performance is interesting. When the assumed payload mass is not greater than actual one, the RMSE values are very close. The mismatch case performed even better than no mismatch case. This may be caused by the controller gains were tuned for zero payload case which makes the controller "under react" when a payload is carried. Similar results occurred with trajectory 1 tracking as well. Although the RMSE values were very similar, one may notice that having a smaller payload tended to improve the position tracking.

Table 5.4.3 List of backstepping control types.

| Backstepping Control Type | Number |
|---|---|
| Backstepping only | 1 |
| Backstepping with electric motor compensation only | 2 |
| Backstepping with pneumatic FF compensation only | 3 |
| Backstepping with both compensations | 4 |

Table 5.4.4 RMSE value (radian) for small payload mismatch cases under backstepping control

| | | Trajectory 1 | | | Trajectory 4 | | |
|---|---|---|---|---|---|---|---|
| **Controller Payload (kg)** | | 0.2 | | | 0.2 | | |
| **Actual Payload (kg)** | | 0.1 | 0.2 | 0.3 | 0.1 | 0.2 | 0.3 |
| **Pneum Mode** | **Type #1** | $9.94 \times 10^{-3}$ | $1.02 \times 10^{-2}$ | $1.04 \times 10^{-2}$ | $3.16 \times 10^{-2}$ | $8.59 \times 10^{-2}$ | $1.07 \times 10^{-1}$ |
| | **Type #3** | $2.28 \times 10^{-3}$ | $2.25 \times 10^{-3}$ | $2.25 \times 10^{-3}$ | $1.09 \times 10^{-2}$ | $1.28 \times 10^{-2}$ | $2.99 \times 10^{-2}$ |
| **Hybrid Mode** | **Type #1** | $8.27 \times 10^{-3}$ | $8.47 \times 10^{-3}$ | $8.64 \times 10^{-3}$ | $1.44 \times 10^{-2}$ | $2.23 \times 10^{-2}$ | $2.96 \times 10^{-2}$ |
| | **Type #2** | $2.54 \times 10^{-3}$ | $2.56 \times 10^{-3}$ | $2.57 \times 10^{-3}$ | $9.35 \times 10^{-3}$ | $1.08 \times 10^{-2}$ | $1.40 \times 10^{-2}$ |
| | **Type #3** | $2.24 \times 10^{-3}$ | $2.18 \times 10^{-3}$ | $2.16 \times 10^{-3}$ | $7.97 \times 10^{-3}$ | $8.52 \times 10^{-3}$ | $1.40 \times 10^{-2}$ |
| | **Type #4** | $1.29 \times 10^{-3}$ | $1.31 \times 10^{-3}$ | $1.33 \times 10^{-3}$ | $8.76 \times 10^{-3}$ | $9.77 \times 10^{-3}$ | $1.04 \times 10^{-2}$ |

Table 5.4.5 RMSE value (radian) for medium payload mismatch cases under backstepping control

| | | Trajectory 1 | | | Trajectory 4 | | |
|---|---|---|---|---|---|---|---|
| **Controller Payload (kg)** | | 0.5 | | | 0.5 | | |
| **Actual Payload (kg)** | | 0.1 | 0.5 | 0.9 | 0.1 | 0.5 | 0.9 |
| **Pneum Mode** | **Type #1** | $5.85 \times 10^{-3}$ | $6.35 \times 10^{-3}$ | $6.68 \times 10^{-3}$ | $3.40 \times 10^{-2}$ | $1.35 \times 10^{-1}$ | $1.64 \times 10^{-1}$ |
| | **Type #3** | $1.70 \times 10^{-3}$ | $1.59 \times 10^{-3}$ | $2.14 \times 10^{-3}$ | $1.48 \times 10^{-2}$ | $1.27 \times 10^{-1}$ | $1.82 \times 10^{-1}$ |
| **Hybrid Mode** | **Type #1** | $4.92 \times 10^{-3}$ | $5.34 \times 10^{-3}$ | $5.59 \times 10^{-3}$ | $1.12 \times 10^{-2}$ | $8.33 \times 10^{-2}$ | $1.04 \times 10^{-1}$ |
| | **Type #2** | $2.21 \times 10^{-3}$ | $2.23 \times 10^{-3}$ | $2.25 \times 10^{-3}$ | $9.58 \times 10^{-3}$ | $5.80 \times 10^{-2}$ | $9.45 \times 10^{-2}$ |
| | **Type #3** | $1.66 \times 10^{-3}$ | $1.55 \times 10^{-3}$ | $1.95 \times 10^{-3}$ | $1.09 \times 10^{-2}$ | $1.34 \times 10^{-2}$ | $1.42 \times 10^{-1}$ |
| | **Type #4** | $1.37 \times 10^{-3}$ | $1.38 \times 10^{-3}$ | $1.40 \times 10^{-3}$ | $9.30 \times 10^{-3}$ | $1.19 \times 10^{-2}$ | $1.21 \times 10^{-1}$ |

Table 5.4.6 RMSE value (radian) for large payload mismatch cases under backstepping control

| | | Trajectory 1 | | | Trajectory 4 | | |
|---|---|---|---|---|---|---|---|
| **Controller Payload(kg)** | | 0.8 | | | 0.8 | | |
| **Actual Payload (kg)** | | 0.4 | 0.8 | 1.2 | 0.4 | 0.8 | 1.2 |
| **Pneum Mode** | **Type #1** | $4.67\times10^{-3}$ | $4.91\times10^{-3}$ | $5.14\times10^{-3}$ | $9.38\times10^{-2}$ | $1.63\times10^{-1}$ | $1.63\times10^{-1}$ |
| | **Type #3** | $1.58\times10^{-3}$ | $1.52\times10^{-3}$ | $1.54\times10^{-3}$ | $1.77\times10^{-2}$ | $1.74\times10^{-1}$ | $5.64\times10^{-1}$ |
| **Hybrid Mode** | **Type #1** | $3.98\times10^{-3}$ | $4.18\times10^{-3}$ | $4.31\times10^{-3}$ | $5.29\times10^{-2}$ | $9.92\times10^{-2}$ | $1.07\times10^{-1}$ |
| | **Type #2** | $2.10\times10^{-3}$ | $2.11\times10^{-3}$ | $2.12\times10^{-3}$ | $1.46\times10^{-2}$ | $8.67\times10^{-2}$ | $9.81\times10^{-2}$ |
| | **Type #3** | $1.54\times10^{-3}$ | $1.44\times10^{-3}$ | $1.44\times10^{-3}$ | $1.17\times10^{-2}$ | $9.92\times10^{-2}$ | $1.05\times10^{-1}$ |
| | **Type #4** | $1.49\times10^{-3}$ | $1.50\times10^{-3}$ | $1.51\times10^{-3}$ | $1.23\times10^{-2}$ | $2.19\times10^{-2}$ | $1.40\times10^{-1}$ |

### 5.4.1.2　Backstepping Control with Payload Estimator

The purpose of payload estimation algorithm is to improve the robustness of DVMPC to payload mismatch. In Chapter 4, the payload estimation algorithm was shown to be effective in the previous version of the hybrid actuator with a smooth trajectory. In this section the model-based payload estimator proposed in Chapter 4 will be incorporated into backstepping control and studied by simulation.

The trajectory 1 has a smooth position and velocity reference, and the angular acceleration relatively small. This is the reason why, in the previous section, the controller performances are close in trajectory 1 despite of the presence of payload

mismatches. The payload estimation algorithm was designed primarily to compensate for gravity torque mismatch, thus it might not be either quick or accurate enough to compensate for the effects of inertia mismatch in the horizontal configuration.

The same backstepping control types and trajectories as the previous section are simulated. The estimator is switched on and off for all the cases.  The RMSE values are listed in Table 5.4.7 to Table 5.4.12. For the small payload cases, the estimator did not help in most cases for both trajectories except for very limited improvement in trajectory 1 hybrid mode type #3. The normal and large payload had similar results. The reason is when angular acceleration is small the payload has limited impact to system dynamics in horizontal configuration. For rapidly changing references like trajectory 4, the convergence of the payload estimation is slower than the change of trajectory. The tracking performance is much worse for such trajectories when the estimator is switched on than when it is off.

Table 5.4.7 RMSE values (radian) for small payload under backstepping control with/without payload estimator, tracking trajectory 1

| | | Estimator OFF | | | Estimator ON | | |
|---|---|---|---|---|---|---|---|
| **Controller Payload (kg)** | | 0.2 | | | 0.2 | | |
| **Actual Payload (kg)** | | 0.1 | 0.2 | 0.3 | 0.1 | 0.2 | 0.3 |
| **Pneum Mode** | **Type #1** | $9.94{\times}10^{-3}$ | $1.02{\times}10^{-2}$ | $1.03{\times}10^{-2}$ | $9.94{\times}10^{-3}$ | $1.02{\times}10^{-2}$ | $1.04{\times}10^{-2}$ |
| | **Type #3** | $2.34{\times}10^{-3}$ | $2.31{\times}10^{-3}$ | $2.26{\times}10^{-3}$ | $2.35{\times}10^{-3}$ | $2.30{\times}10^{-3}$ | $2.27{\times}10^{-3}$ |
| **Hybrid Mode** | **Type #1** | $8.27{\times}10^{-3}$ | $8.47{\times}10^{-3}$ | $8.64{\times}10^{-3}$ | $8.27{\times}10^{-3}$ | $8.47{\times}10^{-3}$ | $8.63{\times}10^{-3}$ |
| | **Type #2** | $2.54{\times}10^{-3}$ | $2.56{\times}10^{-3}$ | $2.57{\times}10^{-3}$ | $7.06{\times}10^{-1}$ | $7.06{\times}10^{-1}$ | $7.06{\times}10^{-1}$ |
| | **Type #3** | $2.50{\times}10^{-3}$ | $2.41{\times}10^{-3}$ | $2.31{\times}10^{-3}$ | $2.29{\times}10^{-3}$ | $2.26{\times}10^{-3}$ | $2.23{\times}10^{-3}$ |
| | **Type #4** | $1.35{\times}10^{-3}$ | $1.35{\times}10^{-3}$ | $1.35{\times}10^{-3}$ | $1.57{\times}10^{-2}$ | $1.35{\times}10^{-2}$ | $1.48{\times}10^{-2}$ |

Table 5.4.8 RMSE values (radian) for small payload under backstepping control with/without payload estimator, tracking trajectory 4

| | | Estimator OFF | | | Estimator ON | | |
|---|---|---|---|---|---|---|---|
| **Controller Payload (kg)** | | 0.2 | | | 0.2 | | |
| **Actual Payload (kg)** | | 0.1 | 0.2 | 0.3 | 0.1 | 0.2 | 0.3 |
| **Pneum Mode** | **Type #1** | $3.53{\times}10^{-2}$ | $8.66{\times}10^{-2}$ | $1.07{\times}10^{-1}$ | $4.35{\times}10^{-2}$ | $1.04{\times}10^{-1}$ | $1.26{\times}10^{-1}$ |
| | **Type #3** | $2.91{\times}10^{-2}$ | $6.64{\times}10^{-2}$ | $5.28{\times}10^{-2}$ | $2.38{\times}10^{-2}$ | $1.26{\times}10^{-1}$ | $1.98{\times}10^{-1}$ |
| **Hybrid Mode** | **Type #1** | $1.59{\times}10^{-2}$ | $2.67{\times}10^{-2}$ | $2.97{\times}10^{-2}$ | $2.00{\times}10^{-2}$ | $3.42{\times}10^{-2}$ | $6.29{\times}10^{-2}$ |
| | **Type #2** | $1.14{\times}10^{-2}$ | $1.39{\times}10^{-2}$ | $1.76{\times}10^{-2}$ | $1.06{\times}10^{-2}$ | $1.38{\times}10^{-2}$ | $3.39{\times}10^{-2}$ |
| | **Type #3** | $1.15{\times}10^{-2}$ | $1.24{\times}10^{-2}$ | $1.67{\times}10^{-2}$ | $1.22{\times}10^{-2}$ | $2.43{\times}10^{-2}$ | $5.64{\times}10^{-2}$ |
| | **Type #4** | $1.06{\times}10^{-2}$ | $1.67{\times}10^{-2}$ | $2.05{\times}10^{-2}$ | $1.16{\times}10^{-2}$ | $4.05{\times}10^{-1}$ | $5.19{\times}10^{-1}$ |

Table 5.4.9 RMSE values (radian) for medium payload under backstepping control with/without payload estimator, tracking trajectory 1

| | | Estimator OFF | | | Estimator ON | | |
|---|---|---|---|---|---|---|---|
| **Controller Payload (kg)** | | 0.5 | | | 0.5 | | |
| **Actual Payload (kg)** | | 0.1 | 0.5 | 0.9 | 0.1 | 0.5 | 0.9 |
| **Pneum Mode** | **Type #1** | $5.84\times10^{-3}$ | $6.35\times10^{-3}$ | $6.68\times10^{-3}$ | $5.83\times10^{-3}$ | $6.35\times10^{-3}$ | $6.68\times10^{-3}$ |
| | **Type #3** | $1.75\times10^{-3}$ | $1.61\times10^{-3}$ | $2.11\times10^{-3}$ | $1.75\times10^{-3}$ | $1.61\times10^{-3}$ | $2.12\times10^{-3}$ |
| **Hybrid Mode** | **Type #1** | $4.92\times10^{-3}$ | $5.33\times10^{-3}$ | $5.59\times10^{-3}$ | $4.92\times10^{-3}$ | $5.34\times10^{-3}$ | $5.59\times10^{-3}$ |
| | **Type #2** | $2.21\times10^{-3}$ | $2.23\times10^{-3}$ | $2.25\times10^{-3}$ | $7.04\times10^{-1}$ | $7.05\times10^{-1}$ | $7.05\times10^{-1}$ |
| | **Type #3** | $1.80\times10^{-3}$ | $1.64\times10^{-3}$ | $1.99\times10^{-3}$ | $1.69\times10^{-3}$ | $1.57\times10^{-3}$ | $1.96\times10^{-3}$ |
| | **Type #4** | $1.54\times10^{-3}$ | $1.54\times10^{-3}$ | $1.54\times10^{-3}$ | $1.10\times10^{-2}$ | $1.11\times10^{-2}$ | $1.40\times10^{-2}$ |

Table 5.4.10 RMSE values (radian) for medium payload under backstepping control with/without payload estimator, tracking trajectory 4

| | | Estimator OFF | | | Estimator ON | | |
|---|---|---|---|---|---|---|---|
| **Controller Payload (kg)** | | 0.5 | | | 0.5 | | |
| **Actual Payload (kg)** | | 0.1 | 0.5 | 0.9 | 0.1 | 0.5 | 0.9 |
| **Pneum Mode** | **Type #1** | $3.89\times10^{-2}$ | $1.33\times10^{-1}$ | $1.62\times10^{-1}$ | $4.13\times10^{-2}$ | $1.34\times10^{-1}$ | $1.28\times10^{-1}$ |
| | **Type #3** | $3.80\times10^{-2}$ | $1.24\times10^{-1}$ | $2.08\times10^{-1}$ | $2.90\times10^{-2}$ | $1.85\times10^{-1}$ | $1.70\times10^{-1}$ |
| **Hybrid Mode** | **Type #1** | $1.32\times10^{-2}$ | $8.33\times10^{-2}$ | $1.04\times10^{-1}$ | $1.48\times10^{-2}$ | $1.10\times10^{-1}$ | $1.22\times10^{-1}$ |
| | **Type #2** | $1.19\times10^{-2}$ | $5.81\times10^{-2}$ | $9.47\times10^{-2}$ | $1.11\times10^{-2}$ | $7.51\times10^{-2}$ | $1.11\times10^{-1}$ |
| | **Type #3** | $1.52\times10^{-2}$ | $1.90\times10^{-2}$ | $1.39\times10^{-1}$ | $1.25\times10^{-2}$ | $1.12\times10^{-1}$ | $1.30\times10^{-1}$ |
| | **Type #4** | $1.50\times10^{-2}$ | $1.75\times10^{-2}$ | $1.27\times10^{-1}$ | $1.20\times10^{-1}$ | $3.57\times10^{-1}$ | $1.32\times10^{-1}$ |

Table 5.4.11 RMSE values (radian) for large payload under backstepping control with/without payload estimator, tracking trajectory 1

| | | Estimator OFF | | | Estimator ON | | |
|---|---|---|---|---|---|---|---|
| Controller Payload (kg) | | 0.8 | | | 0.8 | | |
| Actual Payload (kg) | | 0.4 | 0.8 | 1.2 | 0.4 | 0.8 | 1.2 |
| Pneum Mode | Type #1 | $4.67 \times 10^{-3}$ | $4.91 \times 10^{-3}$ | $5.14 \times 10^{-3}$ | $4.67 \times 10^{-3}$ | $4.91 \times 10^{-3}$ | $5.13 \times 10^{-3}$ |
| | Type #3 | $1.60 \times 10^{-3}$ | $1.51 \times 10^{-3}$ | $1.52 \times 10^{-3}$ | $1.59 \times 10^{-3}$ | $1.52 \times 10^{-3}$ | $1.53 \times 10^{-3}$ |
| Hybrid Mode | Type #1 | $3.98 \times 10^{-3}$ | $4.18 \times 10^{-3}$ | $4.31 \times 10^{-3}$ | $3.98 \times 10^{-3}$ | $4.18 \times 10^{-3}$ | $4.31 \times 10^{-3}$ |
| | Type #2 | $2.10 \times 10^{-3}$ | $2.11 \times 10^{-3}$ | $2.12 \times 10^{-3}$ | $7.00 \times 10^{-1}$ | $7.04 \times 10^{-1}$ | $7.04 \times 10^{-1}$ |
| | Type #3 | $1.60 \times 10^{-3}$ | $1.47 \times 10^{-3}$ | $1.47 \times 10^{-3}$ | $1.56 \times 10^{-3}$ | $1.44 \times 10^{-3}$ | $1.44 \times 10^{-3}$ |
| | Type #4 | $1.63 \times 10^{-3}$ | $1.64 \times 10^{-3}$ | $1.64 \times 10^{-3}$ | $1.22 \times 10^{-2}$ | $1.55 \times 10^{-2}$ | $1.20 \times 10^{-2}$ |

Table 5.4.12 RMSE values (radian) for large payload under backstepping control with/without payload estimator, tracking trajectory 4

| | | Estimator OFF | | | Estimator ON | | |
|---|---|---|---|---|---|---|---|
| Controller Payload (kg) | | 0.8 | | | 0.8 | | |
| Actual Payload (kg) | | 0.4 | 0.8 | 1.2 | 0.4 | 0.8 | 1.2 |
| Pneum Mode | Type #1 | $9.48 \times 10^{-2}$ | $1.58 \times 10^{-1}$ | $1.65 \times 10^{-1}$ | $1.31 \times 10^{-1}$ | $1.29 \times 10^{-1}$ | $1.25 \times 10^{-1}$ |
| | Type #3 | $2.18 \times 10^{-2}$ | $1.76 \times 10^{-1}$ | $5.65 \times 10^{-1}$ | $1.98 \times 10^{-1}$ | $1.74 \times 10^{-1}$ | $1.65 \times 10^{-1}$ |
| Hybrid Mode | Type #1 | $5.29 \times 10^{-2}$ | $9.92 \times 10^{-2}$ | $1.07 \times 10^{-1}$ | $9.32 \times 10^{-2}$ | $1.21 \times 10^{-1}$ | $1.23 \times 10^{-1}$ |
| | Type #2 | $1.66 \times 10^{-2}$ | $8.71 \times 10^{-2}$ | $9.83 \times 10^{-2}$ | $3.60 \times 10^{-2}$ | $1.06 \times 10^{-1}$ | $1.17 \times 10^{-1}$ |
| | Type #3 | $2.30 \times 10^{-2}$ | $9.82 \times 10^{-2}$ | $1.06 \times 10^{-1}$ | $8.73 \times 10^{-2}$ | $1.25 \times 10^{-1}$ | $1.29 \times 10^{-1}$ |
| | Type #4 | $2.37 \times 10^{-2}$ | $2.33 \times 10^{-2}$ | $1.42 \times 10^{-1}$ | $4.00 \times 10^{-1}$ | $4.52 \times 10^{-1}$ | $1.40 \times 10^{-1}$ |

### 5.4.1.3   DVMPC

The DVMPC has two control types that need to be tested as listed in Table 5.4.13. Both control types will be simulated for trajectories 1 and 4. The same payload mismatch cases as before will be used.

The results are listed in Table 5.4.14. The DVMPC + IDC (type #1) reduced RMSE values significantly compared with type #2. However, regarding the robustness, these two modes are almost identical for trajectory 1 tracking. The IDC was tuned for zero payload, the smaller payload situations tended to have superior tracking performance over the larger payloads without mismatch. With trajectory 4, the RMSE values greater than 0.1 were produced by unstable responses. Although the prediction horizon was tuned at 40 for zero payloads in last section, the only stable case for type #2 was with the 0.1kg actual payload and controller payloads of 0.2 or 0.5 kg.

The DVMPC is not as robust as the backstepping controller. Although both of these two controllers were tuned for the zero payload, the DVMPC was much more sensitive to mismatch. However, the DVMPC did have an advantage in tracking performance. For example, in trajectory 1, the RMSE values averaged around $1 \times 10^{-4}$ compared to $1.4 \times 10^{-3}$ for the backstepping controller.

Table 5.4.13 DVMPC mode list

| DVMPC Type | Number |
|---|---|
| DVMPC+IDC, in hybrid mode | 1 |
| DVMPC only, in pneumatic mode | 2 |

Table 5.4.14 RMSE values (radian) for a range of payloads and mismatch cases under DVMPC

| | Trajectory 1 | | | Trajectory 4 | | |
|---|---|---|---|---|---|---|
| **Controller Payload(kg)** | 0.2 | | | 0.2 | | |
| **Actual Payload (kg)** | 0.1 | 0.2 | 0.3 | 0.1 | 0.2 | 0.3 |
| **Type #1** | $2.61\times10^{-4}$ | $2.60\times10^{-4}$ | $2.43\times10^{-4}$ | $2.14\times10^{-3}$ | $3.81\times10^{-3}$ | $6.49\times10^{-3}$ |
| **Type #2** | $8.09\times10^{-4}$ | $9.07\times10^{-4}$ | $9.02\times10^{-4}$ | $4.12\times10^{-1}$ | $3.58\times10^{-1}$ | $3.19\times10^{-1}$ |
| | **Trajectory 1** | | | **Trajectory 4** | | |
| **Controller Payload(kg)** | 0.5 | | | 0.5 | | |
| **Actual Payload (kg)** | 0.1 | 0.5 | 0.9 | 0.1 | 0.5 | 0.9 |
| **Type #1** | $3.11\times10^{-4}$ | $3.09\times10^{-4}$ | $3.02\times10^{-4}$ | $3.31\times10^{-3}$ | $2.91\times10^{-1}$ | $2.27\times10^{-1}$ |
| **Type #2** | $3.82\times10^{-4}$ | $4.81\times10^{-4}$ | $4.97\times10^{-4}$ | $4.39\times10^{-1}$ | $2.63\times10^{-1}$ | $2.08\times10^{-1}$ |
| | **Trajectory 1** | | | **Trajectory 4** | | |
| **Controller Payload(kg)** | 0.8 | | | 0.8 | | |
| **Actual Payload (kg)** | 0.4 | 0.8 | 1.2 | 0.4 | 0.8 | 1.2 |
| **Type #1** | $3.38\times10^{-4}$ | $3.38\times10^{-4}$ | $3.36\times10^{-4}$ | $3.17\times10^{-1}$ | $2.40\times10^{-1}$ | $2.01\times10^{-1}$ |
| **Type #2** | $2.95\times10^{-4}$ | $3.30\times10^{-4}$ | $3.25\times10^{-4}$ | $2.86\times10^{-1}$ | $2.19\times10^{-1}$ | $1.84\times10^{-1}$ |

## 5.4.1.4  DVMPC with Payload Estimator

In this section, simulations will be performed for DVMPC type #1 with the payload estimator on.  The simulation parameters remained the same as the previous section. The valve model for discrete valve input was included in the simulated plant.

The RMSE values are listed in Table 5.4.15. The payload estimation helped to reduce the RMSE in nominal payload when the actual payload is 0.1 kg (trajectory 4). However, in most cases, the payload estimation was not helpful. Recall that the payload estimation was proposed based on the torque error which was calculated by the difference between actual total actuation torque and the desired torque. Normally, the horizontal configuration will have a smaller desired torque because it has only friction torque and the torque needed to produce the angular acceleration. The pneumatic cylinder torque fluctuations may make the torque error estimation inaccurate. The threshold of the payload estimation is therefore difficult to be determined. This explains why in trajectory 1 the performances with estimator on and off are identical. The simulation results suggest that payload estimation is not suitable for DVMPC in the horizontal configuration.

Table 5.4.15 RMSE values (radian) for a range of payloads and mismatch cases under DVMPC with payload estimation

| | Trajectory 1 | | | Trajectory 4 | | |
|---|---|---|---|---|---|---|
| **Controller Payload(kg)** | 0.2 | | | 0.2 | | |
| **Actual Payload (kg)** | 0.1 | 0.2 | 0.3 | 0.1 | 0.2 | 0.3 |
| **Estimator ON** | $4.24\times10^{-4}$ | $4.23\times10^{-4}$ | $4.23\times10^{-4}$ | $2.2\times10^{-3}$ | $3.9\times10^{-3}$ | $8.5\times10^{-3}$ |
| **Estimator OFF** | $4.24\times10^{-4}$ | $4.23\times10^{-4}$ | $4.23\times10^{-4}$ | $2.3\times10^{-3}$ | $3.9\times10^{-3}$ | $6.6\times10^{-3}$ |
| | **Trajectory 1** | | | **Trajectory 4** | | |
| **Controller Payload(kg)** | 0.5 | | | 0.5 | | |
| **Actual Payload (kg)** | 0.1 | 0.5 | 0.9 | 0.1 | 0.5 | 0.9 |
| **Estimator ON** | $4.25\times10^{-4}$ | $4.23\times10^{-4}$ | $4.23\times10^{-4}$ | $2.9\times10^{-3}$ | 0.28 | 0.22 |
| **Estimator OFF** | $4.25\times10^{-4}$ | $4.23\times10^{-4}$ | $4.23\times10^{-4}$ | $3.4\times10^{-3}$ | 0.29 | 0.23 |
| | **Trajectory 1** | | | **Trajectory 4** | | |
| **Controller Payload(kg)** | 0.8 | | | 0.8 | | |
| **Actual Payload (kg)** | 0.4 | 0.8 | 1.2 | 0.4 | 0.8 | 1.2 |
| **Estimator ON** | $4.24\times10^{-4}$ | $4.24\times10^{-4}$ | $4.23\times10^{-4}$ | 0.31 | 0.23 | 0.2 |
| **Estimator OFF** | $4.24\times10^{-4}$ | $4.24\times10^{-4}$ | $4.23\times10^{-4}$ | 0.32 | 0.24 | 0.2 |

**5.4.2    Vertical Configuration with Payload Mismatch**

The vertical configuration of the hybrid actuator system was modeled in Chapter 3. In such configuration, the gravity torque greatly increases the desired torque making the servo control more difficult. The payload mismatch in the horizontal configuration was simulated in previous section. Trajectories used for the vertical configuration were slightly different those used previously due to the gravity torque as shown in Figure 5.5.
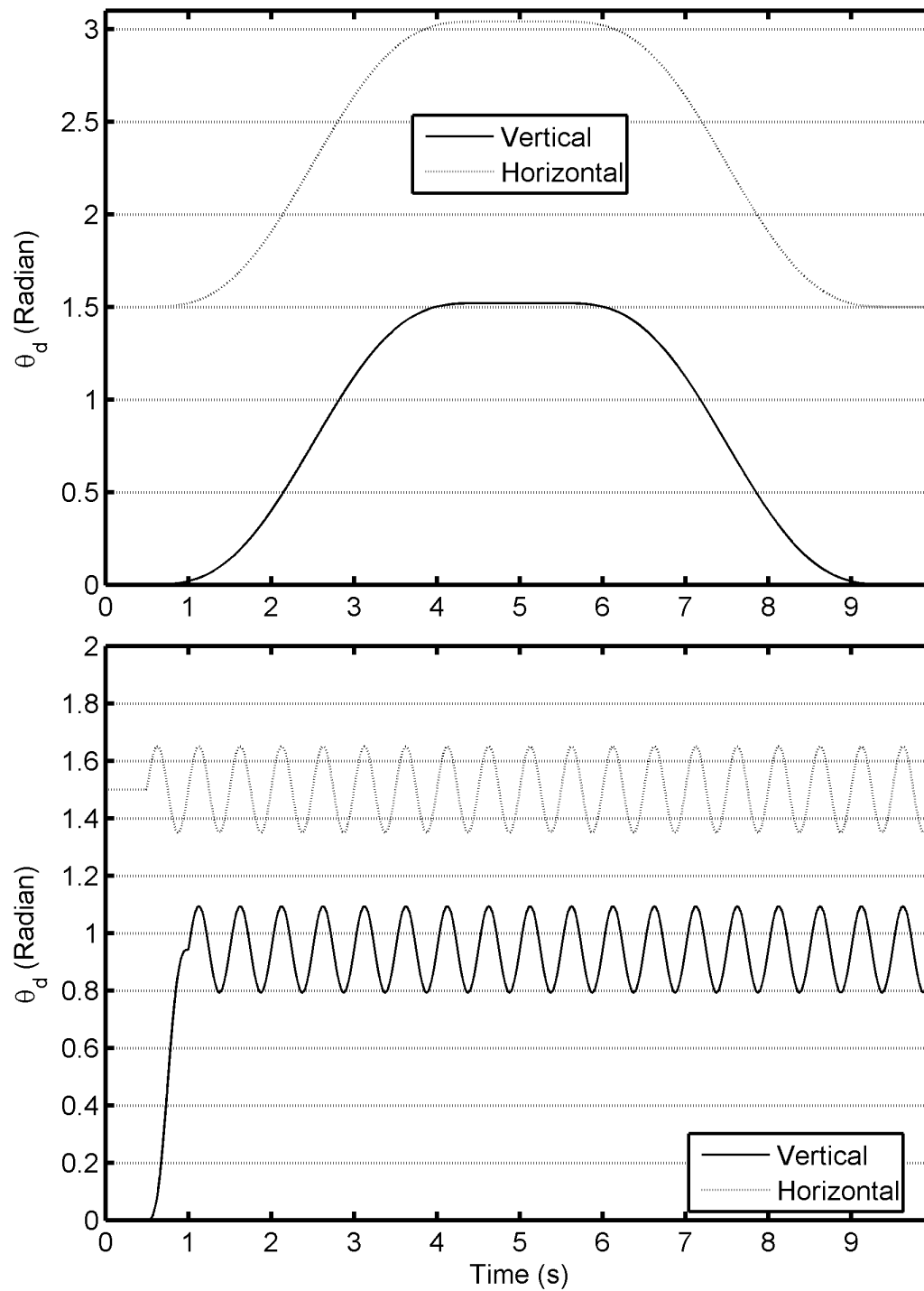
Figure 5.5 Trajectories used in vertical and horizontal configurations.

### 5.4.2.1   Backstepping Control

The same backstepping control types will be simulated. The RMSE value results are listed Table 5.4.16 to Table 5.4.18. When the tracking was stable, compared to the horizontal configuration the RMSE increased by 40% to 500% (within $10^{-3}$ radian).

Based on the Table 5.4.16 results, the RMSE values were not greatly affected by the changes in payload when the nominal payload was small. Controller type #4 had the smallest RMSE values.

Based on the Table 5.4.17 results, the normal payload case demonstrated the robustness of the backstepping controller type #4. The 0.1 kg payload is within the load capability of hybrid actuator. Although controller expected a 0.5 kg payload, the tracking RMSE for trajectory 1 and 4 was similar for the 0.1 kg and 0.5 kg payloads. Obviously, the 0.9 kg payload was beyond the maximum load that the hybrid actuator could stably control.

The large payload case had the worst performance as shown by the Table 5.4.18 results. This was caused by exceeding of the maximum load capacity. The backstepping controller type #4 was the only one capable of stabilizing the tracking with a 0.4 kg payload.

Table 5.4.16 RMSE value (radian) of small payload mismatch cases under backstepping control

| | | Trajectory 1 | | | Trajectory 4 | | |
|---|---|---|---|---|---|---|---|
| **Controller Payload (kg)** | | 0.2 | | | 0.2 | | |
| **Actual Payload (kg)** | | 0.1 | 0.2 | 0.3 | 0.1 | 0.2 | 0.3 |
| **Pneum Mode** | **Type #1** | $1.60{\times}10^{-2}$ | $6.84{\times}10^{-2}$ | $5.00{\times}10^{-1}$ | $9.20{\times}10^{-2}$ | $1.58{\times}10^{-1}$ | $4.89{\times}10^{-1}$ |
| | **Type #3** | $1.35{\times}10^{-2}$ | $6.85{\times}10^{-3}$ | $4.71{\times}10^{-3}$ | $7.99{\times}10^{-2}$ | $6.95{\times}10^{-2}$ | $1.14{\times}10^{-1}$ |
| **Hybrid Mode** | **Type #1** | $1.24{\times}10^{-2}$ | $1.71{\times}10^{-2}$ | $2.88{\times}10^{-2}$ | $3.17{\times}10^{-2}$ | $5.37{\times}10^{-2}$ | $7.87{\times}10^{-2}$ |
| | **Type #2** | $2.79{\times}10^{-3}$ | $4.40{\times}10^{-3}$ | $9.81{\times}10^{-3}$ | $1.45{\times}10^{-2}$ | $3.78{\times}10^{-2}$ | $7.38{\times}10^{-2}$ |
| | **Type #3** | $1.37{\times}10^{-2}$ | $8.01{\times}10^{-3}$ | $3.69{\times}10^{-3}$ | $1.81{\times}10^{-2}$ | $1.75{\times}10^{-2}$ | $2.15{\times}10^{-2}$ |
| | **Type #4** | $3.08{\times}10^{-3}$ | $2.24{\times}10^{-3}$ | $1.79{\times}10^{-3}$ | $1.64{\times}10^{-2}$ | $2.36{\times}10^{-2}$ | $3.06{\times}10^{-2}$ |

Table 5.4.17 RMSE value (radian) of normal payload mismatch cases under backstepping control

| | | Trajectory 1 | | | Trajectory 4 | | |
|---|---|---|---|---|---|---|---|
| **Controller Payload (kg)** | | 0.5 | | | 0.5 | | |
| **Actual Payload (kg)** | | 0.1 | 0.5 | 0.9 | 0.1 | 0.5 | 0.9 |
| **Pneum Mode** | **Type #1** | $6.47{\times}10^{-3}$ | $6.60{\times}10^{-1}$ | $7.99{\times}10^{-1}$ | $6.65{\times}10^{-2}$ | $7.15{\times}10^{-1}$ | $8.02{\times}10^{-1}$ |
| | **Type #3** | $1.90{\times}10^{-2}$ | $4.73{\times}10^{-3}$ | $4.72{\times}10^{-1}$ | $6.87{\times}10^{-2}$ | $2.87{\times}10^{-1}$ | $5.35{\times}10^{-1}$ |
| **Hybrid Mode** | **Type #1** | $5.45{\times}10^{-3}$ | $7.10{\times}10^{-2}$ | $5.86{\times}10^{-1}$ | $1.73{\times}10^{-2}$ | $2.61{\times}10^{-1}$ | $5.18{\times}10^{-1}$ |
| | **Type #2** | $2.42{\times}10^{-3}$ | $4.19{\times}10^{-2}$ | $5.74{\times}10^{-1}$ | $1.19{\times}10^{-2}$ | $2.58{\times}10^{-1}$ | $5.16{\times}10^{-1}$ |
| | **Type #3** | $1.87{\times}10^{-2}$ | $4.22{\times}10^{-3}$ | $3.38{\times}10^{-1}$ | $2.36{\times}10^{-2}$ | $9.10{\times}10^{-2}$ | $3.48{\times}10^{-1}$ |
| | **Type #4** | $8.31{\times}10^{-3}$ | $2.02{\times}10^{-3}$ | $3.39{\times}10^{-1}$ | $1.79{\times}10^{-2}$ | $4.54{\times}10^{-2}$ | $3.47{\times}10^{-1}$ |

Table 5.4.18 RMSE value (radian) of large payload mismatch cases under backstepping control

| | | Trajectory 1 | | | Trajectory 4 | | |
|---|---|---|---|---|---|---|---|
| **Controller Payload (kg)** | | 0.8 | | | 0.8 | | |
| **Actual Payload (kg)** | | 0.4 | 0.8 | 1.2 | 0.4 | 0.8 | 1.2 |
| **Pneum Mode** | **Type #1** | $2.84 \times 10^{-1}$ | $7.74 \times 10^{-1}$ | $8.44 \times 10^{-1}$ | $6.04 \times 10^{-1}$ | $7.78 \times 10^{-1}$ | $8.20 \times 10^{-1}$ |
| | **Type #3** | $1.05 \times 10^{-2}$ | $4.34 \times 10^{-1}$ | $6.21 \times 10^{-1}$ | $1.94 \times 10^{-1}$ | $5.41 \times 10^{-1}$ | $6.29 \times 10^{-1}$ |
| **Hybrid Mode** | **Type #1** | $1.20 \times 10^{-2}$ | $4.22 \times 10^{-1}$ | $6.81 \times 10^{-1}$ | $1.95 \times 10^{-1}$ | $5.10 \times 10^{-1}$ | $6.29 \times 10^{-1}$ |
| | **Type #2** | $2.50 \times 10^{-3}$ | $6.11 \times 10^{-1}$ | $6.78 \times 10^{-1}$ | $1.94 \times 10^{-1}$ | $5.10 \times 10^{-1}$ | $6.27 \times 10^{-1}$ |
| | **Type #3** | $1.13 \times 10^{-2}$ | $2.78 \times 10^{-1}$ | $4.49 \times 10^{-1}$ | $3.28 \times 10^{-2}$ | $3.22 \times 10^{-1}$ | $4.87 \times 10^{-1}$ |
| | **Type #4** | $3.08 \times 10^{-3}$ | $2.79 \times 10^{-1}$ | $4.51 \times 10^{-1}$ | $2.43 \times 10^{-2}$ | $3.20 \times 10^{-1}$ | $4.85 \times 10^{-1}$ |

### 5.4.2.2   Backstepping Control with Payload Estimator

The results presented in section 5.4.1.2 showed that the payload estimator was not helpful in the horizontal configuration. However, as it was designed for payload gravity torque compensation, the estimator should be helpful when the actuator operates in the vertical configuration.

The same backstepping control types were simulated with and without the estimator. The simulated RMSE values are listed in Table 5.4.19 to Table 5.4.24. When the payload was within the maximum load capacity of the hybrid actuator and the

trajectory was slowly varying, the improvement is obvious. In trajectory 1 hybrid mode, with all types of backstepping control the RMSE values were reduced by about 50% when the actual payload was less than 0.4 kg.  However, the performance with the estimator was not consistent with the backstepping controller due to the slow convergence speed of the estimation. With the rapidly changing trajectory 4, the tracking performance was degraded by more than 50% in average.

Table 5.4.19 RMSE values (radian) for small payload under backstepping control with/without payload estimator, tracking trajectory 1

| | | Estimator OFF | | | Estimator ON | | |
|---|---|---|---|---|---|---|---|
| **Controller Payload (kg)** | | 0.2 | | | 0.2 | | |
| **Actual Payload (kg)** | | 0.1 | 0.2 | 0.3 | 0.1 | 0.2 | 0.3 |
| **Pneum Mode** | **Type #1** | $1.60\times10^{-2}$ | $6.61\times10^{-2}$ | $5.00\times10^{-1}$ | $1.77\times10^{-2}$ | $6.73\times10^{-2}$ | $5.00\times10^{-1}$ |
| | **Type #3** | $1.35\times10^{-2}$ | $6.85\times10^{-3}$ | $4.71\times10^{-3}$ | $1.44\times10^{-2}$ | $6.71\times10^{-3}$ | $4.00\times10^{-3}$ |
| **Hybrid Mode** | **Type #1** | $1.24\times10^{-2}$ | $1.71\times10^{-2}$ | $2.88\times10^{-2}$ | $3.65\times10^{-3}$ | $3.54\times10^{-3}$ | $3.37\times10^{-3}$ |
| | **Type #2** | $2.79\times10^{-3}$ | $4.40\times10^{-3}$ | $9.81\times10^{-3}$ | $1.89\times10^{-3}$ | $2.01\times10^{-3}$ | $2.03\times10^{-3}$ |
| | **Type #3** | $1.37\times10^{-2}$ | $8.01\times10^{-3}$ | $3.70\times10^{-3}$ | $1.44\times10^{-2}$ | $7.70\times10^{-3}$ | $7.30\times10^{-3}$ |
| | **Type #4** | $3.08\times10^{-3}$ | $2.24\times10^{-3}$ | $1.79\times10^{-3}$ | $2.07\times10^{-3}$ | $2.08\times10^{-3}$ | $1.84\times10^{-3}$ |

Table 5.4.20 RMSE values (radian) for small payload under backstepping control with/without payload estimator, tracking trajectory 4

| | | Estimator OFF | | | Estimator ON | | |
|---|---|---|---|---|---|---|---|
| **Controller Payload (kg)** | | 0.2 | | | 0.2 | | |
| **Actual Payload (kg)** | | 0.1 | 0.2 | 0.3 | 0.1 | 0.2 | 0.3 |
| **Pneum Mode** | **Type #1** | $9.09{\times}10^{-2}$ | $1.58{\times}10^{-1}$ | $4.89{\times}10^{-1}$ | $1.91{\times}10^{-1}$ | $2.83{\times}10^{-1}$ | $5.84{\times}10^{-1}$ |
| | **Type #3** | $8.38{\times}10^{-2}$ | $7.19{\times}10^{-2}$ | $1.13{\times}10^{-1}$ | $7.35{\times}10^{-2}$ | $6.99{\times}10^{-2}$ | $1.14{\times}10^{-1}$ |
| **Hybrid Mode** | **Type #1** | $3.18{\times}10^{-2}$ | $5.35{\times}10^{-2}$ | $7.87{\times}10^{-2}$ | $4.28{\times}10^{-1}$ | $9.03{\times}10^{-1}$ | $9.10{\times}10^{-1}$ |
| | **Type #2** | $1.45{\times}10^{-2}$ | $3.78{\times}10^{-2}$ | $7.31{\times}10^{-2}$ | $1.40{\times}10^{-2}$ | $1.75{\times}10^{-2}$ | $1.67{\times}10^{-1}$ |
| | **Type #3** | $1.80{\times}10^{-2}$ | $1.84{\times}10^{-2}$ | $2.16{\times}10^{-2}$ | $2.35{\times}10^{-1}$ | $1.94{\times}10^{-1}$ | $1.90{\times}10^{-1}$ |
| | **Type #4** | $8.04{\times}10^{-3}$ | $2.13{\times}10^{-2}$ | $2.74{\times}10^{-2}$ | $7.31{\times}10^{-2}$ | $7.97{\times}10^{-2}$ | $1.06{\times}10^{-1}$ |

Table 5.4.21 RMSE values (radian) for medium payload under backstepping control with/without payload estimator, tracking trajectory 1

| | | Estimator OFF | | | Estimator ON | | |
|---|---|---|---|---|---|---|---|
| **Controller Payload (kg)** | | 0.5 | | | 0.5 | | |
| **Actual Payload (kg)** | | 0.1 | 0.5 | 0.9 | 0.1 | 0.5 | 0.9 |
| **Pneum Mode** | **Type #1** | $6.46{\times}10^{-3}$ | $6.60{\times}10^{-1}$ | $7.99{\times}10^{-1}$ | $1.92{\times}10^{-2}$ | $6.58{\times}10^{-1}$ | $7.99{\times}10^{-1}$ |
| | **Type #3** | $1.91{\times}10^{-2}$ | $4.73{\times}10^{-3}$ | $4.72{\times}10^{-1}$ | $9.38{\times}10^{-3}$ | $4.51{\times}10^{-3}$ | $5.52{\times}10^{-1}$ |
| **Hybrid Mode** | **Type #1** | $5.44{\times}10^{-3}$ | $7.10{\times}10^{-2}$ | $5.86{\times}10^{-1}$ | $2.56{\times}10^{-3}$ | $5.82{\times}10^{-3}$ | $6.56{\times}10^{-1}$ |
| | **Type #2** | $2.42{\times}10^{-3}$ | $4.19{\times}10^{-2}$ | $5.74{\times}10^{-1}$ | $1.88{\times}10^{-3}$ | $3.90{\times}10^{-3}$ | $6.56{\times}10^{-1}$ |
| | **Type #3** | $1.87{\times}10^{-2}$ | $4.22{\times}10^{-3}$ | $3.38{\times}10^{-1}$ | $1.09{\times}10^{-2}$ | $5.07{\times}10^{-3}$ | $3.88{\times}10^{-1}$ |
| | **Type #4** | $8.31{\times}10^{-3}$ | $2.02{\times}10^{-3}$ | $3.39{\times}10^{-1}$ | $1.90{\times}10^{-3}$ | $1.97{\times}10^{-3}$ | $3.89{\times}10^{-1}$ |

Table 5.4.22 RMSE values (radian) for medium payload under backstepping control with/without payload estimator, tracking trajectory 4

| | | Estimator OFF | | | Estimator ON | | |
|---|---|---|---|---|---|---|---|
| **Controller Payload (kg)** | | 0.5 | | | 0.5 | | |
| **Actual Payload (kg)** | | 0.1 | 0.5 | 0.9 | 0.1 | 0.5 | 0.9 |
| **Pneum Mode** | **Type #1** | $6.58\times10^{-2}$ | $7.16\times10^{-1}$ | $8.02\times10^{-1}$ | $1.14\times10^{-1}$ | $7.76\times10^{-1}$ | $8.20\times10^{-1}$ |
| | **Type #3** | $7.60\times10^{-2}$ | $2.86\times10^{-1}$ | $5.35\times10^{-1}$ | $6.57\times10^{-2}$ | $3.19\times10^{-1}$ | $6.24\times10^{-1}$ |
| **Hybrid Mode** | **Type #1** | $1.82\times10^{-2}$ | $2.61\times10^{-1}$ | $5.18\times10^{-1}$ | $9.10\times10^{-1}$ | $9.09\times10^{-1}$ | $6.82\times10^{-1}$ |
| | **Type #2** | $1.19\times10^{-2}$ | $2.58\times10^{-1}$ | $5.17\times10^{-1}$ | $1.40\times10^{-2}$ | $3.93\times10^{-1}$ | $6.05\times10^{-1}$ |
| | **Type #3** | $2.37\times10^{-2}$ | $9.12\times10^{-2}$ | $3.49\times10^{-1}$ | $1.61\times10^{-1}$ | $1.43\times10^{-1}$ | $4.97\times10^{-1}$ |
| | **Type #4** | $2.03\times10^{-2}$ | $4.70\times10^{-2}$ | $3.48\times10^{-1}$ | $1.13\times10^{-1}$ | $2.31\times10^{-1}$ | $5.11\times10^{-1}$ |

Table 5.4.23 RMSE values (radian) for large payload under backstepping control with/without payload estimator, tracking trajectory 1

| | | Estimator OFF | | | Estimator ON | | |
|---|---|---|---|---|---|---|---|
| **Controller Payload (kg)** | | 0.8 | | | 0.8 | | |
| **Actual Payload (kg)** | | 0.4 | 0.8 | 1.2 | 0.4 | 0.8 | 1.2 |
| **Pneum Mode** | **Type #1** | $2.85\times10^{-1}$ | $7.74\times10^{-1}$ | $8.44\times10^{-1}$ | $3.70\times10^{-1}$ | $7.72\times10^{-1}$ | $8.44\times10^{-1}$ |
| | **Type #3** | $1.05\times10^{-2}$ | $4.34\times10^{-1}$ | $6.21\times10^{-1}$ | $5.38\times10^{-3}$ | $5.08\times10^{-1}$ | $7.45\times10^{-1}$ |
| **Hybrid Mode** | **Type #1** | $1.20\times10^{-2}$ | $4.22\times10^{-1}$ | $6.81\times10^{-1}$ | $3.42\times10^{-3}$ | $6.38\times10^{-1}$ | $7.05\times10^{-1}$ |
| | **Type #2** | $2.50\times10^{-3}$ | $6.11\times10^{-1}$ | $6.78\times10^{-1}$ | $1.98\times10^{-3}$ | $6.39\times10^{-1}$ | $7.03\times10^{-1}$ |
| | **Type #3** | $1.13\times10^{-2}$ | $2.78\times10^{-1}$ | $4.49\times10^{-1}$ | $7.99\times10^{-3}$ | $3.31\times10^{-1}$ | $5.09\times10^{-1}$ |
| | **Type #4** | $3.08\times10^{-3}$ | $2.79\times10^{-1}$ | $4.51\times10^{-1}$ | $1.89\times10^{-3}$ | $3.30\times10^{-1}$ | $5.06\times10^{-1}$ |

Table 5.4.24 RMSE values (radian) for large payload under backstepping control with/without payload estimator, tracking trajectory 4

| | | Estimator OFF | | | Estimator ON | | |
|---|---|---|---|---|---|---|---|
| **Controller Payload (kg)** | | 0.8 | | | 0.8 | | |
| **Actual Payload (kg)** | | 0.4 | 0.8 | 1.2 | 0.4 | 0.8 | 1.2 |
| **Pneum Mode** | **Type #1** | $6.07{\times}10^{-1}$ | $7.78{\times}10^{-1}$ | $8.20{\times}10^{-1}$ | $6.09{\times}10^{-1}$ | $8.09{\times}10^{-1}$ | $8.36{\times}10^{-1}$ |
| | **Type #3** | $1.95{\times}10^{-1}$ | $5.39{\times}10^{-1}$ | $6.29{\times}10^{-1}$ | $1.43{\times}10^{-1}$ | $5.67{\times}10^{-1}$ | $6.99{\times}10^{-1}$ |
| **Hybrid Mode** | **Type #1** | $1.95{\times}10^{-1}$ | $5.10{\times}10^{-1}$ | $6.29{\times}10^{-1}$ | $5.57{\times}10^{-1}$ | $6.06{\times}10^{-1}$ | $6.87{\times}10^{-1}$ |
| | **Type #2** | $1.95{\times}10^{-1}$ | $5.10{\times}10^{-1}$ | $6.27{\times}10^{-1}$ | $2.97{\times}10^{-1}$ | $5.70{\times}10^{-1}$ | $6.73{\times}10^{-1}$ |
| | **Type #3** | $3.34{\times}10^{-2}$ | $3.21{\times}10^{-1}$ | $4.85{\times}10^{-1}$ | $1.18{\times}10^{-1}$ | $4.46{\times}10^{-1}$ | $5.98{\times}10^{-1}$ |
| | **Type #4** | $2.44{\times}10^{-2}$ | $3.17{\times}10^{-1}$ | $4.84{\times}10^{-1}$ | $1.87{\times}10^{-1}$ | $4.68{\times}10^{-1}$ | $6.09{\times}10^{-1}$ |

### 5.4.2.3  DVMPC

The results for DVMPC in the vertical configuration with various payloads and mismatches are listed in Table 5.4.25.  The performances with the small payload were much less robust than the horizontal configuration. When the controller payload matched the actual payload, the RMSE was significantly reduced in both trajectories 1 and 4. The normal payload case reiterated this situation in trajectory 1, especially when the actual payload was smaller than the payload used by the controller. However, when the actual payload was 0.9 kg, the tracking was not stable. The same lack of robustness was shown with trajectory 4. The controller was barely able to track a 2 Hz sine wave reference

carrying a 0.1 kg payload with payload mismatch. When the actual payload was over 0.5

kg the tracking was not stable.

Table 5.4.25 RMSE values (radian) for a range of payloads and mismatch cases
under DVMPC

| | Trajectory 1 | | | Trajectory 4 | | |
|---|---|---|---|---|---|---|
| **Controller Payload(kg)** | 0.2 | | | 0.2 | | |
| **Actual Payload (kg)** | 0.1 | 0.2 | 0.3 | 0.1 | 0.2 | 0.3 |
| **Type #1** | $4.53\times10^{-4}$ | $2.41\times10^{-4}$ | $4.80\times10^{-4}$ | $1.18\times10^{-1}$ | $3.69\times10^{-2}$ | $5.09\times10^{-2}$ |
| **Type #2** | $2.33\times10^{-3}$ | $7.61\times10^{-2}$ | $7.66\times10^{-2}$ | $7.41\times10^{-2}$ | $4.07\times10^{-1}$ | $3.64\times10^{-1}$ |
| | **Trajectory 1** | | | **Trajectory 4** | | |
| **Controller Payload(kg)** | 0.5 | | | 0.5 | | |
| **Actual Payload (kg)** | 0.1 | 0.5 | 0.9 | 0.1 | 0.5 | 0.9 |
| **Type #1** | $2.12\times10^{-3}$ | $3.19\times10^{-4}$ | $1.37\times10^{-1}$ | $9.27\times10^{-2}$ | $3.45\times10^{-1}$ | $2.91\times10^{-1}$ |
| **Type #2** | $7.60\times10^{-2}$ | $8.41\times10^{-2}$ | $3.53\times10^{-1}$ | $2.04\times10^{-1}$ | $3.02\times10^{-1}$ | $2.83\times10^{-1}$ |
| | **Trajectory 1** | | | **Trajectory 4** | | |
| **Controller Payload(kg)** | 0.8 | | | 0.8 | | |
| **Actual Payload (kg)** | 0.4 | 0.8 | 1.2 | 0.4 | 0.8 | 1.2 |
| **Type #1** | $1.26\times10^{-3}$ | $1.65\times10^{-2}$ | $3.76\times10^{-1}$ | $3.63\times10^{-1}$ | $3.41\times10^{-1}$ | $2.13\times10^{-1}$ |
| **Type #2** | $8.10\times10^{-2}$ | $2.88\times10^{-1}$ | $5.26\times10^{-1}$ | $3.36\times10^{-1}$ | $4.18\times10^{-1}$ | $4.18\times10^{-1}$ |

### 5.4.2.4 DVMPC with Payload Estimator

The vertical configuration assessment of the estimator was simulated in this section. The RMSE results are listed in Table 5.4.26. Only DVMPC type 1 was simulated with and without the estimator.

In two of the 12 mismatch cases (normal controller payload and 0.1 kg actual payload; and large controller payload with 0.4 kg actual payload) the estimator produced a significant performance improvement.  In the other cases its performance was disappointing.

Table 5.4.26 RMSE value (radian) for a range of payloads and mismatch cases under DVMPC with payload estimation

| | Trajectory 1 | | | Trajectory 4 | | |
|---|---|---|---|---|---|---|
| **Controller Payload(kg)** | 0.2 | | | 0.2 | | |
| **Actual Payload (kg)** | 0.1 | 0.2 | 0.3 | 0.1 | 0.2 | 0.3 |
| **Estimator ON** | $4.65 \times 10^{-4}$ | $2.42 \times 10^{-4}$ | $4.41 \times 10^{-4}$ | $3.15 \times 10^{-3}$ | $4.93 \times 10^{-3}$ | $9.08 \times 10^{-3}$ |
| **Estimator OFF** | $4.53 \times 10^{-4}$ | $2.41 \times 10^{-4}$ | $4.80 \times 10^{-4}$ | $3.18 \times 10^{-3}$ | $4.89 \times 10^{-3}$ | $7.36 \times 10^{-3}$ |
| | Trajectory 1 | | | Trajectory 4 | | |
| **Controller Payload(kg)** | 0.5 | | | 0.5 | | |
| **Actual Payload (kg)** | 0.1 | 0.5 | 0.9 | 0.1 | 0.5 | 0.9 |
| **Estimator ON** | $3.86 \times 10^{-4}$ | $3.19 \times 10^{-4}$ | $1.31 \times 10^{-1}$ | $3.59 \times 10^{-3}$ | $3.43 \times 10^{-1}$ | $2.76 \times 10^{-1}$ |
| **Estimator OFF** | $2.12 \times 10^{-3}$ | $3.19 \times 10^{-4}$ | $1.37 \times 10^{-1}$ | $5.13 \times 10^{-3}$ | $3.38 \times 10^{-1}$ | $2.95 \times 10^{-1}$ |
| | Trajectory 1 | | | Trajectory 4 | | |
| **Controller Payload(kg)** | 0.8 | | | 0.8 | | |
| **Actual Payload (kg)** | 0.4 | 0.8 | 1.2 | 0.4 | 0.8 | 1.2 |
| **Estimator ON** | $2.96 \times 10^{-4}$ | $1.65 \times 10^{-2}$ | $3.77 \times 10^{-1}$ | $3.64 \times 10^{-1}$ | $3.43 \times 10^{-1}$ | $3.96 \times 10^{-1}$ |
| **Estimator OFF** | $1.26 \times 10^{-3}$ | $1.65 \times 10^{-2}$ | $3.76 \times 10^{-1}$ | $3.58 \times 10^{-1}$ | $3.27 \times 10^{-1}$ | $2.02 \times 10^{-1}$ |

## 5.5   Limitations of the Valve Modeling

The valve model for a discrete valve input that is used with DVMPC is relatively accurate because a single chamber pressure response was measured and fitted rather than an entire surface. The valve model for the PWM input used with the backstepping controller was modeled by measuring the chamber pressure changes for a series of PWM

inputs. The mass flow rates were estimated by numerical differentiation of the chamber pressures. Then a surface of PWM input, chamber pressure and mass flow rate was fitted by surface fitting methods.

How the accuracy of the valve model limits the performance of the backstepping control will be studied in this section. The controller will be simulated in different conditions. If the controller has low gains, the desired mass flow rate will be limited to a small number because of the low desired chamber pressure. On the other hand, when high gains are used, it is possible for the backstepping controller to saturate the valves. The low gains listed in Table 5.5.2 are identical to those used in Chapter  4. They were manually tuned to prevent the saturation of mass flow rates in the valve dynamic model. The high gains were selected to occasionally saturate the mass flow rate of the valve model.

Several sine wave trajectories (see Table 5.5.1 ) will be simulated. A similar set of sine waves were used by Rao (2005) to discuss the limitations of his valve dynamic model.  The hybrid mode with backstepping controller type 4 was chosen for the simulations, although the choice of actuation mode is not critical for studying the effects of the valve dynamics model difference. The RMSE values for the position tracking and chamber pressure tracking using the bipolynomial valve model and an ideal valve (i.e. a perfect model) are listed in Table 5.5.3.

Table 5.5.1 Trajectory list

|  | **Test trajectory** |
|---|---|
| **Trajectory 1** | Sine wave at 1Hz with 0.3 radian amplitude |
| **Trajectory 2** | Sine wave at 2Hz with 0.3 radian amplitude |
| **Trajectory 3** | Sine wave at 3Hz with 0.3 radian amplitude |
| **Trajectory 4** | Sine wave at 4Hz with 0.3 radian amplitude |

Table 5.5.2 Low and high controller gains used in simulation

| **Low Gains** | **Value** | **Unit** | **High Gains** | **Value** | **Unit** |
|---|---|---|---|---|---|
| $k_1$ | 60 | $s^{-1}$ | $k_1$ | 60 | $s^{-1}$ |
| $k_2$ | 20 | $s^{-1}$ | $k_2$ | 20 | $s^{-1}$ |
| $k_3$ | 65 | $s^{-1}$ | $k_3$ | 165 | $s^{-1}$ |
| $k_4$ | 65 | $s^{-1}$ | $k_4$ | 165 | $s^{-1}$ |

With the small gains, the valve model was relatively accurate since the desired mass flow rates did not saturate the valves. The difference of the RMSE values was relatively small. When using ideal valve models, the RMSE reduced about 60% for chamber pressure tracking, and around 20% for position tracking.

With the high gains, the ideal valve produced a consistent position tracking performance for all of the trajectories. The position tracking error for the real valve model reduced for trajectories 1 to 3, but increased by 400% with trajectory 4. Obviously the 4 Hz sine wave trajectory and the high gains caused the valves to saturate as can be

observed from the large increase in the chamber pressure tracking errors compared to the

low gain case.

Table 5.5.3 RMSE (radian) values for backstepping control with imperfect and perfect valve models

| | Low Gains | | | High Gains | | |
|---|---|---|---|---|---|---|
| | **Trajectory 1** | | | **Trajectory 1** | | |
| **Valve model** | **Position error (radian)** | $P_a$ **error (Pa)** | $P_b$ **error (Pa)** | **Position error (radian)** | $P_a$ **error (Pa)** | $P_b$ **error (Pa)** |
| imperfect | $6.13{\times}10^{-3}$ | $1.22{\times}10^{4}$ | $1.22{\times}10^{4}$ | $5.45{\times}10^{-3}$ | $8.38{\times}10^{3}$ | $8.38{\times}10^{3}$ |
| perfect | $4.73{\times}10^{-3}$ | $4.55{\times}10^{3}$ | $4.55{\times}10^{3}$ | $4.83{\times}10^{-3}$ | $3.31{\times}10^{3}$ | $3.31{\times}10^{3}$ |
| | | | | | | |
| | **Trajectory 2** | | | **Trajectory 2** | | |
| **Valve model** | **Position error (radian)** | $P_a$ **error (Pa)** | $P_b$ **error (Pa)** | **Position error (radian)** | $P_a$ **error (Pa)** | $P_b$ **error (Pa)** |
| imperfect | $7.87{\times}10^{-3}$ | $1.15{\times}10^{4}$ | $1.15{\times}10^{4}$ | $6.64{\times}10^{-3}$ | $8.42{\times}10^{3}$ | $8.42{\times}10^{3}$ |
| perfect | $5.70{\times}10^{-3}$ | $4.44{\times}10^{3}$ | $4.44{\times}10^{3}$ | $5.67{\times}10^{-3}$ | $3.65{\times}10^{3}$ | $3.65{\times}10^{3}$ |
| | | | | | | |
| | **Trajectory 3** | | | **Trajectory 3** | | |
| **Valve model** | **Position error (radian)** | $P_a$ **error (Pa)** | $P_b$ **error (Pa)** | **Position error (radian)** | $P_a$ **error (Pa)** | $P_b$ **error (Pa)** |
| imperfect | $1.26{\times}10^{-2}$ | $1.21{\times}10^{4}$ | $1.21{\times}10^{4}$ | $1.18{\times}10^{-2}$ | $1.11{\times}10^{4}$ | $1.11{\times}10^{4}$ |
| perfect | $8.90{\times}10^{-3}$ | $5.48{\times}10^{3}$ | $5.48{\times}10^{3}$ | $8.71{\times}10^{-3}$ | $3.92{\times}10^{3}$ | $3.92{\times}10^{3}$ |
| | | | | | | |
| | **Trajectory 4** | | | **Trajectory 4** | | |
| **Valve model** | **Position error (radian)** | $P_a$ **error (Pa)** | $P_b$ **error (Pa)** | **Position error (radian)** | $P_a$ **error (Pa)** | $P_b$ **error (Pa)** |
| imperfect | $1.48{\times}10^{-2}$ | $1.66{\times}10^{4}$ | $1.66{\times}10^{4}$ | $7.76{\times}10^{-2}$ | $8.85{\times}10^{4}$ | $8.85{\times}10^{4}$ |
| perfect | $1.22{\times}10^{-2}$ | $1.21{\times}10^{4}$ | $1.21{\times}10^{4}$ | $1.19{\times}10^{-2}$ | $4.54{\times}10^{3}$ | $4.54{\times}10^{3}$ |

## 5.6    Conclusions

Both the DVMPC and backstepping controller were extensively tested by simulations. The effectiveness of compensations by motor and cylinder torque was studied. The tuning of DVMPC prediction horizon was also investigated. The results provided guidance for further experimental tuning.

Payload mismatch in both horizontal and vertical configurations have been simulated for backstepping, backstepping with estimator, DVMPC, and DVMPC with estimator. In general, backstepping controller has better robustness to payload variations. The DVMPC performs better in RMSE value when the payload has no mismatch.

The limitation of the payload estimation algorithm was shown in simulation discussions. The estimator was significantly helpful only in a few specific situations, namely the vertical configuration with a slow reference trajectory and the payload mismatch was large regardless of controllers. Additionally, in vertical configuration, the estimator degraded the backstepping controller performance for trajectory 4 while maintained the similar performance with DVMPC for trajectory 4. Therefore, the payload estimation algorithm needed to be further investigated in vertical configuration for the DVMPC.

The limitations of the PWM input valve dynamic model were investigated in section 5.6. Two conclusions can be drawn. First, the real valve dynamic model is accurate enough when the gains are small. Second, the saturation of the valve will

degrade the tracking performance. Therefore, in the experiments using high $k_3$ and $k_4$

gains will be avoided.

## CHAPTER 6.     EXPERIMENTS

### 6.1   Introduction

The backstepping controller and DVMPC were manually tuned and preliminary simulations and experiments were done with no payload in Chapter 4. The two designed nonlinear controllers were studied through extensive simulations in Chapter 5. In this chapter an extensive set of experiments will be performed for both controllers. A default non-zero payload of 0.22 kg will be used throughout. The controllers will first be tuned in the horizontal configuration with no payload mismatch. Next, robustness experiments will be performed for mismatched payloads. The experiments with payload mismatch in the vertical configuration will be performed at the end of this chapter. In the horizontal configuration, the payload estimation will not be included based on the conclusions from Chapter 5.

### 6.2   Experiment Setup

In this chapter, the hybrid actuator parameters are the same as Chapter 4 except for the payloads. The supply pressure was set to 3E5 Pa. In software, the sampling frequency was set at 1 kHz for both controllers. The PWM frequency for backstepping was 200 Hz. The zero-order hold period for DVMPC was set at 5ms. Actual payloads were installed at the end of the arm. For the backstepping controller, the valve drive circuit was connected to the counter output port on the NI card. For the DVMPC + IDC, the valve drive circuit was connected to the digital output port on the NI card.

### 6.2.1   Payload Mismatch

Table 6.2.1 shows the payload mismatch used in Chapter 5. The problem of using these payloads was that when payload was larger than 0.5 kg or the equivalent inertia was 0.092 kg·m$^2$, both controllers were not able to track the smooth cycloidal trajectory for both vertical and horizontal configuration. The maximum payload used by Chen (2012) was 0.46 kg with the hybrid actuator operated vertically. Considering the similar hardware components and the same relatively low supply pressure, the 0.46 kg maximum payload used by Chen (2012) was close to the stability limits observed in the Chapter 5 simulations. Therefore the nominal payload in the experiment chapter should be less than 0.46 kg.

Table 6.2.1 Payload mismatch used in simulation (both configurations)

|  | Small | | | Nominal | | | Large | | |
|---|---|---|---|---|---|---|---|---|---|
| **Controller Payload (kg)** | 0.2 | | | 0.5 | | | 0.8 | | |
| **Controller inertia(kg·m2)** | 0.051 | | | 0.092 | | | 0.133 | | |
| **Actual Payload (kg)** | 0.1 | 0.2 | 0.3 | 0.1 | 0.5 | 0.9 | 0.4 | 0.8 | 1.2 |
| **Actual inertia (kg·m2)** | 0.037 | 0.051 | 0.065 | 0.037 | 0.092 | 0.147 | 0.078 | 0.133 | 0.188 |
| **Inertia Mismatch (%)** | -27 | 0 | 27 | -60 | 0 | 60 | -41 | 0 | 41 |

Considering the length of the arm, it is 0.46 m which is longer than the 0.35 m used with the previous hardware (Chen 2012). A large payload may significantly deflect the arm. The choice of experimental payloads for the horizontal and vertical

configurations are listed in Table 6.2.2. The nominal payload in both controllers was 0.22 kg. The actual payloads were 0.12, 0.22, and 0.32 kg. The inertia mismatches were 25% and -25%.

Table 6.2.2 Payload mismatch used in horizontal and vertical experiments

|  | Small | Nominal | Large |
|---|---|---|---|
| **Controller Payload (kg)** | 0.22 | | |
| **Actual Payload (kg)** | 0.12 | 0.22 | 0.32 |
| **Actual inertia (kg·m2)** | 0.040 | 0.054 | 0.068 |
| **Inertia Mismatch (%)** | -25 | 0 | 25 |

### 6.2.2    Desired Position Trajectories

Four trajectories were used in the preliminary simulations and experiments. Only two of the trajectories were used in the simulation Chapter 5 due to the similarity of the tracking results. In this chapter, based on the same reasoning, the trajectories listed in Table 6.2.3 were chosen.

Table 6.2.3     Experiment trajectories for two controllers.

|  | **Test trajectory** |
|---|---|
| 1 | Cycloidal |
| 4 | Sine wave at 2 Hz with 0.3 radian amplitude |

### 6.2.3    Controller Types

Original DVMPC has three controller types: DVMPC only (pneumatic mode), DVMPC + IDC (hybrid mode) and IDC (motor mode). However, including the payload estimation algorithm doubles the number of DVMPC controller types. The DVMPC controller types are listed in Table 6.2.4.

Table 6.2.4      Complete list of DVMPC types

| DVMPC Type | Description |
|:---:|:---|
| 1 | DVMPC (pneumatic mode) |
| 2 | DVMPC + IDC (hybrid mode) |
| 3 | DVMPC + Estimator (pneumatic mode) |
| 4 | DVMPC + IDC + Estimator (hybrid mode) |
| 5 | IDC (motor mode) |
| 6 | IDC + Estimator ( motor mode) |

Backstepping has four controller types because of different compensations from electric motor and pneumatic cylinder: backstepping only, backstepping + electric motor compensation, backstepping + pneumatic FF compensation, and backstepping with both compensations. Also, the payload estimation doubles the number of control types. As listed in Table 6.2.5, these types of controller can be applied to different actuation modes.

Table 6.2.5    Complete list of backstepping controller types

| Type | Description |
|---|---|
| 1 | Backstepping (pneumatic, motor, hybrid mode ) |
| 2 | Backstepping + electric motor compensation ( motor, hybrid mode ) |
| 3 | Backstepping + pneumatic FF (pneumatic, hybrid mode ) |
| 4 | Backstepping + double compensations (pneumatic, motor, hybrid mode ) |
| 5 | Backstepping + Estimator |
| 6 | Backstepping + electric motor compensation + Estimator |
| 7 | Backstepping + pneumatic FF + Estimator |
| 8 | Backstepping + double compensations + Estimator |

In Chapter 5, the simulated results suggested that hybrid mode type 4 without the estimator has best performance in terms of both trajectory tracking and robustness to payload mismatch. The payload estimation included in simulation was not helpful in the horizontal configuration. It was helpful in vertical configuration for trajectory 1 while it made the performance much worse for trajectory 4. Therefore the payload estimation algorithm will not be included since it is not consistently helpful for backstepping control.

## 6.3    Tuning Controllers for Nominal Payload

Unlike Chapter 4, the experiments performed in this chapter will have extra payload. Thus, it is essential to retune both controllers for the new nominal payload of 0.22 kg.

To avoid the saturation of the electric motor with trajectory 4 (2 Hz sine wave), only pneumatic and hybrid mode will be used. The reason is that the large angular acceleration will require a larger torque than possible with the motor only mode.

Table 6.3.1　　DVMPC+IDC re-tuned for nominal payload in horizontal configuration

| Parameters | Value | Unit |
|:---:|:---:|:---:|
| $N_p$ | 50 | 1 |
| *ZOH* | 5 | ms |
| $\omega$ | 20 | $s^{-2}$ |
| $\zeta$ | 0.1 | 1 |
| $T_s$ | 1 | ms |

The re-tuned IDC tracking results listed in Table 6.3.2 confirm that the motor only mode is not suitable for hybrid actuator servo control with extra payloads. Only pneumatic mode and hybrid mode will be used for the DVMPC experiments.

Table 6.3.2　　RMSE (radian) of the retuned IDC for nominal payload (0.22kg) at the motor only mode

| Test Number | Trajectory 1 | Trajectory 4 |
|:---:|:---:|:---:|
| 1 | $4.91\times10^{-3}$ | $1.56\times10^{-1}$ |
| 2 | $4.90\times10^{-3}$ | $1.56\times10^{-1}$ |
| 3 | $4.98\times10^{-3}$ | $1.56\times10^{-1}$ |
| 4 | $4.92\times10^{-3}$ | $1.57\times10^{-1}$ |
| 5 | $4.95\times10^{-3}$ | $1.58\times10^{-1}$ |

The backstepping controller was manually re-tuned for the nominal payload. The pneumatic mode actuation is used first to tune the backstepping pneumatic cylinder control for trajectory 1 and 4. Then electric motor compensation was tuned in hybrid

mode with the same trajectories. The re-tuned controller parameters are listed in Table 6.3.3.

Table 6.3.3       Backstepping re-tuned for nominal payload in horizontal configuration

| Pneumatic Parameters | Value | Unit | Electric Motor Parameters | Value | Unit |
|---|---|---|---|---|---|
| $k_1$ | 30 | $\text{s}^{-1}$ | $K_{bs\_motor,p}$ | 197.3 | $\text{Nm}\cdot\text{rad}^{-1}$ |
| $k_2$ | 30 | $\text{s}^{-1}$ | $K_{bs\_motor,d}$ | 1.94 | $\text{Nm}\cdot\text{rad}^{-1}\cdot\text{s}$ |
| $k_3$ | 10 | $\text{s}^{-1}$ | $K_{proportion}$ | 0.1 | 1 |
| $k_4$ | 10 | $\text{s}^{-1}$ | | | |
| $T_{pwm\_period}$ | 5 | ms | | | |
| $T_s$ | 1 | ms | | | |

Since the backstepping controller and DVMPC have similar control strategies for the electric motor, the motor only mode will not be used in backstepping experiments as well. Only pneumatic mode in type 3 and hybrid mode in type 4 from Table 6.2.5 will be used for the backstepping control experiments.

## 6.4   Performance Metrics

Performance metrics were used to quantitatively compare results by Chen (2012). The introduction of performance metrics is described as "The root-mean-square error (RMSE) provides a measure of the average tracking error over the entire trajectory. The maximum absolute error (MAE) provides the worst case of tracking. For the cycloidal trajectory, the steady-state performance will be quantified using the steady-state error

(SSE) and steady-state amplitude (SSA). The SSE equals the mean absolute value of the error when the response is at steady-state. Most control systems never stay at a perfectly constant position when $y_d$ is constant. The SSA quantifies the level of steady-state vibration, and equals the difference between the maximum and minimum values of $y$ in this region." (Chen 2012). In this thesis, the SSE and SSA were calculated from the trajectory 1 results over the time period 5 s to 5.5 s.

For the purpose of comparison, the same performance metrics were applied to the experiment results. The performance metrics of the DVMPC and the backstepping experiments in both configurations are included in the Appendix A to D. Only the RMSE values are listed in this chapter.

## 6.5    Robustness Experiments

In Chapter 5 the robustness of the controllers was assessed by simulating the performance with various payloads and payload mismatches. In this section, small, nominal, and large payloads will be applied to the hybrid actuator. Trajectory 1 and 4 were used as position tracking reference. Experiments were performed in both configurations to identify the robustness of the designed controllers. Note that although the controllers were re-tuned for nominal payload in previous section, the performance of tracking is slightly worse if compared to zero payloads in Chapter 4. Such performance deterioration was also observed in the experiments performed by Chen (2012).

### 6.5.1   Horizontal Configuration

### 6.5.1.1   DVMPC

RMSE values of DVMPC experiments for different payloads are listed in Table 6.5.1 to Table 6.5.6. The hybrid mode of DVMPC reduced the RMSE up to 90% compared to the pneumatic mode for mismatch cases. For large payload, the DVMPC pneumatic mode was not stable for trajectory 4, while it was stable in hybrid mode. The small payload performance had a slightly advantage over the nominal payload. Similar results were observed in the simulations.

The DVMPC was not robust for increased payload, especially with trajectory 4. This is because the model predictive control relies on minimizing the worst case of cost function over a prediction horizon. The current sampling period measured position error is only a certain portion of total cost. Therefore, when the actual payload decreases, the controller will be more aggressive which might improve tracking performance. If the controller reacted over aggressively, the next ZOH will be used to correct overreact caused by the smaller payload. On the other hand if the payload increases, the controller will tend to underreact. The next ZOH will be used to make up insufficient control action which might improve the steady state performance. It is confirmed by the performance metrics listed in Appendix A and the comparison of SSE and SSA of the smaller and larger payload.

As analyzed and simulated in previous chapter, the payload estimation will only be helpful in vertical configuration for trajectory 1. The horizontal experiment results

confirmed those findings. When estimator was turned on for all payloads, the RMSE reduced for trajectory 1, and it was increased for trajectory 4.

The SSE and SSA results presented in Appendix A showed that the DVMPC + IDC in hybrid mode had more reliable steady state performance and the controller with estimator off was clearly better than the estimator on in steady state.

Table 6.5.1      No payload estimation, DVMPC, small payload (0.12kg)

| | Pneumatic Mode | | Hybrid Mode | |
|---|---|---|---|---|
| | Traj. 1 | Traj. 4 | Traj. 1 | Traj. 4 |
| | RMSE(radian) | RMSE(radian) | RMSE(radian) | RMSE(radian) |
| Test 1 | $5.42 \times 10^{-3}$ | $1.72 \times 10^{-2}$ | $2.30 \times 10^{-3}$ | $9.61 \times 10^{-3}$ |
| Test 2 | $5.26 \times 10^{-3}$ | $1.69 \times 10^{-2}$ | $2.33 \times 10^{-3}$ | $7.42 \times 10^{-3}$ |
| Test 3 | $5.52 \times 10^{-3}$ | $1.66 \times 10^{-2}$ | $2.38 \times 10^{-3}$ | $7.97 \times 10^{-3}$ |
| Test 4 | $5.47 \times 10^{-3}$ | $1.70 \times 10^{-2}$ | $2.39 \times 10^{-3}$ | $7.84 \times 10^{-3}$ |
| Test 5 | $5.70 \times 10^{-3}$ | $1.69 \times 10^{-2}$ | $2.48 \times 10^{-3}$ | $7.38 \times 10^{-3}$ |
| Mean | $5.43 \times 10^{-3}$ | $1.69 \times 10^{-2}$ | $2.38 \times 10^{-3}$ | $8.04 \times 10^{-3}$ |

Table 6.5.2     Payload estimation, DVMPC, small payload (0.12kg)

|  | Pneumatic Mode | | Hybrid Mode | |
| --- | --- | --- | --- | --- |
|  | **Traj. 1** | **Traj. 4** | **Traj. 1** | **Traj. 4** |
|  | **RMSE(radian)** | **RMSE(radian)** | **RMSE(radian)** | **RMSE(radian)** |
| **Test 1** | $5.61 \times 10^{-3}$ | $1.78 \times 10^{-2}$ | $1.82 \times 10^{-3}$ | $1.08 \times 10^{-2}$ |
| **Test 2** | $5.66 \times 10^{-3}$ | $1.75 \times 10^{-2}$ | $1.82 \times 10^{-3}$ | $1.05 \times 10^{-2}$ |
| **Test 3** | $5.92 \times 10^{-3}$ | $1.71 \times 10^{-2}$ | $1.81 \times 10^{-3}$ | $1.06 \times 10^{-2}$ |
| **Test 4** | $5.63 \times 10^{-3}$ | $1.69 \times 10^{-2}$ | $1.88 \times 10^{-3}$ | $1.06 \times 10^{-2}$ |
| **Test 5** | $5.80 \times 10^{-3}$ | $1.68 \times 10^{-2}$ | $2.02 \times 10^{-3}$ | $1.05 \times 10^{-2}$ |
| **Mean** | $5.72 \times 10^{-3}$ | $1.72 \times 10^{-2}$ | $1.87 \times 10^{-3}$ | $1.06 \times 10^{-2}$ |

Table 6.5.3     No payload estimation, DVMPC, nominal payload (0.22kg)

|  | Pneumatic Mode | | Hybrid Mode | |
| --- | --- | --- | --- | --- |
|  | **Traj. 1** | **Traj. 4** | **Traj. 1** | **Traj. 4** |
|  | **RMSE(radian)** | **RMSE(radian)** | **RMSE(radian)** | **RMSE(radian)** |
| **Test 1** | $5.59 \times 10^{-3}$ | $3.24 \times 10^{-2}$ | $2.20 \times 10^{-3}$ | $1.37 \times 10^{-2}$ |
| **Test 2** | $5.47 \times 10^{-3}$ | $2.76 \times 10^{-2}$ | $2.22 \times 10^{-3}$ | $1.19 \times 10^{-2}$ |
| **Test 3** | $5.46 \times 10^{-3}$ | $2.64 \times 10^{-2}$ | $2.27 \times 10^{-3}$ | $1.28 \times 10^{-2}$ |
| **Test 4** | $5.78 \times 10^{-3}$ | $2.65 \times 10^{-2}$ | $2.16 \times 10^{-3}$ | $1.19 \times 10^{-2}$ |
| **Test 5** | $5.86 \times 10^{-3}$ | $2.66 \times 10^{-2}$ | $2.26 \times 10^{-3}$ | $1.28 \times 10^{-2}$ |
| **Mean** | $5.63 \times 10^{-3}$ | $2.79 \times 10^{-2}$ | $2.22 \times 10^{-3}$ | $1.26 \times 10^{-2}$ |

Table 6.5.4      Payload estimation, DVMPC, nominal payload (0.22kg)

|  | Pneumatic Mode | | Hybrid Mode | |
| --- | --- | --- | --- | --- |
|  | **Traj. 1** | **Traj. 4** | **Traj. 1** | **Traj. 4** |
|  | **RMSE(radian)** | **RMSE(radian)** | **RMSE(radian)** | **RMSE(radian)** |
| **Test 1** | $5.80 \times 10^{-3}$ | $2.83 \times 10^{-2}$ | $1.79 \times 10^{-3}$ | $1.60 \times 10^{-2}$ |
| **Test 2** | $5.71 \times 10^{-3}$ | $2.73 \times 10^{-2}$ | $1.84 \times 10^{-3}$ | $1.82 \times 10^{-2}$ |
| **Test 3** | $5.70 \times 10^{-3}$ | $2.72 \times 10^{-2}$ | $1.82 \times 10^{-3}$ | $1.63 \times 10^{-2}$ |
| **Test 4** | $5.61 \times 10^{-3}$ | $2.68 \times 10^{-2}$ | $1.81 \times 10^{-3}$ | $1.68 \times 10^{-2}$ |
| **Test 5** | $5.72 \times 10^{-3}$ | $2.85 \times 10^{-2}$ | $1.83 \times 10^{-3}$ | $1.92 \times 10^{-2}$ |
| **Mean** | $5.71 \times 10^{-3}$ | $2.76 \times 10^{-2}$ | $1.82 \times 10^{-3}$ | $1.73 \times 10^{-2}$ |

Table 6.5.5      No payload estimation, DVMPC, large payload (0.32kg)

|  | Pneumatic Mode | | Hybrid Mode | |
| --- | --- | --- | --- | --- |
|  | **Traj. 1** | **Traj. 4** | **Traj. 1** | **Traj. 4** |
|  | **RMSE(radian)** | **RMSE(radian)** | **RMSE(radian)** | **RMSE(radian)** |
| **Test 1** | $7.95 \times 10^{-3}$ | $2.51 \times 10^{-1}$ | $3.63 \times 10^{-3}$ | $2.85 \times 10^{-2}$ |
| **Test 2** | $8.12 \times 10^{-3}$ | $2.53 \times 10^{-1}$ | $3.60 \times 10^{-3}$ | $2.25 \times 10^{-2}$ |
| **Test 3** | $8.16 \times 10^{-3}$ | $2.55 \times 10^{-1}$ | $3.50 \times 10^{-3}$ | $2.20 \times 10^{-2}$ |
| **Test 4** | $8.52 \times 10^{-3}$ | $2.55 \times 10^{-1}$ | $3.49 \times 10^{-3}$ | $2.18 \times 10^{-2}$ |
| **Test 5** | $8.65 \times 10^{-3}$ | $2.56 \times 10^{-1}$ | $3.45 \times 10^{-3}$ | $2.29 \times 10^{-2}$ |
| **Mean** | $8.28 \times 10^{-3}$ | $2.54 \times 10^{-1}$ | $3.53 \times 10^{-3}$ | $2.35 \times 10^{-2}$ |

Table 6.5.6      Payload estimation, DVMPC, large payload (0.32kg)

| | Pneumatic Mode | | Hybrid Mode | |
|---|---|---|---|---|
| | **Traj. 1** | **Traj. 4** | **Traj. 1** | **Traj. 4** |
| | **RMSE(radian)** | **RMSE(radian)** | **RMSE(radian)** | **RMSE(radian)** |
| **Test 1** | $8.61{\times}10^{-3}$ | $2.56{\times}10^{-1}$ | $2.33{\times}10^{-3}$ | $3.14{\times}10^{-2}$ |
| **Test 2** | $8.57{\times}10^{-3}$ | $2.57{\times}10^{-1}$ | $2.31{\times}10^{-3}$ | $3.16{\times}10^{-2}$ |
| **Test 3** | $8.79{\times}10^{-3}$ | $2.55{\times}10^{-1}$ | $2.31{\times}10^{-3}$ | $3.14{\times}10^{-2}$ |
| **Test 4** | $8.86{\times}10^{-3}$ | $2.56{\times}10^{-1}$ | $2.34{\times}10^{-3}$ | $3.26{\times}10^{-2}$ |
| **Test 5** | $8.74{\times}10^{-3}$ | $2.56{\times}10^{-1}$ | $2.39{\times}10^{-3}$ | $3.47{\times}10^{-2}$ |
| **Mean** | $8.71{\times}10^{-3}$ | $2.56{\times}10^{-1}$ | $2.34{\times}10^{-3}$ | $3.23{\times}10^{-2}$ |

### 6.5.1.2   Backstepping

The RMSE values for the horizontal backstepping experiments are recorded in Table 6.5.7 to Table 6.5.9. The pneumatic mode experiments were performed to verify the robustness of backstepping with pneumatic FF. It turned out the backstepping control is more robust than the DVMPC. The tracking RMSE values were close for all three payload mismatches, especially for large payload trajectory 4 in which the DVMPC failed to stabilize the tracking while the RMSE of backstepping only increased 20% compared to the nominal payload case.

The hybrid mode reduced the RMSE in most cases. However the RMSE were increased for large payload trajectory 4 in hybrid mode. At the same payload in hybrid mode, the trajectory 1 RMSE reduced by 50%. It may be caused by the rapid change of position and velocity with trajectory 4 saturated the motor torque. In general, the backstepping control was robust to payload mismatch.

Table 6.5.7      Backstepping, small payload (0.12kg)

| | Pneumatic Mode | | Hybrid Mode | |
|---|---|---|---|---|
| | **Traj. 1** | **Traj. 4** | **Traj. 1** | **Traj. 4** |
| | **RMSE(radian)** | **RMSE(radian)** | **RMSE(radian)** | **RMSE(radian)** |
| **Test 1** | $1.09 \times 10^{-2}$ | $3.72 \times 10^{-2}$ | $1.79 \times 10^{-3}$ | $1.78 \times 10^{-2}$ |
| **Test 2** | $9.53 \times 10^{-3}$ | $3.26 \times 10^{-2}$ | $1.44 \times 10^{-3}$ | $1.95 \times 10^{-2}$ |
| **Test 3** | $1.04 \times 10^{-2}$ | $3.57 \times 10^{-2}$ | $1.71 \times 10^{-3}$ | $1.88 \times 10^{-2}$ |
| **Test 4** | $7.86 \times 10^{-3}$ | $3.67 \times 10^{-2}$ | $1.38 \times 10^{-3}$ | $1.64 \times 10^{-2}$ |
| **Test 5** | $7.84 \times 10^{-3}$ | $3.73 \times 10^{-2}$ | $2.25 \times 10^{-3}$ | $1.96 \times 10^{-2}$ |
| **Mean** | $9.31 \times 10^{-3}$ | $3.59 \times 10^{-2}$ | $1.71 \times 10^{-3}$ | $1.84 \times 10^{-2}$ |

Table 6.5.8     Backstepping, nominal payload (0.22kg)

|  | Pneumatic Mode | | Hybrid Mode | |
| --- | --- | --- | --- | --- |
|  | **Traj. 1** | **Traj. 4** | **Traj. 1** | **Traj. 4** |
|  | **RMSE(radian)** | **RMSE(radian)** | **RMSE(radian)** | **RMSE(radian)** |
| **Test 1** | $9.01 \times 10^{-3}$ | $3.78 \times 10^{-2}$ | $1.91 \times 10^{-3}$ | $4.26 \times 10^{-2}$ |
| **Test 2** | $8.72 \times 10^{-3}$ | $3.85 \times 10^{-2}$ | $1.52 \times 10^{-3}$ | $3.45 \times 10^{-2}$ |
| **Test 3** | $8.20 \times 10^{-3}$ | $3.75 \times 10^{-2}$ | $1.49 \times 10^{-3}$ | $3.87 \times 10^{-2}$ |
| **Test 4** | $8.64 \times 10^{-3}$ | $4.11 \times 10^{-2}$ | $1.54 \times 10^{-3}$ | $2.58 \times 10^{-2}$ |
| **Test 5** | $8.27 \times 10^{-3}$ | $4.44 \times 10^{-2}$ | $1.95 \times 10^{-3}$ | $3.29 \times 10^{-2}$ |
| **Mean** | $8.57 \times 10^{-3}$ | $3.99 \times 10^{-2}$ | $1.68 \times 10^{-3}$ | $3.49 \times 10^{-2}$ |

Table 6.5.9     Backstepping, large payload (0.32kg)

|  | Pneumatic Mode | | Hybrid Mode | |
| --- | --- | --- | --- | --- |
|  | **Traj. 1** | **Traj. 4** | **Traj. 1** | **Traj. 4** |
|  | **RMSE(radian)** | **RMSE(radian)** | **RMSE(radian)** | **RMSE(radian)** |
| **Test 1** | $8.13 \times 10^{-3}$ | $5.39 \times 10^{-2}$ | $4.54 \times 10^{-3}$ | $7.76 \times 10^{-2}$ |
| **Test 2** | $8.26 \times 10^{-3}$ | $5.05 \times 10^{-2}$ | $4.61 \times 10^{-3}$ | $7.67 \times 10^{-2}$ |
| **Test 3** | $8.52 \times 10^{-3}$ | $5.65 \times 10^{-2}$ | $5.09 \times 10^{-3}$ | $7.66 \times 10^{-2}$ |
| **Test 4** | $8.35 \times 10^{-3}$ | $5.88 \times 10^{-2}$ | $4.47 \times 10^{-3}$ | $7.68 \times 10^{-2}$ |
| **Test 5** | $8.23 \times 10^{-3}$ | $5.62 \times 10^{-2}$ | $4.64 \times 10^{-3}$ | $7.69 \times 10^{-2}$ |
| **Mean** | $8.30 \times 10^{-3}$ | $5.52 \times 10^{-2}$ | $4.67 \times 10^{-3}$ | $7.69 \times 10^{-2}$ |

Generally speaking in horizontal configuration, when different payloads were applied to the hybrid actuator, the RMSE of backstepping is slightly worse than DVMPC. However the backstepping controller is more robust to payload variation with slightly better steady state performance confirmed by the detailed performance metrics listed in the Appendix B.

### 6.5.2 Vertical Configuration

The generality of the designed controllers can be evaluated through the change of system configuration because this changes the hybrid actuator's dynamics. The gravity term was added to the controller and experiments were performed in trajectory 1 and 4. Since the configuration changed to vertical, the trajectories were slightly changed as well. For trajectory 4, for safety purpose, it was commanded to move back to initial position smoothly starting at 9.5 seconds as shown in Figure 6.1.
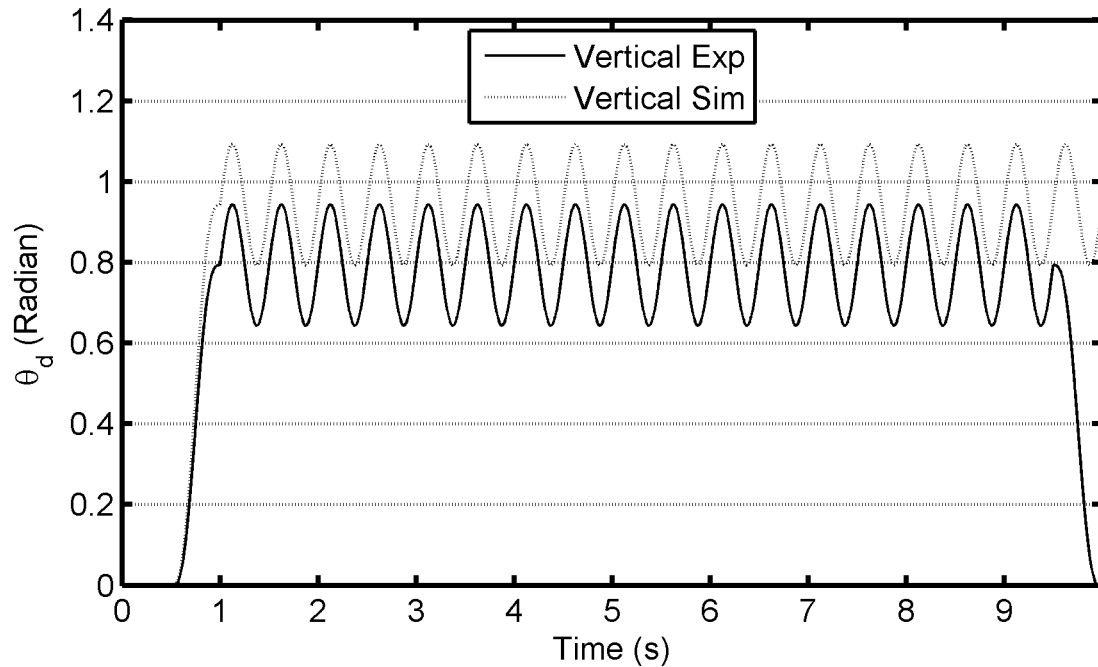
Figure 6.1 Trajectory 4 used in vertical experiments compare with the one used in vertical simulations

In order to compensate for the gravity, extra torque will be required from the pneumatic cylinder due to the limited torque capacity of the electric motor. When applying original re-tuned parameters, the pneumatic mode might not be capable of stabilizing reference tracking. And the maximum cylinder torque from supply pressure might not be sufficient for the original large payload (0.32 kg). Hence, no payload case was added to replace the original "small" payload. Although they were sometimes unstable, the large payload results were still included.

### 6.5.2.1  DVMPC

The same parameters were applied to vertical configuration experiments. The nominal payload (0.22 kg) is selected to be used by the controller compensating payload gravity torque. The same actuation modes and trajectories for horizontal were selected.

The RMSE results of experiments are listed in Table 6.5.10 to Table 6.5.17. In most payloads cases, when the estimator was turned on, the RMSE values of tracking trajectory 1 were reduced up to 50%. However, it worsened the performance of tracking trajectory 4. The Table 6.5.13 in pneumatic mode, trajectory 4 shows the problem of payload estimation, in which the RMSE varies from $9.56 \times 10^{-3}$ radian to unstable.

The DVMPC in vertical was not sensitive to payload variation even without the payload estimator. However the RMSE values of DVMPC in vertical configuration were much worse than the horizontal ones.

The SSE and SSA results listed in Appendix D showed that in vertical configuration, the steady state performance was different to the horizontal configuration. The hybrid mode reduced the SSE and SSA, while the payload estimator reduced the steady state error in some cases.

Table 6.5.10    No payload estimation, DVMPC, no payload (0kg)

|  | Pneumatic Mode | | Hybrid Mode | |
|---|---|---|---|---|
|  | **Traj. 1** | **Traj. 4** | **Traj. 1** | **Traj. 4** |
|  | **RMSE(radian)** | **RMSE(radian)** | **RMSE(radian)** | **RMSE(radian)** |
| **Test 1** | $1.08\times10^{-2}$ | $1.61\times10^{-2}$ | $7.10\times10^{-3}$ | $9.77\times10^{-3}$ |
| **Test 2** | $1.10\times10^{-2}$ | $1.41\times10^{-2}$ | $6.93\times10^{-3}$ | $9.34\times10^{-3}$ |
| **Test 3** | $1.27\times10^{-2}$ | $1.43\times10^{-2}$ | $6.93\times10^{-3}$ | $9.82\times10^{-3}$ |
| **Test 4** | $1.10\times10^{-2}$ | $1.40\times10^{-2}$ | $6.96\times10^{-3}$ | $9.97\times10^{-3}$ |
| **Test 5** | $1.11\times10^{-2}$ | $1.40\times10^{-2}$ | $6.97\times10^{-3}$ | $9.67\times10^{-3}$ |
| **Mean** | $1.13\times10^{-2}$ | $1.45\times10^{-2}$ | $6.98\times10^{-3}$ | $9.71\times10^{-3}$ |

Table 6.5.11    Payload estimation, DVMPC, no payload (0kg)

|  | Pneumatic Mode | | Hybrid Mode | |
|---|---|---|---|---|
|  | **Traj. 1** | **Traj. 4** | **Traj. 1** | **Traj. 4** |
|  | **RMSE(radian)** | **RMSE(radian)** | **RMSE(radian)** | **RMSE(radian)** |
| **Test 1** | $7.23\times10^{-2}$ | $4.34\times10^{-2}$ | $4.47\times10^{-3}$ | $1.26\times10^{-2}$ |
| **Test 2** | $1.36\times10^{-2}$ | $3.76\times10^{-2}$ | $8.71\times10^{-2}$ | $9.43\times10^{-3}$ |
| **Test 3** | $9.82\times10^{-1}$ | $9.46\times10^{-3}$ | $9.83\times10^{-1}$ | $7.67\times10^{-3}$ |
| **Test 4** | $1.12\times10^{-2}$ | $9.94\times10^{-3}$ | $7.15\times10^{-3}$ | $7.44\times10^{-3}$ |
| **Test 5** | $1.05\times10^{-2}$ | $2.21\times10^{-2}$ | $7.08\times10^{-3}$ | $9.60\times10^{-3}$ |
| **Mean** | $2.18\times10^{-1}$ | $2.45\times10^{-2}$ | $2.18\times10^{-1}$ | $9.35\times10^{-3}$ |

Table 6.5.12    No payload estimation, DVMPC, small payload (0.12kg)

|        | Pneumatic Mode | | Hybrid Mode | |
|--------|----------------|----------------|----------------|----------------|
|        | **Traj. 1** | **Traj. 4** | **Traj. 1** | **Traj. 4** |
|        | **RMSE(radian)** | **RMSE(radian)** | **RMSE(radian)** | **RMSE(radian)** |
| **Test 1** | $1.55{\times}10^{-2}$ | $1.69{\times}10^{-2}$ | $1.02{\times}10^{-2}$ | $1.14{\times}10^{-2}$ |
| **Test 2** | $1.52{\times}10^{-2}$ | $1.71{\times}10^{-2}$ | $1.02{\times}10^{-2}$ | $1.10{\times}10^{-2}$ |
| **Test 3** | $1.53{\times}10^{-2}$ | $1.69{\times}10^{-2}$ | $1.02{\times}10^{-2}$ | $1.10{\times}10^{-2}$ |
| **Test 4** | $1.53{\times}10^{-2}$ | $1.66{\times}10^{-2}$ | $1.02{\times}10^{-2}$ | $1.11{\times}10^{-2}$ |
| **Test 5** | $1.54{\times}10^{-2}$ | $1.82{\times}10^{-2}$ | $1.02{\times}10^{-2}$ | $1.15{\times}10^{-2}$ |
| **Mean** | $1.53{\times}10^{-2}$ | $1.71{\times}10^{-2}$ | $1.02{\times}10^{-2}$ | $1.12{\times}10^{-2}$ |

Table 6.5.13    Payload estimation, DVMPC, small payload (0.12kg)

|        | Pneumatic Mode | | Hybrid Mode | |
|--------|----------------|----------------|----------------|----------------|
|        | **Traj. 1** | **Traj. 4** | **Traj. 1** | **Traj. 4** |
|        | **RMSE(radian)** | **RMSE(radian)** | **RMSE(radian)** | **RMSE(radian)** |
| **Test 1** | $1.42{\times}10^{-2}$ | $2.47{\times}10^{-2}$ | $4.70{\times}10^{-3}$ | $7.43{\times}10^{-3}$ |
| **Test 2** | $1.85{\times}10^{-2}$ | $1.37{\times}10^{-2}$ | $4.78{\times}10^{-3}$ | $7.83{\times}10^{-3}$ |
| **Test 3** | $1.84{\times}10^{-2}$ | $1.08{\times}10^{-2}$ | $4.78{\times}10^{-3}$ | $7.77{\times}10^{-3}$ |
| **Test 4** | $1.45{\times}10^{-2}$ | $7.54{\times}10^{-1}$ | $4.76{\times}10^{-3}$ | $7.36{\times}10^{-3}$ |
| **Test 5** | $1.36{\times}10^{-2}$ | $9.56{\times}10^{-3}$ | $4.91{\times}10^{-3}$ | $7.65{\times}10^{-3}$ |
| **Mean** | $1.58{\times}10^{-2}$ | $1.63{\times}10^{-1}$ | $4.79{\times}10^{-3}$ | $7.61{\times}10^{-3}$ |

Table 6.5.14    No payload estimation, DVMPC, nominal payload (0.22kg)

| | Pneumatic Mode | | Hybrid Mode | |
|---|---|---|---|---|
| | **Traj. 1** | **Traj. 4** | **Traj. 1** | **Traj. 4** |
| | **RMSE(radian)** | **RMSE(radian)** | **RMSE(radian)** | **RMSE(radian)** |
| **Test 1** | $1.90 \times 10^{-2}$ | $2.70 \times 10^{-2}$ | $1.22 \times 10^{-2}$ | $1.31 \times 10^{-2}$ |
| **Test 2** | $1.90 \times 10^{-2}$ | $2.35 \times 10^{-2}$ | $1.22 \times 10^{-2}$ | $1.10 \times 10^{-2}$ |
| **Test 3** | $7.22 \times 10^{-2}$ | $2.76 \times 10^{-2}$ | $1.22 \times 10^{-2}$ | $1.12 \times 10^{-2}$ |
| **Test 4** | $1.89 \times 10^{-2}$ | $2.41 \times 10^{-2}$ | $1.23 \times 10^{-2}$ | $1.25 \times 10^{-2}$ |
| **Test 5** | $1.91 \times 10^{-2}$ | $2.25 \times 10^{-2}$ | $1.22 \times 10^{-2}$ | $1.50 \times 10^{-2}$ |
| **Mean** | $2.96 \times 10^{-2}$ | $2.49 \times 10^{-2}$ | $1.22 \times 10^{-2}$ | $1.26 \times 10^{-2}$ |

Table 6.5.15    Payload estimation, DVMPC, nominal payload (0.22kg)

| | Pneumatic Mode | | Hybrid Mode | |
|---|---|---|---|---|
| | **Traj. 1** | **Traj. 4** | **Traj. 1** | **Traj. 4** |
| | **RMSE(radian)** | **RMSE(radian)** | **RMSE(radian)** | **RMSE(radian)** |
| **Test 1** | $2.52 \times 10^{-2}$ | $7.03 \times 10^{-1}$ | $8.20 \times 10^{-3}$ | $1.62 \times 10^{-2}$ |
| **Test 2** | $2.51 \times 10^{-2}$ | $2.35 \times 10^{-2}$ | $9.78 \times 10^{-3}$ | $6.49 \times 10^{-2}$ |
| **Test 3** | $2.85 \times 10^{-2}$ | $6.76 \times 10^{-1}$ | $8.48 \times 10^{-3}$ | $6.69 \times 10^{-2}$ |
| **Test 4** | $3.05 \times 10^{-2}$ | $7.51 \times 10^{-1}$ | $7.43 \times 10^{-3}$ | $6.70 \times 10^{-2}$ |
| **Test 5** | $3.30 \times 10^{-2}$ | $3.24 \times 10^{-2}$ | $8.85 \times 10^{-3}$ | $6.63 \times 10^{-2}$ |
| **Mean** | $2.85 \times 10^{-2}$ | $4.37 \times 10^{-1}$ | $8.55 \times 10^{-3}$ | $5.63 \times 10^{-2}$ |

Table 6.5.16    No payload estimation, DVMPC, large payload (0.32kg)

| | Pneumatic Mode | | Hybrid Mode | |
|---|---|---|---|---|
| | **Traj. 1** | **Traj. 4** | **Traj. 1** | **Traj. 4** |
| | **RMSE(radian)** | **RMSE(radian)** | **RMSE(radian)** | **RMSE(radian)** |
| **Test 1** | $2.29{\times}10^{-2}$ | $3.34{\times}10^{-1}$ | $1.63{\times}10^{-2}$ | $2.87{\times}10^{-2}$ |
| **Test 2** | $2.28{\times}10^{-2}$ | $7.60{\times}10^{-1}$ | $1.62{\times}10^{-2}$ | $2.68{\times}10^{-2}$ |
| **Test 3** | $2.66{\times}10^{-2}$ | $3.33{\times}10^{-1}$ | $1.62{\times}10^{-2}$ | $2.61{\times}10^{-2}$ |
| **Test 4** | $2.29{\times}10^{-2}$ | $7.61{\times}10^{-1}$ | $1.62{\times}10^{-2}$ | $2.24{\times}10^{-2}$ |
| **Test 5** | $2.28{\times}10^{-2}$ | $7.28{\times}10^{-1}$ | $1.63{\times}10^{-2}$ | $2.56{\times}10^{-2}$ |
| **Mean** | $2.36{\times}10^{-2}$ | $5.83{\times}10^{-1}$ | $1.62{\times}10^{-2}$ | $2.59{\times}10^{-2}$ |

Table 6.5.17    Payload estimation, DVMPC, large payload (0.32kg)

| | Pneumatic Mode | | Hybrid Mode | |
|---|---|---|---|---|
| | **Traj. 1** | **Traj. 4** | **Traj. 1** | **Traj. 4** |
| | **RMSE(radian)** | **RMSE(radian)** | **RMSE(radian)** | **RMSE(radian)** |
| **Test 1** | $1.78{\times}10^{-2}$ | $7.53{\times}10^{-1}$ | $1.34{\times}10^{-2}$ | $3.52{\times}10^{-2}$ |
| **Test 2** | $1.79{\times}10^{-2}$ | $7.69{\times}10^{-1}$ | $1.14{\times}10^{-2}$ | $2.24{\times}10^{-2}$ |
| **Test 3** | $1.80{\times}10^{-2}$ | $8.74{\times}10^{-1}$ | $1.09{\times}10^{-2}$ | $2.81{\times}10^{-2}$ |
| **Test 4** | $1.80{\times}10^{-2}$ | $7.54{\times}10^{-1}$ | $1.00{\times}10^{-2}$ | $5.58{\times}10^{-1}$ |
| **Test 5** | $1.90{\times}10^{-2}$ | $7.77{\times}10^{-1}$ | $8.75{\times}10^{-3}$ | $2.80{\times}10^{-2}$ |
| **Mean** | $1.81{\times}10^{-2}$ | $7.85{\times}10^{-1}$ | $1.09{\times}10^{-2}$ | $1.34{\times}10^{-1}$ |

206

### 6.5.2.2 Backstepping

Backstepping controller was re-tuned for the normal payload (0.22 kg). The main reason for re-tuning is that in horizontal configuration, the demanding pneumatic torque is small since there is no gravity torque while the vertical configuration requires larger pneumatic torque. The re-tuned parameters are listed in Table 6.5.18.

Table 6.5.18    Backstepping re-tuned for nominal payload in vertical configuration

| Pneumatic Parameters | Value | Unit | Electric Motor Parameters | Value | Unit |
|:---:|:---:|:---:|:---:|:---:|:---:|
| $k_1$ | 40 | $s^{-1}$ | $K_{bs\_motor,p}$ | 193.7 | $Nm \cdot rad^{-1}$ |
| $k_2$ | 20 | $s^{-1}$ | $K_{bs\_motor,d}$ | 0.65 | $Nm \cdot rad^{-1} \cdot s$ |
| $k_3$ | 45 | $s^{-1}$ | $K_{proportion}$ | 0.1 | 1 |
| $k_4$ | 45 | $s^{-1}$ | | | |
| $T_{pwm\_period}$ | 5 | ms | | | |
| $T_s$ | 1 | ms | | | |

RMSE results of tracking trajectory 1 and 4 are shown in Table 6.5.19 to Table 6.5.22. The large payload 0.32 kg was too big for the hybrid actuator under backstepping control. However it was included because in hybrid mode the actuator was able to track trajectory 1 with good accuracy.

Table 6.5.19    Backstepping, no payload (0 kg)

|  | Pneumatic Mode | | Hybrid Mode | |
|---|---|---|---|---|
|  | **Traj. 1** | **Traj. 4** | **Traj. 1** | **Traj. 4** |
|  | **RMSE(radian)** | **RMSE(radian)** | **RMSE(radian)** | **RMSE(radian)** |
| **Test 1** | $1.75 \times 10^{-2}$ | $2.39 \times 10^{-2}$ | $5.53 \times 10^{-3}$ | $9.08 \times 10^{-3}$ |
| **Test 2** | $1.74 \times 10^{-2}$ | $2.40 \times 10^{-2}$ | $5.45 \times 10^{-3}$ | $1.16 \times 10^{-2}$ |
| **Test 3** | $1.74 \times 10^{-2}$ | $2.48 \times 10^{-2}$ | $5.32 \times 10^{-3}$ | $8.26 \times 10^{-3}$ |
| **Test 4** | $1.74 \times 10^{-2}$ | $2.59 \times 10^{-2}$ | $5.57 \times 10^{-3}$ | $8.78 \times 10^{-3}$ |
| **Test 5** | $1.74 \times 10^{-2}$ | $3.02 \times 10^{-2}$ | $6.30 \times 10^{-3}$ | $9.57 \times 10^{-3}$ |
| **Mean** | $1.74 \times 10^{-2}$ | $2.58 \times 10^{-2}$ | $5.63 \times 10^{-3}$ | $9.46 \times 10^{-3}$ |

Table 6.5.20    Backstepping, small payload (0.12kg)

|  | Pneumatic Mode | | Hybrid Mode | |
|---|---|---|---|---|
|  | **Traj. 1** | **Traj. 4** | **Traj. 1** | **Traj. 4** |
|  | **RMSE(radian)** | **RMSE(radian)** | **RMSE(radian)** | **RMSE(radian)** |
| **Test 1** | $7.73 \times 10^{-3}$ | $2.63 \times 10^{-2}$ | $1.60 \times 10^{-3}$ | $2.42 \times 10^{-2}$ |
| **Test 2** | $7.79 \times 10^{-3}$ | $3.04 \times 10^{-2}$ | $1.61 \times 10^{-3}$ | $1.45 \times 10^{-2}$ |
| **Test 3** | $8.02 \times 10^{-3}$ | $3.51 \times 10^{-2}$ | $1.98 \times 10^{-3}$ | $2.35 \times 10^{-2}$ |
| **Test 4** | $7.87 \times 10^{-3}$ | $2.81 \times 10^{-2}$ | $1.61 \times 10^{-3}$ | $2.61 \times 10^{-2}$ |
| **Test 5** | $7.63 \times 10^{-3}$ | $3.94 \times 10^{-2}$ | $1.62 \times 10^{-3}$ | $1.71 \times 10^{-2}$ |
| **Mean** | $7.81 \times 10^{-3}$ | $3.19 \times 10^{-2}$ | $1.68 \times 10^{-3}$ | $2.11 \times 10^{-2}$ |

Table 6.5.21    Backstepping, nominal payload (0.22kg)

|  | Pneumatic Mode | | Hybrid Mode | |
|---|---|---|---|---|
|  | Traj. 1 | Traj. 4 | Traj. 1 | Traj. 4 |
|  | RMSE(radian) | RMSE(radian) | RMSE(radian) | RMSE(radian) |
| Test 1 | $1.13\times10^{-2}$ | $7.87\times10^{-2}$ | $1.33\times10^{-3}$ | $3.76\times10^{-2}$ |
| Test 2 | $1.09\times10^{-2}$ | $7.85\times10^{-2}$ | $1.34\times10^{-3}$ | $5.18\times10^{-2}$ |
| Test 3 | $1.09\times10^{-2}$ | $7.28\times10^{-2}$ | $3.43\times10^{-3}$ | $3.39\times10^{-2}$ |
| Test 4 | $1.08\times10^{-2}$ | $7.39\times10^{-2}$ | $1.35\times10^{-3}$ | $5.11\times10^{-2}$ |
| Test 5 | $1.11\times10^{-2}$ | $7.40\times10^{-2}$ | $1.32\times10^{-3}$ | $3.46\times10^{-2}$ |
| Mean | $1.10\times10^{-2}$ | $7.56\times10^{-2}$ | $1.75\times10^{-3}$ | $4.18\times10^{-2}$ |

Table 6.5.22    Backstepping, large payload (0.32kg)

|  | Pneumatic Mode | | Hybrid Mode | |
|---|---|---|---|---|
|  | Traj. 1 | Traj. 4 | Traj. 1 | Traj. 4 |
|  | RMSE(radian) | RMSE(radian) | RMSE(radian) | RMSE(radian) |
| Test 1 | $2.68\times10^{-1}$ | $1.79\times10^{-1}$ | $4.37\times10^{-3}$ | $1.45\times10^{-1}$ |
| Test 2 | $1.97\times10^{-1}$ | $1.74\times10^{-1}$ | $3.75\times10^{-3}$ | $1.40\times10^{-1}$ |
| Test 3 | $1.92\times10^{-1}$ | $1.77\times10^{-1}$ | $3.71\times10^{-3}$ | $1.30\times10^{-1}$ |
| Test 4 | $1.90\times10^{-1}$ | $1.76\times10^{-1}$ | $3.78\times10^{-3}$ | $1.38\times10^{-1}$ |
| Test 5 | $1.87\times10^{-1}$ | $1.85\times10^{-1}$ | $3.98\times10^{-3}$ | $1.36\times10^{-1}$ |
| Mean | $2.07\times10^{-1}$ | $1.78\times10^{-1}$ | $3.92\times10^{-3}$ | $1.38\times10^{-1}$ |

Except the for large payload (0.32 kg) case, the RMSE values with the backstepping controller were not significantly affected by the payload variations. The vertical RMSE values with backstepping were close to the values for the horizontal

configuration (see section 6.5.1.2).  The SSE and SSA listed in Appendix C showed that compared to the DVMPC, the backstepping controller had smaller steady state errors, especially for the large payload case.

## 6.6   Conclusions

The robustness of the backstepping controller and the DVMPC + IDC was verified by experiments. Payload variations and different system configurations were applied to the experiments for the re-tuned controllers. The payload estimation algorithm was examined extensively over different conditions. The payload estimation was confirmed to be helpful for the DVMPC in certain situations. The experiment results suggested that both of the designed controllers were insensitive to payload variations in the horizontal configuration, while only the backstepping controller was robust to payload variations in the vertical configuration. Additionally, the backstepping controller worked well in both horizontal and vertical configurations after re-tuning.

# CHAPTER 7.     CONCLUSIONS

## 7.1   Summary

In this research, the modeling and control of an improved pneumatic-electric actuator was presented. The mass flow rate model for discrete valve input and PWM input were developed and validated. Two surface fitting methods were used for obtaining the valve model for PWM input. The comparison of the two methods was given. The connection between the valve models for different input was shown and validated by open-loop experiments. The system dynamic models with and without the valve dynamic model were validated separately. Two model-based nonlinear position controllers, using the DVMPC and backstepping methods, were designed, simulated and extensively tested. The simulations and experiments over a wide range of conditions demonstrated the performance of the designed controllers.

## 7.2   Achievements

The achievements of this thesis are summarized as below:

( 1 )    This thesis investigated on modeling and position control of an improved hybrid electric-pneumatic actuator. It confirmed the benefit of combining the advantages of the pneumatic actuator and the electric actuator.

( 2 )    ANN was used to fit the estimated mass flow rate surface. The fitting results shown were better than the bipolynomial fitting. The comparison of these two methods was given.

( 3 )   Valve dynamic model for a discrete input was used in the simulated plant for PWM valve input. This proved that the two valve models can both be used to describe the valve dynamics equivalently.

( 4 )   Novel compensation terms for electric motor and pneumatic cylinder in backstepping controller were proposed. The performance of the backstepping controller with compensation terms was significantly improved.

( 5 )   Stability analyses were completed for DVMPC and backstepping controller.

( 6 )   Proposed a novel model-based payload estimation algorithm for DVMPC + IDC in vertical configuration. Simulation and experiments with estimator were performed. The limitations of the payload estimation were identified.

( 7 )   In experiments, the RMSE values of DVMPC and the backstepping + FF controller were less than 0.01 rad, the MAE is often less than 0.1 rad in pneumatic mode. The hybrid mode reduced the RMSE up to 80%.

( 8 )   The two model-based controllers were shown to be robust to some payload variations.

## 7.3   Recommendations for Future Work

( 1 )   The valves should be replaced with valves with a higher mass flow rate. The simulations performed in Chapter 5 suggested that a higher mass flow rate will increase the system bandwidth, and improve the tracking precision.

( 2 )  Accuracy of the friction model should be improved. It was found that when arm/payload was installed the friction model parameters would be different from the actuator without the arm/payload. A better friction model might be able to compensate for the changes caused by a new component.

( 3 )  Simplify the ANN structure and implement the simplified ANN into the backstepping controller. The structure used in this thesis produced accurate results, but the number of parameters made it inconvenient to implement. If the ANN can be simplified without sacrificing fitting accuracy significantly, the control performance might be improved.

( 4 )  A method for systematically tuning the backstepping controller should be developed. The gains of backstepping controller were difficult to tune properly. According to Chapter 4, large gains will stabilize tracking. However, large gains tend to require a large the mass flow rate through the orifice which may saturate the valve and degrade the performance.

( 5 )  The DVMPC + IDC prediction assumed that valve input remained the same over the prediction horizon to reduce the computation load. However, changing the valve inputs over the prediction horizon may help to improve the pneumatic actuator performance.

( 6 )  The accuracy of the model-based payload estimation algorithm should be improved. When the payload estimate is close to the actual payload, it will significantly reduce the RMSE as seen in the simulations and experiments.

( 7 )    For the purpose of using this actuation solution for a collaborative robot, force

control will be required, and should be developed, in addition to position control.

# REFERENCE

Ahn, K. and Yokota, S. (2005), 'Intelligent Switching Control of Pneumatic Actuator Using ON/OFF Solenoid Valves', *Mechatronics,* 15 (6), 683-702.

Bone, G. M. and Chen, X. (2012), 'Position Control of Hybrid Pneumatic-Electric Actuators', *2012 American Control Conference (ACC)*, 1793-99.

Carneiro, J. F. and de Almeida, F. G. (2012), 'A Neural Network Based Nonlinear Model of A Servopneumatic System', *Journal of Dynamic Systems Measurement and Control-Transactions of the ASME,* 134 (2).

Chen, Xing (2012), 'Development of A Hybrid Pneumatic-Electic Actutator', M.A.Sc (McMaster University).

Guizzo, E. and Ackerman, E. (2012), 'The Rise of the ROBOT WORKER', *IEEE Spectrum,* 49 (10), 34-41.

Hodgson, S., et al. (2012), 'Improved Tracking and Switching Performance of an Electro-Pneumatic Positioning System', *Mechatronics,* 22 (1), 1-12.

Jobin, Jean P. 'Industrial Robots: 5 Most Popular Applications',
<http://blog.robotiq.com/bid/52886/Industrial-robots-5-most-popular-applications>,
accessed.

Jones, J. B. and Hawkins, George A. (1986), *Engineering Thermodynamics : An Introductory Textbook* (2nd edn.; New York: Wiley).

Krstić, Miroslav, Kanellakopoulos, Ioannis, and Kokotović, Petar V. (1995), *Nonlinear and Adaptive Control Design* (Adaptive and Learning Systems for Signal Processing, Communications, and Control; New York: Wiley) xiii, 563 p.

Mayne, D. Q., et al. (2000), 'Constrained Model Predictive Control: Stability and Optimality', *Automatica,* 36 (6), 789-814.

Messina, A., Giannoccaro, N. I., and Gentile, A. (2005), 'Experimenting and Modelling the Dynamics of Pneumatic Actuators Controlled by the Pulse Width Modulation (PWM) Technique', *Mechatronics,* 15 (7), 859-81.

Mills, J. K. (1993), 'Hybrid Actuator for Robot Manipulators - Design, Control and Performance', *Mechatronics,* 3 (1), 19-38.

Nicolaisen, P. (1987), 'Safety problems related to robots', *Robotics,* 3 (2), 205-11.

Ning, S and Bone, G. M. (2002), 'High Steady-State Accuracy Pneumatic Servo Positioning System with PVA/PV Control and Friction Compensation', *2002 IEEE International Conference on Robotics and Automation (ICRA)*, Vols I-IV, Proceedings, 2824-29.

--- (2005), 'Experimental Comparison of Two Pneumatic Servo Position Control Algorithms', *2005 IEEE International Conference on Mechatronics and Automations, Vols 1-4, Conference Proceedings*, 37-42.

Petrosky, Lyman J. (1988), 'Hybrid Electro-Pneumatic Robot Joint Actuator', (Westinghouse Electric Corp.).

Rao, Z (2005), 'Modeling and Control of Miniature Servo Pneumatic Actuators', M.A.Sc (McMaster University).

Rao, Z and Bone, G. M. (2008), 'Nonlinear Modeling and Control of Servo Pneumatic Actuators', *IEEE Transactions on Control Systems Technology,* 16 (3), 562-69.

Shafi, Adil 'How Robots Create Jobs', <http://www.robotics.org/content-detail.cfm/Industrial-Robotics-Featured-Articles/How-Robots-Create-Jobs/content_id/3360>, accessed.

Shearer, J. L. (1956), 'Study of Pneumatic Processes in the Continuous Control of Motion with Compressed Air - i,ii,' *Transactions of ASME*, 233-42.

Shen, X. R., et al. (2006), 'Nonlinear Model-Based Control of Pulse Width Modulated Pneumatic Servo Systems', *Journal of Dynamic Systems Measurement and Control-Transactions of the ASME,* 128 (3), 663-69.

Shin, D. J., et al. (2010), 'Design and Control of a Bio-Inspired Human-Friendly Robot', *International Journal of Robotics Research,* 29 (5), 571-84.

Smaoui, M., Brun, X., and Thomasset, D. (2006), 'A Study on Tracking Position Control of an Electro-Pneumatic System Using Backstepping Design', *Control Engineering Practice,* 14 (8), 923-33.

Spong, Mark W. and Vidyasagar, M. (1989), *Robot Dynamics and Control* (New York: Wiley) xvi, 336 p.

Takemura, F., et al. (2000), 'Control of a Hybrid Pneumatic/Electric Motor', *2000 IEEE/RSJ International Conference on Intelligent Robots and Systems (IROS 2000), Vols 1-3, Proceedings*, 209-14.

van Varseveld, R. B. and Bone, G. M. (1997), 'Accurate Position Control of a Pneumatic Actuator Using ON/OFF Solenoid Valves', *IEEE-ASME Transactions on Mechatronics,* 2 (3), 195-204.

Wang, H. B., Mo, J. P. T., and Chen, N. (1998), 'On the Estimation of On-Off Valve Parameters for Control of Programmable Pneumatic Actuators', *Transactions of the Institute of Measurement and Control,* 20 (5), 211-20.

Zinn, M., et al. (2004), 'A New Actuation Approach for Human Friendly Robot Design', *International Journal of Robotics Research,* 23 (4-5), 379-98.

## APPENDIX.A     HORIZONTAL DVMPC EXPERIMENT RESULTS

Table A.1     Performance of retuned DVMPC for small payload (0.12kg) at pneumatic mode, without payload estimation, trajectory 1

| Errors(radian) | RMSE | MAE | SSE | SSA |
|---|---|---|---|---|
| Test 1 | $5.42\times10^{-4}$ | $1.19\times10^{-2}$ | $6.20\times10^{-3}$ | 0.00 |
| Test 2 | $5.26\times10^{-3}$ | $1.18\times10^{-2}$ | $5.76\times10^{-3}$ | $4.00\times10^{-4}$ |
| Test 3 | $5.52\times10^{-3}$ | $1.28\times10^{-2}$ | $6.07\times10^{-3}$ | $1.00\times10^{-4}$ |
| Test 4 | $5.47\times10^{-3}$ | $1.30\times10^{-2}$ | $6.39\times10^{-3}$ | $3.00\times10^{-4}$ |
| Test 5 | $5.70\times10^{-3}$ | $1.34\times10^{-2}$ | $6.61\times10^{-3}$ | $6.00\times10^{-4}$ |
| Mean | $5.47\times10^{-3}$ | $1.26\times10^{-2}$ | $6.20\times10^{-3}$ | $2.80\times10^{-4}$ |

Table A.2     Performance of retuned DVMPC for small payload (0.12kg) at hybrid mode, without payload estimation, trajectory 1

| Errors(radian) | RMSE | MAE | SSE | SSA |
|---|---|---|---|---|
| Test 1 | $2.30\times10^{-3}$ | $6.60\times10^{-3}$ | $3.20\times10^{-3}$ | 0.00 |
| Test 2 | $2.33\times10^{-3}$ | $6.60\times10^{-3}$ | $3.30\times10^{-3}$ | 0.00 |
| Test 3 | $2.38\times10^{-3}$ | $6.70\times10^{-3}$ | $3.50\times10^{-3}$ | 0.00 |
| Test 4 | $2.39\times10^{-3}$ | $6.40\times10^{-3}$ | $3.50\times10^{-3}$ | 0.00 |
| Test 5 | $2.48\times10^{-3}$ | $6.90\times10^{-3}$ | $3.90\times10^{-3}$ | 0.00 |
| Mean | $2.38\times10^{-3}$ | $6.64\times10^{-3}$ | $3.48\times10^{-3}$ | 0.00 |

Table A.3       Performance of retuned DVMPC for small payload (0.12kg) at pneumatic mode, without payload estimation, trajectory 4

|        | RMSE(radian)          | MAE(radian)           |
|--------|-----------------------|-----------------------|
| Test 1 | $1.72\times10^{-2}$   | $8.54\times10^{-2}$   |
| Test 2 | $1.69\times10^{-2}$   | $8.74\times10^{-2}$   |
| Test 3 | $1.66\times10^{-2}$   | $8.84\times10^{-2}$   |
| Test 4 | $1.70\times10^{-2}$   | $8.88\times10^{-2}$   |
| Test 5 | $1.69\times10^{-2}$   | $8.87\times10^{-2}$   |
| Mean   | $1.69\times10^{-2}$   | $8.77\times10^{-2}$   |

Table A.4       Performance of retuned DVMPC for small payload (0.12kg) at hybrid mode, without payload estimation, trajectory 4

|        | RMSE(radian)          | MAE(radian)           |
|--------|-----------------------|-----------------------|
| Test 1 | $9.61\times10^{-3}$   | $7.34\times10^{-2}$   |
| Test 2 | $7.42\times10^{-3}$   | $6.63\times10^{-2}$   |
| Test 3 | $7.97\times10^{-3}$   | $6.96\times10^{-2}$   |
| Test 4 | $7.84\times10^{-3}$   | $6.60\times10^{-2}$   |
| Test 5 | $7.38\times10^{-3}$   | $6.63\times10^{-2}$   |
| Mean   | $8.04\times10^{-3}$   | $6.83\times10^{-2}$   |

Table A.5      Performance of retuned DVMPC for small payload (0.12kg) at pneumatic

mode, with payload estimation, trajectory 1

| Errors(radian) | RMSE | MAE | SSE | SSA |
|---|---|---|---|---|
| Test 1 | $5.61 \times 10^{-3}$ | $1.26 \times 10^{-2}$ | $6.48 \times 10^{-3}$ | $5.00 \times 10^{-4}$ |
| Test 2 | $5.66 \times 10^{-3}$ | $1.06 \times 10^{-2}$ | $6.53 \times 10^{-3}$ | $5.00 \times 10^{-4}$ |
| Test 3 | $5.92 \times 10^{-3}$ | $1.40 \times 10^{-2}$ | $6.83 \times 10^{-3}$ | $5.00 \times 10^{-4}$ |
| Test 4 | $5.63 \times 10^{-3}$ | $1.13 \times 10^{-2}$ | $7.03 \times 10^{-3}$ | $1.00 \times 10^{-4}$ |
| Test 5 | $5.80 \times 10^{-3}$ | $1.25 \times 10^{-2}$ | $6.60 \times 10^{-3}$ | $4.00 \times 10^{-4}$ |
| Mean | $5.72 \times 10^{-3}$ | $1.22 \times 10^{-2}$ | $6.69 \times 10^{-3}$ | $4.00 \times 10^{-4}$ |

Table A.6      Performance of retuned DVMPC for small payload (0.12kg) at hybrid
mode, with payload estimation, trajectory 1

| Errors(radian) | RMSE | MAE | SSE | SSA |
|---|---|---|---|---|
| Test 1 | $1.82 \times 10^{-3}$ | $7.00 \times 10^{-3}$ | $1.25 \times 10^{-3}$ | $3.00 \times 10^{-4}$ |
| Test 2 | $1.82 \times 10^{-3}$ | $7.30 \times 10^{-3}$ | $1.27 \times 10^{-3}$ | $4.00 \times 10^{-4}$ |
| Test 3 | $1.81 \times 10^{-3}$ | $7.50 \times 10^{-3}$ | $1.24 \times 10^{-3}$ | $3.00 \times 10^{-4}$ |
| Test 4 | $1.88 \times 10^{-3}$ | $7.60 \times 10^{-3}$ | $1.24 \times 10^{-3}$ | $3.00 \times 10^{-4}$ |
| Test 5 | $2.02 \times 10^{-3}$ | $9.00 \times 10^{-3}$ | $1.28 \times 10^{-3}$ | $4.00 \times 10^{-4}$ |
| Mean | $1.87 \times 10^{-3}$ | $0.77 \times 10^{-2}$ | $1.26 \times 10^{-3}$ | $3.40 \times 10^{-4}$ |

Table A.7      Performance of retuned DVMPC for small payload (0.12kg) at pneumatic mode, with payload estimation, trajectory 4

|        | RMSE(radian) | MAE(radian) |
|--------|--------------|-------------|
| **Test 1** | $1.78 \times 10^{-2}$ | $8.94 \times 10^{-2}$ |
| **Test 2** | $1.75 \times 10^{-2}$ | $8.73 \times 10^{-2}$ |
| **Test 3** | $1.71 \times 10^{-2}$ | $8.71 \times 10^{-2}$ |
| **Test 4** | $1.69 \times 10^{-2}$ | $8.68 \times 10^{-2}$ |
| **Test 5** | $1.68 \times 10^{-2}$ | $8.83 \times 10^{-2}$ |
| **Mean**   | $1.72 \times 10^{-2}$ | $8.78 \times 10^{-2}$ |

Table A.8      Performance of retuned DVMPC for small payload (0.12kg) at hybrid mode, with payload estimation, trajectory 4

|        | RMSE(radian) | MAE(radian) |
|--------|--------------|-------------|
| **Test 1** | $1.08 \times 10^{-2}$ | $6.62 \times 10^{-2}$ |
| **Test 2** | $1.05 \times 10^{-2}$ | $6.58 \times 10^{-2}$ |
| **Test 3** | $1.06 \times 10^{-2}$ | $6.50 \times 10^{-2}$ |
| **Test 4** | $1.06 \times 10^{-2}$ | $6.50 \times 10^{-2}$ |
| **Test 5** | $1.05 \times 10^{-2}$ | $6.51 \times 10^{-2}$ |
| **Mean**   | $1.06 \times 10^{-2}$ | $6.54 \times 10^{-2}$ |

Table A.9      Performance of retuned DVMPC for nominal payload (0.22kg) at pneumatic mode, without payload estimation, trajectory 1

| Errors(radian) | RMSE | MAE | SSE | SSA |
|---|---|---|---|---|
| Test 1 | $5.59\times10^{-3}$ | $1.47\times10^{-2}$ | $6.10\times10^{-3}$ | $1.00\times10^{-4}$ |
| Test 2 | $5.47\times10^{-3}$ | $1.03\times10^{-2}$ | $6.83\times10^{-3}$ | $4.00\times10^{-4}$ |
| Test 3 | $5.46\times10^{-3}$ | $1.07\times10^{-2}$ | $6.38\times10^{-3}$ | $1.00\times10^{-4}$ |
| Test 4 | $5.78\times10^{-3}$ | $1.45\times10^{-2}$ | $6.47\times10^{-3}$ | $4.00\times10^{-4}$ |
| Test 5 | $5.86\times10^{-3}$ | $1.45\times10^{-2}$ | $6.54\times10^{-3}$ | $3.00\times10^{-4}$ |
| Mean | $5.63\times10^{-3}$ | $1.29\times10^{-2}$ | $6.46\times10^{-3}$ | $2.60\times10^{-4}$ |

Table A.10      Performance of retuned DVMPC for nominal payload (0.22kg) at hybrid mode, without payload estimation, trajectory 1

| Errors(radian) | RMSE | MAE | SSE | SSA |
|---|---|---|---|---|
| Test 1 | $2.20\times10^{-3}$ | $4.20\times10^{-3}$ | $3.60\times10^{-3}$ | 0.00 |
| Test 2 | $2.22\times10^{-3}$ | $4.30\times10^{-3}$ | $3.54\times10^{-3}$ | $1.00\times10^{-4}$ |
| Test 3 | $2.27\times10^{-3}$ | $4.20\times10^{-3}$ | $3.80\times10^{-3}$ | 0.00 |
| Test 4 | $2.16\times10^{-3}$ | $4.20\times10^{-3}$ | $3.30\times10^{-3}$ | 0.00 |
| Test 5 | $2.26\times10^{-3}$ | $4.00\times10^{-3}$ | $3.80\times10^{-3}$ | 0.00 |
| Mean | $2.22\times10^{-3}$ | $4.18\times10^{-3}$ | $3.61\times10^{-3}$ | $2.00\times10^{-5}$ |

Table A.11    Performance of retuned DVMPC for nominal payload (0.22kg) at pneumatic mode, without payload estimation, trajectory 4

|        | RMSE(radian)         | MAE(radian)          |
|--------|----------------------|----------------------|
| Test 1 | $3.24 \times 10^{-2}$ | $1.47 \times 10^{-1}$ |
| Test 2 | $2.76 \times 10^{-2}$ | $1.10 \times 10^{-1}$ |
| Test 3 | $2.64 \times 10^{-2}$ | $9.45 \times 10^{-2}$ |
| Test 4 | $2.65 \times 10^{-2}$ | $9.42 \times 10^{-2}$ |
| Test 5 | $2.66 \times 10^{-2}$ | $9.19 \times 10^{-2}$ |
| Mean   | $2.79 \times 10^{-2}$ | $10.75 \times 10^{-2}$ |

Table A.12    Performance of retuned DVMPC for nominal payload (0.22kg) at hybrid mode, without payload estimation, trajectory 4

|        | RMSE(radian)         | MAE(radian)          |
|--------|----------------------|----------------------|
| Test 1 | $1.37 \times 10^{-2}$ | $8.94 \times 10^{-2}$ |
| Test 2 | $1.19 \times 10^{-2}$ | $7.27 \times 10^{-2}$ |
| Test 3 | $1.28 \times 10^{-2}$ | $8.38 \times 10^{-2}$ |
| Test 4 | $1.19 \times 10^{-2}$ | $7.24 \times 10^{-2}$ |
| Test 5 | $1.28 \times 10^{-2}$ | $8.13 \times 10^{-2}$ |
| Mean   | $1.26 \times 10^{-2}$ | $7.99 \times 10^{-2}$ |

Table A.13      Performance of retuned DVMPC for nominal payload (0.22kg) at
pneumatic mode, with payload estimation, trajectory 1

| Errors(radian) | RMSE | MAE | SSE | SSA |
|---|---|---|---|---|
| Test 1 | $5.80 \times 10^{-3}$ | $1.24 \times 10^{-2}$ | $6.31 \times 10^{-3}$ | $1.00 \times 10^{-4}$ |
| Test 2 | $5.71 \times 10^{-3}$ | $1.41 \times 10^{-2}$ | $6.78 \times 10^{-3}$ | $4.00 \times 10^{-4}$ |
| Test 3 | $5.70 \times 10^{-3}$ | $1.28 \times 10^{-2}$ | $6.60 \times 10^{-3}$ | $3.00 \times 10^{-4}$ |
| Test 4 | $5.61 \times 10^{-3}$ | $1.09 \times 10^{-2}$ | $6.60 \times 10^{-3}$ | $1.00 \times 10^{-4}$ |
| Test 5 | $5.72 \times 10^{-3}$ | $1.22 \times 10^{-2}$ | $7.00 \times 10^{-3}$ | $5.00 \times 10^{-4}$ |
| Mean | $5.71 \times 10^{-3}$ | $1.25 \times 10^{-2}$ | $6.66 \times 10^{-3}$ | $2.80 \times 10^{-4}$ |

Table A.14      Performance of retuned DVMPC for nominal payload (0.22kg) at hybrid

mode, with payload estimation, trajectory 1

| Errors(radian) | RMSE | MAE | SSE | SSA |
|---|---|---|---|---|
| Test 1 | $1.79 \times 10^{-3}$ | $4.00 \times 10^{-3}$ | $1.42 \times 10^{-3}$ | $5.00 \times 10^{-4}$ |
| Test 2 | $1.84 \times 10^{-3}$ | $4.10 \times 10^{-3}$ | $1.54 \times 10^{-3}$ | $6.00 \times 10^{-4}$ |
| Test 3 | $1.82 \times 10^{-3}$ | $4.00 \times 10^{-3}$ | $1.51 \times 10^{-3}$ | $5.00 \times 10^{-4}$ |
| Test 4 | $1.81 \times 10^{-3}$ | $4.10 \times 10^{-3}$ | $1.47 \times 10^{-3}$ | $5.00 \times 10^{-4}$ |
| Test 5 | $1.83 \times 10^{-3}$ | $4.20 \times 10^{-3}$ | $1.47 \times 10^{-3}$ | $5.00 \times 10^{-4}$ |
| Mean | $1.82 \times 10^{-3}$ | $4.08 \times 10^{-3}$ | $1.48 \times 10^{-3}$ | $5.20 \times 10^{-4}$ |

Table A.15    Performance of retuned DVMPC for nominal payload (0.22kg) at pneumatic mode, with payload estimation, trajectory 4

|         | RMSE(radian) | MAE(radian) |
|---------|--------------|-------------|
| Test 1  | $2.83\times10^{-2}$ | $1.08\times10^{-1}$ |
| Test 2  | $2.73\times10^{-2}$ | $1.05\times10^{-1}$ |
| Test 3  | $2.72\times10^{-2}$ | $1.08\times10^{-1}$ |
| Test 4  | $2.68\times10^{-2}$ | $1.02\times10^{-1}$ |
| Test 5  | $2.85\times10^{-2}$ | $1.14\times10^{-1}$ |
| Mean    | $2.76\times10^{-2}$ | $1.07\times10^{-1}$ |

Table A.16    Performance of retuned DVMPC for nominal payload (0.22kg) at hybrid mode, with payload estimation, trajectory 4

|         | RMSE(radian) | MAE(radian) |
|---------|--------------|-------------|
| Test 1  | $1.60\times10^{-2}$ | $7.36\times10^{-2}$ |
| Test 2  | $1.82\times10^{-2}$ | $9.33\times10^{-2}$ |
| Test 3  | $1.63\times10^{-2}$ | $7.24\times10^{-2}$ |
| Test 4  | $1.68\times10^{-2}$ | $7.23\times10^{-2}$ |
| Test 5  | $1.92\times10^{-2}$ | $8.42\times10^{-2}$ |
| Mean    | $1.73\times10^{-2}$ | $7.92\times10^{-2}$ |

Table A.17    Performance of retuned DVMPC for large payload (0.32kg) at pneumatic

mode, without payload estimation, trajectory 1

| Errors(radian) | RMSE | MAE | SSE | SSA |
|---|---|---|---|---|
| Test 1 | $7.95 \times 10^{-3}$ | $1.36 \times 10^{-2}$ | $1.27 \times 10^{-2}$ | $2.00 \times 10^{-4}$ |
| Test 2 | $8.12 \times 10^{-3}$ | $1.33 \times 10^{-2}$ | $1.28 \times 10^{-2}$ | $1.00 \times 10^{-4}$ |
| Test 3 | $8.16 \times 10^{-3}$ | $1.51 \times 10^{-2}$ | $1.34 \times 10^{-2}$ | $2.00 \times 10^{-4}$ |
| Test 4 | $8.52 \times 10^{-3}$ | $1.82 \times 10^{-2}$ | $1.34 \times 10^{-2}$ | 0.00 |
| Test 5 | $8.65 \times 10^{-3}$ | $1.67 \times 10^{-2}$ | $1.37 \times 10^{-2}$ | $2.00 \times 10^{-4}$ |
| Mean | $8.28 \times 10^{-3}$ | $1.54 \times 10^{-2}$ | $1.32 \times 10^{-2}$ | $1.40 \times 10^{-4}$ |

Table A.18    Performance of retuned DVMPC for large payload (0.32kg) at hybrid

mode, without payload estimation, trajectory 1

| Errors(radian) | RMSE | MAE | SSE | SSA |
|---|---|---|---|---|
| Test 1 | $3.63 \times 10^{-3}$ | $9.30 \times 10^{-3}$ | $5.40 \times 10^{-3}$ | 0.00 |
| Test 2 | $3.60 \times 10^{-3}$ | $9.40 \times 10^{-3}$ | $5.42 \times 10^{-3}$ | $3.00 \times 10^{-4}$ |
| Test 3 | $3.50 \times 10^{-3}$ | $9.50 \times 10^{-3}$ | $5.34 \times 10^{-3}$ | $1.00 \times 10^{-4}$ |
| Test 4 | $3.49 \times 10^{-3}$ | $9.00 \times 10^{-3}$ | $5.35 \times 10^{-3}$ | $3.00 \times 10^{-4}$ |
| Test 5 | $3.45 \times 10^{-3}$ | $8.60 \times 10^{-3}$ | $5.16 \times 10^{-3}$ | $2.00 \times 10^{-4}$ |
| Mean | $3.53 \times 10^{-3}$ | $9.16 \times 10^{-3}$ | $5.33 \times 10^{-3}$ | $1.80 \times 10^{-4}$ |

Table A.19     Performance of retuned DVMPC for large payload (0.32kg) at pneumatic mode, without payload estimation, trajectory 4

|        | RMSE(radian)          | MAE(radian)           |
|--------|-----------------------|-----------------------|
| **Test 1** | $2.51 \times 10^{-1}$ | $5.20 \times 10^{-1}$ |
| **Test 2** | $2.53 \times 10^{-1}$ | $5.36 \times 10^{-1}$ |
| **Test 3** | $2.55 \times 10^{-1}$ | $5.04 \times 10^{-1}$ |
| **Test 4** | $2.55 \times 10^{-1}$ | $5.26 \times 10^{-1}$ |
| **Test 5** | $2.56 \times 10^{-1}$ | $5.33 \times 10^{-1}$ |
| **Mean**   | $2.54 \times 10^{-1}$ | $5.24 \times 10^{-1}$ |

Table A.20     Performance of retuned DVMPC for large payload (0.32kg) at hybrid mode, without payload estimation, trajectory 4

|        | RMSE(radian)          | MAE(radian)           |
|--------|-----------------------|-----------------------|
| **Test 1** | $2.85 \times 10^{-2}$ | $1.56 \times 10^{-1}$ |
| **Test 2** | $2.25 \times 10^{-2}$ | $1.15 \times 10^{-1}$ |
| **Test 3** | $2.20 \times 10^{-2}$ | $1.13 \times 10^{-1}$ |
| **Test 4** | $2.18 \times 10^{-2}$ | $1.08 \times 10^{-1}$ |
| **Test 5** | $2.29 \times 10^{-2}$ | $1.21 \times 10^{-1}$ |
| **Mean**   | $2.35 \times 10^{-2}$ | $1.23 \times 10^{-1}$ |

Table A.21    Performance of retuned DVMPC for large payload (0.32kg) at pneumatic mode, with payload estimation, trajectory 1

| Errors(radian) | RMSE | MAE | SSE | SSA |
|---|---|---|---|---|
| **Test 1** | $8.61 \times 10^{-3}$ | $1.90 \times 10^{-2}$ | $1.35 \times 10^{-2}$ | $0.00$ |
| **Test 2** | $8.57 \times 10^{-3}$ | $2.30 \times 10^{-2}$ | $1.28 \times 10^{-2}$ | $1.00 \times 10^{-4}$ |
| **Test 3** | $8.79 \times 10^{-3}$ | $2.29 \times 10^{-2}$ | $1.29 \times 10^{-2}$ | $3.00 \times 10^{-4}$ |
| **Test 4** | $8.86 \times 10^{-3}$ | $2.31 \times 10^{-2}$ | $1.35 \times 10^{-2}$ | $2.00 \times 10^{-4}$ |
| **Test 5** | $8.74 \times 10^{-3}$ | $2.08 \times 10^{-2}$ | $1.29 \times 10^{-2}$ | $4.00 \times 10^{-4}$ |
| **Mean** | $8.71 \times 10^{-3}$ | $2.18 \times 10^{-2}$ | $1.31 \times 10^{-2}$ | $2.00 \times 10^{-4}$ |

Table A.22    Performance of retuned DVMPC for large payload (0.32kg) at hybrid mode, with payload estimation, trajectory 1

| Errors(radian) | RMSE | MAE | SSE | SSA |
|---|---|---|---|---|
| **Test 1** | $2.33 \times 10^{-3}$ | $7.30 \times 10^{-3}$ | $1.40 \times 10^{-3}$ | $0.00$ |
| **Test 2** | $2.31 \times 10^{-3}$ | $7.20 \times 10^{-3}$ | $1.40 \times 10^{-3}$ | $0.00$ |
| **Test 3** | $2.31 \times 10^{-3}$ | $7.30 \times 10^{-3}$ | $1.40 \times 10^{-3}$ | $0.00$ |
| **Test 4** | $2.34 \times 10^{-3}$ | $7.10 \times 10^{-3}$ | $1.50 \times 10^{-3}$ | $0.00$ |
| **Test 5** | $2.39 \times 10^{-3}$ | $7.10 \times 10^{-3}$ | $1.40 \times 10^{-3}$ | $0.00$ |
| **Mean** | $2.34 \times 10^{-3}$ | $7.20 \times 10^{-3}$ | $1.42 \times 10^{-3}$ | $0.00$ |

Table A.23     Performance of retuned DVMPC for large payload (0.32kg) at pneumatic mode, with payload estimation, trajectory 4

|        | RMSE(radian)          | MAE(radian)           |
|--------|-----------------------|-----------------------|
| Test 1 | $2.56\times10^{-1}$   | $5.31\times10^{-1}$   |
| Test 2 | $2.57\times10^{-1}$   | $5.24\times10^{-1}$   |
| Test 3 | $2.55\times10^{-1}$   | $5.23\times10^{-1}$   |
| Test 4 | $2.56\times10^{-1}$   | $5.09\times10^{-1}$   |
| Test 5 | $2.56\times10^{-1}$   | $5.18\times10^{-1}$   |
| Mean   | $2.56\times10^{-1}$   | $5.21\times10^{-1}$   |

Table A.24     Performance of retuned DVMPC for large payload (0.32kg) at hybrid mode, with payload estimation, trajectory 4

|        | RMSE(radian)          | MAE(radian)           |
|--------|-----------------------|-----------------------|
| Test 1 | $3.14\times10^{-2}$   | $1.30\times10^{-1}$   |
| Test 2 | $3.16\times10^{-2}$   | $1.22\times10^{-1}$   |
| Test 3 | $3.14\times10^{-2}$   | $1.10\times10^{-1}$   |
| Test 4 | $3.26\times10^{-2}$   | $1.23\times10^{-1}$   |
| Test 5 | $3.47\times10^{-2}$   | $1.39\times10^{-1}$   |
| Mean   | $3.23\times10^{-2}$   | $1.25\times10^{-1}$   |

# APPENDIX.B    HORIZONTAL BACKSTEPPING EXPERIMENT

# RESULTS

Table B.1    Performance of retuned backstepping for small payload (0.12kg) at pneumatic mode, trajectory 1

| Errors(radian) | RMSE | MAE | SSE | SSA |
|---|---|---|---|---|
| Test 1 | $1.09 \times 10^{-2}$ | $4.10 \times 10^{-2}$ | $1.36 \times 10^{-2}$ | 0.00 |
| Test 2 | $9.53 \times 10^{-3}$ | $4.35 \times 10^{-2}$ | $1.35 \times 10^{-2}$ | 0.00 |
| Test 3 | $1.04 \times 10^{-2}$ | $4.51 \times 10^{-2}$ | $1.45 \times 10^{-2}$ | $1.00 \times 10^{-4}$ |
| Test 4 | $7.86 \times 10^{-3}$ | $2.97 \times 10^{-2}$ | $1.35 \times 10^{-2}$ | 0.00 |
| Test 5 | $7.84 \times 10^{-3}$ | $2.81 \times 10^{-2}$ | $1.42 \times 10^{-2}$ | $1.00 \times 10^{-4}$ |
| Mean | $9.31 \times 10^{-3}$ | $3.75 \times 10^{-2}$ | $1.39 \times 10^{-2}$ | $4.00 \times 10^{-5}$ |

Table B.2    Performance of retuned backstepping for small payload (0.12kg) at hybrid mode, trajectory 1

| Errors(radian) | RMSE | MAE | SSE | SSA |
|---|---|---|---|---|
| Test 1 | $1.79 \times 10^{-3}$ | $1.24 \times 10^{-2}$ | $1.10 \times 10^{-3}$ | 0.00 |
| Test 2 | $1.44 \times 10^{-3}$ | $6.70 \times 10^{-3}$ | $1.10 \times 10^{-3}$ | 0.00 |
| Test 3 | $1.71 \times 10^{-3}$ | $1.09 \times 10^{-2}$ | $1.20 \times 10^{-3}$ | $1.00 \times 10^{-4}$ |
| Test 4 | $1.38 \times 10^{-3}$ | $6.10 \times 10^{-3}$ | $1.10 \times 10^{-3}$ | 0.00 |
| Test 5 | $3.31 \times 10^{-3}$ | $3.65 \times 10^{-2}$ | $1.60 \times 10^{-3}$ | 0.00 |
| Mean | $1.93 \times 10^{-3}$ | $1.45 \times 10^{-2}$ | $1.22 \times 10^{-3}$ | $2.00 \times 10^{-5}$ |

Table B.3        Performance of retuned backstepping for small payload (0.12kg) at
pneumatic mode, trajectory 4

|  | RMSE(radian) | MAE(radian) |
|---|---|---|
| **Test 1** | $3.72 \times 10^{-2}$ | $1.36 \times 10^{-1}$ |
| **Test 2** | $3.26 \times 10^{-2}$ | $1.35 \times 10^{-1}$ |
| **Test 3** | $3.57 \times 10^{-2}$ | $1.35 \times 10^{-1}$ |
| **Test 4** | $3.67 \times 10^{-2}$ | $1.44 \times 10^{-1}$ |
| **Test 5** | $3.73 \times 10^{-2}$ | $1.37 \times 10^{-1}$ |
| **Mean** | $3.59 \times 10^{-2}$ | $1.37 \times 10^{-1}$ |

Table B.4        Performance of retuned backstepping for small payload (0.12kg) at hybrid

mode, trajectory 4

|  | RMSE(radian) | MAE(radian) |
|---|---|---|
| **Test 1** | $1.78 \times 10^{-2}$ | $1.02 \times 10^{-1}$ |
| **Test 2** | $1.95 \times 10^{-2}$ | $1.01 \times 10^{-1}$ |
| **Test 3** | $1.88 \times 10^{-2}$ | $9.75 \times 10^{-2}$ |
| **Test 4** | $1.64 \times 10^{-2}$ | $9.74 \times 10^{-2}$ |
| **Test 5** | $1.96 \times 10^{-2}$ | $9.70 \times 10^{-2}$ |
| **Mean** | $1.84 \times 10^{-2}$ | $9.90 \times 10^{-2}$ |

Table B.5     Performance of retuned backstepping for normal payload (0.22kg) at pneumatic mode, trajectory 1

| Errors(radian) | RMSE | MAE | SSE | SSA |
|:---:|:---:|:---:|:---:|:---:|
| **Test 1** | $9.01 \times 10^{-3}$ | $2.52 \times 10^{-2}$ | $1.52 \times 10^{-2}$ | 0.00 |
| **Test 2** | $8.72 \times 10^{-3}$ | $2.33 \times 10^{-2}$ | $1.55 \times 10^{-2}$ | 0.00 |
| **Test 3** | $8.20 \times 10^{-3}$ | $2.95 \times 10^{-2}$ | $1.25 \times 10^{-2}$ | 0.00 |
| **Test 4** | $8.64 \times 10^{-3}$ | $2.21 \times 10^{-2}$ | $1.50 \times 10^{-2}$ | 0.00 |
| **Test 5** | $8.27 \times 10^{-3}$ | $1.62 \times 10^{-2}$ | $1.50 \times 10^{-2}$ | 0.00 |
| **Mean** | $8.57 \times 10^{-3}$ | $2.33 \times 10^{-2}$ | $1.46 \times 10^{-2}$ | 0.00 |

Table B.6     Performance of retuned backstepping for normal payload (0.22kg) at hybrid mode, trajectory 1

| Errors(radian) | RMSE | MAE | SSE | SSA |
|:---:|:---:|:---:|:---:|:---:|
| **Test 1** | $1.91 \times 10^{-3}$ | $1.07 \times 10^{-2}$ | $6.93 \times 10^{-4}$ | $1.00 \times 10^{-4}$ |
| **Test 2** | $1.52 \times 10^{-3}$ | $7.20 \times 10^{-3}$ | $1.10 \times 10^{-3}$ | 0.00 |
| **Test 3** | $1.49 \times 10^{-3}$ | $9.70 \times 10^{-3}$ | $1.10 \times 10^{-3}$ | 0.00 |
| **Test 4** | $1.54 \times 10^{-3}$ | $7.00 \times 10^{-3}$ | $1.10 \times 10^{-3}$ | 0.00 |
| **Test 5** | $1.95 \times 10^{-3}$ | $1.00 \times 10^{-2}$ | $2.20 \times 10^{-3}$ | 0.00 |
| **Mean** | $1.68 \times 10^{-3}$ | $0.89 \times 10^{-2}$ | $1.24 \times 10^{-3}$ | $2.00 \times 10^{-5}$ |

Table B.7      Performance of retuned backstepping for normal payload (0.22kg) at pneumatic mode, trajectory 4

|           | RMSE(radian)          | MAE(radian)           |
|-----------|-----------------------|-----------------------|
| **Test 1** | $3.78 \times 10^{-2}$ | $1.37 \times 10^{-1}$ |
| **Test 2** | $3.85 \times 10^{-2}$ | $1.37 \times 10^{-1}$ |
| **Test 3** | $3.75 \times 10^{-2}$ | $1.39 \times 10^{-1}$ |
| **Test 4** | $4.11 \times 10^{-2}$ | $1.36 \times 10^{-1}$ |
| **Test 5** | $4.44 \times 10^{-2}$ | $1.41 \times 10^{-1}$ |
| **Mean**   | $3.99 \times 10^{-2}$ | $1.38 \times 10^{-1}$ |

Table B.8      Performance of retuned backstepping for normal payload (0.22kg) at hybrid mode, trajectory 4

|           | RMSE(radian)          | MAE(radian)           |
|-----------|-----------------------|-----------------------|
| **Test 1** | $4.26 \times 10^{-2}$ | $1.50 \times 10^{-1}$ |
| **Test 2** | $3.45 \times 10^{-2}$ | $1.38 \times 10^{-1}$ |
| **Test 3** | $3.87 \times 10^{-2}$ | $1.05 \times 10^{-1}$ |
| **Test 4** | $2.58 \times 10^{-2}$ | $1.05 \times 10^{-1}$ |
| **Test 5** | $3.29 \times 10^{-2}$ | $1.38 \times 10^{-1}$ |
| **Mean**   | $3.49 \times 10^{-2}$ | $1.27 \times 10^{-1}$ |

Table B.9      Performance of retuned backstepping for large payload (0.32kg) at pneumatic mode, trajectory 1

| Errors(radian) | RMSE | MAE | SSE | SSA |
|---|---|---|---|---|
| Test 1 | $8.13\times10^{-3}$ | $2.18\times10^{-2}$ | $1.10\times10^{-2}$ | $1.00\times10^{-4}$ |
| Test 2 | $8.26\times10^{-3}$ | $2.74\times10^{-2}$ | $1.31\times10^{-2}$ | 0.00 |
| Test 3 | $8.52\times10^{-3}$ | $2.27\times10^{-2}$ | $1.39\times10^{-2}$ | 0.00 |
| Test 4 | $8.35\times10^{-3}$ | $2.40\times10^{-2}$ | $1.37\times10^{-2}$ | 0.00 |
| Test 5 | $8.23\times10^{-3}$ | $2.45\times10^{-2}$ | $1.36\times10^{-2}$ | 0.00 |
| Mean | $8.30\times10^{-3}$ | $2.41\times10^{-2}$ | $1.31\times10^{-2}$ | $2.00\times10^{-5}$ |

Table B.10      Performance of retuned backstepping for large payload (0.32kg) at hybrid mode, trajectory 1

| Errors(radian) | RMSE | MAE | SSE | SSA |
|---|---|---|---|---|
| Test 1 | $4.54\times10^{-3}$ | $1.11\times10^{-2}$ | $1.08\times10^{-2}$ | 0.00 |
| Test 2 | $4.61\times10^{-3}$ | $1.13\times10^{-2}$ | $1.10\times10^{-2}$ | 0.00 |
| Test 3 | $5.09\times10^{-3}$ | $1.63\times10^{-2}$ | $1.17\times10^{-2}$ | 0.00 |
| Test 4 | $4.47\times10^{-3}$ | $1.11\times10^{-2}$ | $1.08\times10^{-2}$ | 0.00 |
| Test 5 | $4.64\times10^{-3}$ | $1.15\times10^{-2}$ | $1.12\times10^{-2}$ | 0.00 |
| Mean | $4.67\times10^{-3}$ | $1.23\times10^{-2}$ | $1.11\times10^{-2}$ | 0.00 |

Table B.11      Performance of retuned backstepping for large payload (0.32kg) at
pneumatic mode, trajectory 4

|        | RMSE(radian) | MAE(radian) |
|--------|--------------|-------------|
| Test 1 | $5.39 \times 10^{-2}$ | $1.39 \times 10^{-1}$ |
| Test 2 | $5.05 \times 10^{-2}$ | $1.42 \times 10^{-1}$ |
| Test 3 | $5.65 \times 10^{-2}$ | $1.45 \times 10^{-1}$ |
| Test 4 | $5.88 \times 10^{-2}$ | $1.46 \times 10^{-1}$ |
| Test 5 | $5.62 \times 10^{-2}$ | $1.44 \times 10^{-1}$ |
| Mean   | $5.52 \times 10^{-2}$ | $1.43 \times 10^{-1}$ |

Table B.12      Performance of retuned backstepping for large payload (0.32kg) at hybrid

mode, trajectory 4

|        | RMSE(radian) | MAE(radian) |
|--------|--------------|-------------|
| Test 1 | $7.76 \times 10^{-2}$ | $1.70 \times 10^{-1}$ |
| Test 2 | $7.67 \times 10^{-2}$ | $1.55 \times 10^{-1}$ |
| Test 3 | $7.66 \times 10^{-2}$ | $1.69 \times 10^{-1}$ |
| Test 4 | $7.68 \times 10^{-2}$ | $1.73 \times 10^{-1}$ |
| Test 5 | $7.69 \times 10^{-2}$ | $1.63 \times 10^{-1}$ |
| Mean   | $7.69 \times 10^{-2}$ | $1.66 \times 10^{-1}$ |

# APPENDIX.C    VERTICAL BACKSTEPPING EXPERIMENT

## RESULTS

Table C.1      Performance of retuned backstepping for no payload (0 kg) at pneumatic mode, trajectory 1

| Errors(radian) | RMSE | MAE | SSE | SSA |
|---|---|---|---|---|
| Test 1 | $1.75 \times 10^{-2}$ | $4.44 \times 10^{-2}$ | $4.41 \times 10^{-2}$ | $7.00 \times 10^{-4}$ |
| Test 2 | $1.74 \times 10^{-2}$ | $4.38 \times 10^{-2}$ | $4.36 \times 10^{-2}$ | $7.00 \times 10^{-4}$ |
| Test 3 | $1.74 \times 10^{-2}$ | $4.40 \times 10^{-2}$ | $4.37 \times 10^{-2}$ | $6.00 \times 10^{-4}$ |
| Test 4 | $1.74 \times 10^{-2}$ | $4.40 \times 10^{-2}$ | $4.38 \times 10^{-2}$ | $6.00 \times 10^{-4}$ |
| Test 5 | $1.74 \times 10^{-2}$ | $4.37 \times 10^{-2}$ | $4.34 \times 10^{-2}$ | $7.00 \times 10^{-4}$ |
| Mean | $1.74 \times 10^{-2}$ | $4.40 \times 10^{-2}$ | $4.37 \times 10^{-2}$ | $6.60 \times 10^{-4}$ |

Table C.2      Performance of retuned backstepping for no payload (0 kg) at hybrid mode, trajectory 1

| Errors(radian) | RMSE | MAE | SSE | SSA |
|---|---|---|---|---|
| Test 1 | $5.53 \times 10^{-3}$ | $1.69 \times 10^{-2}$ | $1.69 \times 10^{-2}$ | 0.00 |
| Test 2 | $5.45 \times 10^{-3}$ | $1.63 \times 10^{-2}$ | $1.63 \times 10^{-2}$ | $1.00 \times 10^{-4}$ |
| Test 3 | $5.32 \times 10^{-3}$ | $1.60 \times 10^{-2}$ | $1.58 \times 10^{-2}$ | $5.00 \times 10^{-4}$ |
| Test 4 | $5.57 \times 10^{-3}$ | $1.68 \times 10^{-2}$ | $1.67 \times 10^{-2}$ | $2.00 \times 10^{-4}$ |
| Test 5 | $6.30 \times 10^{-3}$ | $1.98 \times 10^{-2}$ | $1.97 \times 10^{-2}$ | $6.00 \times 10^{-4}$ |
| Mean | $5.63 \times 10^{-3}$ | $1.72 \times 10^{-2}$ | $1.71 \times 10^{-2}$ | $2.80 \times 10^{-4}$ |

Table C.3          Performance of retuned backstepping for no payload (0 kg) at pneumatic mode, trajectory 4

|  | RMSE(radian) | MAE(radian) |
|---|---|---|
| **Test 1** | $2.39 \times 10^{-2}$ | $1.08 \times 10^{-1}$ |
| **Test 2** | $2.40 \times 10^{-2}$ | $9.95 \times 10^{-2}$ |
| **Test 3** | $2.48 \times 10^{-2}$ | $9.98 \times 10^{-2}$ |
| **Test 4** | $2.59 \times 10^{-2}$ | $1.05 \times 10^{-1}$ |
| **Test 5** | $3.02 \times 10^{-2}$ | $1.28 \times 10^{-1}$ |
| **Mean** | $2.58 \times 10^{-2}$ | $1.08 \times 10^{-1}$ |

Table C.4          Performance of retuned backstepping for no payload (0 kg) at hybrid mode, trajectory 4

|  | RMSE(radian) | MAE(radian) |
|---|---|---|
| **Test 1** | $9.08 \times 10^{-3}$ | $6.18 \times 10^{-2}$ |
| **Test 2** | $1.16 \times 10^{-2}$ | $8.62 \times 10^{-2}$ |
| **Test 3** | $8.26 \times 10^{-3}$ | $5.75 \times 10^{-2}$ |
| **Test 4** | $8.78 \times 10^{-3}$ | $6.59 \times 10^{-2}$ |
| **Test 5** | $9.57 \times 10^{-3}$ | $6.99 \times 10^{-2}$ |
| **Mean** | $9.46 \times 10^{-3}$ | $6.83 \times 10^{-2}$ |

Table C.5      Performance of retuned backstepping for small payload (0.12 kg) at pneumatic mode, trajectory 1

| Errors(radian) | RMSE | MAE | SSE | SSA |
|---|---|---|---|---|
| Test 1 | $7.73 \times 10^{-3}$ | $2.13 \times 10^{-2}$ | $2.09 \times 10^{-2}$ | $1.10 \times 10^{-3}$ |
| Test 2 | $7.79 \times 10^{-3}$ | $2.21 \times 10^{-2}$ | $2.17 \times 10^{-2}$ | $1.10 \times 10^{-3}$ |
| Test 3 | $8.02 \times 10^{-3}$ | $2.15 \times 10^{-2}$ | $2.11 \times 10^{-2}$ | $1.10 \times 10^{-3}$ |
| Test 4 | $7.87 \times 10^{-3}$ | $2.19 \times 10^{-2}$ | $2.17 \times 10^{-2}$ | $7.00 \times 10^{-4}$ |
| Test 5 | $7.63 \times 10^{-3}$ | $2.09 \times 10^{-2}$ | $2.05 \times 10^{-2}$ | $1.00 \times 10^{-3}$ |
| Mean | $7.81 \times 10^{-3}$ | $2.15 \times 10^{-2}$ | $2.12 \times 10^{-2}$ | $1.00 \times 10^{-3}$ |

Table C.6      Performance of retuned backstepping for small payload (0.12kg) at hybrid mode, trajectory 1

| Errors(radian) | RMSE | MAE | SSE | SSA |
|---|---|---|---|---|
| Test 1 | $1.60 \times 10^{-3}$ | $4.60 \times 10^{-3}$ | $4.50 \times 10^{-3}$ | 0.00 |
| Test 2 | $1.61 \times 10^{-3}$ | $4.60 \times 10^{-3}$ | $4.56 \times 10^{-3}$ | $1.00 \times 10^{-4}$ |
| Test 3 | $1.98 \times 10^{-3}$ | $1.44 \times 10^{-2}$ | $4.73 \times 10^{-3}$ | $1.00 \times 10^{-4}$ |
| Test 4 | $1.61 \times 10^{-3}$ | $4.80 \times 10^{-3}$ | $4.62 \times 10^{-3}$ | $3.00 \times 10^{-4}$ |
| Test 5 | $1.62 \times 10^{-3}$ | $4.60 \times 10^{-3}$ | $4.60 \times 10^{-3}$ | 0.00 |
| Mean | $1.68 \times 10^{-3}$ | $6.60 \times 10^{-3}$ | $4.60 \times 10^{-3}$ | $1.00 \times 10^{-4}$ |

Table C.7      Performance of retuned backstepping for small payload (0.12kg) at pneumatic mode, trajectory 4

|  | RMSE(radian) | MAE(radian) |
|---|---|---|
| **Test 1** | $2.63\times10^{-2}$ | $1.37\times10^{-1}$ |
| **Test 2** | $3.04\times10^{-2}$ | $1.44\times10^{-1}$ |
| **Test 3** | $3.51\times10^{-2}$ | $1.57\times10^{-1}$ |
| **Test 4** | $2.81\times10^{-2}$ | $1.38\times10^{-1}$ |
| **Test 5** | $3.94\times10^{-2}$ | $1.48\times10^{-1}$ |
| **Mean** | $3.19\times10^{-2}$ | $1.45\times10^{-1}$ |

Table C.8      Performance of retuned backstepping for small payload (0.12kg) at hybrid mode, trajectory 4

|  | RMSE(radian) | MAE(radian) |
|---|---|---|
| **Test 1** | $2.42\times10^{-2}$ | $9.31\times10^{-2}$ |
| **Test 2** | $1.45\times10^{-2}$ | $8.84\times10^{-2}$ |
| **Test 3** | $2.35\times10^{-2}$ | $1.15\times10^{-1}$ |
| **Test 4** | $2.61\times10^{-2}$ | $1.33\times10^{-1}$ |
| **Test 5** | $1.71\times10^{-2}$ | $1.06\times10^{-1}$ |
| **Mean** | $2.11\times10^{-2}$ | $1.07\times10^{-1}$ |

Table C.9          Performance of retuned backstepping for normal payload (0.22kg) at pneumatic mode, trajectory 1

| Errors(radian) | RMSE | MAE | SSE | SSA |
|---|---|---|---|---|
| **Test 1** | $1.13\times10^{-2}$ | $2.82\times10^{-2}$ | $7.86\times10^{-3}$ | $1.00\times10^{-3}$ |
| **Test 2** | $1.09\times10^{-2}$ | $2.51\times10^{-2}$ | $8.07\times10^{-3}$ | $3.00\times10^{-4}$ |
| **Test 3** | $1.09\times10^{-2}$ | $2.50\times10^{-2}$ | $8.26\times10^{-3}$ | $1.00\times10^{-3}$ |
| **Test 4** | $1.08\times10^{-2}$ | $2.43\times10^{-2}$ | $7.29\times10^{-3}$ | $3.00\times10^{-4}$ |
| **Test 5** | $1.11\times10^{-2}$ | $2.65\times10^{-2}$ | $7.62\times10^{-3}$ | $5.00\times10^{-4}$ |
| **Mean** | $1.10\times10^{-2}$ | $2.58\times10^{-2}$ | $7.82\times10^{-3}$ | $6.20\times10^{-4}$ |

Table C.10          Performance of retuned backstepping for normal payload (0.22kg) at hybrid mode, trajectory 1

| Errors(radian) | RMSE | MAE | SSE | SSA |
|---|---|---|---|---|
| **Test 1** | $1.33\times10^{-3}$ | $2.90\times10^{-3}$ | $2.68\times10^{-3}$ | $1.00\times10^{-4}$ |
| **Test 2** | $1.34\times10^{-3}$ | $3.10\times10^{-3}$ | $2.67\times10^{-3}$ | $1.00\times10^{-4}$ |
| **Test 3** | $3.43\times10^{-3}$ | $3.26\times10^{-2}$ | $2.69\times10^{-3}$ | $1.00\times10^{-4}$ |
| **Test 4** | $1.35\times10^{-3}$ | $3.10\times10^{-3}$ | $2.70\times10^{-3}$ | 0.00 |
| **Test 5** | $1.32\times10^{-3}$ | $3.00\times10^{-3}$ | $2.60\times10^{-3}$ | $2.00\times10^{-4}$ |
| **Mean** | $1.75\times10^{-3}$ | $8.94\times10^{-3}$ | $2.67\times10^{-3}$ | $1.00\times10^{-4}$ |

Table C.11     Performance of retuned backstepping for normal payload (0.22kg) at pneumatic mode, trajectory 4

|  | RMSE(radian) | MAE(radian) |
|---|---|---|
| **Test 1** | $7.87\times10^{-2}$ | $2.11\times10^{-1}$ |
| **Test 2** | $7.85\times10^{-2}$ | $2.06\times10^{-1}$ |
| **Test 3** | $7.28\times10^{-2}$ | $2.21\times10^{-1}$ |
| **Test 4** | $7.39\times10^{-2}$ | $1.80\times10^{-1}$ |
| **Test 5** | $7.40\times10^{-2}$ | $1.93\times10^{-1}$ |
| **Mean** | $7.56\times10^{-2}$ | $2.02\times10^{-1}$ |

Table C.12     Performance of retuned backstepping for normal payload (0.22kg) at hybrid mode, trajectory 4

|  | RMSE(radian) | MAE(radian) |
|---|---|---|
| **Test 1** | $3.76\times10^{-2}$ | $1.64\times10^{-1}$ |
| **Test 2** | $5.18\times10^{-2}$ | $2.21\times10^{-1}$ |
| **Test 3** | $3.39\times10^{-2}$ | $1.55\times10^{-1}$ |
| **Test 4** | $5.11\times10^{-2}$ | $1.68\times10^{-1}$ |
| **Test 5** | $3.46\times10^{-2}$ | $1.39\times10^{-1}$ |
| **Mean** | $4.18\times10^{-2}$ | $1.69\times10^{-1}$ |

Table C.13    Performance of retuned backstepping for large payload (0.32kg) at pneumatic mode, trajectory 1

| Errors(radian) | RMSE | MAE | SSE | SSA |
|---|---|---|---|---|
| **Test 1** | $2.68 \times 10^{-1}$ | $4.73 \times 10^{-1}$ | $4.71 \times 10^{-1}$ | 0.00 |
| **Test 2** | $1.97 \times 10^{-1}$ | $3.61 \times 10^{-1}$ | $3.61 \times 10^{-1}$ | 0.00 |
| **Test 3** | $1.92 \times 10^{-1}$ | $3.54 \times 10^{-1}$ | $3.54 \times 10^{-1}$ | 0.00 |
| **Test 4** | $1.90 \times 10^{-1}$ | $3.50 \times 10^{-1}$ | $3.50 \times 10^{-1}$ | 0.00 |
| **Test 5** | $1.87 \times 10^{-1}$ | $3.46 \times 10^{-1}$ | $3.46 \times 10^{-1}$ | 0.00 |
| **Mean** | $2.07 \times 10^{-1}$ | $3.77 \times 10^{-1}$ | $3.76 \times 10^{-1}$ | 0.00 |

Table C.14    Performance of retuned backstepping for large payload (0.32kg) at hybrid mode, trajectory 1

| Errors(radian) | RMSE | MAE | SSE | SSA |
|---|---|---|---|---|
| **Test 1** | $4.37 \times 10^{-3}$ | $1.70 \times 10^{-2}$ | $5.58 \times 10^{-4}$ | $1.00 \times 10^{-4}$ |
| **Test 2** | $3.75 \times 10^{-3}$ | $1.35 \times 10^{-2}$ | $5.00 \times 10^{-4}$ | 0.00 |
| **Test 3** | $3.71 \times 10^{-3}$ | $1.23 \times 10^{-2}$ | $5.93 \times 10^{-4}$ | $1.00 \times 10^{-4}$ |
| **Test 4** | $3.78 \times 10^{-3}$ | $1.24 \times 10^{-2}$ | $6.39 \times 10^{-4}$ | $1.00 \times 10^{-4}$ |
| **Test 5** | $3.98 \times 10^{-3}$ | $1.27 \times 10^{-2}$ | $3.79 \times 10^{-4}$ | $1.00 \times 10^{-4}$ |
| **Mean** | $3.92 \times 10^{-3}$ | $1.36 \times 10^{-2}$ | $5.34 \times 10^{-4}$ | $8.00 \times 10^{-5}$ |

Table C.15     Performance of retuned backstepping for large payload (0.32kg) at pneumatic mode, trajectory 4

|          | RMSE(radian)        | MAE(radian)         |
|----------|---------------------|---------------------|
| Test 1   | $1.79 \times 10^{-1}$ | $3.23 \times 10^{-1}$ |
| Test 2   | $1.74 \times 10^{-1}$ | $3.08 \times 10^{-1}$ |
| Test 3   | $1.77 \times 10^{-1}$ | $3.16 \times 10^{-1}$ |
| Test 4   | $1.76 \times 10^{-1}$ | $3.19 \times 10^{-1}$ |
| Test 5   | $1.85 \times 10^{-1}$ | $3.30 \times 10^{-1}$ |
| Mean     | $1.78 \times 10^{-1}$ | $3.19 \times 10^{-1}$ |

Table C.16     Performance of retuned backstepping for large payload (0.32kg) at hybrid mode, trajectory 4

|          | RMSE(radian)        | MAE(radian)         |
|----------|---------------------|---------------------|
| Test 1   | $1.45 \times 10^{-1}$ | $3.91 \times 10^{-1}$ |
| Test 2   | $1.40 \times 10^{-1}$ | $3.81 \times 10^{-1}$ |
| Test 3   | $1.30 \times 10^{-1}$ | $2.95 \times 10^{-1}$ |
| Test 4   | $1.38 \times 10^{-1}$ | $3.43 \times 10^{-1}$ |
| Test 5   | $1.36 \times 10^{-1}$ | $2.99 \times 10^{-1}$ |
| Mean     | $1.38 \times 10^{-1}$ | $3.42 \times 10^{-1}$ |

# APPENDIX.D     VERTICAL DVMPC EXPERIMENT RESULTS

Table D.1      Performance of retuned DVMPC for no payload (0kg) at pneumatic mode, without payload estimation, trajectory 1

| Errors(radian) | RMSE | MAE | SSE | SSA |
|---|---|---|---|---|
| **Test 1** | $1.08 \times 10^{-2}$ | $2.93 \times 10^{-2}$ | $1.22 \times 10^{-2}$ | $1.40 \times 10^{-3}$ |
| **Test 2** | $1.10 \times 10^{-2}$ | $3.03 \times 10^{-2}$ | $1.27 \times 10^{-2}$ | $2.20 \times 10^{-3}$ |
| **Test 3** | $1.27 \times 10^{-2}$ | $7.24 \times 10^{-2}$ | $1.22 \times 10^{-2}$ | $1.40 \times 10^{-3}$ |
| **Test 4** | $1.10 \times 10^{-2}$ | $3.20 \times 10^{-2}$ | $1.24 \times 10^{-2}$ | $2.10 \times 10^{-3}$ |
| **Test 5** | $1.11 \times 10^{-2}$ | $3.25 \times 10^{-2}$ | $1.24 \times 10^{-2}$ | $1.90 \times 10^{-3}$ |
| **Mean** | $1.13 \times 10^{-2}$ | $3.93 \times 10^{-2}$ | $1.24 \times 10^{-2}$ | $1.80 \times 10^{-3}$ |

Table D.2      Performance of retuned DVMPC for no payload (0kg) at hybrid mode, without payload estimation, trajectory 1

| Errors(radian) | RMSE | MAE | SSE | SSA |
|---|---|---|---|---|
| **Test 1** | $7.10 \times 10^{-3}$ | $3.35 \times 10^{-2}$ | $9.16 \times 10^{-3}$ | $8.00 \times 10^{-4}$ |
| **Test 2** | $6.93 \times 10^{-3}$ | $1.26 \times 10^{-2}$ | $9.18 \times 10^{-3}$ | $6.00 \times 10^{-4}$ |
| **Test 3** | $6.93 \times 10^{-3}$ | $1.28 \times 10^{-2}$ | $9.25 \times 10^{-3}$ | $6.00 \times 10^{-4}$ |
| **Test 4** | $6.96 \times 10^{-3}$ | $1.27 \times 10^{-2}$ | $9.23 \times 10^{-3}$ | $5.00 \times 10^{-4}$ |
| **Test 5** | $6.97 \times 10^{-3}$ | $1.25 \times 10^{-2}$ | $9.28 \times 10^{-3}$ | $5.00 \times 10^{-4}$ |
| **Mean** | $6.98 \times 10^{-3}$ | $1.68 \times 10^{-2}$ | $9.22 \times 10^{-3}$ | $6.00 \times 10^{-4}$ |

Table D.3      Performance of retuned DVMPC for no payload (0kg) at pneumatic mode, without payload estimation, trajectory 4

|        | RMSE(radian) | MAE(radian) |
|--------|--------------|-------------|
| Test 1 | $1.61 \times 10^{-2}$ | $5.84 \times 10^{-2}$ |
| Test 2 | $1.41 \times 10^{-2}$ | $3.00 \times 10^{-2}$ |
| Test 3 | $1.43 \times 10^{-2}$ | $5.46 \times 10^{-2}$ |
| Test 4 | $1.40 \times 10^{-2}$ | $5.15 \times 10^{-2}$ |
| Test 5 | $1.40 \times 10^{-2}$ | $4.88 \times 10^{-2}$ |
| Mean   | $1.45 \times 10^{-2}$ | $4.87 \times 10^{-2}$ |

Table D.4      Performance of retuned DVMPC for no payload (0kg) at hybrid mode, without payload estimation, trajectory 4

|        | RMSE(radian) | MAE(radian) |
|--------|--------------|-------------|
| Test 1 | $9.77 \times 10^{-3}$ | $5.13 \times 10^{-2}$ |
| Test 2 | $9.34 \times 10^{-3}$ | $2.33 \times 10^{-2}$ |
| Test 3 | $9.82 \times 10^{-3}$ | $5.11 \times 10^{-2}$ |
| Test 4 | $9.97 \times 10^{-3}$ | $5.52 \times 10^{-2}$ |
| Test 5 | $9.67 \times 10^{-3}$ | $4.84 \times 10^{-2}$ |
| Mean   | $9.71 \times 10^{-3}$ | $4.59 \times 10^{-2}$ |

Table D.5      Performance of retuned DVMPC for no payload (0kg) at pneumatic mode, with payload estimation, trajectory 1

| Errors(radian) | RMSE | MAE | SSE | SSA |
|---|---|---|---|---|
| Test 1 | $7.23 \times 10^{-2}$ | $2.18 \times 10^{-1}$ | $8.29 \times 10^{-2}$ | $2.38 \times 10^{-1}$ |
| Test 2 | $1.36 \times 10^{-2}$ | $5.30 \times 10^{-2}$ | $1.24 \times 10^{-2}$ | $2.40 \times 10^{-3}$ |
| Test 3 | $9.82 \times 10^{-1}$ | 1.52 | 1.52 | 0.00 |
| Test 4 | $1.12 \times 10^{-2}$ | $2.60 \times 10^{-2}$ | $1.37 \times 10^{-2}$ | $2.50 \times 10^{-3}$ |
| Test 5 | $1.05 \times 10^{-2}$ | $3.06 \times 10^{-2}$ | $1.20 \times 10^{-2}$ | $1.80 \times 10^{-3}$ |
| Mean | $2.18 \times 10^{-1}$ | $3.70 \times 10^{-1}$ | $3.28 \times 10^{-1}$ | $4.89 \times 10^{-2}$ |

Table D.6      Performance of retuned DVMPC for no payload (0kg) at hybrid mode, with payload estimation, trajectory 1

| Errors(radian) | RMSE | MAE | SSE | SSA |
|---|---|---|---|---|
| Test 1 | $4.47 \times 10^{-3}$ | $1.06 \times 10^{-2}$ | $5.87 \times 10^{-3}$ | $8.00 \times 10^{-4}$ |
| Test 2 | $8.71 \times 10^{-2}$ | $2.89 \times 10^{-1}$ | $1.35 \times 10^{-1}$ | $3.87 \times 10^{-1}$ |
| Test 3 | $9.83 \times 10^{-1}$ | 1.52 | 1.52 | 0.00 |
| Test 4 | $7.15 \times 10^{-3}$ | $1.42 \times 10^{-2}$ | $9.40 \times 10^{-3}$ | $5.00 \times 10^{-4}$ |
| Test 5 | $7.08 \times 10^{-3}$ | $1.44 \times 10^{-2}$ | $9.52 \times 10^{-3}$ | $5.00 \times 10^{-4}$ |
| Mean | $2.18 \times 10^{-1}$ | $3.70 \times 10^{-2}$ | $3.36 \times 10^{-1}$ | $7.78 \times 10^{-2}$ |

Table D.7      Performance of retuned DVMPC for no payload (0kg) at pneumatic mode, with payload estimation, trajectory 4

|        | RMSE(radian)          | MAE(radian)           |
|--------|-----------------------|-----------------------|
| **Test 1** | $4.34 \times 10^{-2}$ | $9.70 \times 10^{-2}$ |
| **Test 2** | $3.76 \times 10^{-2}$ | $1.25 \times 10^{-1}$ |
| **Test 3** | $9.46 \times 10^{-3}$ | $3.82 \times 10^{-2}$ |
| **Test 4** | $9.94 \times 10^{-3}$ | $2.61 \times 10^{-2}$ |
| **Test 5** | $2.21 \times 10^{-2}$ | $5.71 \times 10^{-2}$ |
| **Mean**   | $2.45 \times 10^{-2}$ | $6.87 \times 10^{-2}$ |

Table D.8      Performance of retuned DVMPC for no payload (0kg) at hybrid mode, with payload estimation, trajectory 4

|        | RMSE(radian)          | MAE(radian)           |
|--------|-----------------------|-----------------------|
| **Test 1** | $1.26 \times 10^{-2}$ | $6.85 \times 10^{-2}$ |
| **Test 2** | $9.43 \times 10^{-3}$ | $5.82 \times 10^{-2}$ |
| **Test 3** | $7.67 \times 10^{-3}$ | $3.99 \times 10^{-2}$ |
| **Test 4** | $7.44 \times 10^{-3}$ | $3.63 \times 10^{-2}$ |
| **Test 5** | $9.60 \times 10^{-3}$ | $3.89 \times 10^{-2}$ |
| **Mean**   | $9.35 \times 10^{-3}$ | $4.84 \times 10^{-2}$ |

Table D.9      Performance of retuned DVMPC for small payload (0.12kg) at pneumatic mode, without payload estimation, trajectory 1

| Errors(radian) | RMSE | MAE | SSE | SSA |
|---|---|---|---|---|
| **Test 1** | $1.55 \times 10^{-2}$ | $2.58 \times 10^{-2}$ | $2.14 \times 10^{-2}$ | $7.00 \times 10^{-4}$ |
| **Test 2** | $1.52 \times 10^{-2}$ | $2.52 \times 10^{-2}$ | $2.00 \times 10^{-2}$ | $8.00 \times 10^{-4}$ |
| **Test 3** | $1.53 \times 10^{-2}$ | $2.57 \times 10^{-2}$ | $2.03 \times 10^{-2}$ | $5.00 \times 10^{-4}$ |
| **Test 4** | $1.53 \times 10^{-2}$ | $2.57 \times 10^{-2}$ | $2.03 \times 10^{-2}$ | $6.00 \times 10^{-4}$ |
| **Test 5** | $1.54 \times 10^{-2}$ | $2.47 \times 10^{-2}$ | $2.14 \times 10^{-2}$ | $3.00 \times 10^{-4}$ |
| **Mean** | $1.53 \times 10^{-2}$ | $2.54 \times 10^{-2}$ | $2.07 \times 10^{-2}$ | $5.80 \times 10^{-4}$ |

Table D.10      Performance of retuned DVMPC for small payload (0.12kg) at hybrid mode, without payload estimation, trajectory 1

| Errors(radian) | RMSE | MAE | SSE | SSA |
|---|---|---|---|---|
| **Test 1** | $1.02 \times 10^{-2}$ | $1.83 \times 10^{-2}$ | $1.37 \times 10^{-2}$ | $4.00 \times 10^{-4}$ |
| **Test 2** | $1.02 \times 10^{-2}$ | $1.88 \times 10^{-2}$ | $1.39 \times 10^{-2}$ | $3.00 \times 10^{-4}$ |
| **Test 3** | $1.02 \times 10^{-2}$ | $1.85 \times 10^{-2}$ | $1.39 \times 10^{-2}$ | $3.00 \times 10^{-4}$ |
| **Test 4** | $1.02 \times 10^{-2}$ | $1.84 \times 10^{-2}$ | $1.40 \times 10^{-2}$ | $3.00 \times 10^{-4}$ |
| **Test 5** | $1.02 \times 10^{-2}$ | $1.80 \times 10^{-2}$ | $1.40 \times 10^{-2}$ | $4.00 \times 10^{-4}$ |
| **Mean** | $1.02 \times 10^{-2}$ | $1.84 \times 10^{-2}$ | $1.39 \times 10^{-2}$ | $3.40 \times 10^{-4}$ |

Table D.11     Performance of retuned DVMPC for small payload (0.12kg) at pneumatic mode, without payload estimation, trajectory 4

|  | RMSE(radian) | MAE(radian) |
|---|---|---|
| Test 1 | $1.69 \times 10^{-2}$ | $6.32 \times 10^{-2}$ |
| Test 2 | $1.71 \times 10^{-2}$ | $5.13 \times 10^{-2}$ |
| Test 3 | $1.69 \times 10^{-2}$ | $7.07 \times 10^{-2}$ |
| Test 4 | $1.66 \times 10^{-2}$ | $6.38 \times 10^{-2}$ |
| Test 5 | $1.82 \times 10^{-2}$ | $7.50 \times 10^{-2}$ |
| Mean | $1.71 \times 10^{-2}$ | $6.48 \times 10^{-2}$ |

Table D.12     Performance of retuned DVMPC for small payload (0.12kg) at hybrid mode, without payload estimation, trajectory 4

|  | RMSE(radian) | MAE(radian) |
|---|---|---|
| Test 1 | $1.14 \times 10^{-2}$ | $6.46 \times 10^{-2}$ |
| Test 2 | $1.10 \times 10^{-2}$ | $5.90 \times 10^{-2}$ |
| Test 3 | $1.10 \times 10^{-2}$ | $6.08 \times 10^{-2}$ |
| Test 4 | $1.11 \times 10^{-2}$ | $6.17 \times 10^{-2}$ |
| Test 5 | $1.15 \times 10^{-2}$ | $6.83 \times 10^{-2}$ |
| Mean | $1.12 \times 10^{-2}$ | $6.29 \times 10^{-2}$ |

Table D.13    Performance of retuned DVMPC for small payload (0.12kg) at pneumatic

mode, with payload estimation, trajectory 1

| Errors(radian) | RMSE | MAE | SSE | SSA |
|---|---|---|---|---|
| Test 1 | $1.42\times10^{-2}$ | $2.39\times10^{-2}$ | $1.87\times10^{-2}$ | $1.00\times10^{-3}$ |
| Test 2 | $1.85\times10^{-2}$ | $3.03\times10^{-2}$ | $2.46\times10^{-2}$ | $1.00\times10^{-3}$ |
| Test 3 | $1.84\times10^{-2}$ | $3.12\times10^{-2}$ | $2.45\times10^{-2}$ | $7.00\times10^{-4}$ |
| Test 4 | $1.45\times10^{-2}$ | $2.45\times10^{-2}$ | $1.91\times10^{-2}$ | $5.00\times10^{-4}$ |
| Test 5 | $1.36\times10^{-2}$ | $2.28\times10^{-2}$ | $1.77\times10^{-2}$ | $7.00\times10^{-4}$ |
| Mean | $1.58\times10^{-2}$ | $2.65\times10^{-2}$ | $2.09\times10^{-2}$ | $7.80\times10^{-4}$ |

Table D.14    Performance of retuned DVMPC for small payload (0.12kg) at hybrid

mode, with payload estimation, trajectory 1

| Errors(radian) | RMSE | MAE | SSE | SSA |
|---|---|---|---|---|
| Test 1 | $4.70\times10^{-3}$ | $1.15\times10^{-2}$ | $5.93\times10^{-3}$ | $6.00\times10^{-4}$ |
| Test 2 | $4.78\times10^{-3}$ | $9.50\times10^{-3}$ | $6.19\times10^{-3}$ | $5.00\times10^{-4}$ |
| Test 3 | $4.78\times10^{-3}$ | $9.10\times10^{-3}$ | $6.27\times10^{-3}$ | $5.00\times10^{-4}$ |
| Test 4 | $4.76\times10^{-3}$ | $9.50\times10^{-3}$ | $6.39\times10^{-3}$ | $4.00\times10^{-4}$ |
| Test 5 | $4.91\times10^{-3}$ | $9.20\times10^{-3}$ | $6.55\times10^{-3}$ | $7.00\times10^{-4}$ |
| Mean | $4.79\times10^{-3}$ | $0.98\times10^{-2}$ | $6.26\times10^{-3}$ | $5.40\times10^{-4}$ |

Table D.15     Performance of retuned DVMPC for small payload (0.12kg) at pneumatic

mode, with payload estimation, trajectory 4

|  | RMSE(radian) | MAE(radian) |
|---|---|---|
| **Test 1** | $2.47\times10^{-2}$ | $9.10\times10^{-2}$ |
| **Test 2** | $1.37\times10^{-2}$ | $6.77\times10^{-2}$ |
| **Test 3** | $1.08\times10^{-2}$ | $5.10\times10^{-2}$ |
| **Test 4** | $7.54\times10^{-1}$ | $9.42\times10^{-1}$ |
| **Test 5** | $9.56\times10^{-3}$ | $4.22\times10^{-2}$ |
| **Mean** | $1.63\times10^{-1}$ | $2.39\times10^{-1}$ |

Table D.16     Performance of retuned DVMPC for small payload (0.12kg) at hybrid

mode, with payload estimation, trajectory 4

|  | RMSE(radian) | MAE(radian) |
|---|---|---|
| **Test 1** | $7.43\times10^{-3}$ | $5.10\times10^{-2}$ |
| **Test 2** | $7.83\times10^{-3}$ | $5.91\times10^{-2}$ |
| **Test 3** | $7.77\times10^{-3}$ | $5.61\times10^{-2}$ |
| **Test 4** | $7.36\times10^{-3}$ | $4.79\times10^{-2}$ |
| **Test 5** | $7.65\times10^{-3}$ | $5.24\times10^{-2}$ |
| **Mean** | $7.61\times10^{-3}$ | $5.33\times10^{-2}$ |

Table D.17     Performance of retuned DVMPC for nominal payload (0.22kg) at pneumatic mode, without payload estimation, trajectory 1

| Errors(radian) | RMSE | MAE | SSE | SSA |
|---|---|---|---|---|
| Test 1 | $1.90 \times 10^{-2}$ | $3.01 \times 10^{-2}$ | $2.57 \times 10^{-2}$ | $4.00 \times 10^{-4}$ |
| Test 2 | $1.90 \times 10^{-2}$ | $3.02 \times 10^{-2}$ | $2.55 \times 10^{-2}$ | $4.00 \times 10^{-4}$ |
| Test 3 | $7.22 \times 10^{-2}$ | $4.37 \times 10^{-1}$ | $2.57 \times 10^{-2}$ | $4.00 \times 10^{-4}$ |
| Test 4 | $1.89 \times 10^{-2}$ | $2.96 \times 10^{-2}$ | $2.59 \times 10^{-2}$ | $5.00 \times 10^{-4}$ |
| Test 5 | $1.91 \times 10^{-2}$ | $3.03 \times 10^{-2}$ | $2.57 \times 10^{-2}$ | $4.00 \times 10^{-4}$ |
| Mean | $2.96 \times 10^{-2}$ | $1.11 \times 10^{-1}$ | $2.57 \times 10^{-2}$ | $4.20 \times 10^{-4}$ |

Table D.18     Performance of retuned DVMPC for nominal payload (0.22kg) at hybrid mode, without payload estimation, trajectory 1

| Errors(radian) | RMSE | MAE | SSE | SSA |
|---|---|---|---|---|
| Test 1 | $1.22 \times 10^{-2}$ | $2.11 \times 10^{-2}$ | $1.71 \times 10^{-2}$ | $5.00 \times 10^{-4}$ |
| Test 2 | $1.22 \times 10^{-2}$ | $2.15 \times 10^{-2}$ | $1.72 \times 10^{-2}$ | $3.00 \times 10^{-4}$ |
| Test 3 | $1.22 \times 10^{-2}$ | $2.18 \times 10^{-2}$ | $1.72 \times 10^{-2}$ | $3.00 \times 10^{-4}$ |
| Test 4 | $1.23 \times 10^{-2}$ | $2.20 \times 10^{-2}$ | $1.71 \times 10^{-2}$ | $3.00 \times 10^{-4}$ |
| Test 5 | $1.22 \times 10^{-2}$ | $2.17 \times 10^{-2}$ | $1.69 \times 10^{-2}$ | $6.00 \times 10^{-4}$ |
| Mean | $1.22 \times 10^{-2}$ | $2.17 \times 10^{-2}$ | $1.71 \times 10^{-2}$ | $4.00 \times 10^{-4}$ |

Table D.19     Performance of retuned DVMPC for nominal payload (0.22kg) at pneumatic mode, without payload estimation, trajectory 4

|        | RMSE(radian)          | MAE(radian)           |
|--------|-----------------------|-----------------------|
| Test 1 | $2.70 \times 10^{-2}$ | $1.19 \times 10^{-1}$ |
| Test 2 | $2.35 \times 10^{-2}$ | $8.80 \times 10^{-2}$ |
| Test 3 | $2.76 \times 10^{-2}$ | $1.14 \times 10^{-1}$ |
| Test 4 | $2.41 \times 10^{-2}$ | $9.70 \times 10^{-2}$ |
| Test 5 | $2.25 \times 10^{-2}$ | $9.30 \times 10^{-2}$ |
| Mean   | $2.49 \times 10^{-2}$ | $1.02 \times 10^{-1}$ |

Table D.20     Performance of retuned DVMPC for nominal payload (0.22kg) at hybrid mode, without payload estimation, trajectory 4

|        | RMSE(radian)          | MAE(radian)           |
|--------|-----------------------|-----------------------|
| Test 1 | $1.31 \times 10^{-2}$ | $7.69 \times 10^{-2}$ |
| Test 2 | $1.10 \times 10^{-2}$ | $5.02 \times 10^{-2}$ |
| Test 3 | $1.12 \times 10^{-2}$ | $5.84 \times 10^{-2}$ |
| Test 4 | $1.25 \times 10^{-2}$ | $6.94 \times 10^{-2}$ |
| Test 5 | $1.50 \times 10^{-2}$ | $7.95 \times 10^{-2}$ |
| Mean   | $1.26 \times 10^{-2}$ | $6.69 \times 10^{-2}$ |

Table D.21    Performance of retuned DVMPC for nominal payload (0.22kg) at pneumatic mode, with payload estimation, trajectory 1

| Errors(radian) | RMSE | MAE | SSE | SSA |
|---|---|---|---|---|
| Test 1 | $2.52 \times 10^{-2}$ | $3.94 \times 10^{-2}$ | $3.50 \times 10^{-2}$ | $4.00 \times 10^{-4}$ |
| Test 2 | $2.51 \times 10^{-2}$ | $3.89 \times 10^{-2}$ | $3.50 \times 10^{-2}$ | $1.00 \times 10^{-4}$ |
| Test 3 | $2.85 \times 10^{-2}$ | $4.33 \times 10^{-2}$ | $3.91 \times 10^{-2}$ | $8.00 \times 10^{-4}$ |
| Test 4 | $3.05 \times 10^{-2}$ | $4.68 \times 10^{-2}$ | $4.23 \times 10^{-2}$ | $6.00 \times 10^{-4}$ |
| Test 5 | $3.30 \times 10^{-2}$ | $1.81 \times 10^{-1}$ | $3.49 \times 10^{-2}$ | $7.00 \times 10^{-4}$ |
| Mean | $2.85 \times 10^{-2}$ | $6.99 \times 10^{-2}$ | $3.73 \times 10^{-2}$ | $5.20 \times 10^{-4}$ |

Table D.22    Performance of retuned DVMPC for nominal payload (0.22kg) at hybrid mode, with payload estimation, trajectory 1

| Errors(radian) | RMSE | MAE | SSE | SSA |
|---|---|---|---|---|
| Test 1 | $8.20 \times 10^{-3}$ | $1.53 \times 10^{-2}$ | $1.09 \times 10^{-2}$ | $3.00 \times 10^{-4}$ |
| Test 2 | $9.78 \times 10^{-3}$ | $1.77 \times 10^{-2}$ | $1.34 \times 10^{-2}$ | $5.00 \times 10^{-4}$ |
| Test 3 | $8.48 \times 10^{-3}$ | $1.56 \times 10^{-2}$ | $1.16 \times 10^{-2}$ | $5.00 \times 10^{-4}$ |
| Test 4 | $7.43 \times 10^{-3}$ | $1.31 \times 10^{-2}$ | $9.78 \times 10^{-3}$ | $6.00 \times 10^{-4}$ |
| Test 5 | $8.85 \times 10^{-3}$ | $3.26 \times 10^{-2}$ | $1.13 \times 10^{-2}$ | $2.00 \times 10^{-4}$ |
| Mean | $8.55 \times 10^{-3}$ | $1.89 \times 10^{-2}$ | $1.14 \times 10^{-2}$ | $4.20 \times 10^{-4}$ |

Table D.23    Performance of retuned DVMPC for nominal payload (0.22kg) at pneumatic mode, with payload estimation, trajectory 4

|  | RMSE(radian) | MAE(radian) |
|---|---|---|
| **Test 1** | $7.03 \times 10^{-1}$ | $9.58 \times 10^{-1}$ |
| **Test 2** | $2.35 \times 10^{-2}$ | $1.37 \times 10^{-1}$ |
| **Test 3** | $6.76 \times 10^{-1}$ | $9.86 \times 10^{-1}$ |
| **Test 4** | $7.51 \times 10^{-1}$ | 1.05 |
| **Test 5** | $3.24 \times 10^{-2}$ | $1.40 \times 10^{-1}$ |
| **Mean** | $4.37 \times 10^{-1}$ | $6.54 \times 10^{-1}$ |

Table D.24    Performance of retuned DVMPC for nominal payload (0.22kg) at hybrid mode, with payload estimation, trajectory 4

|  | RMSE(radian) | MAE(radian) |
|---|---|---|
| **Test 1** | $1.62 \times 10^{-2}$ | $7.90 \times 10^{-2}$ |
| **Test 2** | $6.49 \times 10^{-2}$ | $1.88 \times 10^{-1}$ |
| **Test 3** | $6.69 \times 10^{-2}$ | $1.73 \times 10^{-1}$ |
| **Test 4** | $6.70 \times 10^{-2}$ | $1.69 \times 10^{-1}$ |
| **Test 5** | $6.63 \times 10^{-2}$ | $1.56 \times 10^{-1}$ |
| **Mean** | $5.63 \times 10^{-2}$ | $1.53 \times 10^{-1}$ |

Table D.25     Performance of retuned DVMPC for large payload (0.32kg) at pneumatic mode, without payload estimation, trajectory 1

| Errors(radian) | RMSE | MAE | SSE | SSA |
|---|---|---|---|---|
| **Test 1** | $2.29\times10^{-2}$ | $4.12\times10^{-2}$ | $3.19\times10^{-2}$ | $2.00\times10^{-4}$ |
| **Test 2** | $2.28\times10^{-2}$ | $3.61\times10^{-2}$ | $3.21\times10^{-2}$ | $1.00\times10^{-4}$ |
| **Test 3** | $2.66\times10^{-2}$ | $1.06\times10^{-1}$ | $3.22\times10^{-2}$ | $2.00\times10^{-4}$ |
| **Test 4** | $2.29\times10^{-2}$ | $3.64\times10^{-2}$ | $3.25\times10^{-2}$ | $0.00$ |
| **Test 5** | $2.28\times10^{-2}$ | $3.66\times10^{-2}$ | $3.23\times10^{-2}$ | $1.00\times10^{-4}$ |
| **Mean** | $2.36\times10^{-2}$ | $5.13\times10^{-2}$ | $3.22\times10^{-2}$ | $1.20\times10^{-4}$ |

Table D.26     Performance of retuned DVMPC for large payload (0.32kg) at hybrid mode, without payload estimation, trajectory 1

| Errors(radian) | RMSE | MAE | SSE | SSA |
|---|---|---|---|---|
| **Test 1** | $1.63\times10^{-2}$ | $2.74\times10^{-2}$ | $2.30\times10^{-2}$ | $1.00\times10^{-4}$ |
| **Test 2** | $1.62\times10^{-2}$ | $2.83\times10^{-2}$ | $2.27\times10^{-2}$ | $1.00\times10^{-4}$ |
| **Test 3** | $1.62\times10^{-2}$ | $2.81\times10^{-2}$ | $2.24\times10^{-2}$ | $4.00\times10^{-4}$ |
| **Test 4** | $1.62\times10^{-2}$ | $2.79\times10^{-2}$ | $2.24\times10^{-2}$ | $4.00\times10^{-4}$ |
| **Test 5** | $1.63\times10^{-2}$ | $2.81\times10^{-2}$ | $2.27\times10^{-2}$ | $0.00$ |
| **Mean** | $1.62\times10^{-2}$ | $2.80\times10^{-2}$ | $2.27\times10^{-2}$ | $2.00\times10^{-4}$ |

Table D.27    Performance of retuned DVMPC for large payload (0.32kg) at pneumatic mode, without payload estimation, trajectory 4

|        | RMSE(radian)        | MAE(radian)         |
|--------|---------------------|---------------------|
| Test 1 | $3.34\times10^{-1}$ | $7.37\times10^{-1}$ |
| Test 2 | $7.60\times10^{-1}$ | 1.03                |
| Test 3 | $3.33\times10^{-1}$ | $7.22\times10^{-1}$ |
| Test 4 | $7.61\times10^{-1}$ | 1.03                |
| Test 5 | $7.28\times10^{-1}$ | $9.94\times10^{-1}$ |
| Mean   | $5.83\times10^{-1}$ | $9.03\times10^{-1}$ |

Table D.28    Performance of retuned DVMPC for large payload (0.32kg) at hybrid mode, without payload estimation, trajectory 4

|        | RMSE(radian)        | MAE(radian)         |
|--------|---------------------|---------------------|
| Test 1 | $2.87\times10^{-2}$ | $1.57\times10^{-1}$ |
| Test 2 | $2.68\times10^{-2}$ | $1.44\times10^{-1}$ |
| Test 3 | $2.61\times10^{-2}$ | $1.36\times10^{-1}$ |
| Test 4 | $2.24\times10^{-2}$ | $1.06\times10^{-1}$ |
| Test 5 | $2.56\times10^{-2}$ | $1.37\times10^{-1}$ |
| Mean   | $2.59\times10^{-2}$ | $1.36\times10^{-1}$ |

Table D.29      Performance of retuned DVMPC for large payload (0.32kg) at
pneumatic mode, with payload estimation, trajectory 1

| Errors(radian) | RMSE | MAE | SSE | SSA |
|---|---|---|---|---|
| Test 1 | $1.78 \times 10^{-2}$ | $2.96 \times 10^{-2}$ | $2.48 \times 10^{-2}$ | $2.00 \times 10^{-4}$ |
| Test 2 | $1.79 \times 10^{-2}$ | $2.89 \times 10^{-2}$ | $2.48 \times 10^{-2}$ | $2.00 \times 10^{-4}$ |
| Test 3 | $1.80 \times 10^{-2}$ | $3.05 \times 10^{-2}$ | $2.51 \times 10^{-2}$ | $2.00 \times 10^{-4}$ |
| Test 4 | $1.80 \times 10^{-2}$ | $3.05 \times 10^{-2}$ | $2.51 \times 10^{-2}$ | $3.00 \times 10^{-4}$ |
| Test 5 | $1.90 \times 10^{-2}$ | $6.66 \times 10^{-2}$ | $2.48 \times 10^{-2}$ | $1.00 \times 10^{-4}$ |
| Mean | $1.81 \times 10^{-2}$ | $3.72 \times 10^{-2}$ | $2.49 \times 10^{-2}$ | $2.00 \times 10^{-4}$ |

Table D.30      Performance of retuned DVMPC for large payload (0.32kg) at hybrid

mode, with payload estimation, trajectory 1

| Errors(radian) | RMSE | MAE | SSE | SSA |
|---|---|---|---|---|
| Test 1 | $1.34 \times 10^{-2}$ | $2.39 \times 10^{-2}$ | $1.88 \times 10^{-2}$ | $1.00 \times 10^{-4}$ |
| Test 2 | $1.14 \times 10^{-2}$ | $2.02 \times 10^{-2}$ | $1.58 \times 10^{-2}$ | $6.00 \times 10^{-4}$ |
| Test 3 | $1.09 \times 10^{-2}$ | $1.89 \times 10^{-2}$ | $1.53 \times 10^{-2}$ | $1.00 \times 10^{-4}$ |
| Test 4 | $1.00 \times 10^{-2}$ | $1.82 \times 10^{-2}$ | $1.37 \times 10^{-2}$ | $3.00 \times 10^{-4}$ |
| Test 5 | $8.75 \times 10^{-3}$ | $1.56 \times 10^{-2}$ | $1.19 \times 10^{-2}$ | $4.00 \times 10^{-4}$ |
| Mean | $1.09 \times 10^{-2}$ | $1.94 \times 10^{-2}$ | $1.51 \times 10^{-2}$ | $3.00 \times 10^{-4}$ |

Table D.31      Performance of retuned DVMPC for large payload (0.32kg) at pneumatic mode, with payload estimation, trajectory 4

|        | RMSE(radian) | MAE(radian) |
|--------|--------------|-------------|
| Test 1 | $7.53 \times 10^{-1}$ | $9.97 \times 10^{-1}$ |
| Test 2 | $7.69 \times 10^{-1}$ | 1.02 |
| Test 3 | $8.74 \times 10^{-1}$ | 1.13 |
| Test 4 | $7.54 \times 10^{-1}$ | $9.99 \times 10^{-1}$ |
| Test 5 | $7.77 \times 10^{-1}$ | 1.03 |
| Mean   | $7.85 \times 10^{-1}$ | 1.04 |

Table D.32      Performance of retuned DVMPC for large payload (0.32kg) at hybrid mode, with payload estimation, trajectory 4

|        | RMSE(radian) | MAE(radian) |
|--------|--------------|-------------|
| Test 1 | $3.52 \times 10^{-2}$ | $1.27 \times 10^{-1}$ |
| Test 2 | $2.24 \times 10^{-2}$ | $1.27 \times 10^{-1}$ |
| Test 3 | $2.81 \times 10^{-2}$ | $1.65 \times 10^{-1}$ |
| Test 4 | $5.58 \times 10^{-1}$ | 1.03 |
| Test 5 | $2.80 \times 10^{-2}$ | $1.65 \times 10^{-1}$ |
| Mean   | $1.34 \times 10^{-1}$ | $3.23 \times 10^{-1}$ |